The Thesis Committee for Anthony William Barone
Certifies that this is the approved version of the following thesis:

Anisotropic Analysis and Fracture Characterization of the Haynesville Shale, Panola County, Texas

APPROVED BY
SUPERVISING COMMITTEE:

Supervisor:

Mrinal K. Sen

Kyle T. Spikes

Stephen P. Grand

Anisotropic Analysis and Fracture Characterization of the Haynesville Shale, Panola County, Texas

by

Anthony William Barone, B.A. Geophysics

Thesis

Presented to the Faculty of the Graduate School of

The University of Texas at Austin

in Partial Fulfillment

of the Requirements

for the Degree of

Master of Science in Geological Sciences

The University of Texas at Austin

August 2015

Dedication

I would like to dedicate this thesis to my family. They have been wonderfully supportive of my education throughout the years, and without them I would not be where I am today.

Acknowledgements

A number of people have been instrumental both in my success in graduate school and in helping me complete this thesis. First and foremost, I would like to thank my advisor, Dr. Mrinal Sen, both for giving me the opportunity to carry out this research and for helping me throughout its completion. I would like to thank Thomas Hess for aiding me with new software and helping to figure out software issues on numerous occasions. I would like to thank Philip Guerrero for ensuring that I made it through all the parts of graduate school that aren't related to research and academics. Lastly, I would like to thank my fellow grad students, especially those in my research group, for helping me to learn and understand new concepts, finish homework assignments on time, prepare for exams, make deadlines for submitting papers, and generally succeed in graduate school.

Abstract

Anisotropic Analysis and Fracture Characterization of the Haynesville Shale, Panola County, Texas

Anthony William Barone, M.S.Geo.Sci.

The University of Texas at Austin, 2015

Supervisor: Mrinal K. Sen

In unconventional resources such as the Haynesville Shale, a proper understanding of natural fracture patterns is essential to enhancing the economic success of petroleum extraction. The spatial density of naturally occurring fracture sets affects drainage area and optimal drilling location(s), and the azimuth of the strike of the predominant fracture set affects the ideal orientation of wells. In the absence of data to directly determine these fracture characteristics, such as Formation Microimaging (FMI) logs, these natural fracture patterns can be analyzed by examining the seismic anisotropy present in the reservoir. Anisotropy introduced from aligned fracture sets creates predictable azimuthal variations in the seismic wavefield. This allows the reservoir anisotropy, and thus the fracturing present in the reservoir, to be studied indirectly through the azimuthal analysis of industry standard 3D seismic data.

The work presented here outlines three distinct methodologies, which utilize azimuthal amplitude variations (AVAZ) present in 3D seismic data, to infer fracture characteristics without the need for substantial well log information. Two of these

methods have been previously established and assume the reservoir to be characteristic of Horizontally Transverse Isotropic (HTI). The last method is novel and assumes orthorhombic anisotropy when inverting for fracture density and is able to unambiguously invert for fracture azimuth.

All methodologies used in this work produced similar results, increasing confidence in the accuracy of these results through statistical repeatability. Fracture density inversion results indicate spatially varying fracture density throughout the area, with a distinct area of higher fracture density present in the Northwestern corner of the area analyzed. Spatially varying fracture density and localized pockets of fracturing is consistent with expectation from analyzing production data and FMI logs from other areas of the Haynesville. Fracture azimuth inversion results showed some variability; however, the novel method presented in this thesis indicates that the azimuth of the predominant fracture set is oriented at a compass bearing of approximately 82 degrees – rotated slightly counterclockwise from an east-west orientation. Fracture azimuth results agree well with expectations from a regional stress analysis and from examining comparable formations with known fracture patterns in the surrounding area.

Table of Contents

List of Tables x

List of Figures xi

Chapter 1: Introduction 1

1.1 Motivation 1

1.2 Objectives 6

1.3 Thesis Organization 7

Chapter 2: Background 8

2.1 Geologic Background of the Haynesville 8

2.2 Data Overview 11

2.3 Seismic Processing 16

Chapter 3: Theory 23

3.1 Wave Equation For Elastic Anisotropic Homogeneous Media 23

3.2 Solving for Reflectivity 26

3.3 Tensor Analysis 31

3.4 Linear Slip Theory and Effective Anisotropy 41

3.5 Inversion 47

Chapter 4: Existing Fracture Characterization Methods 52

4.1 Introduction 52

4.2 Rüger Method 53

4.3 Fourier Coefficient Decomposition Method 56

4.4 Results 60

4.5 Discussion 86

4.6 Summary 91

Chapter 5: Modified Fourier Coefficient Fracture Characterization Method 93

5.1 Introduction 93

5.2 Fourier Coefficient Decomposition Method 96

5.3 Algorithm 104
5.4 Generating Synthetic Data 112
5.5 Results 119
5.5.1 Synthetic Example – Fracture Azimuth 119
5.5.2 Haynesville Data – Fracture Azimuth 126
5.5.3 Synthetic Example – Fracture Density 142
5.5.4 Haynesville Data – Fracture Density 144
5.6 Discussion 162
5.7 Summary 172
Chapter 6: Conclusions and Future Work 173
6.1 Conclusions 173
6.2 Future Work 174
References 176
Vita 179

List of Tables

Table 2.1: A comprehensive list of all processing steps implemented by CGG: Veritas in June 2011. Steps are shown in the approximate order they were implemented. All processing steps shown here were completed prior to the onset of the work presented in this thesis. Refer to the text for explanations regarding each processing step and additional processing performed by the author.....18

Table 5.1: A table showing the different properties associated with the 62 synthetic cases generated and used in this study. e represents fracture density.115

Table 5.2: A table summarizing the results of the 38 synthetic cases with fracture azimuth ranging from 0 to 180 degrees in 10 degree increments. All cases represent the case of orthorhombic anisotropy and high fracture density. The inverted azimuth is considered correct if it lies within 5 degrees of the true azimuth. The column titled “Percent Correct” represents all data, and the column titled “Percent Correct (far offset)” represents data with an incident angle of greater than or equal to 30 degrees. 125

Table 5.3: A table summarizing the results of fracture density inversion for 24 synthetic cases with various properties. Inverted fracture density values for strong and weak fracturing are shown, as well as a multiplier which measures the relative difference in response between the strong and weak fracturing cases. 143

List of Figures

Figure 1.1: A simplified comparison of different fracture characterization techniques currently in use. Formation Microimaging (FMI), shown in the leftmost figure, produces an electrical-image of the rock formation surrounding the borehole, allowing for direct determination of fracturing characteristics immediately surrounding the borehole. The center figure depicts an analogous outcrop that has been interpreted with large fractures depicted with thick black lines and smaller fractures depicted with thin gray lines. The rightmost figure depicts a synthetic seismic wavefield associated with anisotropic media, where azimuthal variations in both seismic amplitude and seismic traveltime can be easily identified. Figure from Becker (2014). Leftmost figure originally from Xiao and Li (2011). Central figure originally from Strijker et al. (2012). 3

Figure 2.1: Paleogeography associated with Haynesville deposition North of the Gulf of Mexico in present day Eastern Texas and Northwestern Louisiana. The organic rich Haynesville Shale, which is the focus of this work, and surrounding lithofacies can be seen. Panola County is outlined by the red box. Figure from Hammes et al. (2011).....10

Figure 2.2: Isopach thickness map of the Haynesville Shale. Warmer colors indicate areas of thicker Haynesville Shale deposits. Blue areas correspond to carbonate shelves lacking any shale deposition. Panola County is outlined by the red box. Figure from Hammes et al. (2011).....11

Figure 2.3: Comparison of amplitude spectrum of the unmigrated 3D seismic dataset (upper) and the migrated 3D seismic dataset (lower). The X axis corresponds to frequency, and ranges from 0 Hz to 80 Hz. The Y axis represents normalized amplitude. Spectra calculated using Hampson-Russell ©.....13

Figure 2.4: (Upper): Map view of the entire unmigrated 3D seismic dataset, spanning 670 inlines and 300 crosslines. (Lower): Map view of the reduced seismic dataset, spanning 137 inlines and 137 crosslines, and its relative location within the full dataset. The * indicates the well location. The black arrows indicate the direction of north. 15

Figure 2.5: An example inline section of the seismic data with only processing steps shown in Table 2.1 implemented. This slice resides near the center of the area analyzed in this work. A well can be seen at the intersection of inline 3622 and crossline 1274. Data shows time ranges from roughly 1500 ms – 2400 ms. Offsets at each CDP range from 225m to 6025m. The Haynesville Shale is located from about 2040 ms – 2080 ms, between the blue and red horizons shown. 20

Figure 2.6: An example inline section of the seismic data with processing steps shown in Table 2.1 and all additional processing described in the text except azimuthal sorting implemented. Additional processing steps include NMO correction, a 2-6-90-110 bandpass filter, trim statics correction, and parabolic Radon filters for noise and multiple reduction. This slice resides near the center of the area analyzed in this work. A well can be seen at the intersection of inline 3622 and crossline 1274. Data show time ranges from roughly 1500 ms – 2400 ms. Offsets at each CDP range from 225m to 6025m. The Haynesville Shale is located from about 2040 ms – 2080 ms, between the blue and red horizons shown.21

Figure 2.7: An example azimuthal section of the seismic data at the CDP associated with inline 3622 and crossline 1274, with processing steps shown in Table 2.1 and all additional processing described in the text applied. Additional processing steps include NMO correction, a 2-6-90-110 bandpass filter, trim statics correction, and parabolic Radon filters for noise and multiple reduction, and azimuthal sorting. This section resides near the center of the area analyzed in this work. The HTI binning scheme is shown, with 9 azimuthal bins and 30 offset bins. Primary trace sorting is by azimuth, and secondary sorting is by offset. Data show time ranges from roughly 1600 ms – 2400 ms. The Haynesville Shale is located from about 2040 ms – 2080 ms, between the blue and red horizons shown. 22

Figure 3.1: A simplified spring and dashpot system. E represents the stiffness of the spring, and η represents the viscosity of the dashpot. Note that in seismology the analog to spring stiffness (E) is the stiffness tensor (C). 26

Figure 3.2: A graphical representation of stresses τ_{ij}. Stress τ_{ij} represents force on the cube face normal to direction î and acting in direction ĵ. Stresses on adjacent faces of the cube are identical. Strain ε_{kl} can be interpreted in a similar way. Note that normal stresses τ_{ij} have been replaced with σ_i. 32

Figure 3.3: A graphical representation of vectors x_1 and x_2 in 2 dimensions, which correspond to the X and Y axis, being rotated by θ degrees counter clockwise. The resulting rotated vectors are notated x_1' and x_2'. Figure originally from Sen, Seismology III, class notes. 35

Figure 4.1: Comparison of exact and approximate reflectivity, calculated using the Rüger AVO equation shown in Equation 4.1. In all images the solid line represents exact reflectivity, and the dashed line represents approximated reflectivity. The leftmost image depicts the isotropic case. The middle image depicts the HTI case associated with fluid filled fractures. The rightmost image depicts the HTI case associated with dry fractures. The X axis represents incident angle, and the Y axis represents reflectivity. In the center and rightmost images reflectivity for azimuths corresponding to 0 degrees, 30 degrees, 60 degrees and 90 degrees from the symmetry axis are shown. Figure from Rüger and Tsvankin (1997). 54

Figure 4.2: Anisotropic Gradient, a proxy for fracture density, calculated using the Rüger method and vertically averaged within the Haynesville Shale. Warmer colors represent denser fracture spacing. The red arrow indicates the direction of north. 61

Figure 4.3: Fracture orientation and Anisotropic Gradient, a proxy for fracture density, calculated using the Rüger method and vertically averaged within the Haynesville Shale. Fracture orientation is represented by planar features superimposed on the image which are oriented in the plane of fracture strike. Warmer background colors represent denser fracture spacing. The red arrow indicates the direction of north. 62

Figure 4.4: r_2 Fourier coefficient, a proxy for fracture density, calculated using the Fourier coefficient decomposition method and vertically averaged within the Haynesville Shale. Warmer colors represent denser fracture spacing. The red arrow indicates the direction of north. 63

Figure 4.5: Fracture orientation, from 2nd order Fourier coefficient phase φ_{sym}, and r_2 Fourier coefficient, a proxy for fracture density, calculated using the Fourier coefficient decomposition method and vertically averaged within the Haynesville Shale. Fracture orientation is represented by planar features superimposed on the image which are oriented in the plane of fracture strike. Warmer background colors represent denser fracture spacing. The red arrow indicates the direction of north.....63

Figure 4.6: Fracture orientation, from 4th order Fourier coefficient phase φ_{sym}, and r_2 Fourier coefficient, a proxy for fracture density, calculated using the Fourier coefficient decomposition method and vertically averaged within the Haynesville Shale. Fracture orientation is represented by planar features superimposed on the image which are oriented in the plane of fracture strike. Warmer background colors represent denser fracture spacing. The red arrow indicates the direction of north.....64

Figure 4.7: Normal fracture weakness (ΔN), as calculated from a least squares inversion of r_2 and r_4 Fourier coefficients. Warmer colors indicate higher values. The black arrow indicates the direction of north.....65

Figure 4.8: Tangential fracture weakness (ΔN), as calculated from a least squares inversion of r_2 and r_4 Fourier coefficients. Warmer colors indicate higher values. The black arrow indicates the direction of north.....66

Figure 4.9: Anisotropic gradient (B_{ani}), as calculated from the values of normal and tangential fracture weakness (ΔN and ΔT) found via a least squares inversion of r_2 and r_4 Fourier coefficients. Anisotropic gradient is a proxy for fracture density. Warmer colors indicate denser fracture spacing. The black arrow indicates the direction of north. 67

Figure 4.10: Fluid indicator attribute, as calculated from the values of normal and tangential fracture weakness (ΔN and ΔT) found via a least squares inversion of r_2 and r_4 Fourier coefficients. Warmer colors indicate higher values. The colorbar ranges from approximately 0.7 to 1.2. Because the fluid indicator attribute is based on the ratios of velocities and fracture weaknesses, it is unitless. The black arrow indicates the direction of north.....68

Figure 4.11: Comparison of proxies for fracture density from the Rüger and Fourier coefficient decomposition methods. B_{ani} from the Ruger method is shown above, andr_2 from the Fourier coefficient decomposition method is shown below. Values have been vertically averaged throughout the Haynesville using a simple arithmetic mean. Warmer colors indicate denser fracture spacing. The black arrows indicate the direction of north. 70

Figure 4.12: Comparison of proxies for fracture density from the Rüger and Fourier coefficient decomposition methods. B_{ani} from the Ruger method is shown above, and r_2 from the Fourier coefficient decomposition method is shown below. Values corresponding to the top of the Haynesville are shown. Warmer colors indicate denser fracture spacing. The black arrows indicate the direction of north. 71

Figure 4.13: Comparison of proxies for fracture density from the Rüger and Fourier coefficient decomposition methods. B_{ani} from the Ruger method is shown above, and r_2 from the Fourier coefficient decomposition method is shown below. Values corresponding to approximately 15 m from the top of the Haynesville are shown. Warmer colors indicate denser fracture spacing. The black arrows indicate the direction of north...72

Figure 4.14: Comparison of proxies for fracture density from the Rüger and Fourier coefficient decomposition methods. B_{ani} from the Ruger method is shown above, and r_2 from the Fourier coefficient decomposition method is shown below. Values corresponding to approximately 30 m from the top of the Haynesville are shown. Warmer colors indicate denser fracture spacing. The black arrows indicate the direction of north...73

Figure 4.15: Comparison of proxies for fracture density from the Rüger and Fourier coefficient decomposition methods. B_{ani} from the Ruger method is shown above, and r_2 from the Fourier coefficient decomposition method is shown below. Values corresponding to approximately 45 m from the top of the Haynesville are shown. Warmer colors indicate denser fracture spacing. The black arrows indicate the direction of north...74

Figure 4.16: Comparison of proxies for fracture density from the Fourier coefficient decomposition method. r_2 coefficient is shown above, and B_{ani} calculated from inverted normal and tangential fracture weaknesses is shown below. Values have been vertically averaged throughout the Haynesville using a simple arithmetic mean. Warmer colors indicate denser fracture spacing. The black arrows indicate the direction of north. 75

Figure 4.17: Comparison of fracture azimuth as determined from the Rüger and Fourier coefficient decomposition methods. The top image depicts azimuth from the Rüger method, the middle image depicts azimuth from the 2nd Fourier coefficient phase φ_{sym} of the Fourier decomposition method, and the bottom image depicts azimuth from the 4th Fourier coefficient phase φ_{sym} of the Fourier decomposition method. Values have been vertically averaged throughout the Haynesville using the Yamartino method (described in Chapter 5 – see Equation 5.38). Colorbars on the top and middle image range from -90 degrees to 90 degrees. The colorbar on the bottom image ranges from -30 to 30 degrees. The black arrows indicate the direction of north. 76

Figure 4.18: Comparison of fracture azimuth as determined from the Rüger and Fourier coefficient decomposition methods. The top image depicts azimuth from the Rüger method, the middle image depicts azimuth from the 2nd Fourier coefficient phaseφ_{sym} of the Fourier decomposition method, and the bottom image depicts azimuth from the 4th Fourier coefficient phase φ_{sym} of the Fourier decomposition method. Values corresponding to the top of the Haynesville are shown. Colorbars range from -90 degrees to 90 degrees. The black arrows indicate the direction of north. 78

Figure 4.19: Comparison of fracture azimuth as determined from the Rüger and Fourier coefficient decomposition methods. The top image depicts azimuth from the Rüger method, the middle image depicts azimuth from the 2nd Fourier coefficient phase φ_{sym} of the Fourier decomposition method, and the bottom image depicts azimuth from the 4th Fourier coefficient phase φ_{sym} of the Fourier decomposition method. Values corresponding to 15 meters from the top of the Haynesville are shown. Colorbars range from -90 degrees to 90 degrees. The black arrows indicate the direction of north. 80

Figure 4.20: Comparison of fracture azimuth as determined from the Rüger and Fourier coefficient decomposition methods. The top image depicts azimuth from the Rüger method, the middle image depicts azimuth from the 2nd Fourier coefficient phase φ_{sym} of the Fourier decomposition method, and the bottom image depicts azimuth from the 4th Fourier coefficient phase φ_{sym} of the Fourier decomposition method. Values corresponding to 30 meters from the top of the Haynesville are shown. Colorbars range from -90 degrees to 90 degrees. The black arrows indicate the direction of north. 82

Figure 4.21: Comparison of fracture azimuth as determined from the Rüger and Fourier coefficient decomposition methods. The top image depicts azimuth from the Rüger method, the middle image depicts azimuth from the 2nd Fourier coefficient phase φ_{sym} of the Fourier decomposition method, and the bottom image depicts azimuth from the 4th Fourier coefficient phase φ_{sym} of the Fourier decomposition method. Values corresponding to 45 meters from the top of the Haynesville are shown. Colorbars range from -90 degrees to 90 degrees. The black arrows indicate the direction of north. 84

Figure 4.22: An example CDP from the azimuthal super gather depicting uneven azimuthal coverage. Primary trace sorting is by azimuth, and secondary sorting is by offset. Note that azimuthal coverage is dense in azimuths between 120 degrees – 40 degrees, corresponding to the inline direction; and dilute in azimuths between 40 degrees – 120 degrees, corresponding to the crossline direction. Data shows time ranges from roughly 1500 ms – 2400 ms. The Haynesville Shale is located from about 2040 ms – 2080 ms, between the blue and red horizons shown.....88

Figure 4.23: Predicted fracture orientation map, determined from analysis of in-situ geologic stress, in the United States. The red box indicates the approximate location of the Haynesville Shale analyzed in this paper. Figure from Hunt et al. (2009).....91

Figure 5.1: A set of figures depicting azimuthal variations with respect to azimuth in four cases – a HTI medium (upper left), an isotropic medium (lower left), an orthorhombic medium (upper right), and a VTI medium (lower right). The horizontal axis represents azimuth, and ranges from 0 to 180 degrees in all images. The vertical axis represents seismic amplitude, and has a total range of 0.01 in all images. Synthetic data were generated as described in Section 5.4. In these cases, fractures are gas filled and have an azimuth of 0 degrees. Figures show data from the 30 – 35 degree incident angle range. All stiffness tensors used in data generation were calculated from an identical isotropic background stiffness tensor. In the anisotropic cases, anisotropy was introduced using excess compliance theory and tensor rotations, as described in Chapter 3. Phase remains identical in the HTI and Orthorhombic cases, though some variation in the magnitude and shape of these curves can be seen. The VTI and isotropic cases show minimal azimuthal variation. 95

Figure 5.2: A plot indicating the sign of the 2^{nd} and 3^{rd} terms in Equation 5.32 as a function of incident angle and g for the case of either dry or gas filled fractures. Red indicates the combined terms have positive value, while blue indicates the combined terms have a negative value. The x axis represents incident angle and ranges from 0 to 50 degrees. The y axis represents g and ranges from 0.1 to 0.7. 103

Figure 5.3: A diagram depicting the two layer model used in generating the synthetic data. P-wave velocity (V_p), S-wave velocity (V_s), density (ρ) and thickness (h) for the upper isotropic layer are shown. 114

Figure 5.4: A) An example data slice of a synthetic dataset without any processing performed. The horizontal axis represents position, the vertical axis represents time, and color represents seismic amplitude. The upper event represents the P-P reflection data which was used in this study. The lower event represents the P-S reflection which was not used. B) An example data slice of a synthetic dataset with NMO correction and trim statics corrections performed. The horizontal axis represents position, the vertical axis represents time, and color represents seismic amplitude. The black horizontal lines are plot guides to indicate how flat the data is, however are not data themselves. The upper event represents the P-P reflection data which was used in this study. The lower event represents the P-S reflection which was not used. C) An example section of an azimuthal gather at some time, incident angle and position. The horizontal axis represents azimuth and ranges from 0 to 180 degrees. The vertical axis represents seismic amplitude. The blue dots are individual data points and the red line is the Fourier series that the fracture characterization algorithm generates. 117

Figure 5.5: A histogram showing the combined results of fracture azimuth inversion for the 12 synthetic cases where the true fracture azimuth is 0 degrees. Note that 0 and 180 degrees represent the same azimuth. The horizontal axis represents azimuth and ranges from 0 to 180 degrees, and the vertical axis represents bin count. Each bin represents 5 degrees of azimuth. Data from all incident angles are shown. 120

Figure 5.6: A histogram showing the combined results of fracture azimuth inversion for the 12 synthetic cases where the true fracture azimuth is 0 degrees. Note that 0 and 180 degrees represent the same azimuth. The horizontal axis represents azimuth and ranges from 0 to 180 degrees, and the vertical axis represents bin count. Each bin represents 5 degrees of azimuth. Only data corresponding to large offsets (incident angle > 30 degrees) is shown. 121

Figure 5.7: A histogram showing the combined results of fracture azimuth inversion for the 12 synthetic cases where the true fracture azimuth is 135 degrees. The horizontal axis represents azimuth and ranges from 0 to 180 degrees, and the vertical axis represents bin count. Each bin represents 5 degrees of azimuth. Data from all incident angles are shown. 122

Figure 5.8: A histogram showing the combined results of fracture azimuth inversion for the 12 synthetic cases where the true fracture azimuth is 135 degrees. The horizontal axis represents azimuth and ranges from 0 to 180 degrees, and the vertical axis represents bin count. Each bin represents 5 degrees of azimuth. Only data corresponding to large offsets (incident angle > 30 degrees) is shown. 123

Figure 5.9: A histogram showing the combined results of fracture azimuth inversion for the Haynesville dataset. The horizontal axis represents azimuth and ranges from 0 to 180 degrees, and the vertical axis represents bin count. Each bin represents 2.5 degrees of azimuth. Data corresponding to all incident angles are shown. 126

Figure 5.10: A histogram showing the combined results of fracture azimuth inversion for the Haynesville dataset. The horizontal axis represents azimuth and ranges from 0 to 180 degrees, and the vertical axis represents bin count. Each bin represents 2.5 degrees of azimuth. Data corresponding to incident angles greater than or equal to 25 degrees are shown. 127

Figure 5.11: A histogram showing the combined results of fracture azimuth inversion for the Haynesville dataset. The horizontal axis represents azimuth and ranges from 0 to 180 degrees, and the vertical axis represents bin count. Each bin represents 2.5 degrees of azimuth. Data corresponding to incident angles greater than or equal to 33 degrees are shown. 128

Figure 5.12: Fracture azimuth, as calculated by the proposed new Fourier coefficient decomposition method. 2-D lateral smoothing has been applied. Values have been vertically averaged throughout the Haynesville using the Yamartino method. The colorbar ranges from -90 degrees to 90 degrees. The black arrow indicates the direction of north. 129

Figure 5.13: Comparison of fracture orientation as calculated by the proposed new method and the HTI Fourier coefficient decomposition based method. The top image depicts fracture orientation as calculated by the proposed new Fourier coefficient decomposition method. Data from large incident angles have been averaged, and 2-D lateral smoothing has been applied. The bottom image depicts fracture orientation as calculated by the HTI Fourier coefficient decomposition method using the phase of the r_2 Fourier coefficient. Values have been vertically averaged throughout the Haynesville using the Yamartino method. Colorbars range from -90 degrees to 90 degrees. The black arrows indicate the direction of north. 130

Figure 5.14: Fracture azimuth, as calculated by the proposed new Fourier coefficient decomposition method. Data from large incident angles have been averaged, and 2-D lateral smoothing has been applied. Values corresponding to a constant time of 2060 ms are shown. The colorbar ranges from -90 degrees to 90 degrees. The black arrow indicates the direction of north.....131

Figure 5.15: Comparison of fracture orientation as calculated by the proposed new method and the HTI Fourier coefficient decomposition based method. The top image depicts fracture orientation as calculated by the proposed new Fourier coefficient decomposition method. Data from large incident angles have been averaged, and 2-D lateral smoothing has been applied. The bottom image depicts fracture orientation as calculated by the HTI Fourier coefficient decomposition method using the phase of the r_2 Fourier coefficient. Values corresponding to a constant time of 2060 ms are shown. Colorbars range from -90 degrees to 90 degrees. The black arrows indicate the direction of north. 132

Figure 5.16: Fracture azimuth, as calculated by the proposed new Fourier coefficient decomposition method. 2-D lateral smoothing has been applied. Values corresponding to the top of the Haynesville are shown. The colorbar ranges from -90 degrees to 90 degrees. The black arrow indicates the direction of north.....134

Figure 5.17: Fracture azimuth, as calculated by the proposed new Fourier coefficient decomposition method. 2-D lateral smoothing has been applied. Values corresponding to approximately 15 m from the top of the Haynesville are shown. The colorbar ranges from -90 degrees to 90 degrees. The black arrow indicates the direction of north. 135

Figure 5.18: Fracture azimuth, as calculated by the proposed new Fourier coefficient decomposition method. 2-D lateral smoothing has been applied. Values corresponding to approximately 30 m from the top of the Haynesville are shown. The colorbar ranges from -90 degrees to 90 degrees. The black arrow indicates the direction of north. 136

Figure 5.19: Fracture azimuth, as calculated by the proposed new Fourier coefficient decomposition method. 2-D lateral smoothing has been applied. Values corresponding to approximately 45 m from the top of the Haynesville are shown. The colorbar ranges from -90 degrees to 90 degrees. The black arrow indicates the direction of north. 137

Figure 5.20: Comparison of fracture orientation as calculated by the proposed new method and the HTI Fourier coefficient decomposition based method. The top image depicts fracture orientation as calculated by the proposed new Fourier coefficient decomposition method. 2-D lateral smoothing has been applied. The bottom image depicts fracture orientation as calculated by the HTI Fourier coefficient decomposition method using the phase of the r_2 Fourier coefficient. Values corresponding to the top of the Haynesville are shown. Colorbars range from -90 degrees to 90 degrees. The black arrows indicate the direction of north. 138

Figure 5.21: Comparison of fracture orientation as calculated by the proposed new method and the HTI Fourier coefficient decomposition based method. The top image depicts fracture orientation as calculated by the proposed new Fourier coefficient decomposition method. 2-D lateral smoothing has been applied. The bottom image depicts fracture orientation as calculated by the HTI Fourier coefficient decomposition method using the phase of the r_2 Fourier coefficient. Values corresponding to approximately 15 m from the top of the Haynesville are shown. Colorbars range from -90 degrees to 90 degrees. The black arrows indicate the direction of north. 139

Figure 5.22: Comparison of fracture orientation as calculated by the proposed new method and the HTI Fourier coefficient decomposition based method. The top image depicts fracture orientation as calculated by the proposed new Fourier coefficient decomposition method. 2-D lateral smoothing has been applied. The bottom image depicts fracture orientation as calculated by the HTI Fourier coefficient decomposition method using the phase of the r_2 Fourier coefficient. Values corresponding to approximately 30 m from the top of the Haynesville are shown. Colorbars range from -90 degrees to 90 degrees. The black arrows indicate the direction of north. 140

Figure 5.23: Comparison of fracture orientation as calculated by the proposed new method and the HTI Fourier coefficient decomposition based method. The top image depicts fracture orientation as calculated by the proposed new Fourier coefficient decomposition method. 2-D lateral smoothing has been applied. The bottom image depicts fracture orientation as calculated by the HTI Fourier coefficient decomposition method using the phase of the r_2 Fourier coefficient. Values corresponding to approximately 45 m from the top of the Haynesville are shown. Colorbars range from -90 degrees to 90 degrees. The black arrows indicate the direction of north. 141

Figure 5.24: R2*, a proxy for fracture density, as calculated by the Orthorhombic Fourier coefficient decomposition method. R_2^* is a measure of combined evergy in w_{12} and w_{22}, corresponding to 2nd order sine and cosine terms in the Fourier series. 2-D lateral smoothing has not been applied. Values have been vertically averaged throughout the Haynesville using a simple arithmetic mean. Warmer colors indicate denser fracturing. The black arrow indicates the direction of north. 145

Figure 5.25: R_2^*, a proxy for fracture density, as calculated by the Orthorhombic Fourier coefficient decomposition method. R_2^* is a measure of combined evergy in w_{12} and w_{22}, corresponding to 2nd order sine and cosine terms in the Fourier series. 2-D lateral smoothing has been applied. Values have been vertically averaged throughout the Haynesville using a simple arithmetic mean. Warmer colors indicate denser fracturing. The black arrow indicates the direction of north. 146

Figure 5.26: Comparison of proxies for fracture density from the Orthorhombic and HTI Fourier coefficient decomposition based methods. The top image depicts R_2^*, a proxy for fracture density, as calculated by the Orthorhombic Fourier coefficient decomposition method. 2-D lateral smoothing has not been applied. The bottom image depicts r_2 as calculated by the HTI Fourier coefficient decomposition method. The black arrows indicate the direction of north. 147

Figure 5.27: Comparison of proxies for fracture density from the Orthorhombic and HTI Fourier coefficient decomposition based methods. The top image depicts R_2^*, a proxy for fracture density, as calculated by the Orthorhombic Fourier coefficient decomposition method. 2-D lateral smoothing has been applied. The bottom image depicts r_2 as calculated by the HTI Fourier coefficient decomposition method. Values have been vertically averaged throughout the Haynesville using a simple arithmetic mean. Warmer colors indicate denser fracturing. The black arrows indicate the direction of north. 148

Figure 5.28: R_2^*, a proxy for fracture density, as calculated by the Orthorhombic Fourier coefficient decomposition method. R_2^* is a measure of combined evergy in w_{12} and w_{22}, corresponding to 2nd order sine and cosine terms in the Fourier series. 2-D lateral smoothing has not been applied. Values corresponding to a constant time of 2060 ms are shown. Warmer colors indicate denser fracturing. The black arrow indicates the direction of north. 149

Figure 5.29: R_2^*, a proxy for fracture density, as calculated by the Orthorhombic Fourier coefficient decomposition method. R_2^* is a measure of combined evergy in w_{12} and w_{22}, corresponding to 2nd order sine and cosine terms in the Fourier series. 2-D lateral smoothing has been applied. Values corresponding to a constant time of 2060 ms are shown. Warmer colors indicate denser fracturing. The black arrow indicates the direction of north. 150

Figure 5.30: Comparison of proxies for fracture density from the Orthorhombic and HTI Fourier coefficient decomposition based methods. The top image depicts R_2^*, a proxy for fracture density, as calculated by the Orthorhombic Fourier coefficient decomposition method. 2-D lateral smoothing has not been applied. The bottom image depicts r_2 as calculated by the HTI Fourier coefficient decomposition method. Values corresponding to a constant time of 2060 ms are shown. Warmer colors indicate denser fracturing. The black arrows indicate the direction of north. 151

Figure 5.31: Comparison of proxies for fracture density from the Orthorhombic and HTI Fourier coefficient decomposition based methods. The top image depicts R_2^*, a proxy for fracture density, as calculated by the Orthorhombic Fourier coefficient decomposition method. 2-D lateral smoothing has been applied. The bottom image depicts r_2 as calculated by the HTI Fourier coefficient decomposition method. Values corresponding to a constant time of 2060 ms are shown. Warmer colors indicate denser fracturing. The black arrows indicate the direction of north. 152

Figure 5.32: R_2^*, a proxy for fracture density, as calculated by the Orthorhombic Fourier coefficient decomposition method. R_2^* is a measure of combined evergy in w_{12} and w_{22}, corresponding to 2nd order sine and cosine terms in the Fourier series. 2-D lateral smoothing has been applied. Values corresponding to the top of the Haynesville are shown. Warmer colors indicate denser fracturing. The black arrow indicates the direction of north. 154

Figure 5.33: R_2^*, a proxy for fracture density, as calculated by the Orthorhombic Fourier coefficient decomposition method. R_2^* is a measure of combined evergy in w_{12} and w_{22}, corresponding to 2nd order sine and cosine terms in the Fourier series. 2-D lateral smoothing has been applied. Values corresponding to approximately 15 m from the top of the Haynesville are shown. Warmer colors indicate denser fracturing. The black arrow indicates the direction of north. 155

Figure 5.34: R_2^*, a proxy for fracture density, as calculated by the Orthorhombic Fourier coefficient decomposition method. R_2^* is a measure of combined evergy in w_{12} and w_{22}, corresponding to 2nd order sine and cosine terms in the Fourier series. 2-D lateral smoothing has been applied. Values corresponding to approximately 30 m from the top of the Haynesville are shown. Warmer colors indicate denser fracturing. The black arrow indicates the direction of north. 156

Figure 5.35: R_2^*, a proxy for fracture density, as calculated by the Orthorhombic Fourier coefficient decomposition method. R_2^* is a measure of combined evergy in w_{12} and w_{22}, corresponding to 2nd order sine and cosine terms in the Fourier series. 2-D lateral smoothing has been applied. Values corresponding to approximately 45 m from the top of the Haynesville are shown. Warmer colors indicate denser fracturing. The black arrow indicates the direction of north. 157

Figure 5.36: Comparison of proxies for fracture density from the Orthorhombic and HTI Fourier coefficient decomposition based methods. The top image depicts R_2^*, a proxy for fracture density, as calculated by the Orthorhombic Fourier coefficient decomposition method. 2-D lateral smoothing has been applied. The bottom image depicts r_2 as calculated by the HTI Fourier coefficient decomposition method. Values corresponding to the top of the Haynesville are shown. Warmer colors indicate denser fracturing. The black arrows indicate the direction of north. 158

Figure 5.37: Comparison of proxies for fracture density from the Orthorhombic and HTI Fourier coefficient decomposition based methods. The top image depicts R_2^*, a proxy for fracture density, as calculated by the Orthorhombic Fourier coefficient decomposition method. 2-D lateral smoothing has been applied. The bottom image depicts r_2 as calculated by the HTI Fourier coefficient decomposition method. Values corresponding to approximately 15 m from the top of the Haynesville are shown. Warmer colors indicate denser fracturing. The black arrows indicate the direction of north. 159

Figure 5.38: Comparison of proxies for fracture density from the Orthorhombic and HTI Fourier coefficient decomposition based methods. The top image depicts R_2^*, a proxy for fracture density, as calculated by the Orthorhombic Fourier coefficient decomposition method. 2-D lateral smoothing has been applied. The bottom image depicts r_2 as calculated by the HTI Fourier coefficient decomposition method. Values corresponding to approximately 30 m from the top of the Haynesville are shown. Warmer colors indicate denser fracturing. The black arrows indicate the direction of north. 160

Figure 5.39: Comparison of proxies for fracture density from the Orthorhombic and HTI Fourier coefficient decomposition based methods. The top image depicts R_2^*, a proxy for fracture density, as calculated by the Orthorhombic Fourier coefficient decomposition method. 2-D lateral smoothing has been applied. The bottom image depicts r_2 as calculated by the HTI Fourier coefficient decomposition method. Values corresponding to approximately 45 m from the top of the Haynesville are shown. Warmer colors indicate denser fracturing. The black arrows indicate the direction of north. 161

Figure 5.40: Comparison of data slices from the synthetic datasets. The left image shows a slice from the orthorhombic synthetic dataset with gas filled fractures, and the right image shows a slice from the HTI (a) dataset with gas filled fractures. The colorbar represents seismic amplitude. The same color scale is used in both images. The horizontal axis indicates position, and the vertical axis indicates time. No processing has been performed on the data. 165

Figure 5.41: Comparison of proxies for fracture density from the Orthorhombic and HTI Fourier coefficient decomposition based methods. The top image depicts R_2^*, a proxy for fracture density, as calculated by the Orthorhombic Fourier coefficient decomposition method. 2-D lateral smoothing has been applied. The bottom image depicts r_2 as calculated by the HTI Fourier coefficient decomposition method. Values have been vertically averaged throughout the Haynesville using a simple arithmetic mean. Warmer colors indicate denser fracturing. The black circle indicates an area of anomalously high fracture density identified in the orthorhombic method. The black arrows indicate the direction of north. 168

Figure 5.42: Examples of fitting a Fourier series at a specific time / location and constant incident angle with sufficient azimuthal coverage (upper) and insufficient azimuthal coverage (lower). When large chunks of azimuthal coverage are missing (lower) the curve fitting algorithm creates extreme and unrealistic features to better match available data. The X axis represents azimuth (ranging from 0 to 180 degrees), and the Y axis represents seismic amplitude. 171

Chapter 1: Introduction

1.1 MOTIVATION

Characterizing natural fracture networks in unconventional reservoirs is essential both in optimizing current production in existing plays and to find new areas in unconventional plays that are economic to produce. Maximizing the use of existing unconventional resources and ensuring new unconventional discoveries are economically feasible is especially important in today's age of declining conventional field discoveries. Improper understanding of the natural fracture systems present in a reservoir could lead to incorrect well placement and/or incorrect well orientation, significantly reducing the productive potential of the field. Additionally, natural fracturing plays an important role in planning induced hydraulic fracturing for enhanced hydrocarbon recovery. Enhanced recovery projects might aim to avoid fractures that have the ability to consume large amounts of fracturing fluid, reducing fluid pressure and fracturing potential. Alternately, enhanced recovery projects might attempt to connect natural fracture sets, allowing hydrocarbons over a substantial area to be funneled to a single well location (Orangi et al., 2011).

Fracture characteristics can be directly inferred via well logs which aim to directly detect fractures, such as Formation Microimaging (FMI) logs and by examining outcrops of the formation in question (Becker, 2014). Both of these direct methods, however, have limited applicability. In an analogous outcrop analysis there is no guarantee that the reservoir has similar fracture characteristics to the exposed part of the formation, which could be hundreds of miles from the reservoir in question and have undergone uplift, deformation, and weathering. FMI logs, when available, directly indicate fracture characteristics of the reservoir in question and provide high resolution information;

however, they only portray 1D information and are often sparse, leaving the vast majority of the reservoir that is away from well control without information on fracturing. Three dimensional (3D) seismic data, being laterally extensive and sampling the reservoir in question rather than an analog, is not plagued by the downfalls of FMI logs and analogous outcrop examination. Despite having lower resolution and indirectly detecting fracturing, seismic data provides an optimal data type for understanding the fracture characteristics of the entire reservoir and is ideal for 3D reservoir characterization. Figure 1.1 shows a simplified comparison of these different fracture characterization techniques. Ideally, all of the above methods should be used in combination with each other, taking care to correct for issues of scale, resolution, frequency-dependent responses, and lateral variability. This work, however, will focus exclusively on the analysis of 3D seismic data for the purpose of inferring large-scale 3D fracturing characteristics of the reservoir.

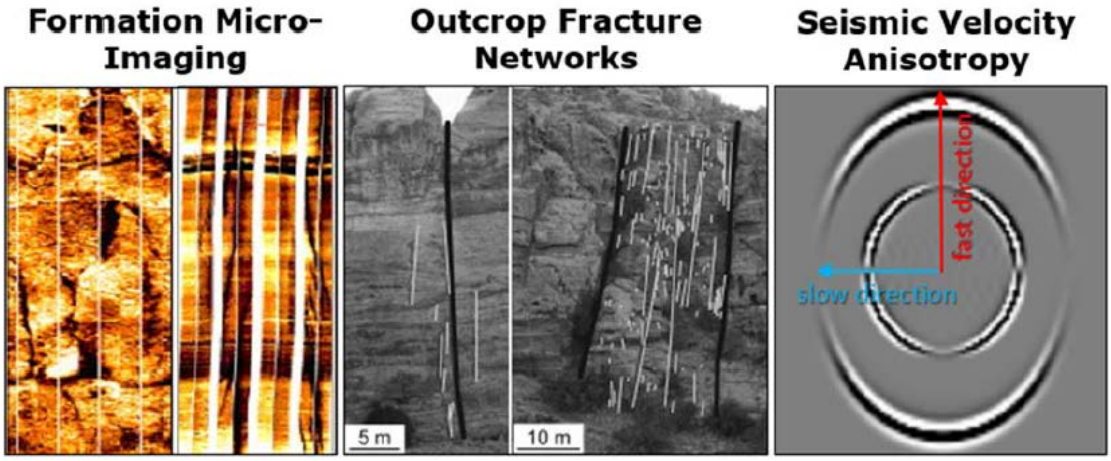

Figure 1.1: A simplified comparison of different fracture characterization techniques currently in use. Formation Microimaging (FMI), shown in the leftmost figure, produces an electrical-image of the rock formation surrounding the borehole, allowing for direct determination of fracturing characteristics immediately surrounding the borehole. The center figure depicts an analogous outcrop that has been interpreted with large fractures depicted with thick black lines and smaller fractures depicted with thin gray lines. The rightmost figure depicts a synthetic seismic wavefield associated with anisotropic media, where azimuthal variations in both seismic amplitude and seismic traveltime can be easily identified. Figure from Becker (2014). Leftmost figure originally from Xiao and Li (2011). Central figure originally from Strijker et al. (2012).

In today's era of computerized data analysis and remarkable computer processing power, routine analysis of 3D seismic data to infer fracture characteristics has become common in industry. The ability to do so is implemented in many major commercial software packages that perform seismic data analysis. Most, if not all, of these software packages, however, suffer from two substantial limitations:

1. An assumption of Horizontally Transverse Isotropic (HTI) medium.
2. An inability to unambiguously determine fracture azimuth.

Effective medium theory indicates that an effective HTI medium is the result of the underlying assumption that fractures are closely spaced (relative to a seismic

wavelength), vertically aligned, rotationally invariant, and embedded in an otherwise homogeneous isotropic rock. Although any of these underlying assumptions could prove to be false, the assumption of an isotropic background rock is certainly incorrect to some degree in the case of a Vertically Transverse Isotropic (VTI) background rock, such as a finely layered medium or a shale. Effective medium theory indicates that a single closely spaced, vertically aligned, rotationally invariant fracture set embedded in a VTI background rock results in orthorhombic anisotropy; however, this VTI component is largely ignored in industry seismic data analysis. Refer to Chapter 3 of this thesis for an overview of effective medium theory. In addition to a potentially incorrect assumption of the anisotropy type of the rock in question, existing fracture characterization methods are plagued by an inability to determine fracture azimuth without a 90-degree ambiguity. This 90-degree ambiguity in fracture azimuth will be further discussed in Chapters 4 and 5. The work presented in this thesis attempts to address both these limitations associated with common industry fracture characterization techniques. In part, this work aims to provide an easy-to-follow orthorhombic fracture characterization procedure that is computationally feasible to apply to large-scale industry seismic datasets. Additionally, this work aims to unambiguously determine fracture azimuth without the aforementioned 90-degree ambiguity in orientation. Furthermore, this work provides a comparison between existing HTI methods and the proposed method to help determine if the extra complexity present in this new proposed method is necessary for accurate fracture characterization.

Although the main objective of developing an orthorhombic fracture characterization procedure in this work is aimed at better characterization of unconventional resources, this work can also be applied to other situations. Beyond fractured shale, the assumption of orthorhombic anisotropy is also applicable in

conventional plays where fracturing has occurred and layer thickness is small compared to a seismic wavelength. In particular, fracturing plays an important role in fluid storage and migration pathways in carbonate reservoirs (Alhussain, 2013). Despite the focus on fractured shale in this work, the methods presented are applicable in any fractured reservoir setting with appropriate seismic data available. The methods proposed in this thesis can be thought of as generalized fracture characterization methods rather than specifically unconventional resource specific or shale characterization methods.

For the sake of completeness, alternate fracture characterization methods utilizing 3D seismic data will be briefly summarized. Other methods that utilize 3D seismic data to determine fracture density and orientation include velocity variation with azimuth analysis (VVAZ) (Grechka and Tsvankin, 1998 and Sun et al., 2013), amplitude analysis in the ray parameter domain (Alhussain, 2013), and post-stack attributes such as curvature and coherence (Alhussain, 2013). VVAZ relies on the analysis of slight travel time differences corresponding to different azimuths. The direction corresponding to minimal travel time corresponds to the “fast direction” and thus the direction parallel to fracture strike. Conversely, the maximum travel time direction corresponds to the “slow direction” and thus the direction perpendicular to fracture strike. The magnitude of the travel time difference between the fast and slow direction provides an indication of fracture density. Amplitude analysis in the ray parameter domain, as proposed by Alhussain (2013), examines the ratio of the reflection amplitude from the top and the bottom of the reservoir for a specific ray parameter. Looking at a specific ray parameter rather than a constant incident angle allows for the same section of the wavefield is compared directly. Examining the ratio of reflected energy of a constant wavefield segment in the reservoir zone allows for any anisotropic overburden as well as any transmission effects to be accounted. Lastly, certain post-stack seismic attributes have

been shown to indicate high fracture density, as demonstrated by Alhussain (2013). In particular, high curvature and low coherence can both be indicative of high fracture density. Examples of this relationship can be seen throughout the literature, including Chopra and Marfurt (2010), Gersztenkorn and Marfurt (1999), and Yenugu and Marfurt (2011). These methods are not utilized in this study, but they do present alternate and independent ways to determine fracture orientation and fracture density from 3D seismic data, and could be considered in future work.

1.2 OBJECTIVES

The objective of this study is to analyze and apply several robust fracture characterization techniques that utilize the azimuthal amplitude analysis of 3D seismic data. This thesis includes the theoretical framework for the analyses used, a step-by-step workflow for performing said analyses, and presents the results from performing said analyses on real data from the Haynesville Shale in Panola County, Texas. In addition to applying existing methods that assume HTI anisotropic media using commercial software (Hampson-Russell ©), this work develops a new method for fracture characterization based on Fourier decomposition of seismic data. This novel method partially assumes orthorhombic anisotropy. Specifically, orthorhombic anisotropy is assumed when inverting for fracture density, although the inversion for fracture azimuth maintains the standard HTI assumption. This method is, however, capable of unambiguously determining fracture azimuth, and it incorporates several advanced inversion techniques. Lastly, this study aims to compare results from this novel method to those from existing HTI methodologies to either confirm or negate the need to implement to the more complex, but more computationally expensive, proposed method.

1.3 THESIS ORGANIZATION

This thesis is divided into six chapters. Chapter 1 provides a brief overview of the motivation behind the work performed in this project, outlines the objectives accomplished by this project, and presents the organization of this thesis. Chapter 2 presents a brief geologic background of the Haynesville Shale, overviews the data used in this study, and summarizes the initial processing steps performed on the data. Chapter 3 provides the theoretical framework for the fundamentals of seismic wave propagation, solving for seismic reflectivity, tensor notation and analysis, linear slip deformation theory, effective anisotropy, and least squares based inversion techniques. Chapter 4 overviews the existing fracture characterization methods used in this work, which assume HTI anisotropy. Included are an overview of the theory behind each method, a step-by-step implementation summary, presentation of results, and a discussion of results from both the Rüger and Fourier decomposition based HTI methods. Chapter 5 overviews the new Fourier decomposition based fracture characterization method. Included are an overview of the theory behind the method, a step-by-step implementation summary, an overview of the generation of a synthetic data presentation of synthetic and real data results, a discussion of results, and a comparison between this novel method and an analogous HTI method. Lastly, Chapter 6 covers conclusions derived from this work and discusses possible future work.

Chapter 2: Background

2.1 Geologic Background of the Haynesville

The Haynesville Shale is a generally organic- and carbonate-rich and clay-poor mudstone spanning areas of Eastern Texas and Northern Louisiana, with mudstone lithofacies laterally varying in carbonate and siliciclastic composition. Upper Jurassic in age, the Haynesville Shale is one of many Kimmeridgian-Tithonian black shales deposited worldwide during a global second-order transgression. These Upper Jurassic black shales have proven to be important source rocks worldwide, and the Haynesville is no exception. The entire Haynesville Shale is estimated to contain natural gas reserves on the order of several hundred trillion cubic feet (tcf), with individual wells often being able to recover as much as 7.5 billion cubic feet (bcf) of natural gas (Hammes et al., 2011). These production rates make the Haynesville one of the most productive shale gas plays in the continental United States. Many Haynesville gas wells experience high initial production (> 30 mmcf/day) and quick decline (~80% in the 1st year). This production trend supports the idea that fracturing plays a crucial role in Haynesville Shale gas production, despite the lack of fracturing seen in FMI log core images gathered throughout the Haynesville (Hammes et al., 2011).

The Haynesville Shale was deposited over the Sabine uplift, one of many large provinces exhibiting structural highs and lows around the Gulf of Mexico Basin. Underlying the Sabine uplift is a region of pseudo-continental crust. This pseudo-continental crust is in many ways indistinguishable from North American continental crust, but is distinct due to being separated from the North American crust by a narrow belt of ocean-like crust. There is extensive speculation and debate regarding the exact nature of the Sabine basement, but it is generally considered a “microcontinent arc”. The organic rich shale, including the part of the Haynesville Shale examined in this work, is

primarily present over the eastern flank of the Sabine uplift. The lateral extent of the Haynesville Shale and a number of additional lithofacies surrounding the Haynesville Shale can be seen in Figure 2.1. Underlying the Haynesville Shale is the Louard Group carbonates, including the Smackover, Buckner, Haynesville and Glimer Limestones. Together, this group is colloquially known as the Cotton Valley Limestone. During the Transgressive rise in sea level associated with Haynesville deposition, carbonate buildup occurred, which formed the Cotton Valley Limestone. Eventually, carbonate buildup was overtaken by deeper-water shale deposition, forming the Haynesville Shale, as sea-level continued to rise. The top of the Haynesville represents a maximum flooding surface (MFS), marking the sequence boundary between the transgressive and highstand system tracks of the 2nd order Jurassic supersequence. This MFS represents the turnaround from Haynesville retrogradation to Bossier progradation. The MFS additionally marks the end of Jurrasic carbonate production – during the highstand following Haynesville deposition, deltaic and barrier bar systems spread across the basin, covering the Haynesville Shale in thick layers of siliciclastic sedimentation (Hammes et al., 2011). These siliciclastic sediments are known as the Cotton Valley Group and include the clay-rich Bossier shale, the Cotton Valley Sands, and the Knowles formation.

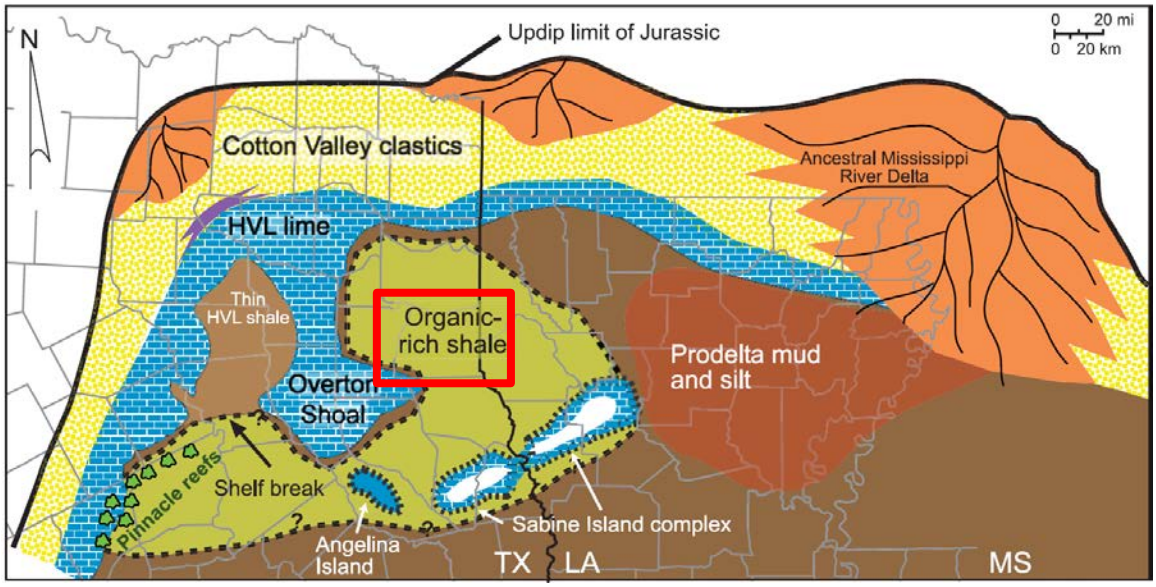

Figure 2.1: Paleogeography associated with Haynesville deposition North of the Gulf of Mexico in present day Eastern Texas and Northwestern Louisiana. The organic rich Haynesville Shale, which is the focus of this work, and surrounding lithofacies can be seen. Panola County is outlined by the red box. Figure from Hammes et al. (2011).

Geographically, the Haynesville is bounded by the Sabine Island Complex to the South, the North Louisiana Salt Basin to the East, and the East Texas Salt Basin and Brazos Basin to the West. The Haynesville generally ranges in depth from 9,000 – 14,000 ft, though it extends to below 18,000 ft depth in areas that extend southward into the Gulf of Mexico. The Haynesville varies in thickness, with a maximum thickness exceeding 350 ft. See Figure 2.2 for an isopach thickness map of the Haynesville Shale. Geographically, the Haynesville Shale-gas play extends over 16 counties in Northwest Louisiana and Eastern Texas, but all work presented here is based on data collected on the Haynesville in Panola County, Texas. In this area, the Haynesville Shale lies approximately 11,000 ft deep and is approximately 200 ft thick.

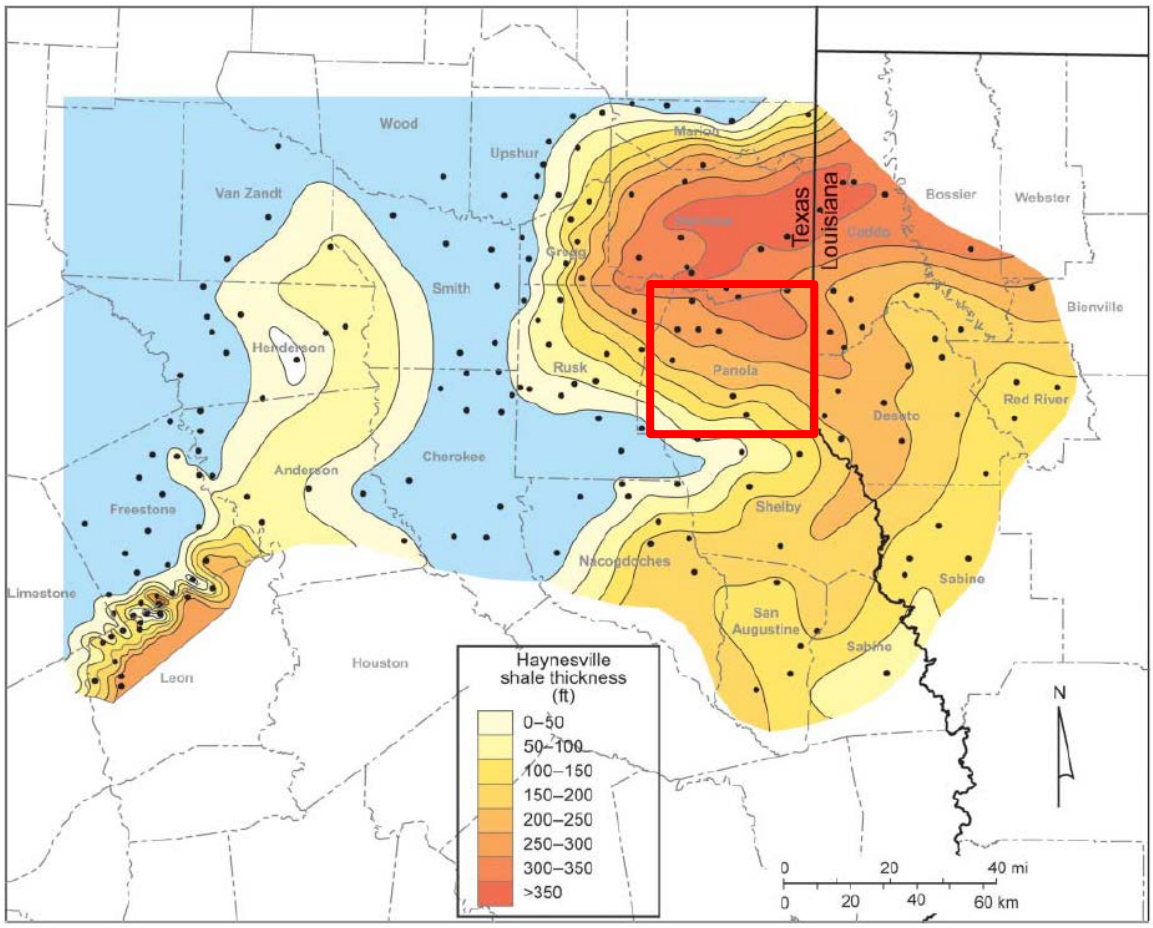

Figure 2.2: Isopach thickness map of the Haynesville Shale. Warmer colors indicate areas of thicker Haynesville Shale deposits. Blue areas correspond to carbonate shelves lacking any shale deposition. Panola County is outlined by the red box. Figure from Hammes et al. (2011).

2.2 DATA OVERVIEW

Data available for this study included both unmigrated and migrated 3D seismic sections and a suite of well logs from two wells located within the bounds of the seismic survey. Both seismic datasets include pre-stack gathers, a post-stack section, a RMS velocity model, and a number of picked horizons. The pre-stack gathers include offsets ranging from 225m to 6025m, allowing for a wide angle range when transformed into the incident angle domain. This results in seismic incident angles spanning from about 5

degrees to about 45 degrees in the vicinity of the Haynesville. Unfortunately, in the high and low extremes of that angle range much azimuthal information is missing, and data are represented by very limited azimuths. At these extreme high and low incident angles, most data tend to reside in the approximate inline direction. Both wells are present within the migrated 3D seismic dataset although only one well is present within the bounds of the unmigrated dataset. The exact geographic location of the survey is confidential and cannot be provided in this thesis; however, all seismic and well data are from within Panola County, Texas. All data were provided by Chevron. In addition to the data provided by Chevron, I generated a number of synthetic seismic datasets. These synthetic data will be further discussed in Chapter 5.

In the work presented in this thesis, only the unmigrated seismic dataset was used. This was done for a number of reasons. The primary reason was that the Kirchhoff pre-stack time migration performed to produce the migrated seismic dataset did not maintain azimuthal information in the dataset headers. The lack of the azimuthal information in the migrated data made the azimuthal analysis performed in this work impossible to perform. However, even if azimuthal information in headers had been maintained, the unmigrated dataset would be preferable for a number of reasons. Seismic imaging (i.e., migration) distorts true seismic amplitudes, making any sort of azimuthal amplitude analysis on a migrated dataset inherently flawed. Additionally, high-frequency information has been lost in the migration, as can be seen in Figure 2.3, which shows a comparison of the spectral compositions of the unmigrated and migrated datasets. The inclusion of higher frequency information indicates that an analysis performed with the unmigrated data will yield higher resolution results. Lastly, due to the relatively simple geology and nearly flat layering present in the survey area, migration is not an absolute necessity. Generally, the unmigrated data does not deviate significantly from the migrated image. For these

reasons, the unmigrated 3D seismic dataset was the obvious choice to be used in this work.

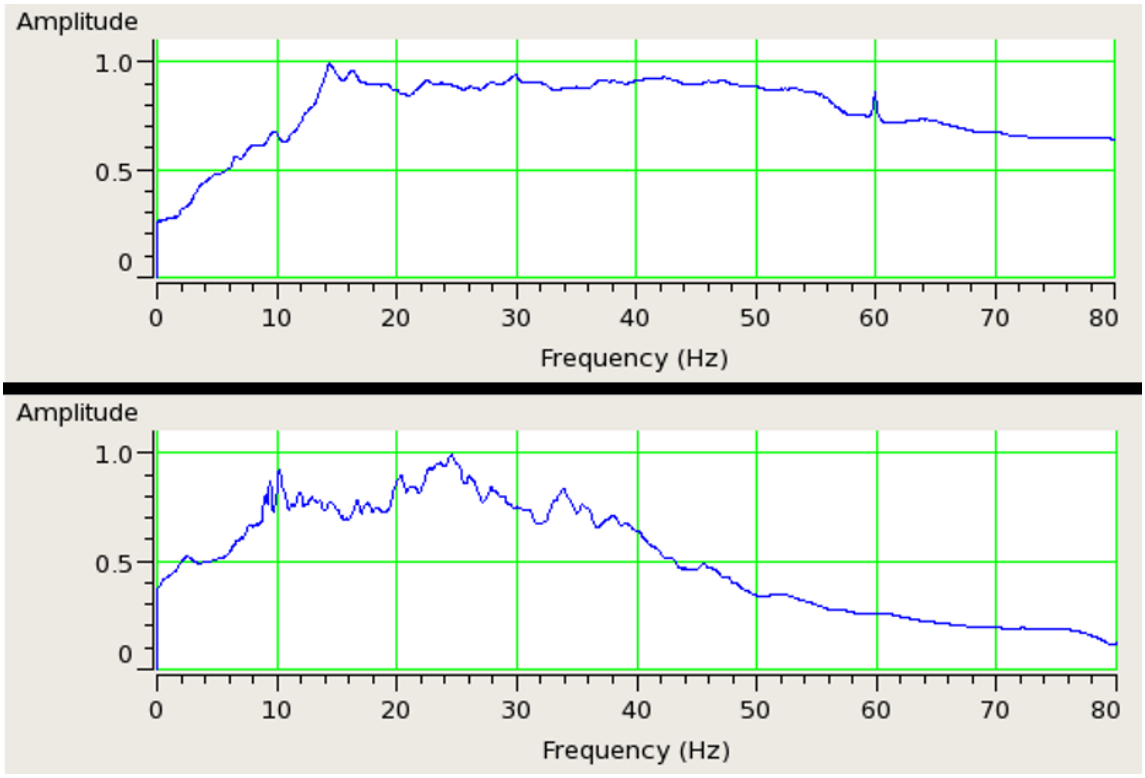

Figure 2.3: Comparison of amplitude spectrum of the unmigrated 3D seismic dataset (upper) and the migrated 3D seismic dataset (lower). The X axis corresponds to frequency, and ranges from 0 Hz to 80 Hz. The Y axis represents normalized amplitude. Spectra calculated using Hampson-Russell ©.

The unmigrated dataset consists of 671 inlines and 301 crosslines, with inline and crossline spacings of 125 ft and 250 ft, respectively. Data is orientated such that inlines are oriented approximately north-south and crosslines are oriented approximately east-west. Data orientation is rotated ~2.5 degrees clockwise from an exact N-S / E-W alignment, but results depicted later in this thesis commonly assume the inline direction to correspond to approximately north-south. This data is a subset of a larger dataset

consisting of 4000 inlines and 1851 crosslines that extends outside of Panola County, and which is proprietary information belonging to a number of companies. In order to reduce computational time associated with the analyses performed in this work, a reduced section of 137 inlines by 137 crosslines was used, corresponding to an area slightly larger than 6 miles by 3 miles. The one well within the bounds of the unmigrated dataset is located at the center of this 137 inline by 137 crossline rectangle. See Figure 2.4 for a graphical description of the location of the reduced dataset used in this work relative to the complete dataset, as well as the relative location of the single available well within each volume. The eastern and southern edges of the reduced dataset border the edges of the complete dataset, allowing for “edge-effects” to be investigated.

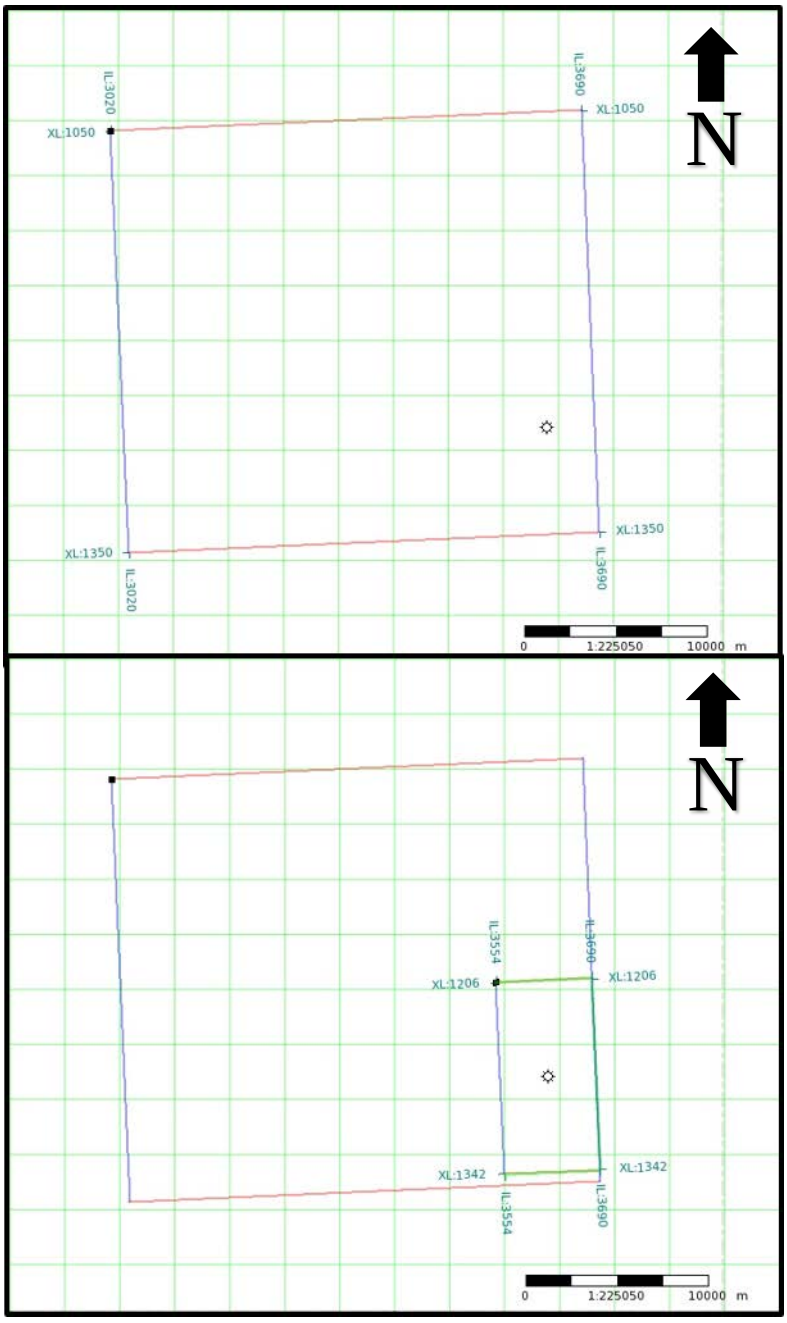

Figure 2.4: (Upper): Map view of the entire unmigrated 3D seismic dataset, spanning 670 inlines and 300 crosslines. (Lower): Map view of the reduced seismic dataset, spanning 137 inlines and 137 crosslines, and its relative location within the full dataset. The $*$ indicates the well location. The black arrows indicate the direction of north.

Due to the absence of FMI logs and the motivation to characterize fractures exclusively through the analysis of 3D seismic data, the use of well logs in this work is very limited. Well log information was, however, used to determine the ratio of the compressional wave velocity (V_p) to that of the shear wave velocity (V_s). Some of the analyses presented in this work are sensitive to a parameter denoted "g", which is defined as V_s^2/V_p^2, and well information was used to approximate this parameter. In the spirit of performing an analysis exclusively on 3D seismic data, however, I note that an approximate value of g could be determined by some general relationship. For example, a value of g determined by Gardner's relation and calibrated to the area in question will generally suffice. Small errors in the chosen value of g normally will not substantially alter results of the analysis.

2.3 SEISMIC PROCESSING

Prior to the commencement of the work described in this thesis, the seismic data were processed by CGG Veritas in June 2011. A full list of processing steps performed by CGG Veritas can be seen in Table 2.1. Initially, data were demultiplexed (i.e., sorted by trace rather than by time), and then reformatted to .SEGY format. Manual trace edits were performed to remove bad, noisy, or mono-frequency traces and to correct traces with incorrect polarity. System-dependent gain correction and spreading gain recovery were applied to correct for geometric spreading of the seismic wavefield. High amplitude noise burst attenuation and high amplitude de-spiking were both applied in the shot domain. Source- and system-phase matching was applied. This dataset was shot using a variety of sources, including dynamite, vibroseis, mini-vibe and airgun sources, each with a unique source signature. Thus, matching and normalizing source signatures was a crucial processing step in order to preserve data continuity. Surface consistent spike

deconvolution with 0.1% prewhitening and a 160ms operator window was applied in order to increase temporal resolution and remove any echoes present in the data. A preliminary velocity analysis was performed. Surface consistent residual statics and surface consistent gain correction were applied to correct for near-surface velocity variation and to redatum the data to a consistent elevation. A number of noise attenuation techniques were applied, including noise burst attenuation, adaptive linear noise attenuation, and radon linear noise attenuation. A second pass velocity analysis was performed. Lastly, Gabor spectral whitening and FX cross-spread random noise attenuation were performed. An example inline from the pre-stack data with the above processing steps implemented can be seen in Figure 2.5. Note that data are reverse polarity compared to the American standard, such that an increase in impedance with depth corresponds to a trough rather than a peak in the wiggle trace.

Processing Steps
Demultiplex / reformat
Manual trace edits
System dependent gain correction
Spreading gain recovery type
High amplitude noise burst attenuation - shot domain
High amplitude de-spiking - shot domain
Source and system phase matching
Surface consistent spike deconvolution: operator 160ms
Prewhitening 0.1 %
Preliminary velocity analysis
Surface consistent residual statics
Surface consistent gain corrections
Noise burst attenuation
Adaptive linear noise attenuation
Radon linear noise attenuation
FX random noise attenuation
Second pass velocity analysis
Gabor spectral whitening
FX cross-spread random noise attenuation

Table 2.1: A comprehensive list of all processing steps implemented by CGG: Veritas in June 2011. Steps are shown in the approximate order they were implemented. All processing steps shown here were completed prior to the onset of the work presented in this thesis. Refer to the text for explanations regarding each processing step and additional processing performed by the author.

Prior to beginning any AVAZ analysis, several additional data processing steps beyond those shown in Table 2.1 were required. All additional processing described here was performed using Hampson-Russell ©, a software suite which includes several seismic data processing and reservoir characterization tools. Initially, the coordinate system of the data was adjusted to coincide with the coordinate system of the available well log. I performed a normal moveout (NMO) correction using the provided RMS

velocity model in order to flatten reflections and applied an early time far offset mute to remove residual effects from the NMO correction. I applied a very broadband frequency filter to remove erroneous low- and high-frequency information, with low cut of 2 Hz, low pass of 6 Hz, high pass of 90 Hz, and high cut of 110 Hz. I applied a trim statics correction to further flatten horizons and remove small residual errors from the NMO correction. Note that adjusting for residual NMO correction errors is essential for any AVAZ analysis. Azimuthal variations in amplitudes at a constant time sample were analyzed, and thus the analysis would not work well if data from all azimuths and offsets/incident-angles were not perfectly aligned at that time. In the final processing step, I applied parabolic radon filters to remove both noise and multiples from the data. See Figure 2.6 for an example slice of the final processed data. Lastly, I reconfigured the data into an azimuthal super-gather, with 3x3 trace blending. In this azimuthal gather, the primary sort is azimuth and secondary sort is offset or incident angle. Various azimuthal super-gathers were generated with varied azimuthal and offset/incident-angle bin sizes. The HTI analyses performed, as described in Chapter 4, used an azimuthal super-gather consisting of 9 azimuth bins, each 20 degrees wide, and 30 offset bins, with ~210m spacing. The novel Fourier coefficient decomposition analysis performed, as described in Chapter 5, used an azimuthal super-gather consisting of 12 azimuth bins, each 15 degrees wide, and 10 incident angle bins, each 4 degrees wide and ranging from 5 to 45 degrees. More azimuthal bins were used in this analysis in order to allow additional azimuthal data points to be used in the robust curve-fitting function utilized. However, fewer incident angle bins were required in order to reduce computation time to a reasonable duration. Had a more powerful computer been available, more incident angle bins would have been used in the analysis. A repeat of the existing HTI Fourier decomposition analysis was performed using the modified binning scheme in order to allow for a direct comparison

between the proposed new Fourier coefficient decomposition method and its analogous HTI method. An example inline slice with all additional processing steps performed except for azimuthal sorting can be seen in Figure 2.6. An example inline slice with all additional processing steps performed and data azimuthally sorted can be seen in Figure 2.7. Figures 2.5 – 2.7 all depict data from the same CDP location.

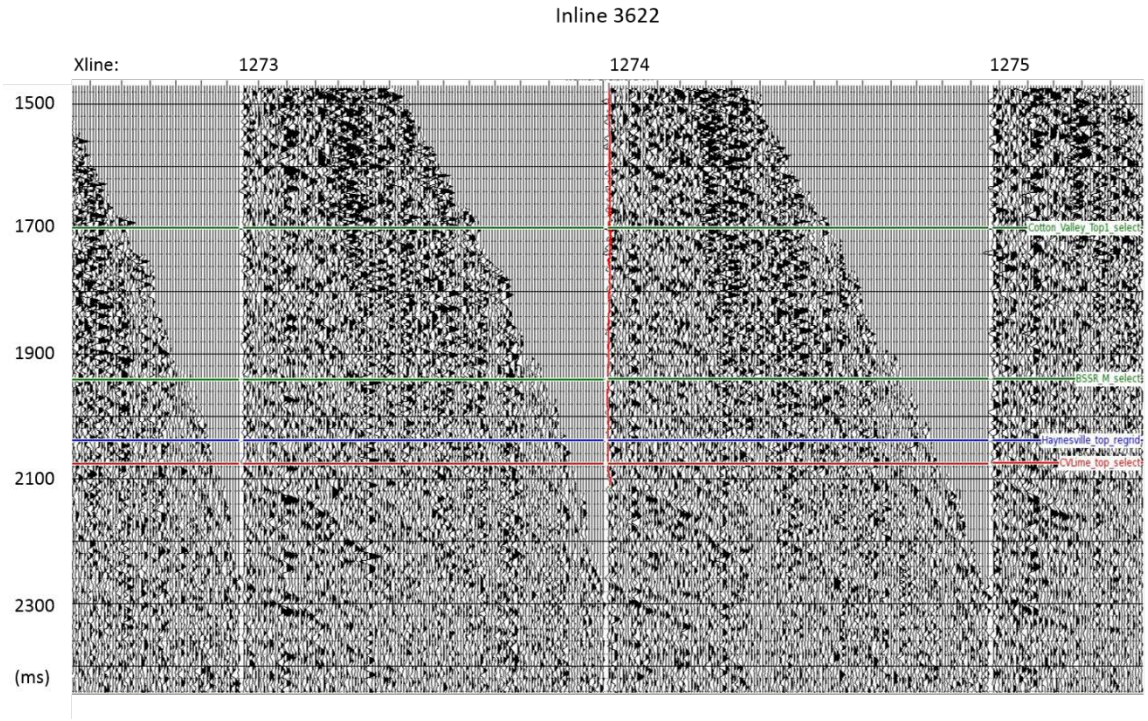

Figure 2.5: An example inline section of the seismic data with only processing steps shown in Table 2.1 implemented. This slice resides near the center of the area analyzed in this work. A well can be seen at the intersection of inline 3622 and crossline 1274. Data shows time ranges from roughly 1500 ms – 2400 ms. Offsets at each CDP range from 225m to 6025m. The Haynesville Shale is located from about 2040 ms – 2080 ms, between the blue and red horizons shown.

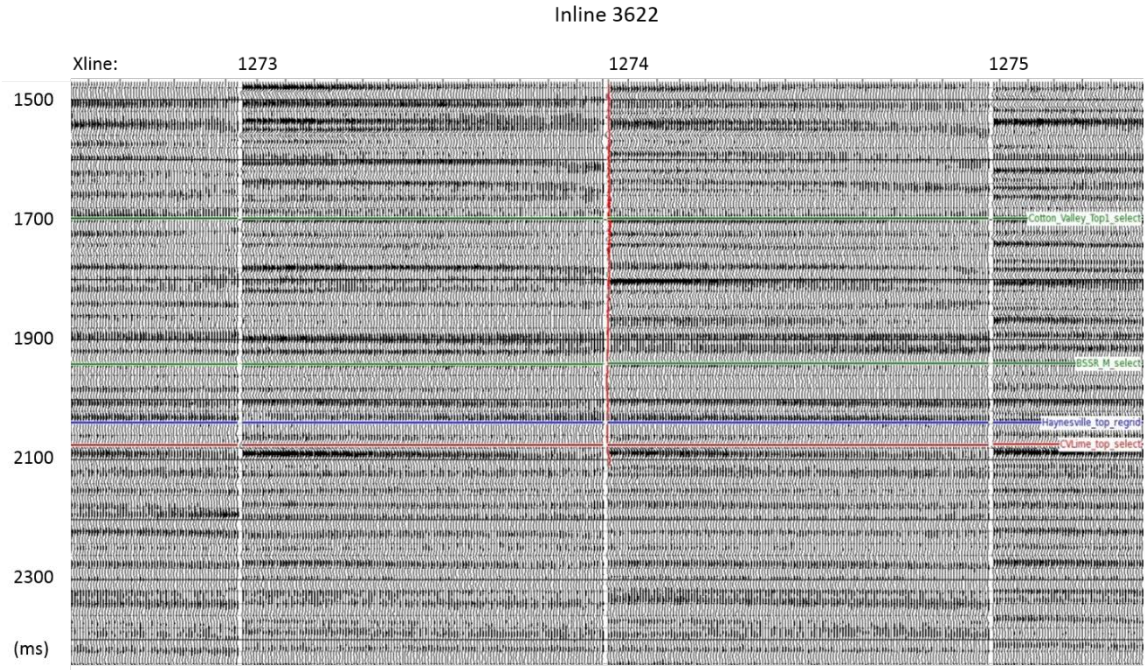

Figure 2.6: An example inline section of the seismic data with processing steps shown in Table 2.1 and all additional processing described in the text except azimuthal sorting implemented. Additional processing steps include NMO correction, a 2-6-90-110 bandpass filter, trim statics correction, and parabolic Radon filters for noise and multiple reduction. This slice resides near the center of the area analyzed in this work. A well can be seen at the intersection of inline 3622 and crossline 1274. Data show time ranges from roughly 1500 ms – 2400 ms. Offsets at each CDP range from 225m to 6025m. The Haynesville Shale is located from about 2040 ms – 2080 ms, between the blue and red horizons shown.

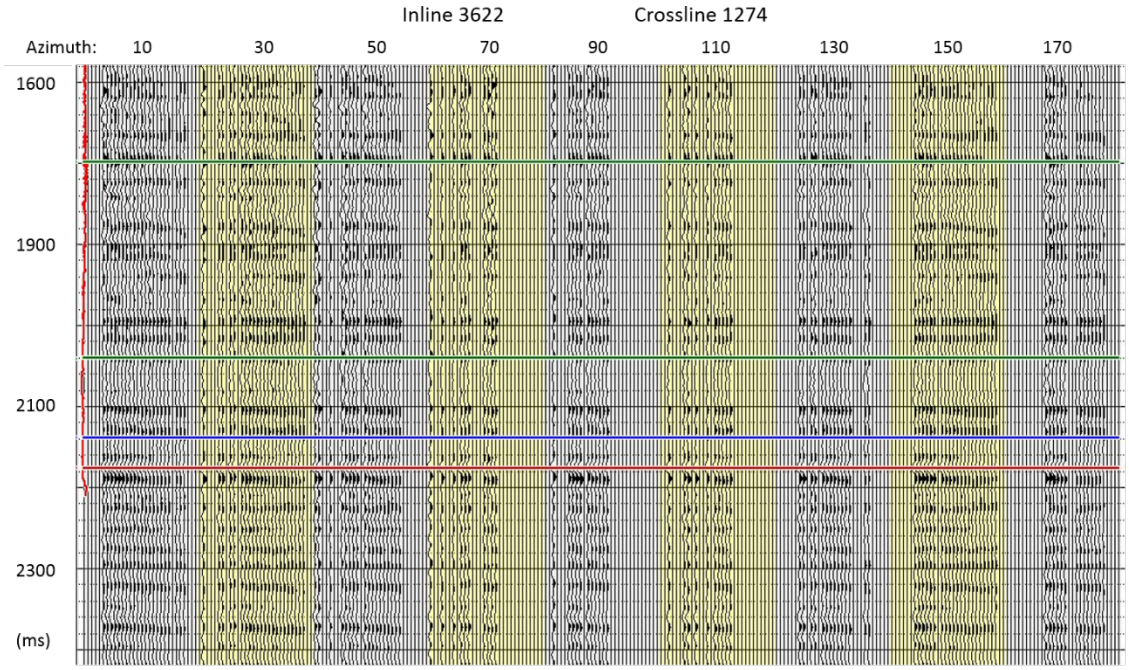

Figure 2.7: An example azimuthal section of the seismic data at the CDP associated with inline 3622 and crossline 1274, with processing steps shown in Table 2.1 and all additional processing described in the text applied. Additional processing steps include NMO correction, a 2-6-90-110 bandpass filter, trim statics correction, and parabolic Radon filters for noise and multiple reduction, and azimuthal sorting. This section resides near the center of the area analyzed in this work. The HTI binning scheme is shown, with 9 azimuthal bins and 30 offset bins. Primary trace sorting is by azimuth, and secondary sorting is by offset. Data show time ranges from roughly 1600 ms – 2400 ms. The Haynesville Shale is located from about 2040 ms – 2080 ms, between the blue and red horizons shown.

Chapter 3: Theory

3.1 Wave Equation For Elastic Anisotropic Homogeneous Media

Elastic seismic wave propagation is physically governed by an equation known as the “Wave Equation”, a differential equation that relates displacement and elastic properties to a time derivative of displacement (Sen, Seismology III, class notes). The solution to this differential equation governs how particle displacement from seismic waves change both spatially and temporally. Analysis of solutions to the wave equation give rise to the different wave types known to exist. In the absence of boundary conditions, compressional and shear waves arise, commonly referred to as P and S waves (Aki and Richards, 1980). If a free surface boundary condition is implemented, solutions corresponding to surface waves arise, specifically Rayleigh and Love waves (Aki and Richards, 1980). Note that Love waves require one or more layers below the surface, with velocity increasing with respect to depth, in order to exist, and that layering causes Rayleigh waves to be dispersive (i.e., to have a velocity which is dependent on frequency).

By analyzing the solutions to the wave equation above and below a boundary between two mediums that have different elastic properties, and imposing boundary conditions, the properties of reflected and transmitted waves can be determined. This is how one can derive the famous “Zoeppritz equations” (Zoeppritz, 1919), which provide analytical solutions for reflected, refracted and transmitted waves in isotropic media. Linear approximations to Zoeppritz equations form the basis for amplitude-vs-offset (AVO) analysis of seismic data, an industry standard practice. The same methodology used to calculate Zeoppritz equations can be applied to anisotropic media to calculate explicit analytical expressions for reflectivity in an anisotropic setting. An approach for solving a more general form of the Zoeppritz equations valid in anisotropic media is

described in detail in Section 3.2 of this chapter. Note that for more complex anisotropic cases, analytic solutions might not exist, and numerical solutions instead must be used. Linearized approximations to anisotropic reflectivity form the theoretical framework behind the work presented in this thesis. In a broader sense, the idea that downgoing seismic waves will be partly reflected and partly transmitted at a boundary between media with different elastic properties is fundamentally why industry standard reflection seismic surveys are informative. This is also the physical justification explaining why companies spend enormous sums of money collecting seismic data for analysis.

The elastic wave equation can be derived from two relatively simple assumptions. The first assumption is that Newton's second law of motion (i.e. the law of inertia) remains valid. Newton's second law can be seen in Equation 3.1.

$$F = ma \ , \tag{3.1}$$

where F represents force, m represents mass, and a represents acceleration, which is the 2nd time derivative of displacement (U). When normalized over a volume, mass reduces to density, and force reduces to the divergence of stress ($\boldsymbol{\tau}$). Rewritten, Equation 3.1 transforms to:

$$\rho \, \partial_t^2 U = \nabla \cdot \boldsymbol{\tau} + f \ , \tag{3.2}$$

where f represents some external force per unit volume. The second assumption needed in the derivation of the seismic wave equation is that of linear elasticity. In the simplified case of an ideal spring attached to a dashpot, shown in Figure 3.1, Hooke's law is stated:

$$F = E \, \Delta x + \eta \, \frac{\Delta x}{\Delta t} \, , \tag{3.3}$$

where E represents the stiffness of the spring, η represents the viscosity of the dashpot, and Δx represents displacement. When transformed into a tensor context and normalized over some volume, Equation 3.3 transforms to:

$$\boldsymbol{\tau} = \boldsymbol{C} : \boldsymbol{\varepsilon} + \boldsymbol{\eta} : \frac{\partial \boldsymbol{\varepsilon}}{\partial t} \ , \tag{3.4}$$

where $\boldsymbol{C}$ and $\boldsymbol{\eta}$ represent stiffness and attenuation tensors, respectively, $\boldsymbol{\varepsilon}$ represents strain, : represents a double dot product, and ∂ represents a partial derivative. Note that strain ($\boldsymbol{\varepsilon}$) is equal to the gradient of displacement (∇U). The work presented here does not consider attenuation, and thus Equation 3.4 reduces to a simple stress-strain relationship:

$$\boldsymbol{\tau} = \boldsymbol{C}:\boldsymbol{\varepsilon} = \boldsymbol{C}:\nabla U \quad . \tag{3.5}$$

When substituting Equation 3.5 into Equation 3.2 and relating strain in terms of displacement, one obtains the wave equation valid for anisotropic elastic homogeneous media, shown in Equation 3.6 (Sen, Seismology III, class notes).

$$\rho\, \partial_t^2 U = \nabla \cdot (\boldsymbol{C}:\nabla U) + f \quad . \tag{3.6}$$

Analysis of the wave equation indicates that solutions in homogeneous media will have the general form shown in Equation 3.7.

$$f(ax \pm t) \quad , \tag{3.7}$$

where f indicates a function, a is some constant, t represents time, and x is a vector representing direction in three dimensional space. In analyzing seismic waves, it is convenient to use the plane wave solution to the wave equation in homogeneous media, shown in Equation 3.8.

$$U = (l \quad m \quad n)\, U_o e^{i\omega(px*x + py*y + q*z - t)} \quad , \tag{3.8}$$

where $(l \quad m \quad n)$ is a directional basis vector and px, py and q are directional slowness's (inverse of velocity) in the x, y and z direction, respectively. Equation 3.8 is valid for downgoing P waves, but $(l \quad m \quad n)$ and px, py and q vary between different wave types. Generally, $(l \quad m \quad n)$ will have a distinct form, and px, py and q will have unique values for upgoing and downgoing compressional waves (P waves), vertically polarized shear waves (SV waves), and horizontally polarized shear waves (SH waves). How Equation 3.8 changes for certain wave types is further discussed in Section 3.2. Analysis of Equation 3.8 indicates that:

$$\partial_t^2 U = \omega^2 U \ , \tag{3.9}$$

and thus Equation 3.2 reduces to:

$$\rho\omega^2 \, U = \nabla \cdot \boldsymbol{\tau} + f \ . \tag{3.10}$$

Equation 3.10 is commonly known as the Equation of Motion or the Momentum Equation, and is one of the fundamental equations in seismology.

Figure 3.1: A simplified spring and dashpot system. E represents the stiffness of the spring, and η represents the viscosity of the dashpot. Note that in seismology the analog to spring stiffness (E) is the stiffness tensor ($\boldsymbol{C}$).

3.2 Solving for Reflectivity

Exact solutions for seismic wave reflection, refraction, transmission and conversion at a layer boundary can be found by analyzing the plane wave solutions to the wave equation, as shown in Equation 3.8, above and below a layer boundary for all incident, reflected and transmitted waves. In the most general case, any incident wave (compressional or shear) intersecting a layer boundary will result in three reflected waves and three transmitted waves. In each set of these three resulting waves, one will be compressional (denoted quasi-P) and two will be shear waves of varying polarization (denoted quasi-SV and quasi-SH). In the case that impedance increases across the layer boundary, refracted waves will arise at high incident angles, identifiable by the introduction of a complex exponential in the transmitted wave solutions for post-critical ray parameters. It is worth noting that in simple cases involving only isotropic or VTI anisotropy, there is a decoupling between P-SV waves and SH waves. This decoupling

reduces the number of possible resultant waves to two reflected and two transmitted waves in the case of an incident P or SV wave, and one reflected and one transmitted wave in the case of an incident SH wave. The process for solving reflectivity in the more general case, however, will be examined here.

Many methods exist to determine exact properties of reflected and transmitted waves at a layer boundary, but only one will be examined in this thesis. This method is a generalization of work by Graebner (1992), which solves for reflectivity generated from a boundary between VTI media. Initially, in order to solve for reflected and transmitted wave characteristics, a matrix known as the Christoffel Matrix needs to be constructed (Greabner, 1992; Sen, Seismology III, class notes). This is accomplished by considering the equation of motion, shown in Equation 3.10, where the external force term (f) is assumed to be zero. Rearranging equation 3.10 under the assumption of no external force provides:

$$\nabla \cdot \boldsymbol{\tau} - \rho\omega^2 U = 0 \, . \tag{3.11}$$

By using the relation

$$\nabla \cdot \boldsymbol{\tau} = \nabla \cdot (\boldsymbol{C} : \nabla U) \ , \tag{3.12}$$

one can construct the Christoffel matrix $\boldsymbol{T}$, which satisfies

$$\boldsymbol{T}\, U - \rho \boldsymbol{I} = 0 \ , \tag{3.13}$$

where $\boldsymbol{I}$ represents the identity matrix and components of $\boldsymbol{T}$ are functions of elastic coefficients and slownesses. Equation 3.13 forms a system of three equations. The three eigenvalues of the matrix $\boldsymbol{T}$ represent the three slownesses px, py and q. By performing an Eigen-decomposition of matrix $\boldsymbol{T}$**,** one is able to solve for vertical slowness q in terms of horizontal slownesses px and py and the elastic coefficients in $\boldsymbol{C}$. Elastic coefficients from $\boldsymbol{C}$ are presumed to be known. In some simple cases analytical solutions for q can be found, but in more complex cases q must be determined numerically. In practice, q can

be numerically determined by creating a grid of possible px and py values and solving for q at each realistic px and py combination. Unrealistic combinations of px and py will result in vertical slowness q being purely imaginary. Note that the different wave types (qP, qSV and qSH) each have unique functions describing vertical slowness .

Once eigenvalue q has been found, its corresponding eigenvectors can be determined. Eigenvectors should be normalized to unity. These eigenvectors represent the direction of particle displacement, otherwise known as the particle polarization. The vector $(l \quad m \quad n)$ shown in Equation 3.8 is a polarization vector. Different wave types have different polarization vectors, indicating unique relationships between the direction of wave propagation and the direction of particle motion for these wave types. These take the form:

- $(l \quad m \quad n)$ for downgoing qP waves. This also represents the direction of wave propagation for downgoing waves.
- $(l \quad m \quad -n)$ for upgoing qP waves. This also represents the direction of wave propagation for upgoing waves.
- $(-n \quad m \quad l)$ for downgoing qSV waves. This is perpendicular to the direction of propagation (90 degrees rotated in the X-Z plane).
- $(n \quad m \quad l)$ for upgoing qSV waves. This is perpendicular to the direction of propagation (90 degrees rotated in the X-Z plane).
- $(m \quad -l \quad n)$ for downgoing qSH waves. This is perpendicular to the direction of propagation (90 degrees rotated in the X-Y plane).
- $(m \quad -l \quad -n)$ for downgoing qSH waves. This is perpendicular to the direction of propagation (90 degrees rotated in the X-Y plane).

Rotating a vector is further discussed in Section 3.3. For each of these polarization vectors, values l, m and n can each be determined in terms horizontal slownesses px and

py and elastic coefficients using standard eigenvector solving techniques. Thus, the displacement equation for the seismic wave, as shown in Equation 3.8, has been entirely parameterized in terms of two variables, px and py, and the elastic coefficients present in the stiffness tensor $\boldsymbol{C}$. This is repeated for all wave types, so displacement equations for upgoing and downgoing qP, qSV and qSH waves are known in terms of slownesses px and py and relevant elastic coefficients. In some simple cases, px and py can further be parameterized in terms of incident angle of the seismic wave at the layer boundary.

Once expressions for displacement parameterized in terms of a horizontal slownesses are known, boundary conditions can be applied in order to solve for reflected and transmitted wave amplitudes. In the case of a solid-solid interface, boundary conditions are as follows:

$$U_x^{upper} = U_x^{lower} \ , \tag{3.14}$$

$$U_y^{upper} = U_y^{lower} \ , \tag{3.15}$$

$$U_z^{upper} = U_z^{lower} \ , \tag{3.16}$$

$$\tau_{xz}^{upper} = \tau_{xz}^{lower} \ , \tag{3.17}$$

$$\tau_{yz}^{upper} = \tau_{yz}^{lower} \ , \tag{3.18}$$

$$\tau_{zz}^{upper} = \tau_{zz}^{lower} \ . \tag{3.19}$$

Equations 3.17 – 3.19 can be parameterized in terms of U_i^{upper} and U_i^{lower} using Equation 3.12. In Equations 3.14 – 3.19, U_i^{upper} and U_i^{lower} indicate the sum of the displacements of all waves in the upper and lower layer, respectively. Subscript i indicates if the x, y or z component of displacement is being considered. Assuming a downgoing incident wave, U_i^{upper} and U_i^{lower} can be denoted as:

$$U_i^{upper} = U_i^{incident} + R_P \, U_i^{qP} + R_{SV} \, U_i^{qSV} + R_{SH} \, U_i^{qSH} \ , \tag{3.20}$$

$$U_i^{lower} = T_P \, U_i^{qP} + T_{SV} \, U_i^{qSV} + T_{SH} \, U_i^{qSH} \ . \tag{3.21}$$

Assuming an upgoing incident wave, U_i^{upper} and U_i^{lower} can be denoted as:

$$U_i^{upper} = T_P\, U_i^{qP} + T_{SV}\, U_i^{qSV} + T_{SH}\, U_i^{qSH} \ , \tag{3.22}$$

$$U_i^{lower} = U_i^{incident} + R_P\, U_i^{qP} + R_{SV}\, U_i^{qSV} + R_{SH}\, U_i^{qSH} \ . \tag{3.23}$$

In Equations 3.20 – 3.23, displacement is defined as in Equation 3.8 with an appropriate polarization vector for the wave type in question. In either the downgoing or upgoing incident wave case, the six desired parameters R_P, R_{SV}, R_{SH}, T_P, T_{SV} and T_{SH} can be determined in terms of px, py, and elastic coefficients by examining Equations 3.14 – 3.19, which form a system of six equations and six unknowns. This methodology can determine reflectivity at layer boundaries between anisotropic media. However, in the limit of isotropy in both the upper and lower layers, the solution will reduce to the well-known Zoeppritz equations. Note that in the Zoeppritz equations, px and py have been parameterized in terms of incident angle at the layer boundary, and P-SV waves have been decoupled from SH waves. In exploration, the R_P coefficient associated with a downgoing incident P wave is the primary parameter of interest, here forth denoted as R_{PP}. Unfortunately, exact expressions for R_{PP} are cumbersome in the simplest isotropic-isotropic case, and generally infeasible to use when anisotropy is present. Additionally, for more complex anisotropic cases, analytical solutions are not often possible to derive and can only be calculated using numerical methods. Numerical calculation of exact reflection coefficients are computationally expensive and generally infeasible to use in large scale data analysis. For this reason, several simplified linear approximations that are valid at incident angle ranges common in industry seismic surveys (generally less than ~40 degrees) have been created. Linear approximations of the simplest isotropic-isotropic case form the basis for conventional amplitude-vs-offset (AVO) analysis. They usually have a form similar to the one shown in Equation 3.24.

$$R(\theta) \approx A + B\ \sin^2\theta + \ C\ \sin^2\theta\ \tan^2\theta \ , \tag{3.24}$$

where θ represents the incident angle of the seismic wave and A, B and C are constants. Often the third term is ignored, resulting in a two term AVO expression. When azimuthal anisotropy is present, Equation 3.24 can be expanded to include an azimuthal term. Linear approximations to reflectivity in anisotropic media in terms of incident angle (θ) and azimuth (φ) form the basis for the AVAZ methods performed in this work, which will be examined in detail later in this thesis.

Note that the method outlined above utilizing the Christoffel matrix method is not the only possible way to determine analytical expressions for reflectivity in arbitrarily anisotropic media. However, all methods for calculating reflectivity are fundamentally based on solving the boundary conditions stated in Equations 3.14 – 3.19. Other methods, however, will not be explained in this thesis.

3.3 TENSOR ANALYSIS

In the derivations shown above, various 2nd rank and 4th rank tensors are used. In those derivations, τ_{ij} represents a 2nd rank tensor of stress, in which both the i and j subscripts range between one and three, representing the x, y and z directions of three dimensional space. ε_{kl} is similarly a 2nd rank tensor of strain, in which both the k and l subscripts can range between one and three. Physically, these can been interpreted as stress and strain on faces of a cube, as depicted in Figure 3.2. In this physical analogy, the first subscript specifies the face of the cube that stress / strain is occurring on, and the second subscript indicates the direction which the stress / strain is acting along the surface indicated by the first subscript. In the limit of the cube volume reducing to zero, the opposite sides of the cube coincide, resulting in three surfaces experiencing three unique stresses or strains. This indicates that $\boldsymbol{\tau}$ and $\boldsymbol{\varepsilon}$ are each composed of nine values in three dimensional space; however, due to symmetry, namely $\tau_{ij} = \tau_{ji}$ and $\varepsilon_{kl} = \varepsilon_{lk}$, the

number of independent components in each of these tensors is reduced to 6. In order to make computations using these tensors viable, $\boldsymbol{\tau}$ and $\boldsymbol{\varepsilon}$ can be represented as either a symmetric 3x3 matrix, or as a 1x6 vector, each of which has 6 independent components. Matrix forms of these tensors can be seen in Equations 3.25 and 3.26, and vector forms of these tensors can be seen in Equations 3.27 and 3.28. Voigt notation expressions of $\boldsymbol{\tau}$ and $\boldsymbol{\varepsilon}$ are also included in Equations 3.27 and 3.28. In Voigt notation, the six unique dimension combinations that make up elements in $\boldsymbol{\tau}$ and $\boldsymbol{\varepsilon}$ are renumbered from 1 to 6, helping to reduce notational clutter (Sen, Seismology III, class notes).

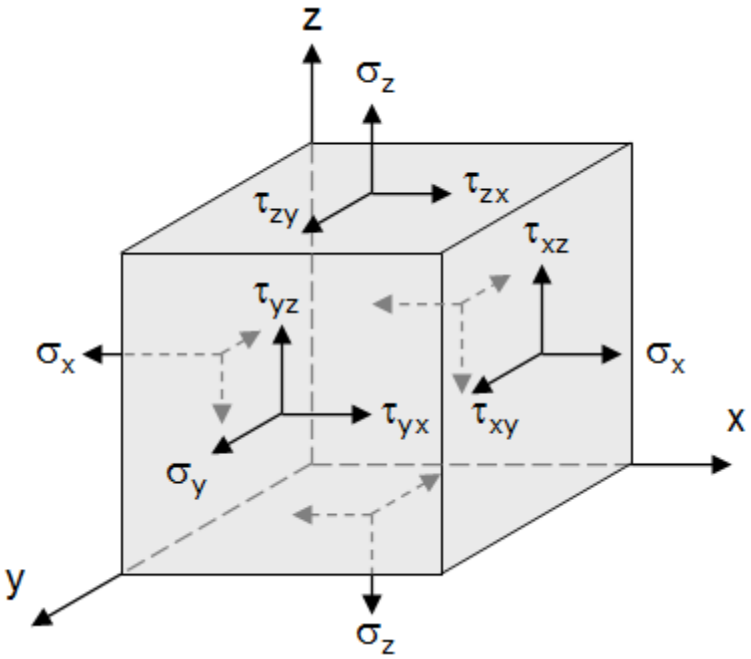

Figure 3.2: A graphical representation of stresses τ_{ij}. Stress τ_{ij} represents force on the cube face normal to direction $\hat{\imath}$ and acting in direction $\hat{\jmath}$. Stresses on adjacent faces of the cube are identical. Strain ε_{kl} can be interpreted in a similar way. Note that normal stresses τ_{ij} have been replaced with σ_i.

$$\boldsymbol{\tau} = \begin{pmatrix} \tau_{xx} & \tau_{xy} & \tau_{xz} \\ \tau_{xy} & \tau_{yy} & \tau_{yz} \\ \tau_{xz} & \tau_{yz} & \tau_{zz} \end{pmatrix}, \tag{3.25}$$

$$\boldsymbol{\varepsilon} = \begin{pmatrix} \varepsilon_{xx} & \varepsilon_{xy} & \varepsilon_{xz} \\ \varepsilon_{xy} & \varepsilon_{yy} & \varepsilon_{yz} \\ \varepsilon_{xz} & \varepsilon_{yz} & \epsilon_{zz} \end{pmatrix}, \tag{3.26}$$

$$\boldsymbol{\tau} = \begin{pmatrix} \tau_{xx} \\ \tau_{yy} \\ \tau_{zz} \\ \tau_{yz} \\ \tau_{xz} \\ \tau_{xy} \end{pmatrix} = \begin{pmatrix} \tau_1 \\ \tau_2 \\ \tau_3 \\ \tau_4 \\ \tau_5 \\ \tau_6 \end{pmatrix}, \tag{3.27}$$

$$\boldsymbol{\varepsilon} = \begin{pmatrix} \varepsilon_{xx} \\ \varepsilon_{yy} \\ \varepsilon_{zz} \\ 2\,\varepsilon_{yz} \\ 2\,\varepsilon_{xz} \\ 2\,\varepsilon_{xy} \end{pmatrix} = \begin{pmatrix} \varepsilon_1 \\ \varepsilon_2 \\ \varepsilon_3 \\ 2\,\varepsilon_4 \\ 2\,\varepsilon_5 \\ 2\,\varepsilon_6 \end{pmatrix}. \tag{3.28}$$

Unlike the stress and strain tensors $\boldsymbol{\tau}$ and $\boldsymbol{\varepsilon}$, the stiffness tensor $\boldsymbol{C}$ is a fourth rank tensor. In C_{ijkl}, subscripts i, j, k and l all range from one to three, again representing the x, y and z directions of three dimensional space. As can be seen in Equation 3.5, each value in C_{ijkl} has the physical significance of relating how an individual strain component ε_{kl} affects an individual stress component τ_{ij}. $\boldsymbol{C}$ describes how each of the nine strain components in the strain tensor $\boldsymbol{\varepsilon}$ affects each of the nine stress components in the stress tensor $\boldsymbol{\tau}$, indicating that there should to be a total of 81 values in stiffness tensor $\boldsymbol{C}$ to fully relate strain to stress. The number of independent components in $\boldsymbol{C}$, however, is fewer than 81. Due to the symmetries in $\boldsymbol{\tau}$ and $\boldsymbol{\varepsilon}$ stated above, namely $\tau_{ij} = \tau_{ji}$ and $\varepsilon_{kl} = \varepsilon_{lk}$, the number of independent components in $\boldsymbol{C}$ is reduced to 36. Because it is

inconvenient to display $\boldsymbol{C}$ as a four dimensional object, the 4th rank tensor $\boldsymbol{C}$ is often displayed as a 6x6 matrix, shown in Equation 3.29. In this formulation Voigt notation is used, where the subscripts 1 through 6 indicate the six unique two-dimension combinations shown in Equations 3.27 and 3.28. Lastly, an additional symmetry imposed by conservation of energy indicates that the 6x6 matrix representation of $\boldsymbol{C}$ must be symmetric, further reducing the number of independent components of stiffness tensor $\boldsymbol{C}$ to 21 (Sen, Seismology III, class notes). This symmetric stiffness tensor can be seen in Equation 3.30. Equation 3.5 rewritten in matrix form using Voigt notation can be seen in Equation 3.31. Note that factors of two are introduced into Equations 3.28 and 3.31 in order to account for the duplicity of ε_{kl} and ε_{lk} when $k \neq l$.

$$\boldsymbol{C} = \begin{pmatrix} C_{11} & C_{21} & C_{31} & C_{41} & C_{51} & C_{61} \\ C_{12} & C_{22} & C_{32} & C_{42} & C_{52} & C_{62} \\ C_{13} & C_{23} & C_{33} & C_{43} & C_{53} & C_{63} \\ C_{14} & C_{24} & C_{34} & C_{44} & C_{54} & C_{64} \\ C_{15} & C_{25} & C_{35} & C_{45} & C_{55} & C_{65} \\ C_{16} & C_{26} & C_{36} & C_{46} & C_{56} & C_{66} \end{pmatrix}, \tag{3.29}$$

$$\boldsymbol{C} = \begin{pmatrix} C_{11} & C_{12} & C_{13} & C_{14} & C_{15} & C_{16} \\ C_{12} & C_{22} & C_{23} & C_{24} & C_{25} & C_{26} \\ C_{13} & C_{23} & C_{33} & C_{34} & C_{35} & C_{36} \\ C_{14} & C_{24} & C_{34} & C_{44} & C_{45} & C_{46} \\ C_{15} & C_{25} & C_{35} & C_{45} & C_{55} & C_{56} \\ C_{16} & C_{26} & C_{36} & C_{46} & C_{56} & C_{66} \end{pmatrix}, \tag{3.30}$$

$$\begin{pmatrix} \tau_1 \\ \tau_2 \\ \tau_3 \\ \tau_4 \\ \tau_5 \\ \tau_6 \end{pmatrix} = \begin{pmatrix} C_{11} & C_{12} & C_{13} & C_{14} & C_{15} & C_{16} \\ C_{12} & C_{22} & C_{23} & C_{24} & C_{25} & C_{26} \\ C_{13} & C_{23} & C_{33} & C_{34} & C_{35} & C_{36} \\ C_{14} & C_{24} & C_{34} & C_{44} & C_{45} & C_{46} \\ C_{15} & C_{25} & C_{35} & C_{45} & C_{55} & C_{56} \\ C_{16} & C_{26} & C_{36} & C_{46} & C_{56} & C_{66} \end{pmatrix} \begin{pmatrix} \varepsilon_1 \\ \varepsilon_2 \\ \varepsilon_3 \\ 2\,\varepsilon_4 \\ 2\,\varepsilon_5 \\ 2\,\varepsilon_6 \end{pmatrix}. \tag{3.31}$$

A proper understanding of the stiffness tensor associated with a particular medium is crucial to understand seismic anisotropy. Despite the generalized meaning that anisotropy means that properties are directionally dependent, seismic anisotropy explicitly indicates the existence, or lack there-of, of rotational symmetry in the stiffness tensor $\boldsymbol{C}$. Rotational symmetry can be proved by applying a rotational operator, known as a Born transform, to a stiffness tensor and showing that the rotated tensor is identical to the un-rotated tensor when specific rotations have been applied. To derive the rotational operator for a stiffness tensor, let us first consider rotating a vector in 2 dimensional space. An example of this can be seen in Figure 3.3.

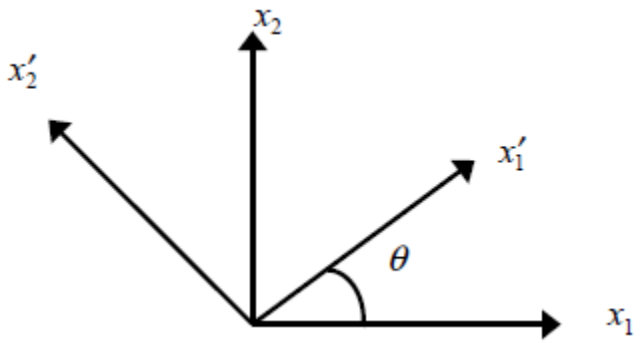

Figure 3.3: A graphical representation of vectors x_1 and x_2 in 2 dimensions, which correspond to the X and Y axis, being rotated by θ degrees counter clockwise. The resulting rotated vectors are notated x_1' and x_2'. Figure originally from Sen, Seismology III, class notes.

Figure 3.3 illustrates how the x component of a vector (represented by x_1) and the y component of a vector (represented by x_2) change under rotation. Simple trigonometry indicates that:

$$x_1' = |x_1| \, (\cos\theta \, \hat{x} + \sin\theta \, \hat{y}) \, , \tag{3.32}$$

$$x_2' = |x_2| \, (-\sin\theta \, \hat{x} + \cos\theta \, \hat{y}) \, . \tag{3.33}$$

Thus, some arbitrary vector x made up of parts x_1 and x_2 can be rotated counter-clockwise by θ:

$$x = \begin{pmatrix} x_1 \\ x_2 \end{pmatrix}, \tag{3.34}$$

$$x' = \begin{pmatrix} \cos\theta & \sin\theta \\ -\sin\theta & \cos\theta \end{pmatrix} x = \boldsymbol{A}x\,, \tag{3.35}$$

where $\boldsymbol{A}$ represents the rotational matrix. This rotational matrix can be expanded to 3 dimensional space. In 3D space, any arbitrary rotation can be constructed from three orthogonal rotations, known as Euler rotations, around the x, y and z axes. A rotation about the z axis indicated change in the x-y plane, and thus the rotational matrix becomes:

$$\boldsymbol{A}_z = \begin{pmatrix} \cos\phi & \sin\phi & 0 \\ -\sin\phi & \cos\phi & 0 \\ 0 & 0 & 1 \end{pmatrix}. \tag{3.36}$$

Rotations about the x and y axis follow a similar pattern, resulting in:

$$\boldsymbol{A}_x = \begin{pmatrix} 1 & 0 & 0 \\ 0 & \cos\theta & \sin\theta \\ 0 & -\sin\theta & \cos\theta \end{pmatrix}, \tag{3.37}$$

$$\boldsymbol{A}_y = \begin{pmatrix} \cos\varphi & 0 & -\sin\varphi \\ 0 & 1 & 0 \\ \sin\varphi & 0 & \cos\varphi \end{pmatrix}. \tag{3.38}$$

A cascaded matrix multiplication of $\boldsymbol{A}_x$, $\boldsymbol{A}_y$ and $\boldsymbol{A}_z$ will allow for any possible rotation of a vector in 3 dimensional space.

Now that it is understood how to rotate a vector, these rotational matrices can be applied to second order stress and strain tensors. A rotation about a single axis can be performed using the following equations:

$$\tau'_{ij} = A_{ik}A_{jl}\tau_{kl} \,, \tag{3.39}$$

$$\varepsilon'_{ij} = A_{ik}A_{jl}\varepsilon_{kl} \,, \tag{3.40}$$

for $\boldsymbol{A} = \boldsymbol{A}_x$, $\boldsymbol{A}_y$ or $\boldsymbol{A}_z$ as described by equations 3.36 – 3.38. This results in

$$\begin{pmatrix} \tau'_{xx} \\ \tau'_{yy} \\ \tau'_{zz} \\ \tau'_{yz} \\ \tau'_{xz} \\ \tau'_{xy} \end{pmatrix} = \boldsymbol{M} \begin{pmatrix} \tau_{xx} \\ \tau_{yy} \\ \tau_{zz} \\ \tau_{yz} \\ \tau_{xz} \\ \tau_{xy} \end{pmatrix} \,, \tag{3.41}$$

$$\begin{pmatrix} \varepsilon'_{xx} \\ \varepsilon'_{yy} \\ \varepsilon'_{zz} \\ 2\,\varepsilon'_{yz} \\ 2\,\varepsilon'_{xz} \\ 2\,\varepsilon'_{xy} \end{pmatrix} = \boldsymbol{N} \begin{pmatrix} \varepsilon_{xx} \\ \varepsilon_{yy} \\ \varepsilon_{zz} \\ 2\,\varepsilon_{yz} \\ 2\,\varepsilon_{xz} \\ 2\,\varepsilon_{xy} \end{pmatrix} \,, \tag{3.42}$$

$$\boldsymbol{M} = \begin{pmatrix} A_{11}^2 & A_{12}^2 & A_{13}^2 & 2\,A_{12}\,A_{13} & 2\,A_{13}\,A_{11} & 2\,A_{11}\,A_{12} \\ A_{21}^2 & A_{22}^2 & A_{23}^2 & 2\,A_{22}\,A_{23} & 2\,A_{23}\,A_{21} & 2\,A_{21}\,A_{22} \\ A_{31}^2 & A_{32}^2 & A_{33}^2 & 2\,A_{32}\,A_{33} & 2\,A_{33}\,A_{31} & 2\,A_{31}\,A_{32} \\ A_{21}\,A_{31} & A_{22}\,A_{32} & A_{23}\,A_{33} & A_{22}\,A_{33} + A_{23}\,A_{32} & A_{21}\,A_{33} + A_{23}\,A_{31} & A_{22}\,A_{31} + A_{21}\,A_{32} \\ A_{31}\,A_{11} & A_{32}\,A_{12} & A_{33}\,A_{13} & A_{12}\,A_{33} + A_{13}\,A_{32} & A_{13}\,A_{31} + A_{11}\,A_{33} & A_{11}\,A_{32} + A_{12}\,A_{31} \\ A_{11}\,A_{12} & A_{12}\,A_{22} & A_{13}\,A_{23} & A_{12}\,A_{23} + A_{13}\,A_{22} & A_{13}\,A_{21} + A_{11}\,A_{23} & A_{11}\,A_{22} + A_{12}\,A_{21} \end{pmatrix}, \tag{3.43}$$

$$\boldsymbol{N} = \begin{pmatrix} A_{11}^2 & A_{12}^2 & A_{13}^2 & A_{12}\,A_{13} & A_{13}\,A_{11} & A_{11}\,A_{12} \\ A_{21}^2 & A_{22}^2 & A_{23}^2 & A_{22}\,A_{23} & A_{23}\,A_{21} & A_{21}\,A_{22} \\ A_{31}^2 & A_{32}^2 & A_{33}^2 & A_{32}\,A_{33} & A_{33}\,A_{31} & A_{31}\,A_{32} \\ 2\,A_{21}\,A_{31} & 2\,A_{22}\,A_{32} & 2\,A_{23}\,A_{33} & A_{22}\,A_{33} + A_{23}\,A_{32} & A_{21}\,A_{33} + A_{23}\,A_{31} & A_{22}\,A_{31} + A_{21}\,A_{32} \\ 2\,A_{31}\,A_{11} & 2\,A_{32}\,A_{12} & 2\,A_{33}\,A_{13} & A_{12}\,A_{33} + A_{13}\,A_{32} & A_{13}\,A_{31} + A_{11}\,A_{33} & A_{11}\,A_{32} + A_{12}\,A_{31} \\ 2\,A_{11}\,A_{12} & 2\,A_{12}\,A_{22} & 2\,A_{13}\,A_{23} & A_{12}\,A_{23} + A_{13}\,A_{22} & A_{13}\,A_{21} + A_{11}\,A_{23} & A_{11}\,A_{22} + A_{12}\,A_{21} \end{pmatrix}. \tag{3.44}$$

It is important to note that $\boldsymbol{M}$ and $\boldsymbol{N}$ share a special relationship (Sen, Seismology III, class notes), such that:

$$\boldsymbol{M}^{-1} = \boldsymbol{N}^{\boldsymbol{T}} . \tag{3.45}$$

We can now apply the stress strain relationship shown in Equations 3.5 and 3.46 to determine the rotated stiffness tensor $\boldsymbol{C}'$, using the equations shown below.

$$\boldsymbol{\tau} = \boldsymbol{C}\,\boldsymbol{\varepsilon} , \tag{3.46}$$

$$\boldsymbol{\tau}' = \boldsymbol{M}\boldsymbol{\tau} = \boldsymbol{M}\boldsymbol{C}\boldsymbol{\varepsilon} , \tag{3.47}$$

$$\boldsymbol{\varepsilon} = \boldsymbol{N}^{-1}\,\boldsymbol{\varepsilon}' , \tag{3.48}$$

$$\boldsymbol{\tau}' = \boldsymbol{M}\boldsymbol{C}\boldsymbol{\varepsilon} = \boldsymbol{M}\boldsymbol{C}\boldsymbol{N}^{-1}\,\boldsymbol{\varepsilon}' = \boldsymbol{M}\boldsymbol{C}\boldsymbol{M}^{T}\,\boldsymbol{\varepsilon}' = \boldsymbol{C}'\,\boldsymbol{\varepsilon}' , \tag{3.49}$$

$$\boldsymbol{C}' = \boldsymbol{M}\boldsymbol{C}\boldsymbol{M}^{T} . \tag{3.50}$$

Equation 3.50 describes a single rotation of a stiffness tensor, and can be extended to any arbitrary rotation in 3 dimensions by cascading up to 3 orthogonal rotations. This results in

$$\boldsymbol{C}' = (\boldsymbol{M}_x\boldsymbol{M}_y\boldsymbol{M}_z)\,\boldsymbol{C}\,(\boldsymbol{M}_x\boldsymbol{M}_y\boldsymbol{M}_z)^{T} , \tag{3.51}$$

where $\boldsymbol{M}_x$, $\boldsymbol{M}_y$ and $\boldsymbol{M}_z$ are determined using Equation 3.43 and rotational matrices $\boldsymbol{A}_x$, $\boldsymbol{A}_y$ and $\boldsymbol{A}_z$ from Equations 3.36 – 3.38 for rotations around the x, y and z axes, respectively. As an example, matrix $\boldsymbol{M}_z$, which applies a counterclockwise rotation (θ) in the x-z plane, has the form:

$$\boldsymbol{M}_x = \begin{pmatrix} \cos^2\theta & \sin^2\theta & 0 & 0 & 0 & -\sin 2\theta \\ \sin^2\theta & \cos^2\theta & 0 & 0 & 0 & \sin 2\theta \\ 0 & 0 & 1 & 0 & 0 & 0 \\ 0 & 0 & 0 & \cos\theta & \sin\theta & 0 \\ 0 & 0 & 0 & -\sin\theta & \cos\theta & 0 \\ \frac{1}{2}\sin 2\theta & -\frac{1}{2}\sin 2\theta & 0 & 0 & 0 & \cos 2\theta \end{pmatrix} . \tag{3.52}$$

Rotational symmetry of a stiffness tensor can be proved by applying the Born transformation rotation shown in Equation 3.51 and showing the input stiffness tensor is identical to the rotated tensor for each symmetry type ($\boldsymbol{C} = \boldsymbol{C}'$). However, explicit proof will not be provided in this thesis. Different combinations of rotational symmetries in the stiffness tensor result in the various types of seismic anisotropy that exist. These rotational symmetries dictate the form of the stiffness tensor associated with a particular anisotropy type and thus determine the number of independent elastic parameters needed to describe that anisotropy type. These symmetry types physically represent the various levels of symmetry in a crystal system. In the most general case, known as triclinic anisotropy, no rotational symmetry exists in the stiffness tensor, and all 21 independent elastic coefficients are needed to describe the medium. This corresponds to the stiffness tensor shown previously in Equation 3.30. In the case of monoclinic symmetry, minimal symmetry is imposed requiring either one mirror plane of symmetry or 180 degree rotational symmetry in a single plane. This leads the stiffness tensor to have the form shown in Equation 3.53, which requires 13 independent elastic constants to fully describe. In the case of orthorhombic symmetry, either 180 degree rotational symmetry around 3 separate planes or 180 degree rotational symmetry around a single plane and two mirror planes are required, resulting in the stiffness tensor shown in Equation 3.54. An orthorhombic stiffness tensor requires 9 independent elastic constants to fully describe. In the case of transversely isotropic media, the stiffness tensor is preserved when rotated by any amount around a single axis of symmetry – a more general form of hexagonal crystal symmetry. This results in two end cases, generally referred to as Vertically Transverse Isotropic (VTI) and Horizontally Transverse Isotropic (HTI). In the VTI case, the plane of symmetry is in the X-Y (i.e., horizontal) plane, while in the HTI case the plane of symmetry is in the X-Z or Y-Z (i.e., vertical) plane. If the plane of

symmetry does not match with those of HTI or VTI, the medium is often said to be characteristic of Tilted Transverse Isotropy (TTI). The stiffness tensor corresponding to the VTI case can be seen in Equation 3.55, and the stiffness tensor corresponding to the HTI case can be seen in Equation 3.56. Both the VTI and HTI stiffness tensors require 5 independent elastic constants to fully describe. Lastly, in the case that the stiffness tensor is rotationally symmetric for all possible rotations, indicating no directional dependence of any kind, the medium is known as isotropic. The stiffness tensor corresponding to the isotropic case can be seen in Equation 3.57, and only requires two independent elastic constants to describe (Sen, Seismology III class notes).

$$\boldsymbol{C}\ (monoclinic) = \begin{pmatrix} C_{11} & C_{12} & C_{13} & 0 & 0 & C_{16} \\ C_{12} & C_{22} & C_{23} & 0 & 0 & C_{26} \\ C_{13} & C_{23} & C_{33} & 0 & 0 & C_{36} \\ 0 & 0 & 0 & C_{44} & C_{45} & 0 \\ 0 & 0 & 0 & C_{45} & C_{55} & 0 \\ C_{16} & C_{26} & C_{36} & 0 & 0 & C_{66} \end{pmatrix}, \tag{3.53}$$

$$\boldsymbol{C}\ (orthorhombic) = \begin{pmatrix} C_{11} & C_{12} & C_{13} & 0 & 0 & 0 \\ C_{12} & C_{22} & C_{23} & 0 & 0 & 0 \\ C_{13} & C_{23} & C_{33} & 0 & 0 & 0 \\ 0 & 0 & 0 & C_{44} & 0 & 0 \\ 0 & 0 & 0 & 0 & C_{55} & 0 \\ 0 & 0 & 0 & 0 & 0 & C_{66} \end{pmatrix}, \tag{3.54}$$

$$\boldsymbol{C}\ (VTI) = \begin{pmatrix} C_{11} & C_{11} - 2\,C_{66} & C_{13} & 0 & 0 & 0 \\ C_{11} - 2\,C_{66} & C_{11} & C_{13} & 0 & 0 & 0 \\ C_{13} & C_{13} & C_{33} & 0 & 0 & 0 \\ 0 & 0 & 0 & C_{44} & 0 & 0 \\ 0 & 0 & 0 & 0 & C_{44} & 0 \\ 0 & 0 & 0 & 0 & 0 & C_{66} \end{pmatrix}, \tag{3.55}$$

$$\boldsymbol{C}\,(HTI) = \begin{pmatrix} C_{11} & C_{13} & C_{13} & 0 & 0 & 0 \\ C_{13} & C_{33} & C_{33} - 2\,C_{44} & 0 & 0 & 0 \\ C_{13} & C_{33} - 2\,C_{44} & C_{33} & 0 & 0 & 0 \\ 0 & 0 & 0 & C_{44} & 0 & 0 \\ 0 & 0 & 0 & 0 & C_{55} & 0 \\ 0 & 0 & 0 & 0 & 0 & C_{55} \end{pmatrix}, \qquad (3.56)$$

$$\boldsymbol{C}\,(isotropic) = \begin{pmatrix} \lambda + 2\mu & \lambda & \lambda & 0 & 0 & 0 \\ \lambda & \lambda + 2\mu & \lambda & 0 & 0 & 0 \\ \lambda & \lambda & \lambda + 2\mu & 0 & 0 & 0 \\ 0 & 0 & 0 & \mu & 0 & 0 \\ 0 & 0 & 0 & 0 & \mu & 0 \\ 0 & 0 & 0 & 0 & 0 & \mu \end{pmatrix}. \qquad (3.57)$$

3.4 Linear Slip Theory and Effective Anisotropy

Effective medium modeling indicates that certain features, for example bedding and fracturing, which are small compared to a seismic wavelength, will be averaged in such a way that the medium has an identical seismic response to one that is homogeneous and anisotropic. The work presented in this thesis aims to characterize fractures in two assumed situations:

1. Fractures are closely spaced, vertically aligned, rotationally invariant, and embedded an otherwise isotropic background rock.
2. Fractures are closely spaced, vertically aligned, rotationally invariant, and embedded an otherwise VTI anisotropic background rock.

Linear slip deformation theory (Schoenberg 1980; Schoenberg and Sayers, 1995; Bakulin et al., 2000, Part I and Part II) will be used to determine and verify the anisotropy type resulting from these two assumed situations. The linear slip model indicates that fractures, which introduce compliance into the rock, linearly add to the compliance of the background rock, such that

$$\boldsymbol{S} = \boldsymbol{S_b} + \boldsymbol{S_f} \ , \tag{3.58}$$

where $\boldsymbol{S_b}$ is the compliance tensor of the background rock and $\boldsymbol{S_f}$ is the excess compliance introduced by the fractures. The effective compliance tensor $\boldsymbol{S}$ is the inverse of the effective stiffness tensor $\boldsymbol{C}$, such that:

$$\boldsymbol{S} = \boldsymbol{C^{-1}} \text{ and } \boldsymbol{C} = \boldsymbol{S^{-1}} \ . \tag{3.59}$$

Note that inverting stiffness and compliance tensors in Voigt notation is rather peculiar due to the factors of 2 in the $\boldsymbol{\varepsilon}$ vector, and in order for a standard matrix inversion to be applicable Equation 3.31 must first be transformed to:

$$\begin{pmatrix} \tau_1 \\ \tau_2 \\ \tau_3 \\ \sqrt{2}*\tau_4 \\ \sqrt{2}*\tau_5 \\ \sqrt{2}*\tau_6 \end{pmatrix} = \begin{pmatrix} C_{11} & C_{12} & C_{13} & \sqrt{2}*C_{14} & \sqrt{2}*C_{15} & \sqrt{2}*C_{16} \\ C_{12} & C_{22} & C_{23} & \sqrt{2}*C_{24} & \sqrt{2}*C_{25} & \sqrt{2}*C_{26} \\ C_{13} & C_{23} & C_{33} & \sqrt{2}*C_{34} & \sqrt{2}*C_{35} & \sqrt{2}*C_{36} \\ \sqrt{2}*C_{14} & \sqrt{2}*C_{24} & \sqrt{2}*C_{34} & 2*C_{44} & 2*C_{45} & 2*C_{46} \\ \sqrt{2}*C_{15} & \sqrt{2}*C_{25} & \sqrt{2}*C_{35} & 2*C_{45} & 2*C_{55} & 2*C_{56} \\ \sqrt{2}*C_{16} & \sqrt{2}*C_{26} & \sqrt{2}*C_{36} & 2*C_{46} & 2*C_{56} & 2*C_{66} \end{pmatrix} \begin{pmatrix} \varepsilon_1 \\ \varepsilon_2 \\ \varepsilon_3 \\ \sqrt{2}*\varepsilon_4 \\ \sqrt{2}*\varepsilon_5 \\ \sqrt{2}*\varepsilon_6 \end{pmatrix} . \tag{3.60}$$

In the case of a single closely spaced vertically aligned fracture set, the fracture induced compliance tensor $\boldsymbol{S_f}$ takes the form (Bakulin et al., 2000, Part I):

$$\boldsymbol{S_f} = \begin{pmatrix} K_N & 0 & 0 & 0 & K_{NV} & K_{NH} \\ 0 & 0 & 0 & 0 & 0 & 0 \\ 0 & 0 & 0 & 0 & 0 & 0 \\ 0 & 0 & 0 & 0 & 0 & 0 \\ K_{NV} & 0 & 0 & 0 & K_V & K_{VH} \\ K_{NH} & 0 & 0 & 0 & K_{VH} & K_H \end{pmatrix} . \tag{3.61}$$

In equation 3.61, K_N physically represents the introduced compliance in the direction normal to the fracture set, K_V and K_H physically represent the introduced compliance in the direction tangential to the fracture set in the vertical (K_V) and horizontal (K_H)

direction, and off-diagonal terms represent coupling associated with K_N, K_V and K_H elements. Off-diagonal terms are a measure of micro corrugation of fracture facies, also known as “fracture roughness”, and are assumed to be zero in this work. In the case that fractures are rotationally invariant and imbedded in an isotropic medium, vertical (K_V) and horizontal (K_H) compliances are identical, and are denoted simply as K_T. The resulting excess compliance tensor resulting from this simplified situation is shown in Equation 3.62. In the case that fractures are embedded in a VTI background rock, rotational symmetry is broken and thus K_V and K_H are not necessarily identical. It is often convenient to normalize these excess compliance terms to range between 0 and 1. These normalized compliance terms are denoted as “fracture weaknesses”. When fractures are imbedded in an otherwise isotropic background rock, this normalization is performed using Equations 3.63 and 3.64 (Bakulin et al., 2000, Part I).

$$\boldsymbol{S_f} = \begin{pmatrix} K_N & 0 & 0 & 0 & 0 & 0 \\ 0 & 0 & 0 & 0 & 0 & 0 \\ 0 & 0 & 0 & 0 & 0 & 0 \\ 0 & 0 & 0 & 0 & 0 & 0 \\ 0 & 0 & 0 & 0 & K_T & 0 \\ 0 & 0 & 0 & 0 & 0 & K_T \end{pmatrix} . \tag{3.62}$$

$$\Delta N = \frac{(\lambda + 2\mu)\, KN}{1+(\lambda + 2\mu)\, KN} , \tag{3.63}$$

$$\Delta T = \frac{\mu\, KT}{1+\mu\, KT} , \tag{3.64}$$

where ΔN and ΔT represent normal and tangential fracture weakness, respectively. ΔN and ΔT both increase with denser fracturing, and can provide useful information regarding if fractures are dry / gas filled or fluid filled (Shaw and Sen, 2006).

In the case of dry or gas filled fractures, compliances are introduced in both the normal and tangential directions. However, in the case of fluid filled fractures, compliance will be primarily introduced in the tangential direction, and thus ΔN will be small compared to ΔT. This phenomenon occurs because liquids are approximately as compressible as rocks, and thus normal compliance (which is related to the inverse of compressibility) is roughly unchanged when fluid in inserted into the rock. However, even at reservoir conditions, gas is significantly less compressible than rock, and thus dry or gas filled fractures introduce significant compliance into the rock. Both fluids and gasses have a shear modulus of zero, and thus tangential compliance (which is related to the inverse of the shear modulus) increases dramatically when dry, gas filled or fluid filled fractures are introduced into a rock. Using this information, one can use the ratio of ΔN and ΔT as a fluid indication attribute. The fluid indicator attribute suggested by Shaw and Sen (2006) is shown in Equation 3.65, which trends towards zero in the case of fluid filled cracks and trends towards unity in the case of dry or gas filled fractures.

$$Fluid\ Indicator = g\ \frac{\Delta N}{\Delta T}\ , \tag{3.65}$$

$$g = \frac{V_s^2}{V_p^2}\ , \tag{3.66}$$

where V_p and V_s represent the velocity of compressional and shear waves, respectively.

In the case of a single rotationally invariant fracture set embedded in either an isotropic or VTI background rock, Bakulin et al. (2000, Part II) show that the effective compliance tensor, calculated by determining the inverse of the effective compliance tensor found using linear slip theory, has the following form:

$$\boldsymbol{C}\,(eff) = \begin{pmatrix} \mathrm{C}_{11b}(1-\Delta N) & \mathrm{C}_{12b}(1-\Delta N) & C_{13b}(1-\Delta N) & 0 & 0 & 0 \\ \mathrm{C}_{12b}(1-\Delta N) & \mathrm{C}_{22b}-\Delta N\left(\frac{C_{12b}^2}{\mathrm{C}_{11b}}\right) & \mathrm{C}_{23b}\left(1-\Delta N\left(\frac{\mathrm{C}_{12b}}{\mathrm{C}_{11b}}\right)\right) & 0 & 0 & 0 \\ \mathrm{C}_{13b}(1-\Delta N) & \mathrm{C}_{23b}\left(1-\Delta N\left(\frac{\mathrm{C}_{12b}}{\mathrm{C}_{11b}}\right)\right) & \mathrm{C}_{33b}-\Delta N\left(\frac{C_{13b}^2}{\mathrm{C}_{11b}}\right) & 0 & 0 & 0 \\ 0 & 0 & 0 & \mathrm{C}_{44b} & 0 & 0 \\ 0 & 0 & 0 & 0 & \mathrm{C}_{55b}(1-\Delta V) & 0 \\ 0 & 0 & 0 & 0 & 0 & \mathrm{C}_{66b}(1-\Delta H) \end{pmatrix}, \tag{3.67}$$

where C_{ijb} represents compliance tensor elements of the background rock. Note that in the isotropic background rock case ΔV and ΔH are identical, and are denoted ΔT.

The compliance tensor elements for the VTI and isotropic background rock cases are shown in Equations 3.55 and 3.57, respectively. By substituting these into the generalized effective stiffness tensor shown in Equation 3.67, one can determine the exact form of the effective stiffness tensor in the two cases of interest. The effective stiffness tensor for the case where fractures are embedded in an isotropic background rock is shown in Equation 3.47.

$$\boldsymbol{C}\,(eff) = \begin{pmatrix} (\lambda+2\mu)\,(1-\Delta\mathrm{N}) & \lambda\,(1-\Delta\mathrm{N}) & \lambda\,(1-\Delta\mathrm{N}) & 0 & 0 & 0 \\ \lambda\,(1-\Delta\mathrm{N}) & (\lambda+2\mu)-\Delta\mathrm{N}\left(\frac{\lambda^2}{\lambda+2\mu}\right) & \lambda\left(1-\Delta\mathrm{N}\left(\frac{\lambda}{\lambda+2\mu}\right)\right) & 0 & 0 & 0 \\ \lambda\,(1-\Delta\mathrm{N}) & \lambda\left(1-\Delta\mathrm{N}\left(\frac{\lambda}{\lambda+2\mu}\right)\right) & (\lambda+2\mu)-\Delta\mathrm{N}\left(\frac{\lambda^2}{\lambda+2\mu}\right) & 0 & 0 & 0 \\ 0 & 0 & 0 & \mu & 0 & 0 \\ 0 & 0 & 0 & 0 & \mu\,(1-\Delta\mathrm{T}) & 0 \\ 0 & 0 & 0 & 0 & 0 & \mu\,(1-\Delta\mathrm{T}) \end{pmatrix}. \tag{3.68}$$

Analysis of Equation 3.68 shows that this stiffness tensor has a form identical to that of a HTI medium, shown in Equation 3.56, proving that treating the medium as effective HTI anisotropic is valid in the case of a single rotationally invariant fracture set embedded in an isotropic background rock, here forth dubbed the “HTI Case”. The effective stiffness

tensor for the case where fractures are embedded in a VTI anisotropic background rock is shown in Equation 3.69.

$$\boldsymbol{C}\,(eff) = \begin{pmatrix} \mathrm{C}_{11b}(1-\Delta N) & (\mathrm{C}_{11b}-2\,\mathrm{C}_{66b})(1-\Delta N) & \mathrm{C}_{13b}(1-\Delta N) & 0 & 0 & 0 \\ (\mathrm{C}_{11b}-2\,\mathrm{C}_{66b})(1-\Delta N) & \mathrm{C}_{11b}-\Delta N\left(\frac{(\mathrm{C}_{11b}-2\,\mathrm{C}_{66b})^2}{\mathrm{C}_{11b}}\right) & \mathrm{C}_{13b}\left(1-\Delta N\left(\frac{\mathrm{C}_{11b}-2\,\mathrm{C}_{66b}}{\mathrm{C}_{11b}}\right)\right) & 0 & 0 & 0 \\ \mathrm{C}_{13b}(1-\Delta N) & \mathrm{C}_{13b}\left(1-\Delta N\left(\frac{\mathrm{C}_{11b}-2\,\mathrm{C}_{66b}}{\mathrm{C}_{11b}}\right)\right) & \mathrm{C}_{33b}-\Delta N\left(\frac{\mathrm{C}_{13b}^2}{\mathrm{C}_{11b}}\right) & 0 & 0 & 0 \\ 0 & 0 & 0 & \mathrm{C}_{44b} & 0 & 0 \\ 0 & 0 & 0 & 0 & \mathrm{C}_{44b}(1-\Delta V) & 0 \\ 0 & 0 & 0 & 0 & 0 & \mathrm{C}_{66b}(1-\Delta H) \end{pmatrix}, \tag{3.69}$$

where C_{ijb} represents compliance tensor elements of the VTI background rock described by Equation 3.55. Analysis of Equation 3.69 shows that this stiffness tensor has a form identical to that of an orthorhombic medium, shown in Equation 3.54, proving that treating the medium as effective orthorhombic anisotropic is valid in the case of a single rotationally invariant fracture set embedded in a VTI anisotropic background rock, here forth dubbed the "Orthorhombic Case". Bakulin et al. (2000, Part I) note that similar results are obtained by assuming aligned penny shaped cracks (Hudson, 1981), but that derivation will not be included in this thesis. It is interesting to note that in both the HTI case and the Orthorhombic case the stiffness tensor contains one fewer independent value than in the archetypal anisotropic case. In the HTI case this corresponds to a special HTI medium, which can be parameterized by four parameters instead of the usual five parameters – two elastic parameters from the isotropic background rock and two fracture weakness parameters. In the orthorhombic case this corresponds to a special orthorhombic medium, which can be parameterized by eight parameters instead of the usual nine parameters – five elastic parameters from the VTI background rock and three fracture weakness parameters. In the orthorhombic case this leads to an additional constraint on the effective stiffness tensor, shown in Equation 3.70.

$$C_{13}\,(C_{22}+C_{12}) = C_{23}\,(C_{11}+C_{12})\ . \tag{3.70}$$

While these special properties are not utilized in this work, they could prove useful in future work that aims to invert directly for elastic properties in HTI or orthorhombic media by reducing the number of unknown elastic parameters.

3.5 INVERSION

In the most general sense, inversion aims to determine the characteristics of causal features by analyzing the effects these features produce. In geophysics, inverse problems generally aim to characterize some subsurface property, for example seismic wave velocity or density, by analyzing a set of observations where the desired parameter(s) induce some causal effect, for example a set of features present in seismic data. In this work, parameters that characterize fractures, namely fracture density and fracture orientation, are the desired earth parameters for which are being inverted. A 3D seismic dataset constitutes the set of observations that are to be analyzed to invert for these fracture characteristics. In any inverse problem, a proper understanding of the forward problem is crucial. The forward problem specifies how changes in the desired model parameters alter certain observations. Generally speaking, the forward problem allows one to generate synthetic data based on a certain set of parameters. The synthetic data is then compared to the real data. The parameters associated with the synthetic dataset that most closely matches the real data are considered to be the most likely parameters, i.e., the “answer” to the inverse problem. Depending on the problem, finding this set of “best-fit” parameters might be an iterative process. The forward problems associated with the methods used in this work will be examined in detail in Chapters 4 and 5; however in the interest of providing the theoretical framework for inversion, the following assumptions are necessairy.

1. The forward problem exists, indicating that fracture density and orientation do causally effect 3D seismic data, and
2. The forward problem is linear in nature.

A linear forward problem can be posed in the general form shown in Equation 3.71.

$$\boldsymbol{d} = \boldsymbol{G}\boldsymbol{m} \ , \tag{3.71}$$

where $\boldsymbol{d}$ is a 1xn column vector representing n data points or observations, $\boldsymbol{m}$ is a 1xm column vector representing m distinct model parameters, and $\boldsymbol{G}$ is a mxn matrix, known as the linear operator or the kernel matrix, which is determined by the (often simplified) physics associated with the forward problem. $\boldsymbol{G}$ is the mathematical operator that governs how model parameters $\boldsymbol{m}$ affect data points $\boldsymbol{d}$. As an example, let us pose the two term AVO equation, shown in Equation 3.72, in the format depicted in Equation 3.71.

$$R(\theta) \approx A + B \sin^2 \theta \ . \tag{3.72}$$

In this case the desired model parameters are the two AVO weights A and B, and observations are seismic reflectivity data collected at unique incident angles $\theta_1, \theta_2, \dots, \theta_N$. Converted to the matrix form shown in Equation 3.71, the two term AVO equation transforms to:

$$\begin{pmatrix} R(\theta_1) \\ R(\theta_2) \\ \vdots \\ R(\theta_N) \end{pmatrix} = \begin{pmatrix} 1 & \sin^2(\theta_1) \\ 1 & \sin^2(\theta_2) \\ \vdots & \vdots \\ 1 & \sin^2(\theta_N) \end{pmatrix} \begin{pmatrix} A \\ B \end{pmatrix} \ . \tag{3.73}$$

After a linear problem has been posed in the general form depicted by Equation 3.71, matrix manipulation using standard linear algebra rules can be applied in order to find a solution for $\boldsymbol{m}$. This is generally accomplished by left-multiplying each side of Equation 3.71 by the inverse of matrix $\boldsymbol{G}$; however, $\boldsymbol{G}$ is not always a square matrix. To

resolve this, both sides of Equation 3.71 are first left-multiplied by the transpose of $\boldsymbol{G}$, denoted $\boldsymbol{G}^T$, resulting in:

$$\boldsymbol{G}^T\boldsymbol{d} = [\boldsymbol{G}^T\boldsymbol{G}]\boldsymbol{m} \ . \tag{3.74}$$

In Equation 3.74, the term $[\boldsymbol{G}^T\boldsymbol{G}]$ is by definition a square matrix, and thus a candidate to be inverted using standard matrix inversion techniques. In some problems, $[\boldsymbol{G}^T\boldsymbol{G}]$ will be singular or near-singular, making matrix inversion difficult. In these cases a pseudoinverse may be used, for example the Moore-Penrose pseudoinverse found by singular value decomposition (SVD). After the (pseudo)inverse of matrix $[\boldsymbol{G}^T\boldsymbol{G}]$ has been calculated, it is left-multiplied to each side of Equation 3.74, resulting in the solution for $\boldsymbol{m}$ shown in Equation 3.75.

$$\boldsymbol{m} = [\boldsymbol{G}^T\boldsymbol{G}]^{-1}\boldsymbol{G}^T\boldsymbol{d} \ . \tag{3.75}$$

The solution for $\boldsymbol{m}$ shown in equation 3.75 is the least-squares solution for model parameters in an overdetermined system, i.e., a system where the number of data points is greater than the number of desired model parameters. A least-squares solution minimizes the square of the data residual, i.e., the square of the difference between the collected data and the synthetic data generated by the forward problem. Proof that Equation 3.75 corresponds to a least squares solution can be found by analyzing an objective function E, which is associated with least-squares problems. In a least-squares problem, E generally consists of the sum of the square of data residual at all data points, as shown in Equation 3.76.

$$E = (\boldsymbol{d} - \boldsymbol{G}\boldsymbol{m})^T\,(\boldsymbol{d} - \boldsymbol{G}\boldsymbol{m}) = \sum[(d_i - \textstyle\sum_j G_{ij}m_j)\,(d_i - \sum_k G_{ik}m_k)] \ . \tag{3.76}$$

The objective function E, also known as the error function, is intended to be minimized in an inversion. The point where E achieves its minimum value is considered the "best-fit" solution, and the model parameters associated with the minimum value of E are the solution to the inverse problem. Note that E may be defined in more complex ways than

shown in Equation 3.76. However, Equation 3.76 represents the standard objective function for a least squares inversion approach, and it is commonly used in many inverse problems (Sen, Inverse Theory, class notes). The minimum value of E can be found by taking the derivative of E with respect to $\boldsymbol{m}$ and setting the said derivative equal to zero. This is shown in Equation 3.77.

$$\frac{\partial E}{\partial \boldsymbol{m}} = 2 \sum_{k=1}^{m} m_k \sum_{i=1}^{n} G_{iq} G_{ik} - 2 \sum_{i=1}^{n} G_{iq} d_i = 0 \ . \tag{3.77}$$

Transformed into matrix form, Equation 3.77 becomes:

$$[\boldsymbol{G}^T \boldsymbol{G}]\boldsymbol{m} - \boldsymbol{G}^T \boldsymbol{d} = 0 \ . \tag{3.78}$$

Note that Equation 3.78 is identical to Equation 3.74, and it can be solved in the same fashion, leading to the least squares solution for $\boldsymbol{m}$ shown in Equation 3.75. Least squares solutions to inverse problems are ideal for linear systems with Gaussian errors in data, as they provide solutions with errors that have a mean of zero, are uncorrelated, and have equal variance. Proof of error characteristics resulting from a least squares inversion is provided by the Gauss-Markov theorem (Plackett, 1950). Additionally, least squares solutions provide the simplest (i.e., minimal length) solutions for underdetermined problems, although in this case the solution has a form different than the one shown in Equation 3.75 (Sen, Inverse Theory, class notes).

In order to perform a more robust least squares regression analysis, one may wish to transform the standard least squares regression into a weighted least squares regression. This is accomplished by altering the objective function shown to the form shown in Equation 3.79 (Sen, Inverse Theory, class notes).

$$E = (\boldsymbol{d} - \boldsymbol{G}\boldsymbol{m})^T \boldsymbol{W}_d (\boldsymbol{d} - \boldsymbol{G}\boldsymbol{m}) \ , \tag{3.79}$$

where $\boldsymbol{W}_d$ represents a weighting matrix. By following the same procedure used in the standard least squares case, we arrive at the weighted least squares solution shown in Equation 3.80.

$$\boldsymbol{m} = [\boldsymbol{G}^T \boldsymbol{W}_d \boldsymbol{G}]^{-1} \boldsymbol{G}^T \boldsymbol{W}_d \boldsymbol{d} \ . \quad (3.80)$$

$\boldsymbol{W}_d$ can be represented in various ways that measure uncertainty, but is often calculated as a diagonal matrix with its n^{th} diagonal element corresponding to the inverse of data variance at the n^{th} data point. This results in data points with higher variance (i.e., worse fit) being given less weight in the inversion. If true data variance is already known, the weighted least squares can be accomplished in a single iteration. However, this formulation of least squares is often used in an iterative fashion, with $\boldsymbol{W}_d$ being updated on every iteration and calculated using data variance results from the previous iteration. In this case, the solution converges as $\boldsymbol{W}_d$ approaches an identity matrix. This iterative formulation of weighted least squares is called Iteratively Reweighted Least Squares (IRLS). Generally, IRLS will continue either until convergence has been achieved, indicating that change in model parameters and/or the objective function between iterations is less than some defined threshold, or until a pre-defined computational time limit has been reached. IRLS can also be used to solve non-linear inversion problems if the problem can be approximated as linear at every iteration. Seismic tomography is an example of a non-linear inverse problem that can be solved using IRLS. Non-linearity is introduced in seismic tomography because altering the subsurface velocity model affects the ray paths of the waves used in the inversion. However, if one makes the assumption that ray paths do not change within a single iteration (and are instead revised between iterations), each individual iteration becomes linearized and IRLS can be applied. Eventually, as the solution converges, velocity changes and thus changes in ray paths will approach zero between iterations, and the ideal solution will be found.

In the work described in the following chapters, standard, weighted and iteratively reweighted least squares inversions will be extensively used.

Chapter 4: Existing Fracture Characterization Methods

4.1 INTRODUCTION

Most fracture characterization methods currently in practice fundamentally assume that fractures are closely spaced, vertically aligned, rotationally invariant, and embedded in an otherwise isotropic background rock. Following the methodology outlined in Chapter 3, these assumptions lead to the fractured medium being characteristic of HTI anisotropic. Several linearized expressions for reflectivity in HTI media have been developed. In the most general sense, these linearized approximations pose reflectivity in terms of two variables: seismic wave incident angle (θ) and azimuth (φ). These equations can be related to fracture properties, and thus manipulating these equations allows one to determine relations for describing fracture characteristics, specifically fracture orientation and fracture density. By examining the equation(s) approximating reflectivity for local minima and maxima, one can find the strike of fracture azimuth. Constants of the equation(s) describing azimuthal variation can be used to determine the magnitude of the azimuthal difference in amplitudes, which is related to fracture density. In some cases, additional useful parameters can also be determined, for example normal and tangential fracture weaknesses.

The work presented in this chapter describes two common HTI fracture characterization techniques that utilize azimuthal variations in seismic amplitude (AVAZ). The first method is based on the Rüger AVO equation, and the second method is based on Fourier decomposition of the seismic data into a modified 4^{th} order Fourier series. Theory, implementation and results from both methods are presented. These methods rely on various least squares inversion techniques, as discussed in Chapter 3. The input for each analysis is a 3D seismic data set consisting of 137 inlines by 137 crosslines with offsets ranging from 225m to 6025m, and a RMS velocity model. Prior to

the onset of the following AVAZ analyses, data was processed as described in Chapter 2. To reiterate, azimuthal super-gathers consisting of 9 azimuth bins, each 20 degrees wide, and 30 offset bins with ~210m spacing is the input to the following analyses. Hampson-Russell © was primarily used to carry out the methods presented in this chapter, but some additional work was implemented using MATLAB ©.

4.2 RÜGER METHOD

The Rüger method is based on the Rüger AVO approximation to reflectivity in HTI media (Rüger, 1997; Rüger and Tsvankin, 1997), shown in Equation 4.1.

$$R(\theta,\varphi) = A + [B_{iso} + B_{ani}\ \sin^2(\varphi - \varphi_{iso})]\ \sin^2\theta\ , \qquad (4.1)$$

where θ represents incident angle, φ represents azimuth, and R represents seismic reflectivity. Equation 4.1 is a modification of the two term conventional AVO equation, shown in Equation 3.72, with the addition of an azimuthally varying gradient term (B_{ani}). Variables A, B_{iso} and B_{ani} can be postulated in terms of elastic properties of the effective media generating the reflectivity (see Rüger, 1997); however, doing so is not necessary in this analysis. Rüger and Tsvankin (1997) conducted a thorough analysis showing that Equation 4.1 is an acceptable approximation to exact reflectivity in HTI media at relatively small incident angles (i.e., less than ~30 degrees) under the assumption of small jumps in reflectivity across the layer interface, arbitrarily weak anisotropy, and sub-critical incident angles. See Figure 4.1 for an evaluation of how Equation 4.1 compares to exact expressions for reflectivity in isotropic, fluid filled fracture, and dry fracture end-cases.

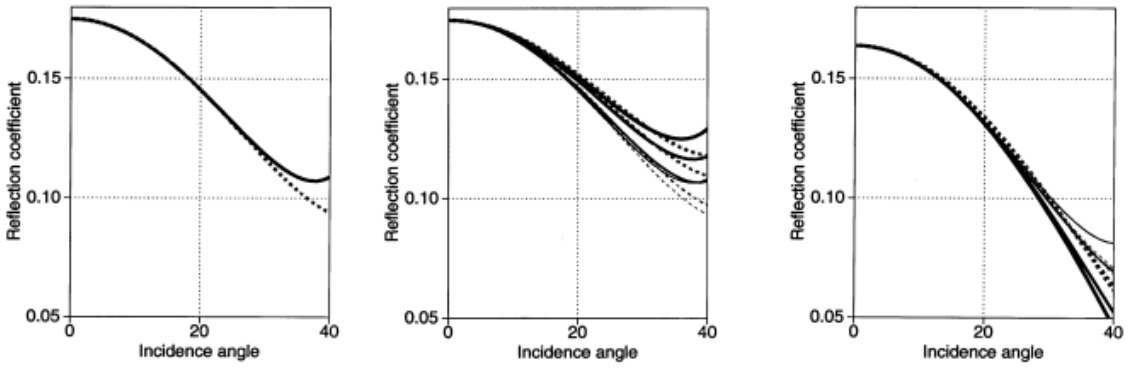

Figure 4.1: Comparison of exact and approximate reflectivity, calculated using the Rüger AVO equation shown in Equation 4.1. In all images the solid line represents exact reflectivity, and the dashed line represents approximated reflectivity. The leftmost image depicts the isotropic case. The middle image depicts the HTI case associated with fluid filled fractures. The rightmost image depicts the HTI case associated with dry fractures. The X axis represents incident angle, and the Y axis represents reflectivity. In the center and rightmost images reflectivity for azimuths corresponding to 0 degrees, 30 degrees, 60 degrees and 90 degrees from the symmetry axis are shown. Figure from Rüger and Tsvankin (1997).

Linearization of Equation 4.1 is performed using the method proposed by Xu and Li (2002), which utilizes trigonometric identities. This results in:

$$R(\theta,\varphi) = A + [B - C\cos(2\varphi) - D\sin(2\varphi)]\sin^2\theta \ , \tag{4.2}$$

where:

$$B \ = \ B_{iso} + \frac{1}{2}B_{ani} \ , \tag{4.3}$$

$$B_{ani}^2 = 4\,(C^2 + D^2) \ , \tag{4.4}$$

$$\tan(2\,\varphi_{iso}) = \frac{D}{C} \ . \tag{4.5}$$

In the context of inversion, Equation 4.2 acts as a linear forward operator, and thus can be rewritten in the form shown in Equation 3.71. This results in:

$$\begin{pmatrix} R(\theta_1,\varphi_1) \\ R(\theta_2,\varphi_1) \\ \vdots \\ R(\theta_N,\varphi_1) \\ R(\theta_1,\varphi_2) \\ R(\theta_2,\varphi_2) \\ \vdots \\ R(\theta_N,\varphi_2) \\ \vdots \\ R(\theta_N,\varphi_n) \end{pmatrix} = \begin{pmatrix} 1 & \sin^2(\theta_1) & -\cos(2\varphi_1)\sin^2(\theta_1) & -\sin(2\varphi_1)\sin^2(\theta_1) \\ 1 & \sin^2(\theta_2) & -\cos(2\varphi_1)\sin^2(\theta_2) & -\sin(2\varphi_1)\sin^2(\theta_2) \\ \vdots & \vdots & \vdots & \vdots \\ 1 & \sin^2(\theta_N) & -\cos(2\varphi_1)\sin^2(\theta_N) & -\sin(2\varphi_1)\sin^2(\theta_N) \\ 1 & \sin^2(\theta_1) & -\cos(2\varphi_2)\sin^2(\theta_1) & -\sin(2\varphi_2)\sin^2(\theta_1) \\ 1 & \sin^2(\theta_2) & -\cos(2\varphi_2)\sin^2(\theta_2) & -\sin(2\varphi_2)\sin^2(\theta_2) \\ \vdots & \vdots & \vdots & \vdots \\ 1 & \sin^2(\theta_N) & -\cos(2\varphi_2)\sin^2(\theta_N) & -\sin(2\varphi_2)\sin^2(\theta_N) \\ \vdots & \vdots & \vdots & \vdots \\ 1 & \sin^2(\theta_N) & -\cos(2\varphi_n)\sin^2(\theta_N) & -\sin(2\varphi_n)\sin^2(\theta_N) \end{pmatrix} \begin{pmatrix} A \\ B \\ C \\ D \end{pmatrix}, \tag{4.6}$$

where there exists N incident angle bins, n azimuthal bins and $N * n$ data points at each location. Note that matrix $\boldsymbol{G}$ and data vector $\boldsymbol{d}$ in Equation 4.6 could be primarily sorted by incident angle rather than azimuth without altering results. Conversion from offset domain to incident angle domain was done automatically by Hampson-Russell © using a RMS velocity section.

After matrices in Equation 4.6 have been populated with specific values corresponding to the azimuthal and incident angle binning scheme used in the analysis, data vector $\boldsymbol{m}$ can be solved using the standard least squares approach shown in Equation 3.75. This is repeated at every Common Depth Point (CDP) location and every time sample. After linearized coefficients A, B, C and D are found, Equations 4.3 – 4.5 are used to calculate the coefficients shown in Equation 4.1, namely A, B_{iso}, B_{ani} and φ_{iso}. φ_{iso} represents the azimuthal isotropy plane, and it is an indicator of fracture strike. Analysis of Equation 4.1 shows that at azimuth $\varphi = \varphi_{iso}$, reflectivity is at a local minimum with respect to azimuth. B_{ani} represents the magnitude of the azimuthal variation, and it is a direct indicator of fracture density. This agrees well with the intuitive notion that denser fracture spacing will result in a larger difference in seismic waves when comparing waves traveling parallel to those traveling perpendicular to fracture strike. Note that seismic trace amplitude data was used in lieu of reflectivity because true

impedances of the section are unknown. Trace amplitude is roughly proportional to reflectivity, but this substitution limits inverted fracture density to be relative, rather than absolute. In practice, the number of fractures per unit length cannot be found, but areas of relatively high and relatively low fracture density can be identified. Unfortunately, substituting seismic amplitude for reflectivity is unavoidable in the analysis of real data.

Regrettably, the Rüger method presented above is fundamentally flawed. This comes largely from the linearization process used in order to make solving the problem computationally feasible. Analysis of Equation 4.4 shows that C and D are used to solve for B_{ani}^2 rather than B_{ani}. This leads to an inherent sign ambiguity in B_{ani} and thus an inherent inability to differentiate between the "fast" direction (parallel to φ_{iso}) and the "slow" direction (perpendicular to φ_{iso}). The sign ambiguity in B_{ani} also indicates that azimuth $\varphi = \varphi_{iso}$ could correspond to either a local maximum or a local minimum in seismic data with respect to azimuth. In practice, this sign ambiguity leads to an inherent 90 degree ambiguity in φ_{iso}, and thus an inherent 90 degree ambiguity in determining fracture azimuth. This 90 degree ambiguity can also be seen by examining Equation 4.5, noting that $\tan(2\,\varphi_{iso})$ is 180 degree periodic and thus will not be affected by any 90 degree change in φ_{iso}. This 90 degree ambiguity in fracture azimuth poses serious problems for well orientation planning and in effect makes the Rüger method unusable for determining fracture azimuth without further modification. Partially for this reason, an alternate HTI method was implemented which utilizes Fourier decomposition of the seismic data.

4.3 Fourier Coefficient Decomposition Method

This AVAZ method is fundamentally based on decomposing azimuthal variations of seismic amplitudes into a Fourier series, and relating the coefficients of the calculated

Fourier series to fracturing characteristics (Downton, 2011 and Downton et al., 2011). A Fourier series takes the general form of:

$$R(\theta,\varphi) = \sum[U_n(\theta)\cos(n\varphi) + V_n(\theta)\sin(n\varphi)] \ , \tag{4.7}$$

where θ represents incident angle, φ represents azimuth, and R represents seismic reflectivity. Note that, as in the Rüger method, seismic trace amplitude must be used in lieu of reflectivity. Downton et al. (2011) show that for P-P reflection data all odd Fourier coefficients are zero, and minimal to no energy is present in the 6th order and higher order Fourier coefficients. Thus, Equation 4.7 reduces to a 4th order Fourier series composed only of even Fourier terms. Downton et al. (2011) show that in the case of HTI anisotropy, Equation 4.7 reduces to:

$$R_{pp}(\theta,\varphi) = r_0 + r_2\ \cos\left(2\left(\varphi - \varphi_{sym}\right)\right) + r_4\ \cos\left(4\left(\varphi - \varphi_{sym}\right)\right) \ , \tag{4.8}$$

where φ_{sym} represents the azimuthal symmetry plane and r_0, r_2 and r_4 represent the 0th, 2nd and 4th order Fourier coefficients, respectively. Azimuthal symmetry plane φ_{sym} is orthogonal to azimuthal isotropy plane φ_{iso} and is thus perpendicular to fracture orientation. It is worth noting that the phase (φ_{sym}) associated with the r_2 coefficient wraps every 90 degrees, and the phase (φ_{sym}) associated with the r_4 coefficient wraps every 45 degrees. Refer to Chapter 5, Equations 5.25 and 5.26, for proof of phase wrapping. Downton et al. (2011) relate the Fourier coefficients r_0, r_2 and r_4 to fracture parameters using Equations 4.9 – 4.16.

$$r_0 = A_0 + B_0\ \sin^2\theta + C_0\ \sin^2\theta\ \tan^2\theta \ , \tag{4.9}$$

$$r_2 = \Delta T\ g\ \frac{\sin^2\theta}{2} - \Delta N\ g\ \frac{\chi}{2}\left(1 + \frac{1+\chi}{2}\right)\sin^2\theta\ \tan^2\theta \ , \tag{4.10}$$

$$r_4 = \frac{1}{8}\ |\kappa|\sin^2\theta\ \tan^2\theta \ , \tag{4.11}$$

$$\kappa = g\ (\Delta T - g\ \Delta N) \ , \tag{4.12}$$

$$\chi = 1 - 2g \ , \tag{4.13}$$

$$g\ = \frac{V_s^2}{V_p^2} \ , \tag{4.14}$$

$$B_{ani} \approx g\,(\Delta T - \chi \Delta N)\ , \tag{4.15}$$

$$r_2(\theta) \approx \frac{1}{2} B_{ani} \sin^2\theta\ , \tag{4.16}$$

where ΔN and ΔT represent normal and tangential fracture weaknesses, respectively, and V_p and V_s represent compressional and shear seismic wave velocities, respectively. Hampson-Russell © was used to invert for φ_{sym}, r_0, r_2 and r_4 using an Iteratively Reweighted Least Squares (IRLS) algorithm using incident angles ranging from 5 to 45 degrees in 5 degree increments at each of the nine azimuthal bins. Being proprietary information of Hampson-Russell ©, the specifics associated with this IRLS algorithm are unknown. This algorithm inverts for two distinct φ_{sym} values – one calculated from the r_2 coefficient and the other calculated from the r_4 coefficient. In theory these two values should be identical, but in practice differences exist between the two due to imperfections in the seismic data as well as the phase wrapping phenomenon. Downton et al. (2011) show that fracture orientation determined from φ_{sym} calculated from the 2nd order Fourier coefficient phase should be used, due to less frequent phase wrapping and there being inherently higher confidence in the r_2 coefficient than in the r_4 coefficient. Refer to the Results section of this chapter for figures depicting both calculated values of φ_{sym}.

Using the Fourier coefficients and azimuthal symmetry planes inverted for using Hampson-Russell ©, one can estimate both fracture density and fracture orientation. Fracture azimuth is perpendicular to the azimuthal isotropy plane, and the r_2 Fourier coefficient is roughly proportional to B_{ani}, which is directly related to fracture density. However, in order to extract more information from the data, data were transferred to MATLAB © and a least squares inversion designed to determine fracture weaknesses was performed. In this inversion, Equations 4.10 and 4.11 act as the forward operator and the 2nd and 4th order Fourier coefficients r_2 and r_4 act as the data. Posed in the format

shown in Equation 3.71, Equations 4.10 and 4.11 transform to:

$$\begin{pmatrix} r_2 \\ r_4 \\ r_2 \\ r_4 \\ \vdots \\ r_2 \\ r_4 \end{pmatrix} = \begin{pmatrix} g\ \frac{\chi}{2}\left(1+\frac{(1+\chi)}{2}\right)\sin^2\theta_1\ \tan^2\theta_1) & \mathrm{g}\ \frac{\sin^2\theta_1}{2} \\ \frac{-g^2}{8}\ \sin^2\theta_1\ \tan^2\theta_1 & \frac{g}{8}\ \sin^2\theta_1\ \tan^2\theta_1 \\ g\ \frac{\chi}{2}\left(1+\frac{(1+\chi)}{2}\right)\sin^2\theta_2\ \tan^2\theta_2) & \mathrm{g}\ \frac{\sin^2\theta_2}{2} \\ \frac{-g^2}{8}\ \sin^2\theta_2\ \tan^2\theta_2 & \frac{g}{8}\ \sin^2\theta_2\ \tan^2\theta_2 \\ & \vdots \\ g\ \frac{\chi}{2}\left(1+\frac{(1+\chi)}{2}\right)\sin^2\theta_N\ \tan^2\theta_N) & \mathrm{g}\ \frac{\sin^2\theta_N}{2} \\ \frac{-g^2}{8}\ \sin^2\theta_N\ \tan^2\theta_N & \frac{g}{8}\ \sin^2\theta_N\ \tan^2\theta_N \end{pmatrix} \begin{pmatrix} \Delta\mathrm{N} \\ \Delta\mathrm{T} \end{pmatrix}, \qquad (4.17)$$

for $\theta_1 = 5$ degrees, $\theta_2 = 10$ degrees, … , $\theta_N = 45$ degrees. These incident angles were chosen to coincide with the incident angles used in the original IRLS inversion to determine Fourier coefficients r_2 and r_4. Based on well data, g was assumed to be 0.4444, corresponding to $V_p/V_s = 1.5$. Note that in Equation 4.17 Fourier coefficients r_2 and r_4 do not change with incident angle. Matrices in Equation 4.17 are generated at every time and CDP location in the Haynesville, and a standard least squares inversion, as shown in Equation 3.75, is performed to solve for ΔN and ΔT. After ΔN and ΔT have been determined, Equation 4.15 is used to calculate B_{ani}, which is proportional to fracture density, and Equation 3.65 is used to calculate the fluid indicator attribute proposed by Shaw and Sen (2006).

The method based on Fourier coefficient decomposition is preferred over the Rüger method for a number of reasons. The most significant reason is that the Fourier coefficient decomposition method is potentially capable of determining fracture azimuth without a 90 degree ambiguity by utilizing second and fourth order Fourier terms at multiple incident angles (Downton, 2011 and Downton et al., 2011). However, resolving

this 90 degree ambiguity is still not trivial due to the 90 degree phase wrapping associated with the r_2 coefficient. Unfortunately, despite numerous attempts to contact Hampson-Russell ©, it is unclear whether Hampson-Russell's © software actively determines the correct symmetry axis. Thus, the Fourier coefficient results shown in this chapter may still contain a 90 degree ambiguity in fracture azimuth. This potential 90 degree ambiguity will be further discussed later in this Thesis; however, comparing the Fourier coefficient based inversion results presented in this Chapter to those presented in Chapter 5 seems to confirm this 90 degree ambiguity.

Despite having an ambiguity in determining fracture azimuth, the Fourier coefficient method is still preferred to the Rüger method because the Fourier coefficient method utilizes a higher order approximation. The Rüger method in effect only utilizes a 2^{nd} order approximation, whereas the use of 4^{th} order terms in the Fourier decomposition based approach results in the approximation being more physically exact and allows it to be valid over a wider range of incident angles than the Rüger method. The inclusion of higher incident angles is ideal because AVAZ effects from fractures are generally more pronounced at larger offsets / higher incident angles, thus increasing the signal-to-noise ratio of any azimuthal variations. The ability to properly utilize this large offset information increases confidence in inversion results. For these reasons I recommend the Fourier decomposition based approach over the Rüger based approach, and will place more weight on the results from the Fourier coefficient based method. The results from implementing both methods are presented and compared in the following section.

4.4 RESULTS

Results from implementing the Rüger method can be seen in Figures 4.2 and 4.3. Values have been vertically averaged throughout the Haynesville, and lateral smoothing

has been automatically applied by Hampson-Russell ©. In these figures, the background color represents fracture density (from B_{ani}), and the small superimposed planar features are oriented in the direction of fracture azimuth (from φ_{iso}). Planar features are not included in Figure 4.2 to allow for unobstructed viewing of fracture density. Values for B_{ani} should be treated as relative, and thus do not include bounds on the colorbar. Warmer background colors indicate higher fracture density. Planar features, which depict fracture azimuth, are only displayed in areas where fracture density is higher than some user-defined threshold, allowing for better visualization of fracturing in more densely fractured areas. The red arrows indicate the direction of north. All images share the same orientation.

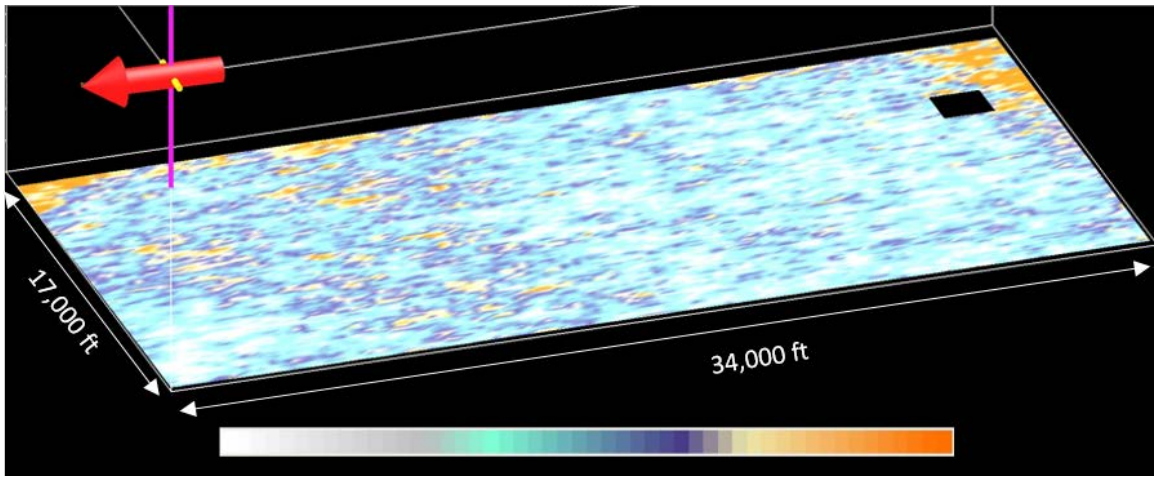

Figure 4.2: Anisotropic Gradient, a proxy for fracture density, calculated using the Rüger method and vertically averaged within the Haynesville Shale. Warmer colors represent denser fracture spacing. The red arrow indicates the direction of north.

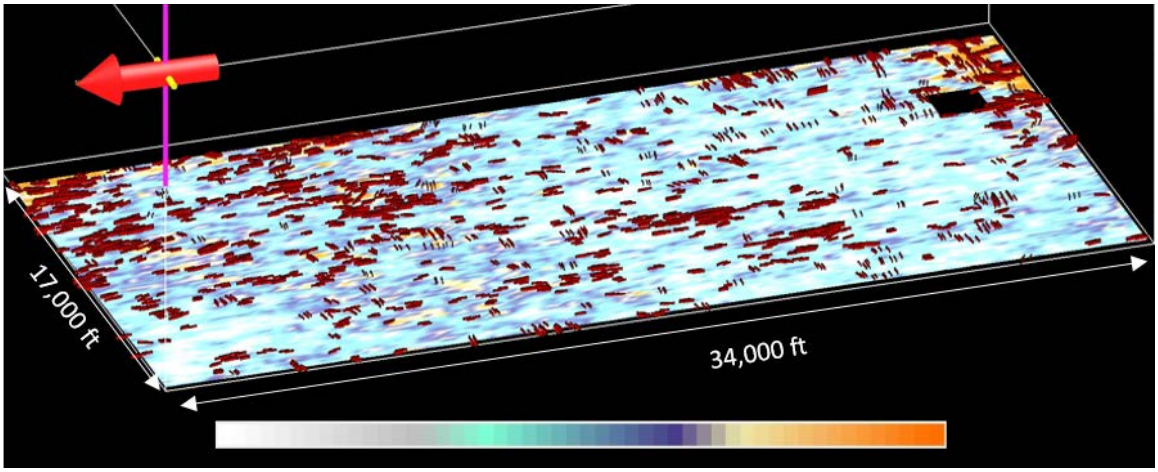

Figure 4.3: Fracture orientation and Anisotropic Gradient, a proxy for fracture density, calculated using the Rüger method and vertically averaged within the Haynesville Shale. Fracture orientation is represented by planar features superimposed on the image which are oriented in the plane of fracture strike. Warmer background colors represent denser fracture spacing. The red arrow indicates the direction of north.

Results from implementing the Fourier coefficient Decomposition method can be seen in Figures 4.4 – 4.6. Values have been vertically averaged throughout the Haynesville, and lateral smoothing has been automatically applied by Hampson-Russell ©. In these figures, the background color represents fracture density (from r_2), and the small superimposed planar features are oriented in the direction of fracture azimuth (from φ_{sym}). Planar features are not included in Figure 4.4 to allow for unobstructed viewing of fracture density. Values for r_2 should be treated as relative, and thus do not include bounds on the colorbar. Warmer background colors indicate higher fracture density. Planar features which depict fracture azimuth are only displayed in areas where fracture density is higher than some user-defined threshold, allowing for better visualization of fracturing in more densely fractured areas. The red arrows indicate the direction of north. All images share the same orientation.

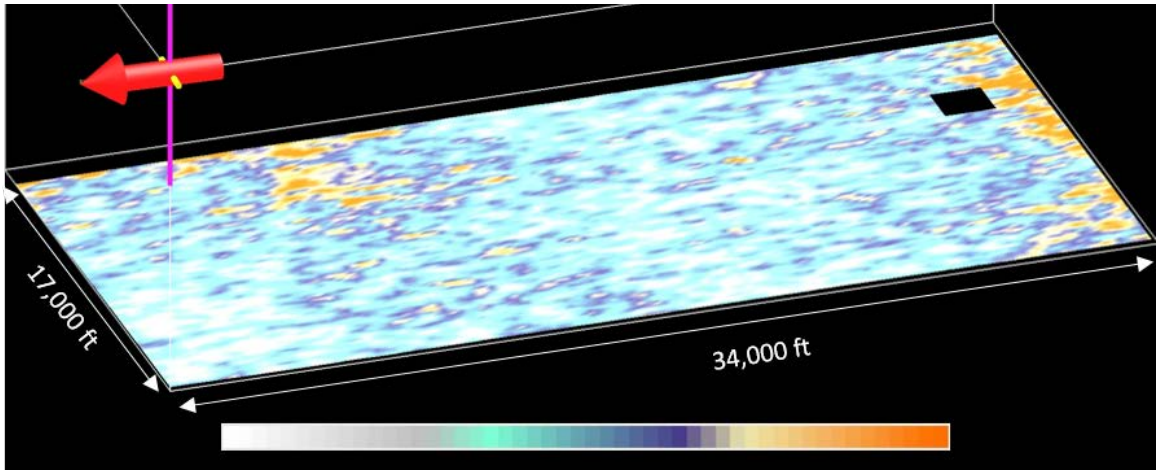

Figure 4.4: r_2 Fourier coefficient, a proxy for fracture density, calculated using the Fourier coefficient decomposition method and vertically averaged within the Haynesville Shale. Warmer colors represent denser fracture spacing. The red arrow indicates the direction of north.

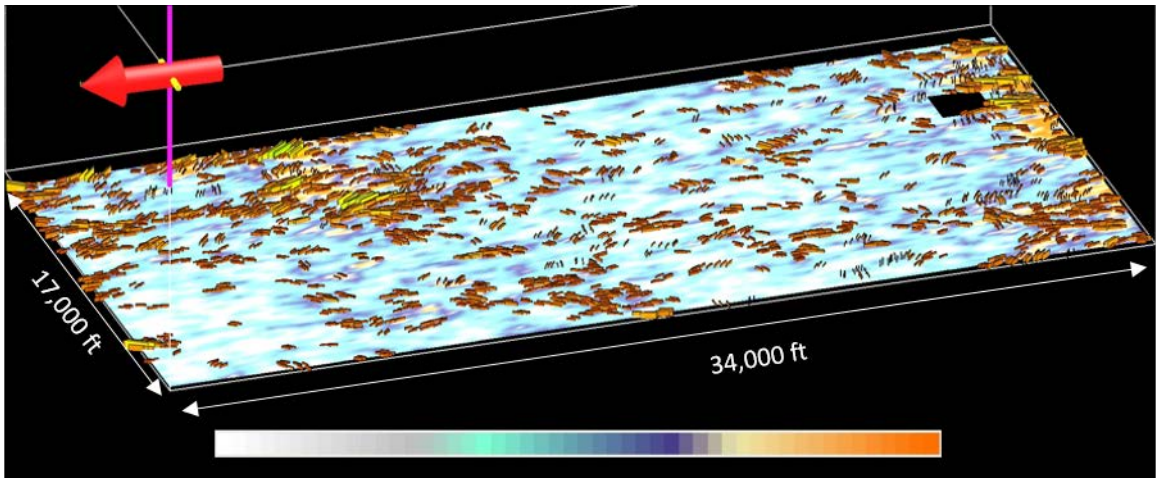

Figure 4.5: Fracture orientation, from 2nd order Fourier coefficient phase φ_{sym}, and r_2 Fourier coefficient, a proxy for fracture density, calculated using the Fourier coefficient decomposition method and vertically averaged within the Haynesville Shale. Fracture orientation is represented by planar features superimposed on the image which are oriented in the plane of fracture strike. Warmer background colors represent denser fracture spacing. The red arrow indicates the direction of north.

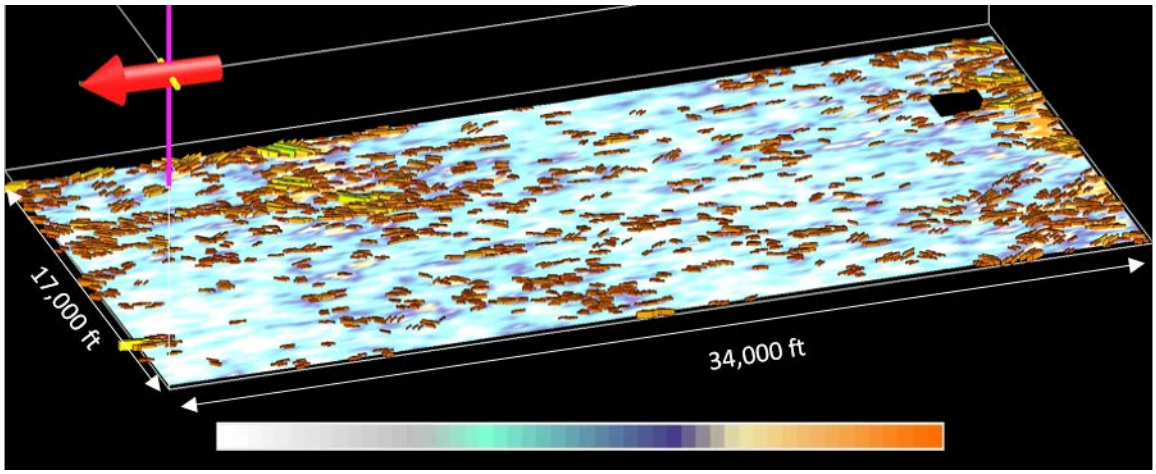

Figure 4.6: Fracture orientation, from 4th order Fourier coefficient phase φ_{sym}, and r_2 Fourier coefficient, a proxy for fracture density, calculated using the Fourier coefficient decomposition method and vertically averaged within the Haynesville Shale. Fracture orientation is represented by planar features superimposed on the image which are oriented in the plane of fracture strike. Warmer background colors represent denser fracture spacing. The red arrow indicates the direction of north.

Figures 4.7 and 4.8 depict results for normal and tangential fracture weaknesses, as determined by a least squares inversion of Equation 4.17. Figures 4.9 and 4.10 depict B_{ani} and fluid indicator attribute as determined from normal and tangential fracture weaknesses using Equations 4.15 and 3.44. Values for fracture weaknesses and B_{ani} should be treated as relative, and thus do not include bounds on the colorbar. Warmer colors indicate high values. Values for the Fluid Indicator attribute range from 0.7 to 1.2. The black arrows indicate the direction of north. All images share the same orientation.

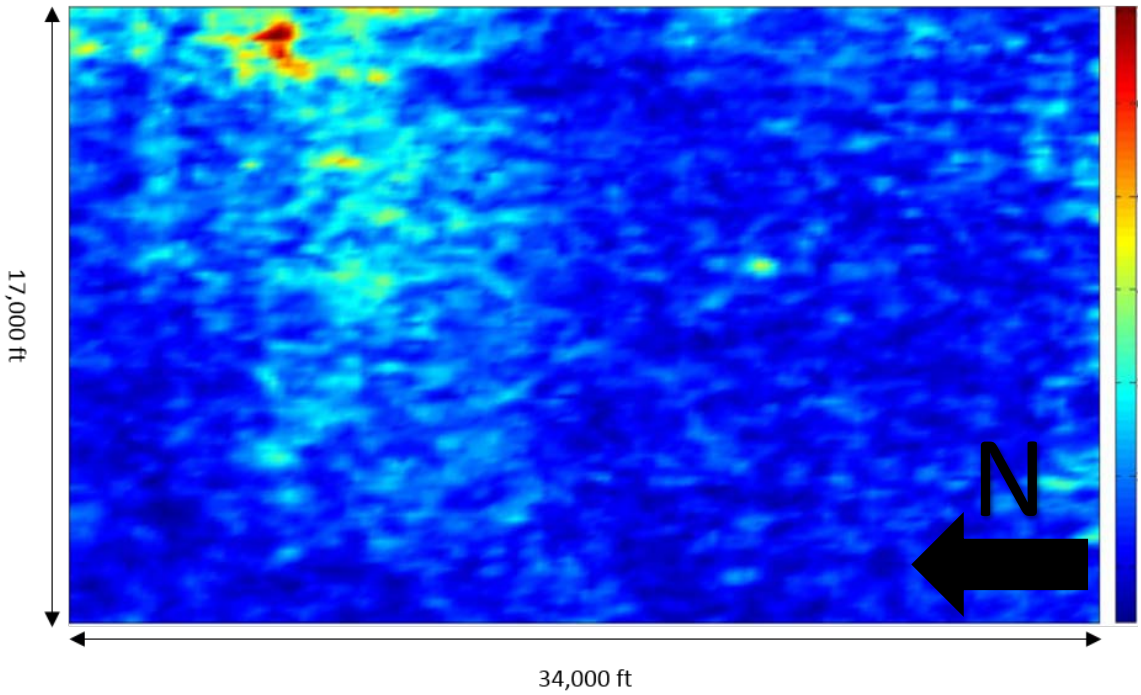

Figure 4.7: Normal fracture weakness (ΔN), as calculated from a least squares inversion of r_2 and r_4 Fourier coefficients. Warmer colors indicate higher values. The black arrow indicates the direction of north.

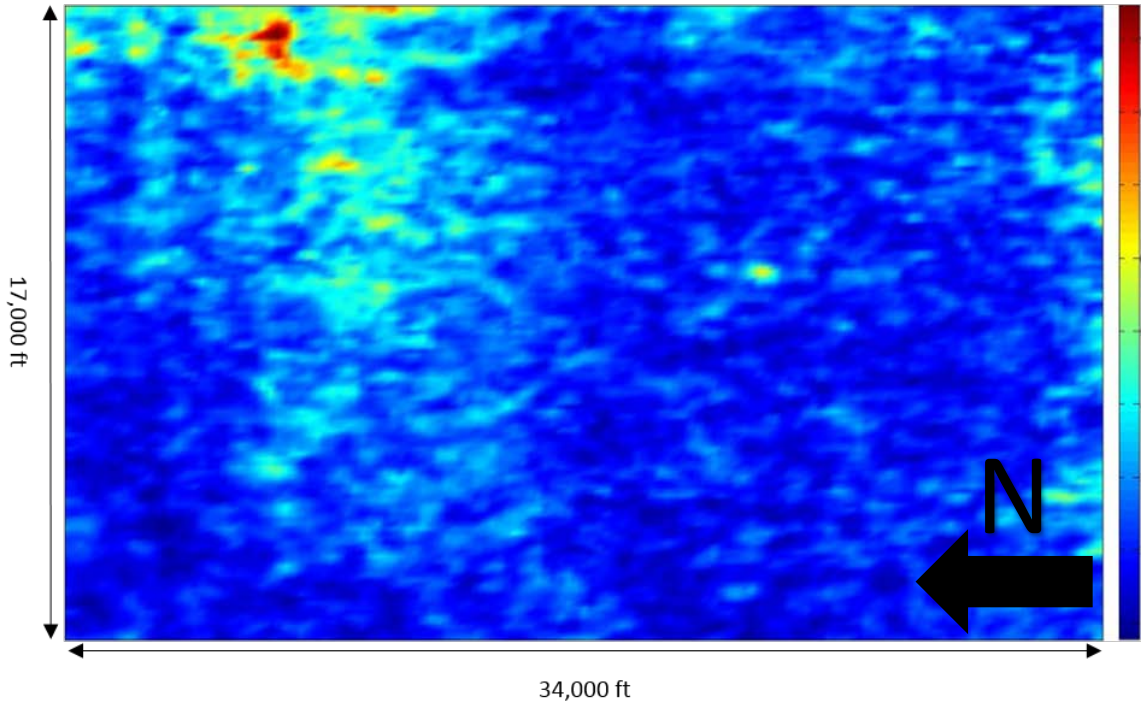

Figure 4.8: Tangential fracture weakness (ΔN), as calculated from a least squares inversion of r_2 and r_4 Fourier coefficients. Warmer colors indicate higher values. The black arrow indicates the direction of north.

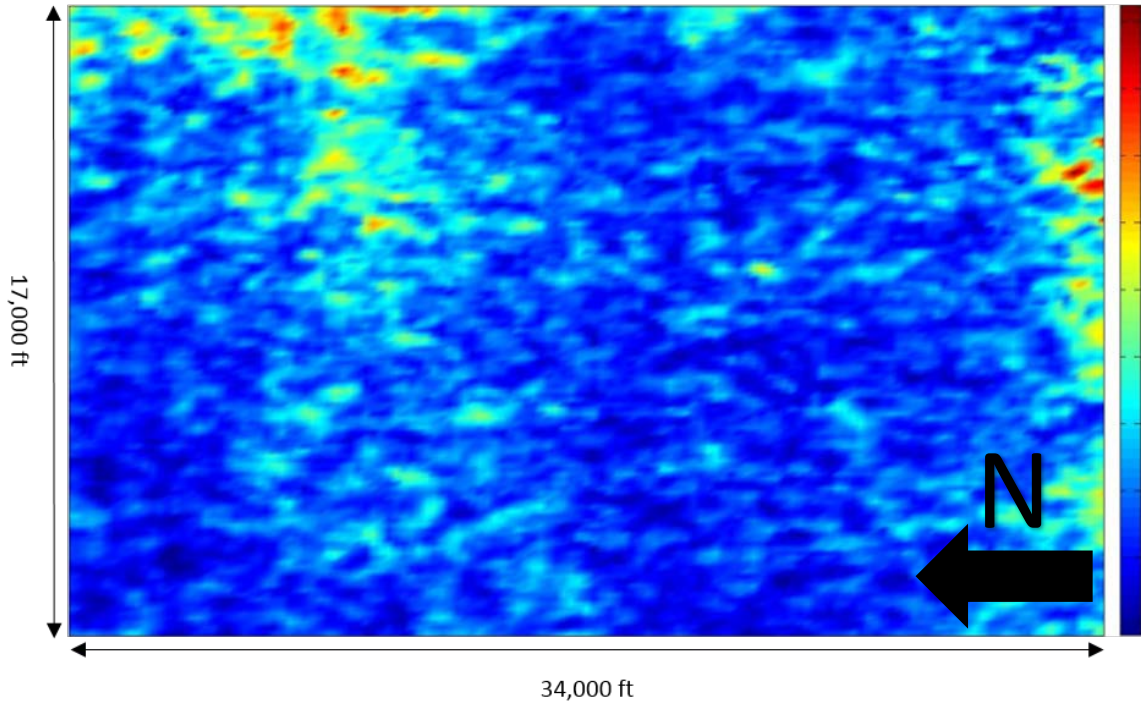

Figure 4.9: Anisotropic gradient (B_{ani}), as calculated from the values of normal and tangential fracture weakness (ΔN and ΔT) found via a least squares inversion of r_2 and r_4 Fourier coefficients. Anisotropic gradient is a proxy for fracture density. Warmer colors indicate denser fracture spacing. The black arrow indicates the direction of north.

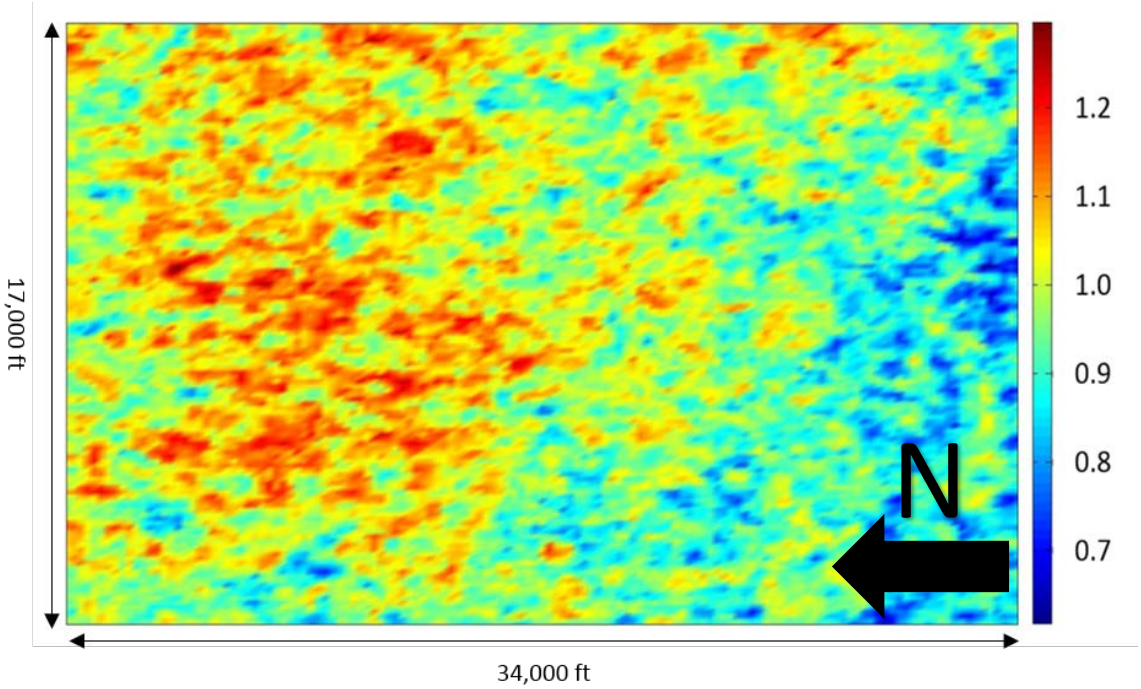

Figure 4.10: Fluid indicator attribute, as calculated from the values of normal and tangential fracture weakness (ΔN and ΔT) found via a least squares inversion of r_2 and r_4 Fourier coefficients. Warmer colors indicate higher values. The colorbar ranges from approximately 0.7 to 1.2. Because the fluid indicator attribute is based on the ratios of velocities and fracture weaknesses, it is unitless. The black arrow indicates the direction of north.

A direct comparison of fracture density results between the Rüger (B_{ani}) and Fourier decomposition (r_2) methods can be seen in Figures 4.11 – 4.15. Figure 4.11 compares these properties as vertically averaged throughout the Haynesville, and Figures 4.12 – 4.15 compare these properties at certain depths from the top of the Haynesville, specifically at depths of 0m, 15m, 30m and 45m. Figure 4.16 compares vertically averaged r_2 and B_{ani} (calculated from inverted ΔN and ΔT values) as proxies for fracture density in the Fourier coefficient decomposition method.

A direct comparison of fracture orientation results between the Rüger and Fourier decomposition methods can be seen in Figures 4.17 – 4.21. Figure 4.17 compares these

properties as vertically averaged throughout the Haynesville, and Figures 4.18 – 4.21 compare these properties at certain depths from the top of the Haynesville, specifically at depths of 0m, 15m, 30m and 45m. Note that 2nd order Fourier coefficient phase is more appropriate to determine fracture orientation than the 4th order Fourier coefficient phase, but both are shown.

"Constant depth" images are generated by rearranging data such that it is sorted a constant number of time samples from the horizon representing the top of the Haynesville. Assuming a constant P-wave velocity of ~3 km/s, each time sample (2 ms) corresponds to approximately 3 meters of depth. Note that time represents two-way travel time (TWT). These constant depth figures allow one to see if and how properties change vertically by examining the upper, middle and lower Haynesville units, as well as how the different HTI methods used in this work compare. Note that values of fracture density proxies are relative, and cannot be explicitly related to crack density in terms of fractures per unit length, nor can crack density be directly compared between the two methods. For this reason, images depicting fracture density do not include labels on color bars, and coloring bounds are chosen to produce an image that is visually appealing, informative, and able to distinguish areas of high fracturing from areas of low fracturing. Comparison of the methods should be based on their ability to delineate areas of relatively high and low fracture density as well as on their ability to produce consistent and geologically reasonable fracture azimuth predictions.

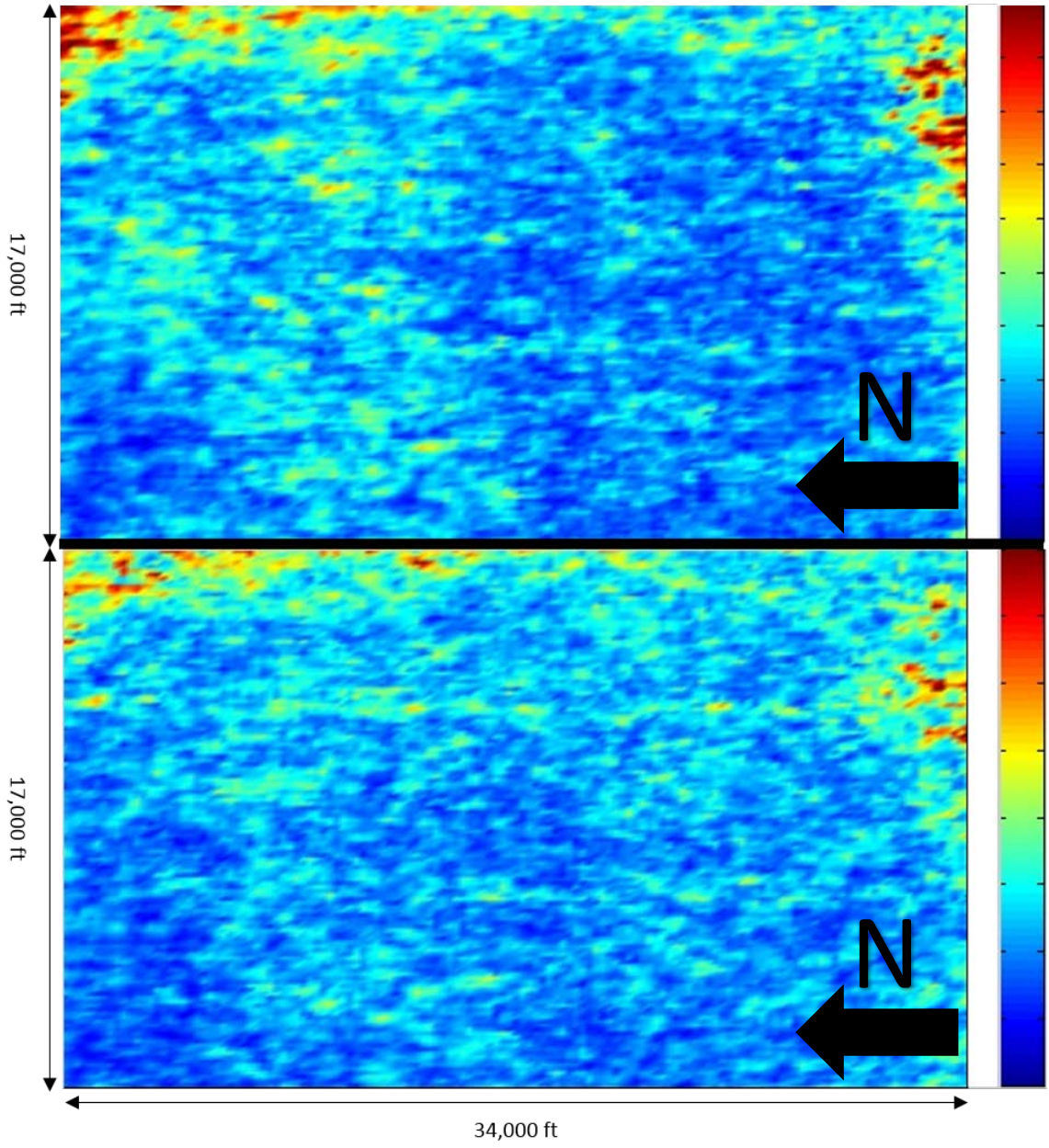

Figure 4.11: Comparison of proxies for fracture density from the Rüger and Fourier coefficient decomposition methods. B_{ani} from the Ruger method is shown above, and r_2 from the Fourier coefficient decomposition method is shown below. Values have been vertically averaged throughout the Haynesville using a simple arithmetic mean. Warmer colors indicate denser fracture spacing. The black arrows indicate the direction of north.

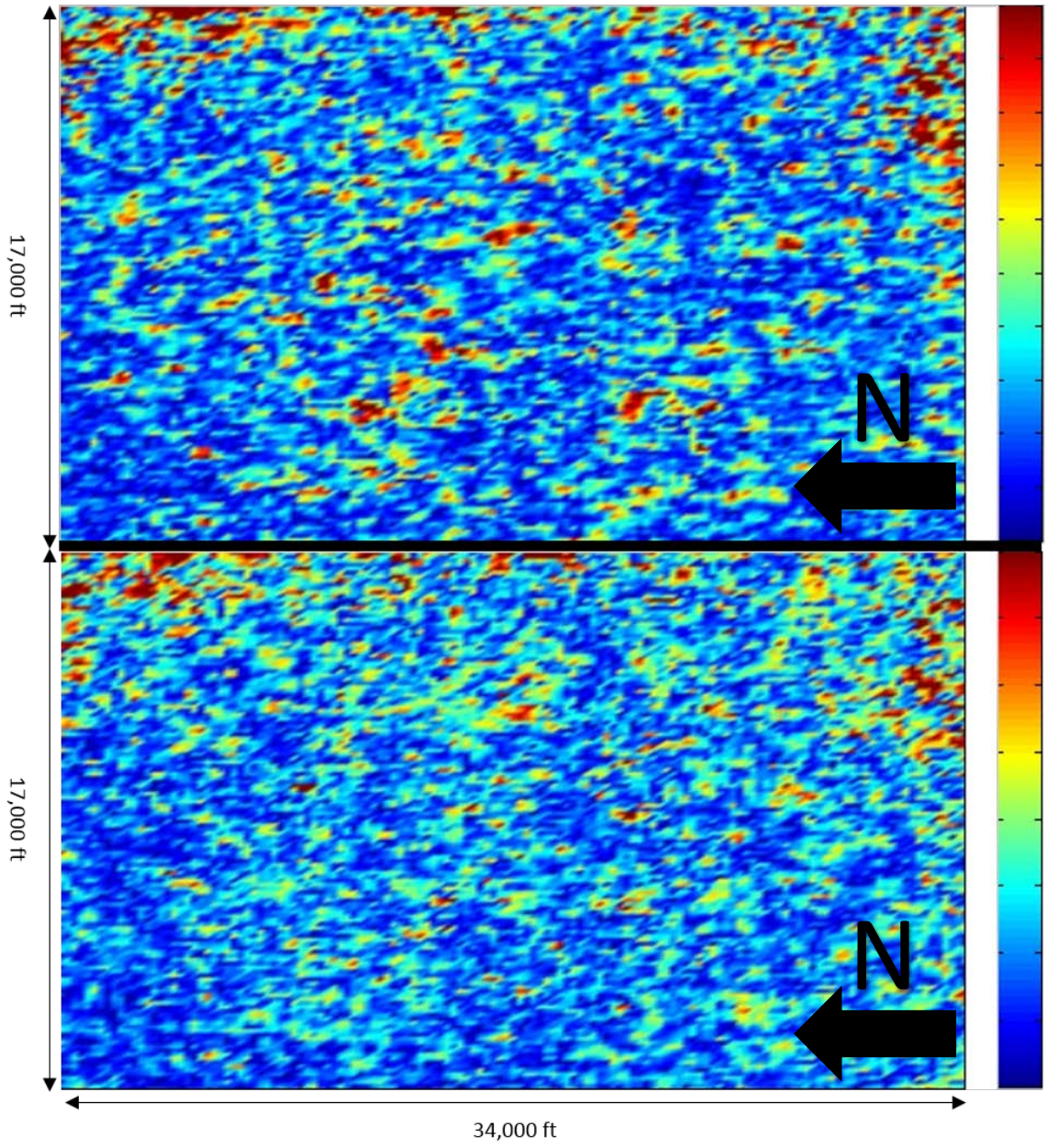

Figure 4.12: Comparison of proxies for fracture density from the Rüger and Fourier coefficient decomposition methods. B_{ani} from the Ruger method is shown above, and r_2 from the Fourier coefficient decomposition method is shown below. Values corresponding to the top of the Haynesville are shown. Warmer colors indicate denser fracture spacing. The black arrows indicate the direction of north.

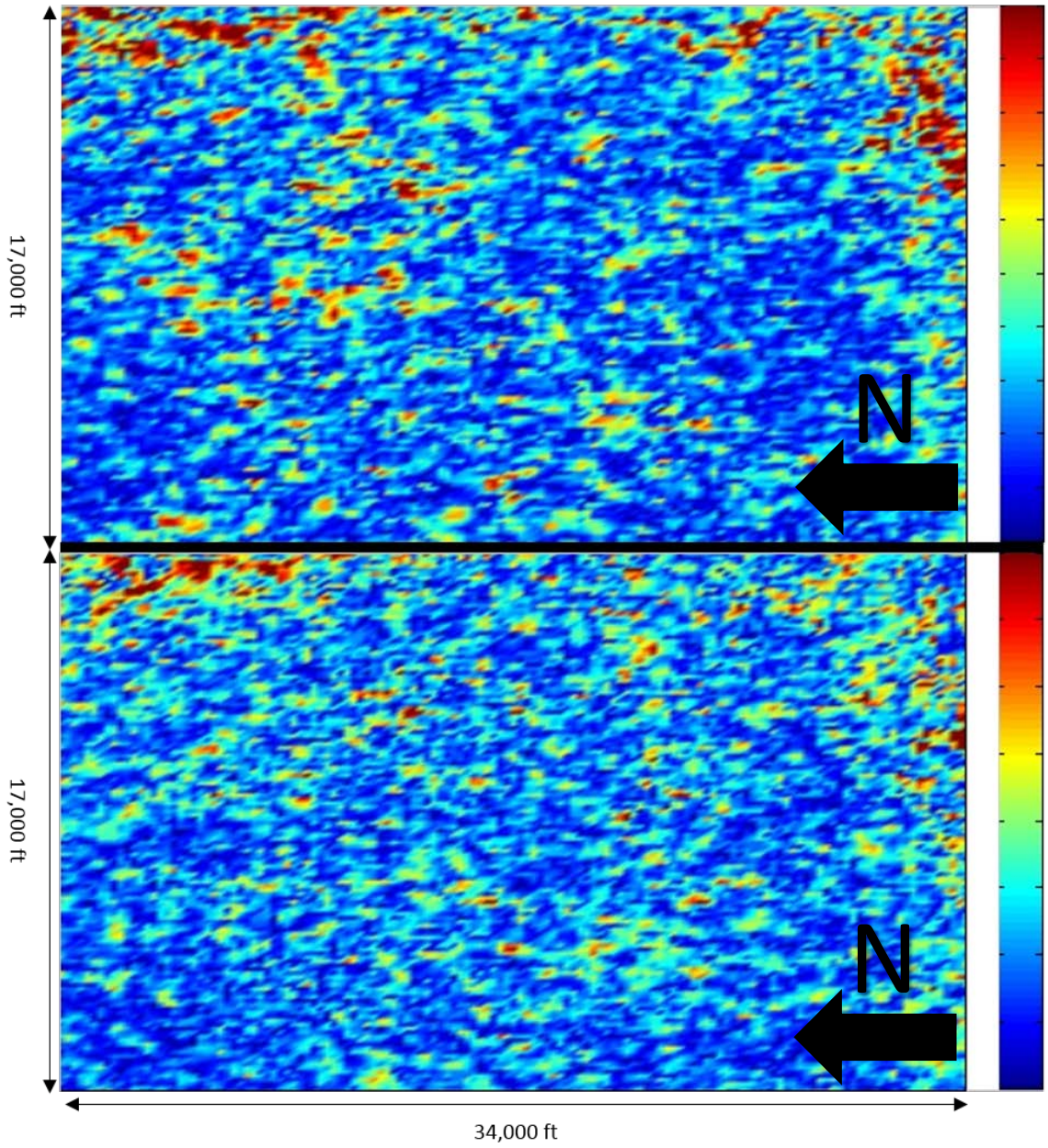

Figure 4.13: Comparison of proxies for fracture density from the Rüger and Fourier coefficient decomposition methods. B_{ani} from the Ruger method is shown above, and r_2 from the Fourier coefficient decomposition method is shown below. Values corresponding to approximately 15 m from the top of the Haynesville are shown. Warmer colors indicate denser fracture spacing. The black arrows indicate the direction of north.

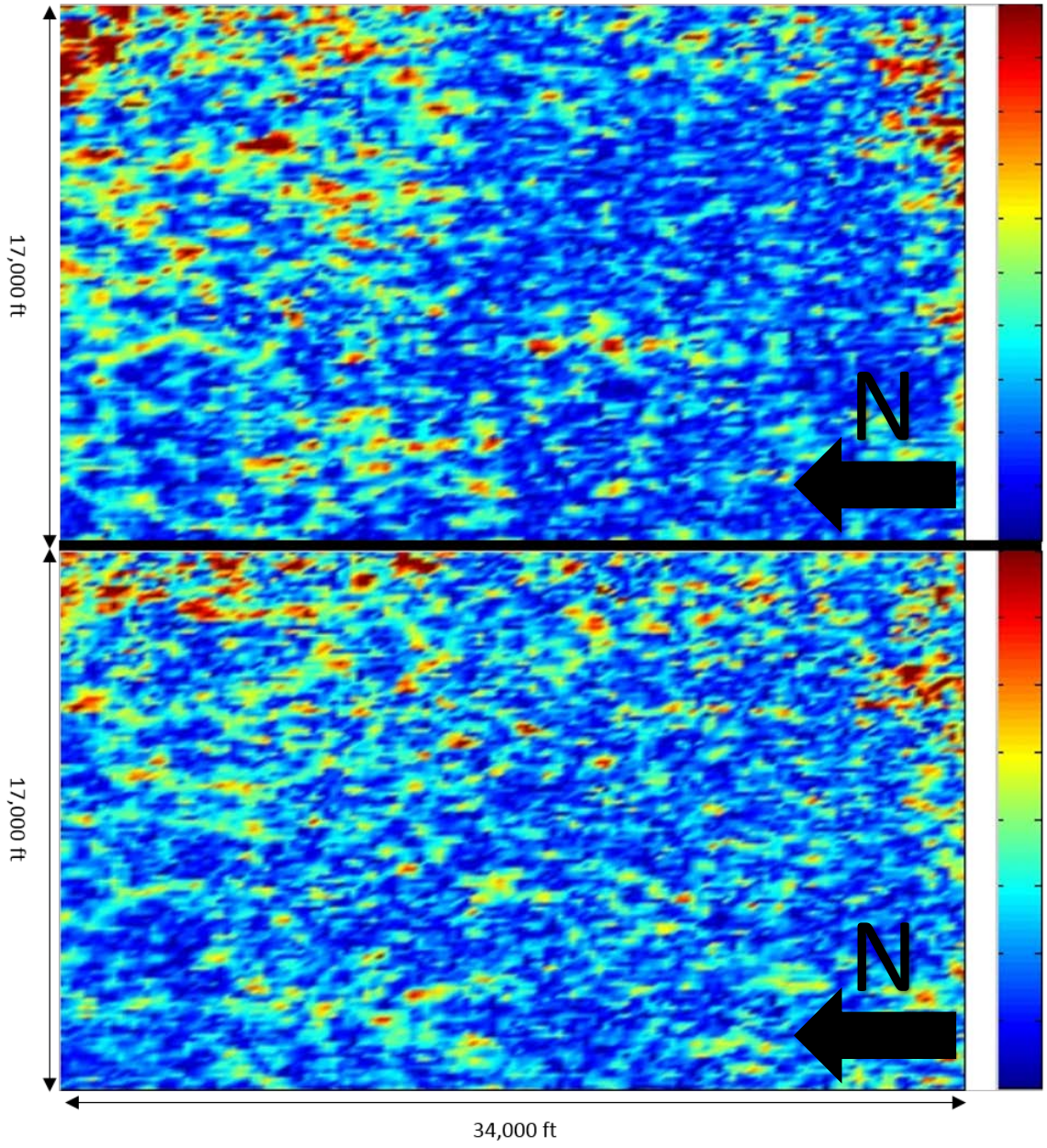

Figure 4.14: Comparison of proxies for fracture density from the Rüger and Fourier coefficient decomposition methods. B_{ani} from the Ruger method is shown above, and r_2 from the Fourier coefficient decomposition method is shown below. Values corresponding to approximately 30 m from the top of the Haynesville are shown. Warmer colors indicate denser fracture spacing. The black arrows indicate the direction of north.

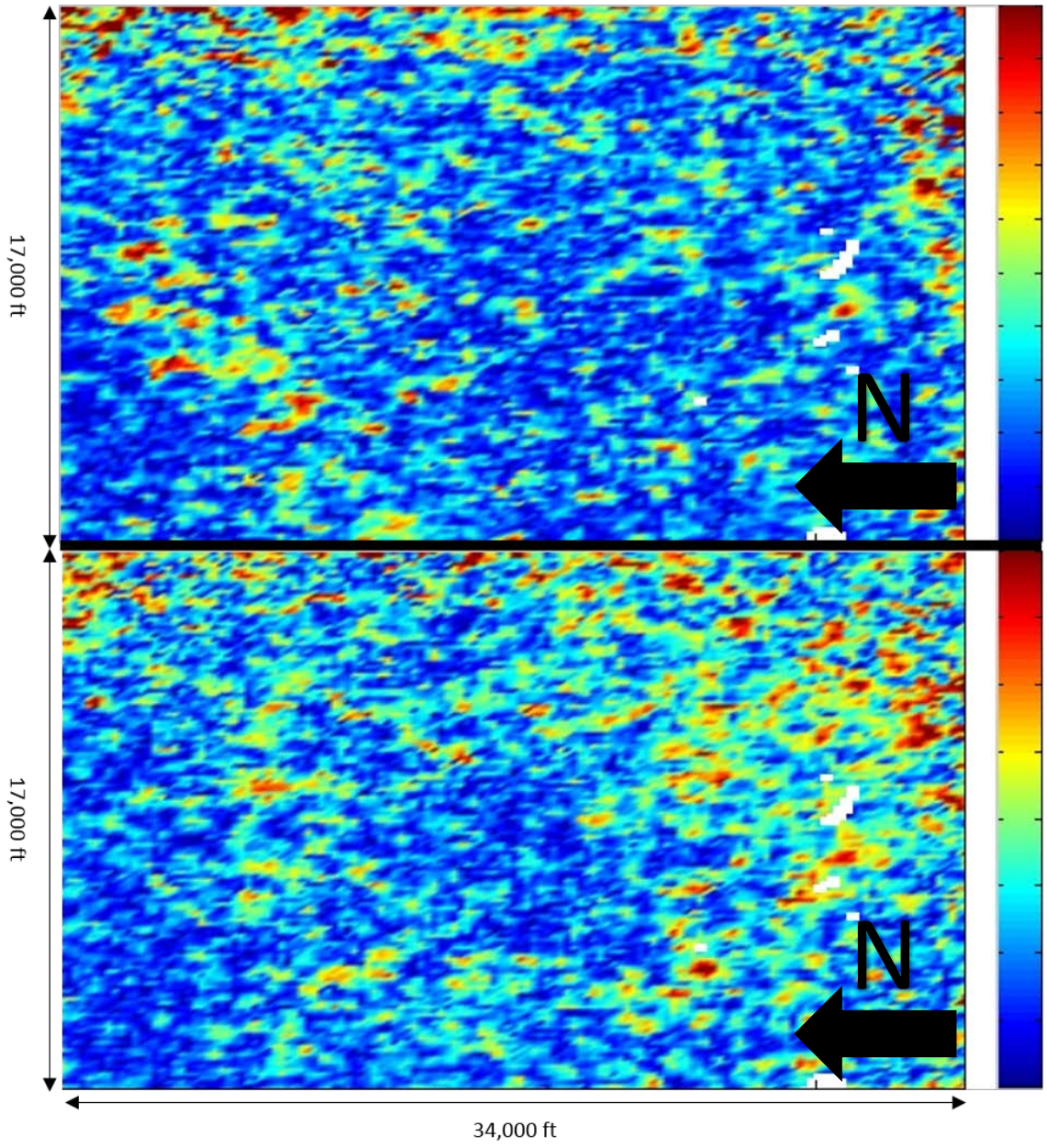

Figure 4.15: Comparison of proxies for fracture density from the Rüger and Fourier coefficient decomposition methods. B_{ani} from the Ruger method is shown above, and r_2 from the Fourier coefficient decomposition method is shown below. Values corresponding to approximately 45 m from the top of the Haynesville are shown. Warmer colors indicate denser fracture spacing. The black arrows indicate the direction of north.

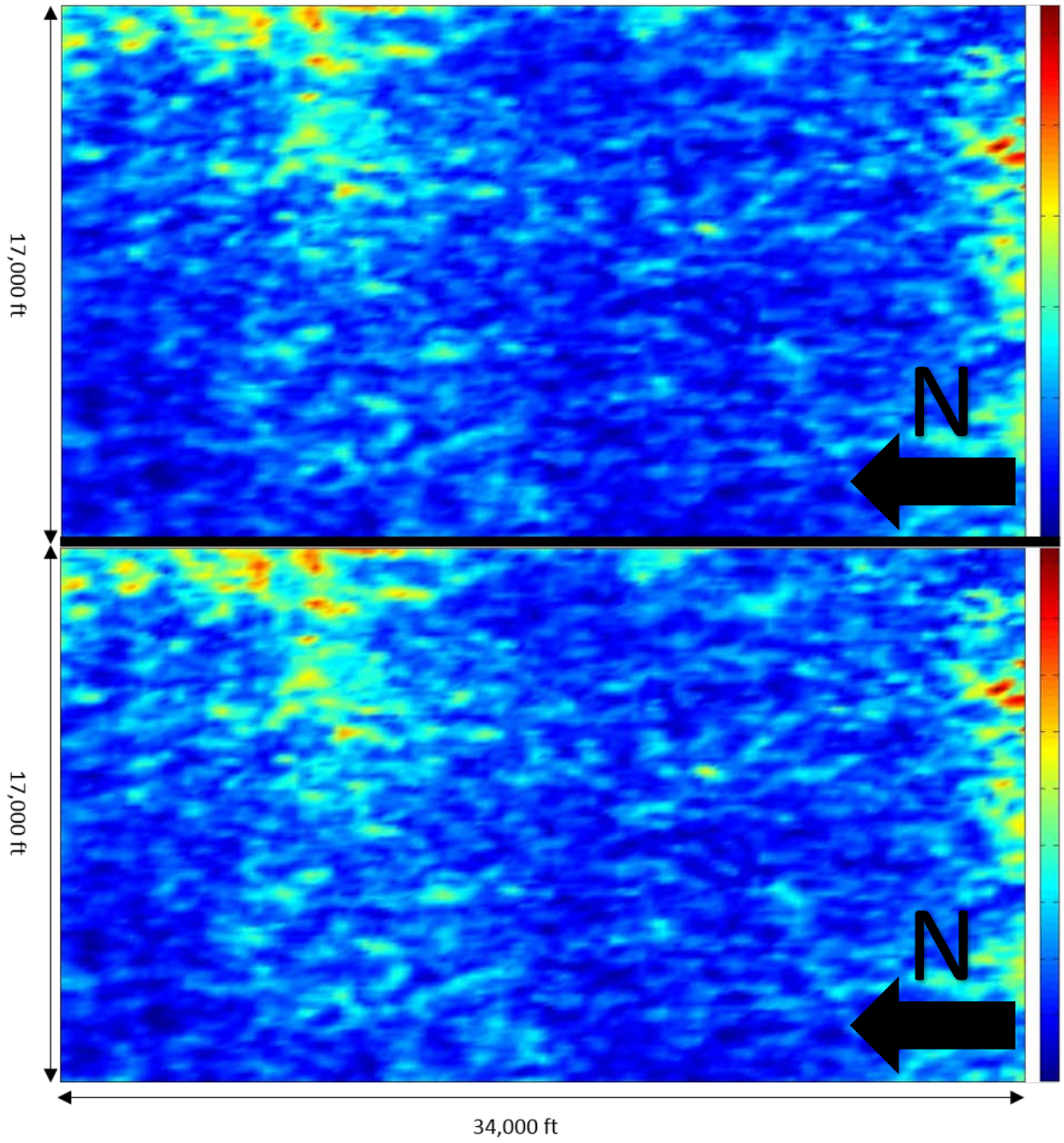

Figure 4.16: Comparison of proxies for fracture density from the Fourier coefficient decomposition method. r_2 coefficient is shown above, and B_{ani} calculated from inverted normal and tangential fracture weaknesses is shown below. Values have been vertically averaged throughout the Haynesville using a simple arithmetic mean. Warmer colors indicate denser fracture spacing. The black arrows indicate the direction of north.

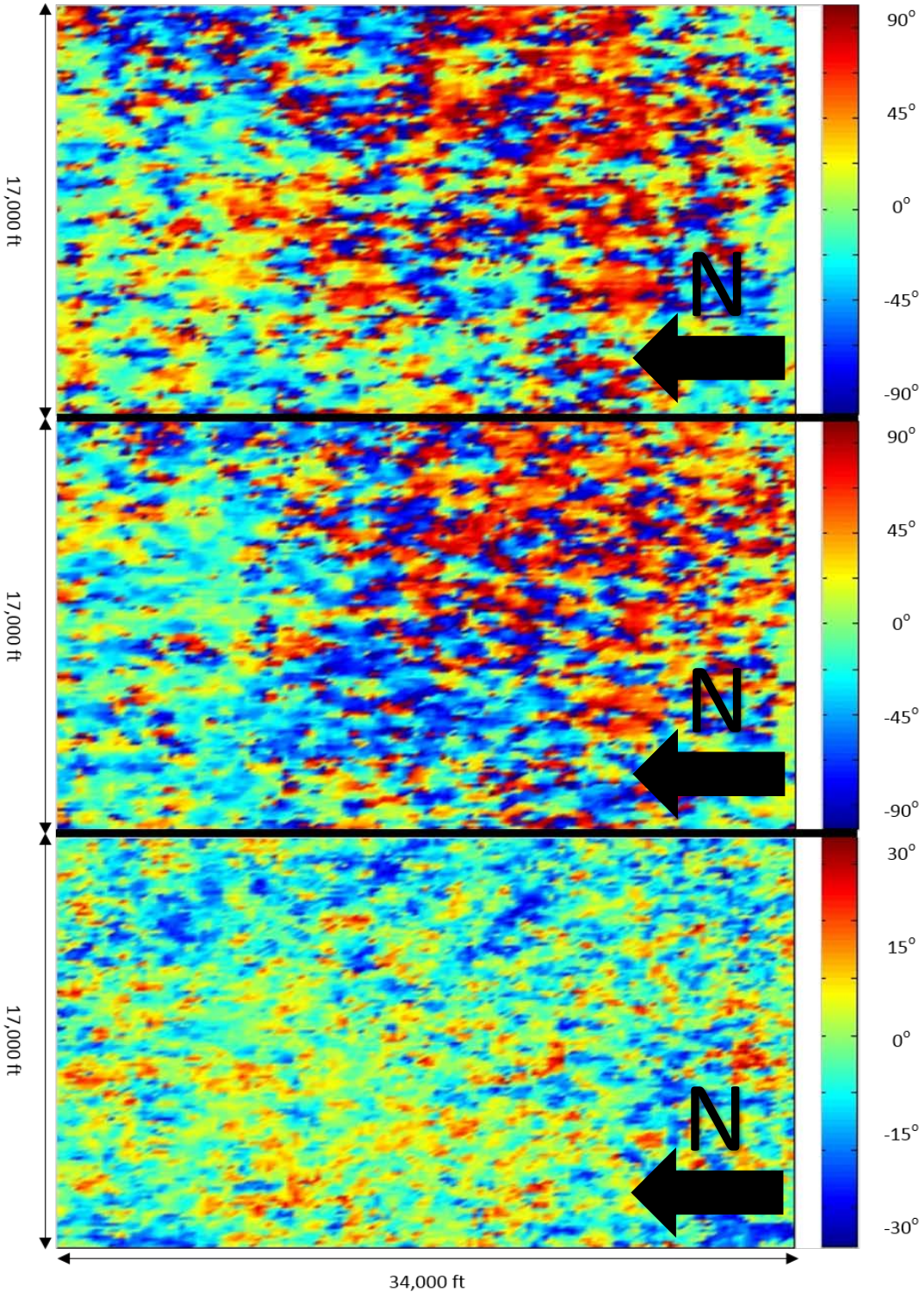

Figure 4.17: Comparison of fracture azimuth as determined from the Rüger and Fourier

coefficient decomposition methods. The top image depicts azimuth from the Rüger method, the middle image depicts azimuth from the 2nd Fourier coefficient phase φ_{sym} of the Fourier decomposition method, and the bottom image depicts azimuth from the 4th Fourier coefficient phase φ_{sym} of the Fourier decomposition method. Values have been vertically averaged throughout the Haynesville using the Yamartino method (described in Chapter 5 – see Equation 5.38). Colorbars on the top and middle image range from -90 degrees to 90 degrees. The colorbar on the bottom image ranges from -30 to 30 degrees. The black arrows indicate the direction of north.

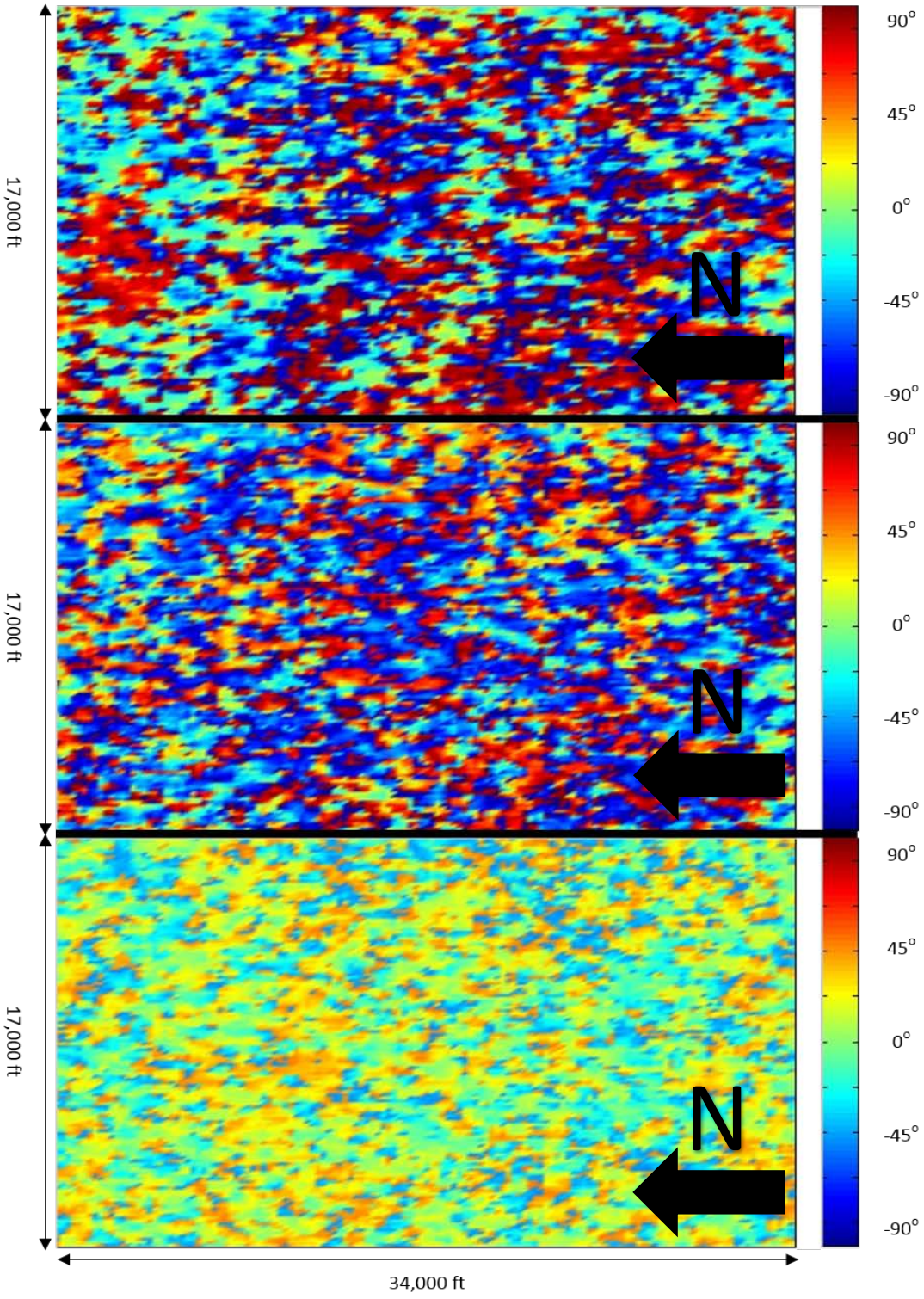

Figure 4.18: Comparison of fracture azimuth as determined from the Rüger and Fourier

coefficient decomposition methods. The top image depicts azimuth from the Rüger method, the middle image depicts azimuth from the 2nd Fourier coefficient phase φ_{sym} of the Fourier decomposition method, and the bottom image depicts azimuth from the 4th Fourier coefficient phase φ_{sym} of the Fourier decomposition method. Values corresponding to the top of the Haynesville are shown. Colorbars range from -90 degrees to 90 degrees. The black arrows indicate the direction of north.

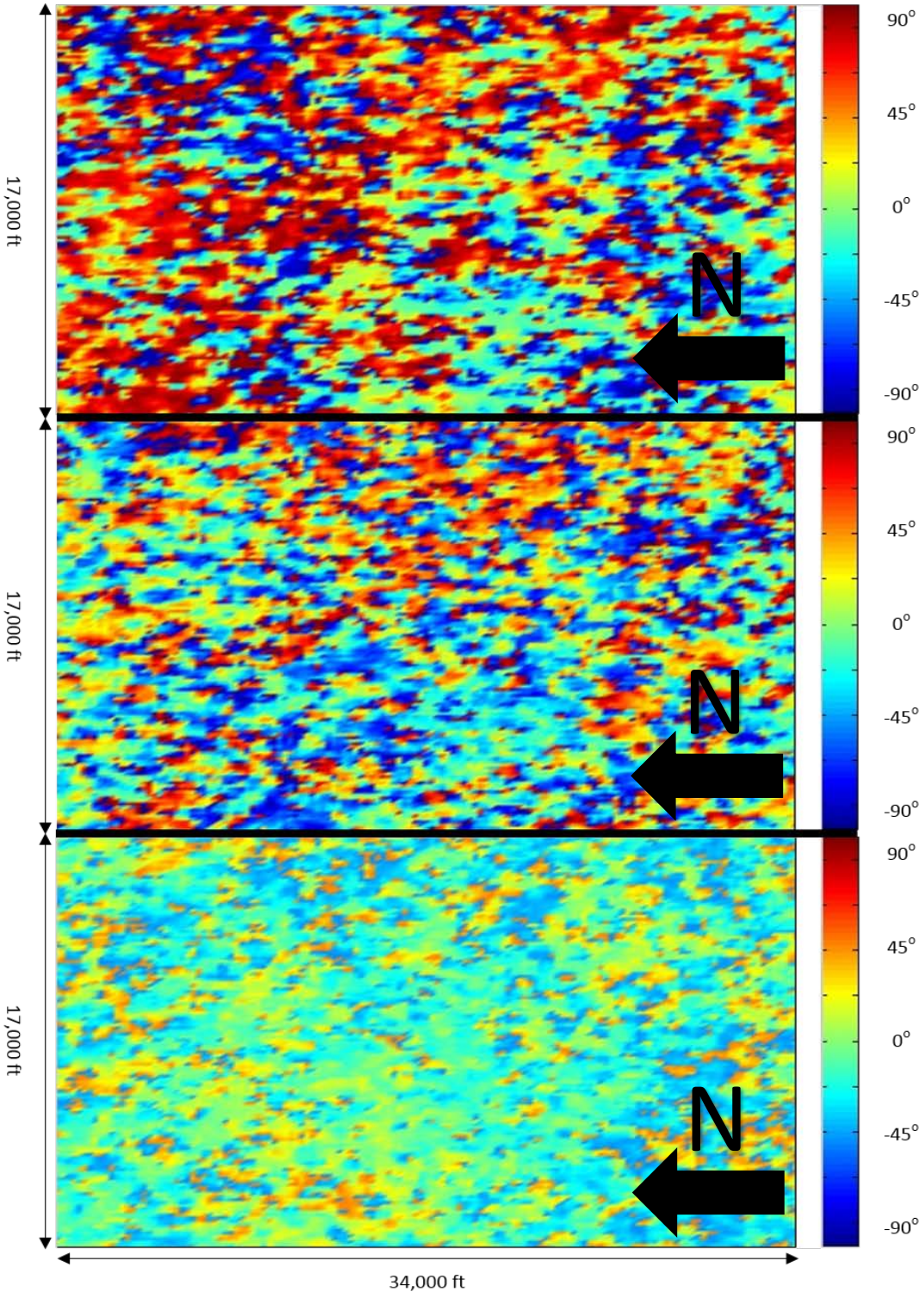

Figure 4.19: Comparison of fracture azimuth as determined from the Rüger and Fourier

coefficient decomposition methods. The top image depicts azimuth from the Rüger method, the middle image depicts azimuth from the 2nd Fourier coefficient phase φ_{sym} of the Fourier decomposition method, and the bottom image depicts azimuth from the 4th Fourier coefficient phase φ_{sym} of the Fourier decomposition method. Values corresponding to 15 meters from the top of the Haynesville are shown. Colorbars range from -90 degrees to 90 degrees. The black arrows indicate the direction of north.

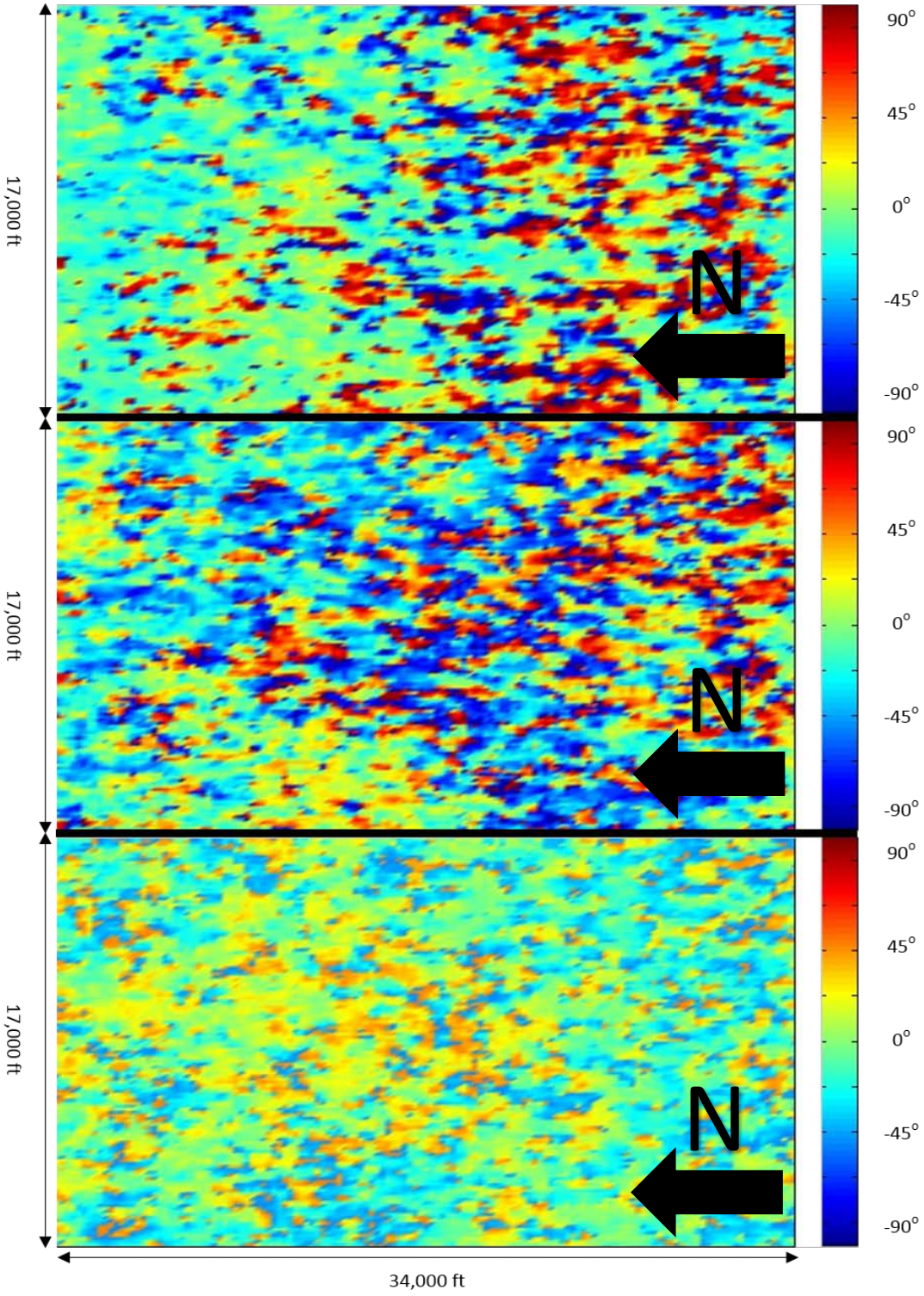

Figure 4.20: Comparison of fracture azimuth as determined from the Rüger and Fourier

coefficient decomposition methods. The top image depicts azimuth from the Rüger method, the middle image depicts azimuth from the 2nd Fourier coefficient phase φ_{sym} of the Fourier decomposition method, and the bottom image depicts azimuth from the 4th Fourier coefficient phase φ_{sym} of the Fourier decomposition method. Values corresponding to 30 meters from the top of the Haynesville are shown. Colorbars range from -90 degrees to 90 degrees. The black arrows indicate the direction of north.

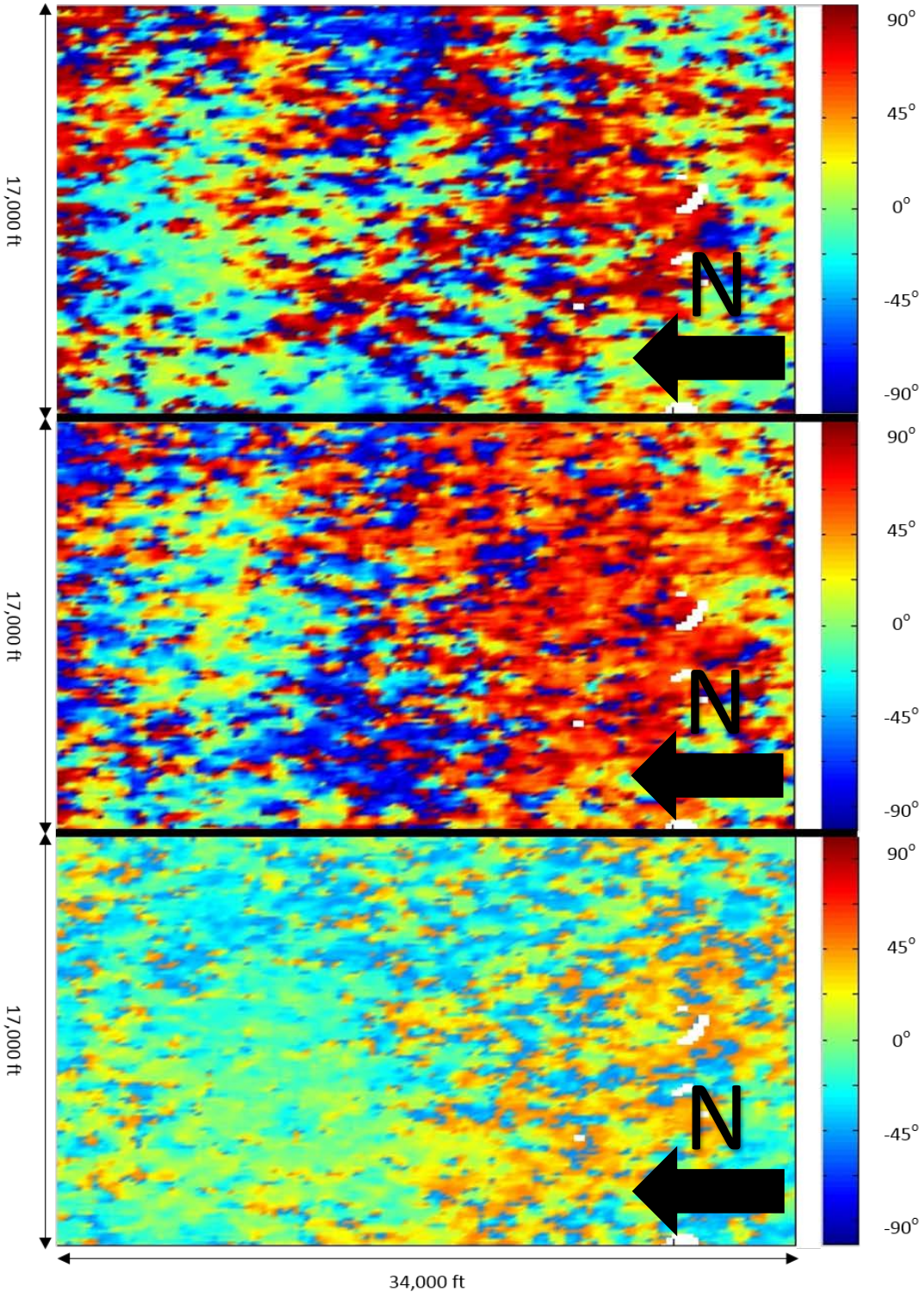

Figure 4.21: Comparison of fracture azimuth as determined from the Rüger and Fourier

coefficient decomposition methods. The top image depicts azimuth from the Rüger method, the middle image depicts azimuth from the 2nd Fourier coefficient phase φ_{sym} of the Fourier decomposition method, and the bottom image depicts azimuth from the 4th Fourier coefficient phase φ_{sym} of the Fourier decomposition method. Values corresponding to 45 meters from the top of the Haynesville are shown. Colorbars range from -90 degrees to 90 degrees. The black arrows indicate the direction of north.

4.5 DISCUSSION

Examining the results from both methodologies leads to an expected conclusion: both methods are capable of determining fracture density; however, neither method is capable of predicting a consistent fracture azimuth. Fracture azimuth results from the Rüger method contain sharp 90 degree changes in fracture azimuth, as seen in Figure 4.3, which are not geologically reasonable. These sharp 90 degree changes are characteristic of the 90 degree ambiguity inherent in determining φ_{iso} associated with the Rüger method, which was discussed earlier in this chapter. Figure 4.5 seemingly indicates that the fracture azimuth results from the Fourier decomposition method do not contain the sharp 90 degree ambiguities that plague the Rüger based method, which initially led me to have significantly higher confidence in fracture azimuth results from the Fourier coefficient decomposition method. However, other figures that depict inverted fracture azimuth from the Fourier coefficient decomposition method indicate significant variability in fracture azimuth. In many cases, the results seem to indicate that fractures are oriented approximately north-south in one area and approximately east-west in another area. For example, in Figure 4.17, middle image, the northern (leftmost) part of the image seems to indicate a north-south fracture orientation, whereas the southern (rightmost) part of the image seems to indicate an east-west fracture orientation. This lateral switching of orientation leads me to believe that the algorithm used by Hampson-Russell © does not rectify the correct symmetry axis, either by not attempting to do so or by implementing an unsuccessful method of doing so. It is interesting to note that the azimuth associated with the r_4 coefficient tends to range from about –22.5 to 22.5 degrees, indicating that phase wrapping associated with the r_4 coefficient is not corrected. While it is possible that significant lateral variation in fracture azimuth is a real feature, I believe it more likely that it is a result of a 90 degree error in determining the correct

azimuth. I believe that it is more geologically reasonable for fracture azimuth to be mostly consistent throughout the entire area rather than for it to switch orientation by 90 degrees several times within a few miles. This leads me to believe the true fracture azimuth is either approximately north-south or approximately east-west, although using these methods alone does provide the confidence needed determine which of these possible orientations correct. In Chapter 5, I present a novel Fourier coefficient based approach for calculating fracture azimuth which resolves this aforementioned 90 degree ambiguity in fracture azimuth.

Fracture density results between the two methods are similar. Both methods show spatially variable fracture density, with generally higher fracture density in the northern area of the section. Unfortunately, neither method seems capable of identifying specific large pockets of dense fracturing. It is unclear if this is due to some flaw in the data, due to some flaw in the methodology, or because these pockets of dense fracturing simply do not exist in this area. In the Fourier decomposition approach, fracture density results using the r_2 coefficient and B_{ani} (calculated from inverted fracture weaknesses) as proxies are effectively identical, indicating that the r_2 coefficient is an acceptable proxy for fracture density. This can be seen in Figure 4.16. All methods produce results that indicate anomalously high fracturing on the eastern and southern edges of the area. I believe these to be caused by "edge effects" which do not indicate real features. In the area analyzed, seismic data continues on in the Northern and Western directions, but no additional data exists in the eastern or southern directions (refer to Figure 2.4). Data near the "edge" generally has less dense azimuthal coverage, and usually has denser coverage in the inline direction than in the crossline direction. An example of this uneven azimuthal coverage can be seen in Figure 4.22. As the inversion algorithms used in these methods are proprietary information of Hampson-Russell ©, it is unclear how exactly this

reduced azimuthal coverage effects inversion results. However, the analysis conducted in Chapter 5 of this thesis clearly demonstrates that significant gaps in azimuthal data coverage can lead curve-fitting algorithms to falsely predict extreme azimuthal variation in order to better fit available data. This can incorrectly result in an anomalously high fracture density results in these areas. Refer to Chapter 5 and Figure 5.52 for more information regarding this phenomenon.

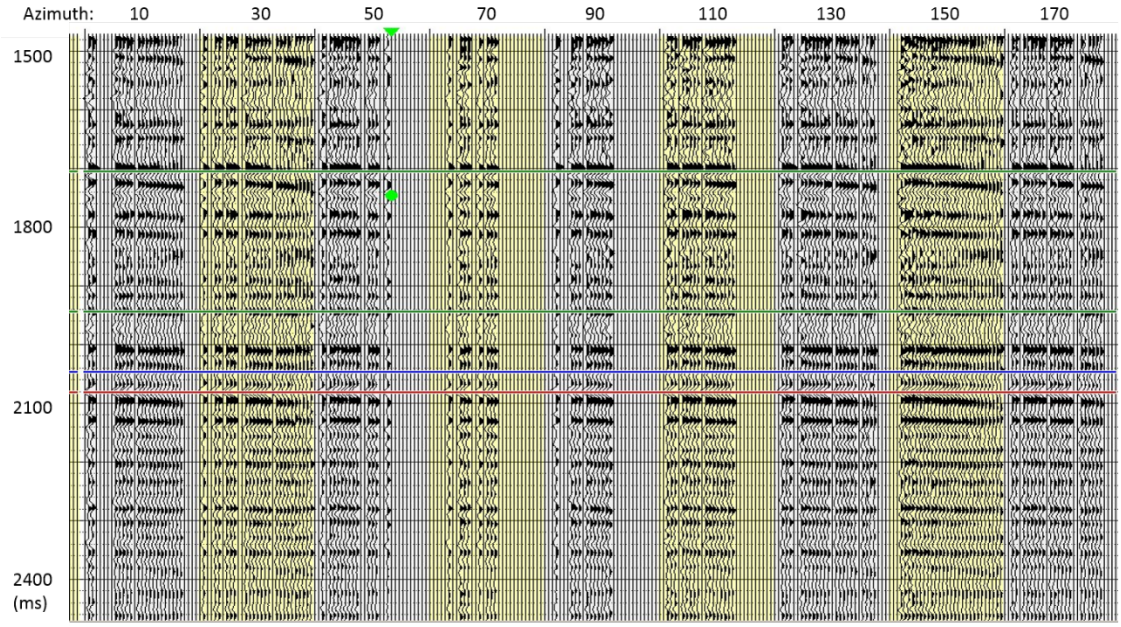

Figure 4.22: An example CDP from the azimuthal super gather depicting uneven azimuthal coverage. Primary trace sorting is by azimuth, and secondary sorting is by offset. Note that azimuthal coverage is dense in azimuths between 120 degrees – 40 degrees, corresponding to the inline direction; and dilute in azimuths between 40 degrees – 120 degrees, corresponding to the crossline direction. Data shows time ranges from roughly 1500 ms – 2400 ms. The Haynesville Shale is located from about 2040 ms – 2080 ms, between the blue and red horizons shown.

Due to the lack of available FMI logs and the general unavailability of published fracture characterization results in this area of the Haynesville, direct verification of fracture characteristics is impossible. Despite this, a number of comparisons can be made to increase confidence in the results presented in this thesis. Regarding fracture density, both methods producing similar results increases confidence in these results by means of statistical repeatability. Results from the method described in Chapter 5 additionally correspond well to the results presented in this chapter, further increasing confidence in results. As discussed in Chapter 2, production data trends from the Haynesville, specifically its characteristic high initial production rate and quick decline, indicate fracturing is present, despite a general lack of fracturing seen in FMI logs (Hammes et al., 2011). This suggests that laterally varied fracturing should be expected, with possible isolated areas of anomalously high fracturing, yet with sparse enough fracturing that fractures will not be seen in FMI logs from several wells. This expectation corresponds very well with the results for fracture density presented here. Some information on fracture orientation can be gained by performing a regional stress analysis of the area. A regional stress analysis with the explicit purpose of fracture azimuth prediction was conducted by Hunt et al. (2009), and results can be seen in Figure 4.23. These results predict fractures to be oriented in the approximate ENE-WSW direction. Unfortunately, due to post-fracturing rotation and changes in stress orientations through time, a regional stress analysis is not a reliable indicator of fracture orientation. However, the regional stress analysis would tend to support a fracture orientation of east-west more than an orientation of north-south. Hammes et al. (2011) additionally note that in formations surrounding the Haynesville, fracturing is generally seen parallel to the Gulf of Mexico Margin. Depending on which part of the Gulf of Mexico Margin you examine will find an orientation ranging from Northeast-Southwest to east-west. This again seems to

support the true fracture orientation being approximately east-west rather than approximately north-south.

Inverted results for normal and tangential fracture weaknesses are incorrect by a scaling factor, due to using seismic trace amplitude rather than true seismic reflectivity in the analysis performed. However, when used as a ratio, as is the case when calculating the Fluid Indicator attribute described by Equation 3.65, this scaling factor disappears and the fracture weaknesses become informative. Fluid indicator results indicate a value of approximately 1 throughout the area (values range from 0.7 to 1.2), which indicated that fractures are either dry or gas filled. This is consistent with a priori knowledge of the area, as several nearby wells are currently producing natural gas with little to no fluids present. Additionally, this fluid indicator attribute showed extreme sensitivity to the choice of g, also consistent with fractures being dry or gas filled (Shaw and Sen, 2006).

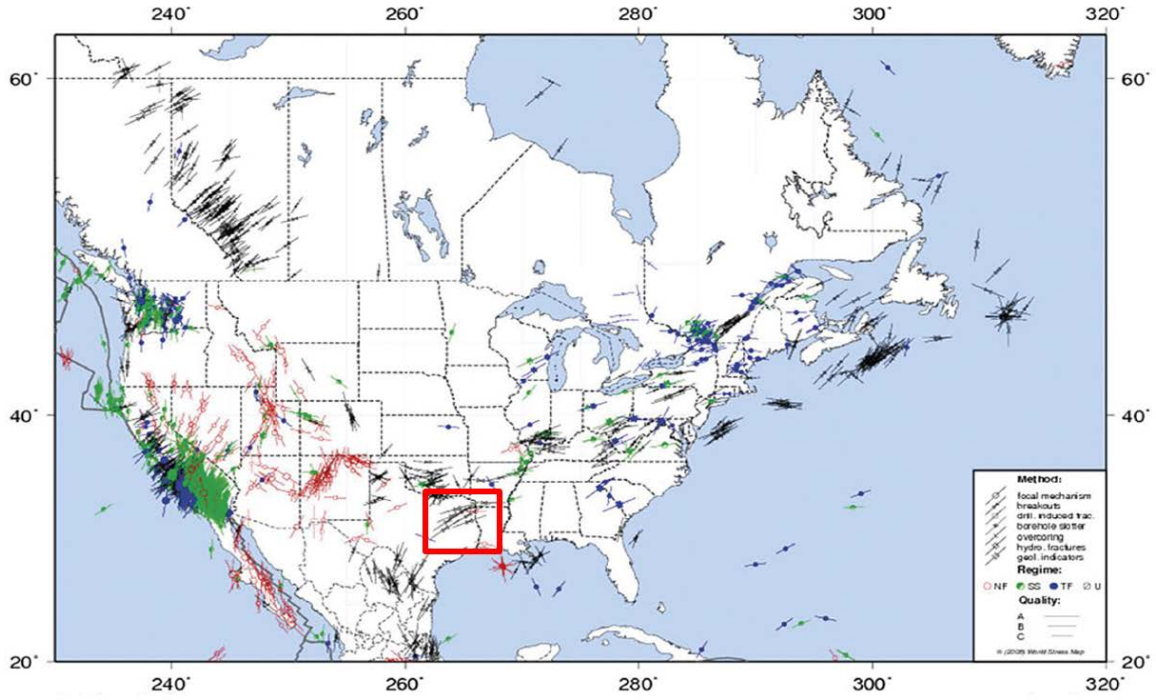

Figure 4.23: Predicted fracture orientation map, determined from analysis of in-situ geologic stress, in the United States. The red box indicates the approximate location of the Haynesville Shale analyzed in this paper. Figure from Hunt et al. (2009).

4.6 SUMMARY

Two methods for determining fracture orientation and fracture density have been presented. The first method is based on the Rüger AVO equation, and the second method is based on Fourier decomposition of the data. Both methods indicate laterally variable fracture density, with generally higher fracturing in the northern part of the area. Anomalously high fracture density on the eastern and southern edges of the survey area are not believed to be real features. Fracture orientation results from the Rüger method proved to be unreliable for well understood reasons, and regrettably the Fourier decomposition method results seem to also contain this 90 degree ambiguity in fracture azimuth. Analysis of the results indicates that there are two possible fracture orientations

– one which is approximately north-south, and another which is approximately east-west. Unfortunately, direct verification of results is not possible; however, a roughly east-west fracture orientation seems to agree better with expectations from a regional stress analysis and analogs from nearby formations. Laterally variable fracture density, which may indicate isolated fracture pockets throughout the area, agree well with the analysis of production data, which indicates fractures play a significant role in production, as well as FMI logs from other areas of the Haynesville, which indicate fractures are sparse. Unfortunately, a large coherent area of dense fracturing was not identified using these analyses. The Fourier decomposition method additionally inverted for normal and tangential fracture weaknesses, and used these values to calculate a fluid indicator attribute. Fracture weaknesses proved to be incorrect by a scaling factor, but this scaling factor is removed by using the ratio of normal and tangential fracture weaknesses in the calculated fluid indicator attribute. The fluid indicator attribute indicated that fractures are likely gas filled, which is consistent with a priori information of the area.

Chapter 5: Modified Fourier Coefficient Fracture Characterization Method

5.1 INTRODUCTION

Most fracture characterization methods currently in use assume that fractures are embedded in an otherwise isotropic rock, resulting in effective HTI anisotropy. This assumption is violated in the case of fractured shale, because shale is inherently VTI anisotropic rather than isotropic. If one considers a situation where closely spaced vertically aligned rotationally invariant fractures are embedded in an otherwise VTI anisotropic background rock, the result is an effective orthorhombic medium (see Chapter 3 for verification of this). Thus, in order to properly characterize fractured shale, an orthorhombic based fracture characterization method must be developed. Additionally, as seen in Chapter 4, an inability to determine the azimuth of fractures without a possible 90 degree ambiguity has plagued previous fracture characterization approaches. The work presented in this section describes a novel method which is based on an extension of the Fourier coefficient method presented in Chapter 4. This proposed method has two goals:

1. Correctly determine fracture density under the assumption of orthorhombic anisotropy.
2. Correctly determine the azimuth of the predominant fracture set without a 90 degree ambiguity.

This method is based on equations derived by Downton et al. (2011). This functionality is not available in any commercial software package, and thus I developed a custom algorithm using the MATLAB © language to execute this method.

The work presented in this chapter will cover the theory, implementation, and results utilizing the modified Fourier decomposition fracture characterization technique. This technique has been applied to data from the Haynesville as well as on several

synthetically generated datasets. This technique is valid in orthorhombic media when inverting for fracture density. However, when determining the azimuth of fractures, this method regresses to using equations describing HTI media. I believe the assumption of HTI anisotropy to still be mostly valid when only considering fracture azimuth, as fracture azimuth is determined by identifying azimuths corresponding to local maxima or minima in the seismic data. Even if the AVAZ component of seismic data is affected by the VTI anisotropy of the background rock, it should not affect the phase of the AVAZ signal. In this context, constant phase indicates that the azimuths associated with local minimum and local maximum reflectivity are unchanging. The phase of the AVAZ signal, which is used in determining fracture azimuth, is almost entirely controlled by the fracture characteristics. I verified this experimentally, as is shown in Figure 5.1. Figure 5.1 compares the AVAZ signal in four synthetically generated datasets – an isotropic dataset, a VTI dataset, a HTI dataset, and an orthorhombic dataset. All datasets were constructed using an identical isotropic background stiffness tensor and anisotropy was introduced using excess compliance theory and tensor rotations, as described in Chapter 3. Fractures are gas filled and oriented at a 0 / 180 degree azimuth. Details of how synthetic data were generated can be found in Section 5.4. Figure 5.1 clearly shows that in both the HTI and orthorhombic cases the azimuth of maximum reflectivity is 90 degrees and the azimuth of minimum reflectivity is 0 / 180 degrees, indicating that phase is identical in these cases. Determining fracture density using this method, however, depends on both the AVAZ and AVO components of the seismic signal. This can also be seen in Figure 5.1, where the AVAZ curves in the HTI and orthorhombic cases differ slightly in shape, magnitude and background reflectivity even though these cases have an identical fracture set. Thus, when analyzing a shale, the VTI component of the seismic signal needs to be considered in the inversion for fracture density, requiring a technique

that is valid for orthorhombic media. Advanced inversion methods are additionally integrated into the methodology to increase confidence in its results.

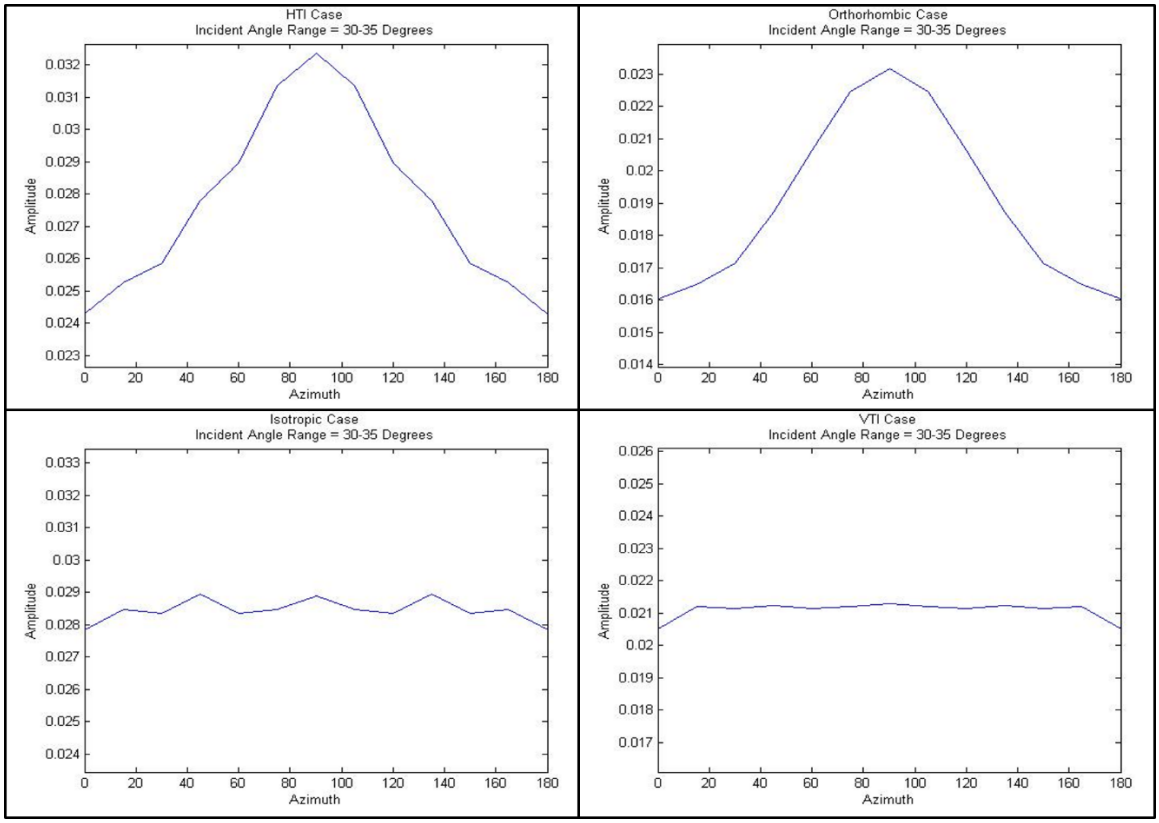

Figure 5.1: A set of figures depicting azimuthal variations with respect to azimuth in four cases – a HTI medium (upper left), an isotropic medium (lower left), an orthorhombic medium (upper right), and a VTI medium (lower right). The horizontal axis represents azimuth, and ranges from 0 to 180 degrees in all images. The vertical axis represents seismic amplitude, and has a total range of 0.01 in all images. Synthetic data were generated as described in Section 5.4. In these cases, fractures are gas filled and have an azimuth of 0 degrees. Figures show data from the 30 – 35 degree incident angle range. All stiffness tensors used in data generation were calculated from an identical isotropic background stiffness tensor. In the anisotropic cases, anisotropy was introduced using excess compliance theory and tensor rotations, as described in Chapter 3. Phase remains identical in the HTI and Orthorhombic cases, though some variation in the magnitude and shape of these curves can be seen. The VTI and isotropic cases show minimal azimuthal variation.

In order to validate the novel technique presented in this chapter, it was first tested on several synthetic datasets where true fracture density and fracture orientation were known. Section 5.4 describes in detail how the synthetic datasets were generated. After successfully predicting fracture density and fracture orientation in the synthetic examples, the analysis was performed on real data from the Haynesville Shale. The Haynesville data consists of a 3D azimuthal super-gather seismic dataset consisting of 137 inlines by 137 crosslines and converted to incident angle domain, with incident angles ranging from 5 to 45 degrees. Data was processed as described in Chapter 2. To reiterate, an azimuthal super-gather consisting of 12 azimuth bins, each 15 degrees wide, and 10 incident angle bins, each 4 degrees wide and ranging from 5 to 45 degrees, is used as the input to the following analysis. Hampson-Russell © was used to create the azimuthal super-gather described above, and all additional data analysis was done in MATLAB ©. Lastly, the HTI Fourier coefficient based method used in Chapter 4 will be repeated using the binning scheme presented above, and results from the old and new Fourier coefficient based methods will be compared.

5.2 Fourier Coefficient Decomposition Method

The Fourier coefficient decomposition method explained in Chapter 4 can be expanded to be valid in a more general anisotropic context. In the most general form, reflectivity can be expressed by a generalized Fourier series, such that:

$$R(\theta,\varphi) = \sum_{i=0}^{2}\sum_{j=0}^{4} w_{ij} f_i(\theta) g_j(\varphi) \ , \tag{5.1}$$

where AVO basis $f_i(\theta)$ can be described as

$$f_i(\theta) = \{1,\ \sin^2\theta\ ,\ \sin^2\theta\tan^2\theta\} \ , \tag{5.2}$$

AVAZ basis $g_j(\varphi)$ can be described as

$$g_j(\varphi) = \{1,\ cos(2\varphi),\ sin(2\varphi),\ cos(4\varphi),\ sin(4\varphi)\} \ , \tag{5.3}$$

and w_{ij} represents various Fourier weights (Downton et al., 2011). When evaluated at a constant angle of incidence (θ), Equation 5.1 reduces to:

$$R(\theta,\varphi) = U_0 + V_2\sin(2\varphi) + U_2\cos(2\varphi) + V_4\sin(4\varphi) + U_4\cos(4\varphi) \ , \quad (5.4)$$

where U_0, U_2, V_2, U_4 and V_4 are functions of AVO basis $f_i(\theta)$ and weights w_{ij}. Downton et al. (2011) note that of the fifteen possible weights w_{ij} only nine are nonzero. This leads to the expressions for U_0, U_2, V_2, U_4 and V_4 as shown in Equations 5.5 – 5.9.

$$U_0 = w_{00} + w_{01}\sin^2\theta + w_{02}\sin^2\theta\tan^2\theta \ , \quad (5.5)$$

$$V_2 = w_{11}\sin^2\theta + w_{12}\sin^2\theta\tan^2\theta \ , \quad (5.6)$$

$$U_2 = w_{21}\sin^2\theta + w_{22}\sin^2\theta\tan^2\theta \ , \quad (5.7)$$

$$V_4 = w_{23}\sin^2\theta\tan^2\theta \ , \quad (5.8)$$

$$U_4 = w_{24}\sin^2\theta\tan^2\theta \ . \quad (5.9)$$

Downton et al. (2011) additionally related all non-zero weights w_{ij} to various anisotropy parameters. This derivation will not be presented in this thesis, but resulting expressions relating w_{ij}'s to anisotropic parameters can be seen in Equations 5.10 – 5.18. The following expressions vary slightly from those presented by Downton et al. (2011) due to the presence of small typos in the Downton et al. (2011) paper.

$$w_{00} = A_{iso} + \frac{1}{2\alpha^2}\Delta(\alpha^2\varepsilon_z) \ , \quad (5.10)$$

$$w_{01} = B_{iso} + \frac{1}{4\alpha^2}[\Delta(\alpha^2\delta_x) - 8\Delta(\beta^2\gamma_x) + \Delta(\alpha^2\delta_y) - 8\Delta(\beta^2\gamma_y) - \frac{1}{2}\Delta(\alpha^2\varepsilon_z)] \ , \quad (5.11)$$

$$w_{02} = C_{iso} + \frac{1}{16\alpha^2}[3\Delta(\alpha^2\varepsilon_x) + 3\Delta(\alpha^2\varepsilon_y) + \Delta(\alpha^2\delta_z)] \ , \quad (5.12)$$

$$w_{11} = \frac{1}{2\alpha^2}[\Delta(\alpha^2\chi_z) - 4\,\Delta(\beta^2\varepsilon_{45})] \ , \quad (5.13)$$

$$w_{12} = \frac{1}{4\alpha^2}[\Delta(\alpha^2\delta_x) - 8\Delta(\beta^2\gamma_x) - \Delta(\alpha^2\delta_y) + 8\Delta(\beta^2\gamma_y)] \ , \quad (5.14)$$

$$w_{21} = \frac{1}{4\alpha^2}[\Delta(\alpha^2\varepsilon_{16}) + \Delta(\alpha^2\varepsilon_{26})] \ , \quad (5.15)$$

$$w_{22} = \frac{1}{4\alpha^2}[\Delta(\alpha^2\varepsilon_x) - \Delta(\alpha^2\varepsilon_y)] \ , \quad (5.16)$$

$$w_{23} = \frac{1}{8\alpha^2}[\Delta(\alpha^2\varepsilon_{16}) - \Delta(\alpha^2\varepsilon_{26})] \ , \quad (5.17)$$

$$w_{24} = \frac{1}{16\alpha^2}[\Delta(\alpha^2\varepsilon_x) - \Delta(\alpha^2\varepsilon_y) - \Delta(\alpha^2\delta_z)] \ , \tag{5.18}$$

where α represents compressional wave velocity (V_p); β represents shear wave velocity (V_s); ε, δ, γ and χ represent anisotropy parameters as defined by Pšenčik and Gajewski (1998); and $\Delta(\ldots)$ represents the difference in parameters between the layers generating the reflectivity. If the assumption is made that the upper layer is isotropic, these "difference in parameters" simply reduce to the anisotropic properties of the lower layer. For α and β which are not velocity differences (i.e. not present in $\Delta(\ldots)$ expressions), it is convenient to choose the average compressional or shear wave velocity of the layers generating reflectivity.

Equations 5.10 – 5.18 hold true for general anisotropic (triclinic) media. In a reduced anisotropic setting, specifically in the assumption of reflectivity generated in orthorhombic media, Equations 5.10 – 5.18 can be further reduced in some situations. In particular, examining the stiffness tensor characteristic of orthorhombic media, as shown in Equation 3.54, χ_z, ε_{16}, ε_{26}, and ε_{45} are seemingly nonexistent. However, the generalized tensor shown in Equation 3.54 is only valid if fractures are aligned in the inline or crossline direction (i.e., fracture azimuth is 0, 90 or 180 degrees). In this special case, w_{11}, w_{21} and w_{23} reduce to zero, and the nine possible non-zeros weights w_{ij} are further reduced to 6 non-zero w_{ij}. This leads Equations 5.5 – 5.9 to be reduced to:

$$U_0 = w_{00} + w_{01}\sin^2\theta + w_{02}\sin^2\theta\tan^2\theta \ , \tag{5.19}$$

$$V_2 = w_{12}\sin^2\theta\tan^2\theta \ , \tag{5.20}$$

$$U_2 = w_{22}\sin^2\theta\tan^2\theta \ , \tag{5.21}$$

$$V_4 = 0 \ , \tag{5.22}$$

$$U_4 = w_{24}\sin^2\theta\tan^2\theta \ . \tag{5.23}$$

Furthermore, Equation 5.4 reduces to

$$R(\theta,\varphi) = U_0 + V_2\sin(2\varphi) + U_2\cos(2\varphi) + U_4\cos(4\varphi) \ . \tag{5.24}$$

More generally, however, if you apply an arbitrary rotation about the z axis to an orthorhombic stiffness tensor, the result is a tensor form similar to a monoclinic stiffness tensor (as shown in Equation 3.53), though with fewer independent values. This can be proven using the methodology for rotating tensors described in Section 3.3. When applying this rotation fractures remain vertically aligned, however, they are no longer forced to be aligned with the x or y axes. The case where fractures are at a 45 or 135 degree azimuth represent another special case: in this rotated tensor $C_{16} = -C_{26}$, resulting in w_{23} and thus V_4 being zero; however, w_{11} and w_{21} are still nonzero. Thus, the first step of the analysis is to determine azimuth assuming the most general case as described by Equations 5.4 – 5.9, and then reduce to a specialized case if fracture azimuth is approximately equal to 0, 45, 90, 135 or 180 degrees. Ideally, applying the generalized method to one of these special cases would produce the same results as applying a specialized method. In practice, however, due to noise and the imperfection of data, this is not always the case. Being able to force these specialized solutions to arise can thus increase confidence in the inverted results by reducing the number of unknown parameters associated with the inversion.

To determine the azimuth of fractures, the phase of the 2nd order Fourier coefficients are considered. Phase can also be determined from the 4th order coefficients, but these coefficients have higher uncertainty (Downton et al., 2011) and more frequent phase wrapping. Thus, the 2nd order coefficients are better candidates for determining fracture azimuth. The trigonometric identity shown in Equation 5.25 can be used to combine the 2nd and 4th order Fourier coefficients into composite coefficients.

$$a \sin t + b \cos t = \sqrt{a^2 + b^2}\ \cos(t - \tan^{-1}\frac{a}{b}) \ . \tag{5.25}$$

Applying Equation 5.25 to Equation 5.4 transforms Equation 5.4 into:

$$R(\theta,\varphi) = U_0 + \sqrt{V_2^2 + U_2^2}\cos\left(2(\varphi - \frac{1}{2}\tan^{-1}\frac{V_2}{U_2})\right) + \sqrt{V_4^2 + U_4^2}\cos\left(4(\varphi - \frac{1}{4}\tan^{-1}\frac{V_4}{U_4})\right). \quad (5.26)$$

In Equation 5.26, the term $\frac{1}{2}\tan^{-1}\frac{V_2}{U_2}$, here forth denoted φ_{sym}, represents the phase of the second order coefficient and one possible symmetry plane azimuth. Note that the function used in determining the 2nd order Fourier coefficient phase has a range between negative 45 and 45 degrees, and thus the phase "wraps" every 90 degrees. Note that the symmetry plane azimuth is perpendicular to fracture azimuth. The 4th order Fourier coefficients provide the same phase, though has higher uncertainty and more frequent phase wrapping (every 45 degrees rather than every 90 degrees). When $\varphi = \varphi_{sym}$, Equation 5.26 reduces to:

$$R(\theta,\varphi) = U_0 + \sqrt{V_2^2 + U_2^2} + \sqrt{V_4^2 + U_4^2}, \quad (5.27)$$

because $\cos 0 = 1$. Unfortunately, because we do not know if positive or negative roots are taken in Equations 5.25 and 5.26, a second possible symmetry plane azimuth is $\varphi_{sym} \pm 90$ degrees. A 90 degree phase shift in effect changes the sign of the square root associated with the 2nd order Fourier coefficient. Note that since the 2nd order Fourier coefficient phase is 180 degree periodic, φ_{sym} +90 degrees is identical to φ_{sym} −90 degrees. Because the possible range of symmetry plane azimuths spans 180 degrees, these two possible solutions (φ_{sym} and $\varphi_{sym} \pm 90$ degrees) span the entire possible range of symmetry plane azimuths.

We can determine which of these possible azimuths represents the actual symmetry plane by determining if the symmetry plane should correspond to a maximum amplitude reflection or a minimum amplitude reflection. To accomplish this, I fall back to an HTI assumption. By analyzing Equations 4.8 – 4.14, which describe how Fourier coefficients relate to fracture weakness in HTI media, I can predict the seismic response

at the azimuth corresponding to the symmetry plane in terms of normal and tangential fracture weakness. After some algebra, I find:

$$R_{pp}(\varphi = \varphi_{sym}) = r_0 + r_2 + r_4$$
$$= r_0 + \Delta T \left(\frac{1}{2} g \sin^2\theta\right)\left(1 - \frac{1}{4}\tan^2\theta\right) - \Delta N \,(2\sin^2\theta\tan^2\theta)(1-g)\,. \quad (5.28)$$

Equation 5.28 can be further simplified by relating ΔN and ΔT to fracture density. Bakulin et al. (2000, Part I) has described this relationship, and their results are shown in Equations 5.29 – 5.31.

$$\Delta N_{wet} = 0\,, \quad (5.29)$$
$$\Delta N_{dry} = \frac{4e}{3g(1-g)}\,, \quad (5.30)$$
$$\Delta T = \frac{16e}{9-6g}\,, \quad (5.31)$$

where e represents fracture density. Note that ΔT is the same when fractures are dry, gas or fluid filled, however ΔN is zero when fractures are fluid filled. Equation 5.28 can be further simplified by dividing by ΔT, resulting in:

$$\frac{R_{pp}}{\Delta T} = \frac{r_0}{\Delta T} + \left(\frac{1}{2} g \sin^2\theta\right)\left(1 - \frac{1}{4}\tan^2\theta\right) - \frac{\Delta N}{\Delta T}(2\sin^2\theta\tan^2\theta)(1-g)\,. \quad (5.32)$$

Using Equations 5.29 – 5.31, I find

$$\frac{\Delta N}{\Delta T}_{wet} = 0\,, \quad (5.33)$$
$$\frac{\Delta N}{\Delta T}_{dry} = \frac{1-2g}{4g(1-g)}\,. \quad (5.34)$$

Equation 5.34 also holds true for gas filled fractures. By plugging Equations 5.33 and 5.34 into Equation 5.32, one can determine the sign of the combined 2nd and 3rd terms in Equations 5.32 as a function of θ and g. Thus, one can determine if the reflection coefficient at the azimuth representing the symmetry axis will be a maximum or minimum amplitude event based on the sign of r_0. In the case of dry or gas filled fractures, this will be based on incident angle (θ) and the square of the V_s to V_p ratio (g). If the combined second and third terms have the same sign as the first term, the symmetry axis will correspond to a maximum amplitude, whereas if the signs are opposing it will

correspond to a minimum amplitude. Note that dividing r_0 and R_{pp} by ΔT does not change their signs, and the change in magnitude can be ignored because only the sign matters in this analysis. The sign of the combined 2nd and 3rd terms of Equation 5.32 under the assumption of dry or gas filled fractures as a function of g and θ can be seen in Figure 5.2. Under the assumption of fluid filled fractures, the combined 2nd and 3rd terms of Equation 5.32 will always have a positive value for incident angles encountered in seismic surveys. To summarize, this indicates that:

1. If fractures are fluid filled, the symmetry plane azimuth will correspond to a maximum amplitude for positive r_0 and a minimum amplitude for negative r_0.
2. If fractures are dry or gas filled, the symmetry plane azimuth will always correspond to a minimum amplitude for positive r_0 and a maximum amplitude for negative r_0 at far offsets (θ > 30 degrees). Figure 5.2 can be used to determine if the symmetry plane azimuth will correspond to a maximum or minimum for smaller incident angles at certain values of g.

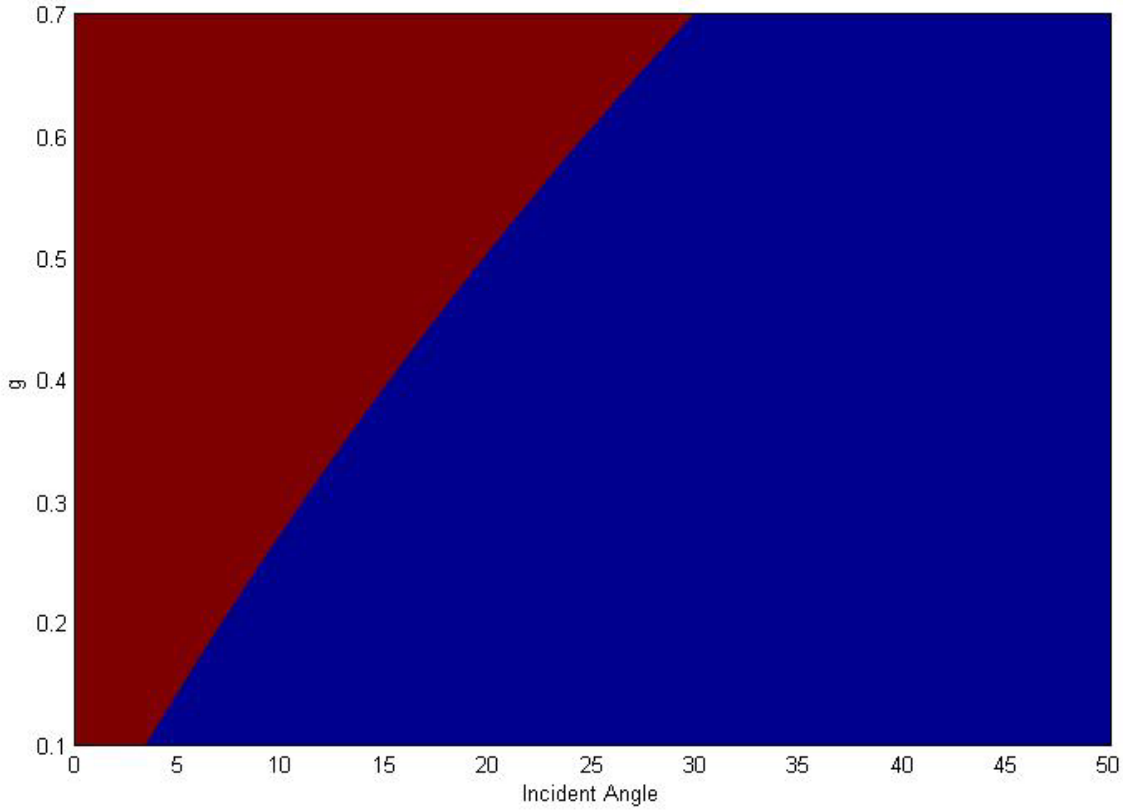

Figure 5.2: A plot indicating the sign of the 2nd and 3rd terms in Equation 5.32 as a function of incident angle and g for the case of either dry or gas filled fractures. Red indicates the combined terms have positive value, while blue indicates the combined terms have a negative value. The x axis represents incident angle and ranges from 0 to 50 degrees. The y axis represents g and ranges from 0.1 to 0.7.

Based on production data from the Haynesville, in which natural gas is being produced with minimal fluids, it is assumed that in this area fractures are nearly entirely gas filled. It is also assumed that r_0 is generally positive, which is supported by available seismic and well data. Note that the relative drop in impedance between the Haynesville and its upper bounding layer would generally dictate that r_0 is negative. However, the reversal in seismic data polarity results in a positive r_0. Lastly, the same value of g used in Chapter

4 ($g = 0.444$) is assumed. Based on these assumptions, I determined that the symmetry axis will correspond to a minimum reflection amplitude for incident angles larger than ~18 degrees and a maximum reflection amplitude for incident angles less than ~18 degrees, as can be seen in Figure 5.2. Thus, by comparing the values of the two possible azimuths determined by the phase of the 2nd order Fourier coefficients, one can determine the proper symmetry plane azimuth (and therefore the proper fracture azimuth). Note that maximum absolute value of the seismic data needs to be used in practice because the data being used is seismic trace amplitude rather than the true reflectivity series. This is best understood by considering the standard isotropic convolution model for seismic reflectivity. In this model, a larger reflection coefficient results in a more positive seismic amplitude corresponding to the peak(s) of the wavelet and a more negative seismic amplitude corresponding to the trough(s) of the wavelet. Although the convolution model is not entirely valid in an anisotropic setting, the idea that a larger reflection coefficient will create a larger magnitude event, regardless of sign, is still valid.

5.3 ALGORITHM

Initially, data from the azimuthal super-gather described in Chapter 2 and the Introduction to this chapter were loaded into MATLAB © as a 5-D array. In order to save memory space, the data were limited in time to only include times between 2020 ms and 2120 ms, which encompasses the entirety of the Haynesville Shale at all CDP locations. The data were cropped a second time to zero out all values between 2020 and 2120 ms which are not in the Haynesville. Seismic amplitude values of exactly zero do not exist anywhere within the Haynesville where data exists, allowing for quick and easy determination regarding whether a data point is in the Haynesville (and thus needs to be analyzed) or is outside of the Haynesville through the use of logical sorting. Certain

incident angles and azimuths associated with the azimuthal super-gather generated by Hampson-Russell © additionally do not have data, and are also assigned a seismic amplitude of exactly zero. This again allows for quick and easy determination that data is not present in these areas.

Data were imported into MATLAB © and stored as a 5D array, where the 5 dimensions represent time, azimuth, incident angle, inline, and crossline. After data were loaded into MATLAB ©, a built-in IRLS curve fitting function *fit* was used to fit a Fourier series to azimuthal variations in the data using the archetypal fitting function shown in Equation 5.4. Logical expressions were implemented to automatically skip fitting at incident angles and locations where a user-defined minimum number of data points were not present. An absolute minimum of five data points are needed to perform the curve fitting; however, I decided to disregard areas where at least eight azimuthal data points were present in order to increase confidence in the fitted curve. Note that at each unique time / incident angle / CDP a maximum of twelve azimuthal data points are present. The algorithm is looped over all incident angles, times, inlines and crosslines, and the Fourier coefficients U_0, U_2, V_2, U_4 and V_4 are recorded. In addition to calculating these five unique Fourier coefficients, the *fit* function automatically generates 95% confidence interval ranges for each calculated Fourier coefficient, which are additionally recorded. The number of data points used in the fitting as well as the data residual, calculated by taking the difference between observed and synthetic data, are also recorded. In order to increase the speed of the algorithm, all appropriate matrices are pre-allocated in the code, and parallelization is implemented. Current parallelization works on the time index, such that the fitting is applied simultaneously to multiple times for some constant incident angle, inline and crossline combination. Note that fitting is independent at each time / incident angle / inline / crossline combination, potentially

allowing this problem to be massively parallelized if modified to run on CPU or GPU clusters. The code is designed to be extremely user friendly – the only parameters which need defining are the ranges of times, azimuths, incident angles, inlines and crosslines present in the data.

After fitting a Fourier series to every unique time, incident angle, inline and crossline, the second order Fourier coefficients are used to determine the two possible symmetry plane azimuths. These are determined for every unique time, incident angle, and CDP, using Equations 5.25 and 5.26. I additionally attempted to find a "best-fit" Fourier series which fit a Fourier series to all incident angles simultaneously, but the significant AVO effects proved to cause unacceptable results and thus this method was abandoned. As described in Section 5.2, each set of two possible azimuths were compared to find a maximum amplitude for smaller incident angles (less than ~18 degrees) and a minimum amplitude for larger incident angles (greater than ~18 degrees). Maximum / minimum amplitude was defined as maximum / minimum absolute value of amplitude. By comparing the reflection magnitude at both possible azimuths, the correct symmetry plane azimuth was determined at each time, incident angle, and CDP. Due to the lower AVAZ signal to noise ratio at smaller incident angles, more weight was put on data corresponding to larger incident angles. In practice, only azimuthal information corresponding to incident angles greater than or equal to 25 degrees was used. These results will be examined in depth in the Results and Discussion sections of this chapter; however, in order to proceed in describing the algorithm used, I will divulge that fracture azimuth proved to be approximately 90 degrees, corresponding to an approximate east-west fracture orientation.

Being that the fracture azimuth corresponded to a special case, as described in Section 5.2, the Fourier curve fitting procedure was repeated using Equation 5.24 as the

archetypal fitting function. I again decided to disregard data where fewer than eight azimuthal data points were present in order to increase confidence in the fitted Fourier series. After fitting a Fourier series to every unique time, incident angle, inline and crossline using the modified curve fitting equation, a weighted least squares inversion is performed to calculate weights w_{ij}. Note that weights w_{ij} do not vary with incident angle, but rather contain information describing data from all incident angles simultaneously. Equation 3.80 described the weighted least squares regression equation used. Initially, weighting matrix $\boldsymbol{W_d}$ was calculated for each time / inline / crossline location. Diagonal values of $\boldsymbol{W_d}$ are calculated by averaging 3 parameters:

1. The number of data points used in the fitting
2. The inverse of the data variance
3. The inverse of the 95% confidence range in Fourier coefficients

All parameters are straightforward to calculate for every time / incident angle / inline / crossline / Fourier coefficient using the arrays generated in the curve fitting part of the algorithm. Prior to being averaged, each of these values are normalized to range between zero and one. All three of these parameters measure uncertainty, with zero corresponding to no confidence and one representing extreme certainty. Thus, an average of these three normalized parameters introduces robustness into the inversion. Note that because matrix $\boldsymbol{W_d}$ is a diagonal matrix, it is preferable to store $\boldsymbol{W_d}$ as a line vector rather than a matrix, and use the *diag* function to diagonalize $\boldsymbol{W_d}$ at each time / inline / crossline location separately. If this is not done, matrix $\boldsymbol{W_d}$ can easily exceed the memory limitations of the computer the analysis is being run on. For example, in this work the uncompressed $\boldsymbol{W_d}$ array spans 40x40x51x137x137, which in double precision format requires slightly over 12 Gb of memory to store.

After generating weighting matrix $\boldsymbol{W_d}$, a weighted least squares inversion is performed using Equation 3.80. In this inversion, data is represented by Fourier coefficients U_0, U_2, V_2 and U_4 calculated at each of the 10 unique incident angles, and model parameters are the six non-zero weights w_{ij} which do not vary with incident angle. The forward operator matrix $\boldsymbol{G}$ consists of Equations 5.19 – 5.23 evaluated at each of the 10 unique incident angles. Expressed in the form shown in Equation 3.71, these take the form:

$$\begin{pmatrix} U_0(\theta_1) \\ V_2(\theta_1) \\ U_2(\theta_1) \\ U_4(\theta_1) \\ U_0(\theta_2) \\ V_2(\theta_2) \\ U_2(\theta_2) \\ U_4(\theta_2) \\ \vdots \\ U_0(\theta_{10}) \\ V_2(\theta_{10}) \\ U_2(\theta_{10}) \\ U_4(\theta_{10}) \end{pmatrix} = \begin{pmatrix} 1 & \sin^2\theta_1 & \sin^2\theta_1 \tan^2\theta_1 & 0 & 0 & 0 \\ 0 & 0 & 0 & \sin^2\theta_1 \tan^2\theta_1 & 0 & 0 \\ 0 & 0 & 0 & 0 & \sin^2\theta_1 \tan^2\theta_1 & 0 \\ 0 & 0 & 0 & 0 & 0 & \sin^2\theta_1 \tan^2\theta_1 \\ 1 & \sin^2\theta_2 & \sin^2\theta_2 \tan^2\theta_2 & 0 & 0 & 0 \\ 0 & 0 & 0 & \sin^2\theta_2 \tan^2\theta_2 & 0 & 0 \\ 0 & 0 & 0 & 0 & \sin^2\theta_2 \tan^2\theta_2 & 0 \\ 0 & 0 & 0 & 0 & 0 & \sin^2\theta_2 \tan^2\theta_2 \\ \vdots & \vdots & \vdots & \vdots & \vdots & \vdots \\ 1 & \sin^2\theta_{10} & \sin^2\theta_{10} \tan^2\theta_{10} & 0 & 0 & 0 \\ 0 & 0 & 0 & \sin^2\theta_{10} \tan^2\theta_{10} & 0 & 0 \\ 0 & 0 & 0 & 0 & \sin^2\theta_{10} \tan^2\theta_{10} & 0 \\ 0 & 0 & 0 & 0 & 0 & \sin^2\theta_{10} \tan^2\theta_{10} \end{pmatrix} \begin{pmatrix} w_{00} \\ w_{01} \\ w_{02} \\ w_{12} \\ w_{22} \\ w_{24} \end{pmatrix}, \tag{5.35}$$

where $\theta_1 = 7$ degrees, $\theta_2 = 11$ degrees, …, $\theta_{10} = 43$ degrees. Arrays $\boldsymbol{d}$, $\boldsymbol{G}$ and $\boldsymbol{m}$, as shown in Equation 5.35, are generated for every time / inline / crossline. A weighted least squares inversion using weight matrix $\boldsymbol{W_d}$ is carried out to determine weights w_{00}, w_{01}, w_{02}, w_{12}, w_{22} and w_{24} at every unique time, inline and crossline combination. In lieu of a conventional matrix inverse, the Moore-Penrose matrix pseudoinverse calculated from Singular Value Decomposition (SVD) was used, which was calculated using the built-in MATLAB © function *pinv*. The Moore-Penrose pseudoinverse is preferable to a conventional matrix inverse as it allows the analysis to be performed when matrix $[\boldsymbol{G}^T \boldsymbol{W}_d \boldsymbol{G}]$ is near-singular or null.

I attempted to use the six nonzero weights w_{00}, w_{01}, w_{02}, w_{12}, w_{22} and w_{24} in an additional inversion to determine anisotropic parameters using Equations 5.10 – 5.18, though due to the highly underdetermined nature of the problem this was not possible. In its current state, this problem consists of six data points and eleven unknowns. I wish to note, however, that if some of the unknown anisotropic parameters could be constrained – for example by well control or by incorporating P-S reflection seismic data – an additional inversion could be performed to calculate the anisotropic parameters which cannot be constrained from other data sources. Unfortunately, this is not the case in this study.

As anisotropic parameters are not possible to directly invert for, I propose a new attribute to be a measure of fracture density, shown in Equation 5.36.

$$R_2^* = \sqrt{w_{12}^2 + w_{22}^2} \ . \tag{5.36}$$

As Downton (2011) and Downton et al. (2011) note, the energy present in the 2nd order Fourier coefficient is approximately equal to anisotropic gradient, which is proportional to fracture density. The analysis conducted in Chapter 4 shows there to be almost zero difference between fracture density predictions using the r_2 Fourier coefficient and using B_{ani} calculated from normal and tangential fracture weaknesses (ΔN and ΔT). Equation 5.36 is the most logical way to calculate the energy in the 2nd order Fourier coefficients, and produces results with desirable qualities – all values are positive, values near zero indicate minimal 2nd order coefficient energy, and high values indicate significant 2nd order coefficient energy. Additionally, Equation 5.36 benefits from capturing the energy present both in 2nd order sine and cosine terms as well as from the increased confidence introduced by the weighted least squares method of determining w_{12} and w_{22}, which contain information from data points at all incident angles.

2-D lateral smoothing and time averaging operators were developed both for Fourier coefficient / fracture density data, and for azimuthal data. 3-D smoothing was not implemented. The time averaging operator averages data from all times at a particular CDP location. The smoothing operators average the central data point four times, laterally adjacent data points twice, and diagonally adjacent data points once, resulting in the 2d convolution smoothing kernel seen in Equation 5.37.

$$\begin{bmatrix} 1/16 & 1/8 & 1/16 \\ 1/8 & 1/4 & 1/8 \\ 1/16 & 1/8 & 1/16 \end{bmatrix}. \tag{5.37}$$

The kernel shown in Equation 5.37 was modified at the edges and corners of the data volume to ensure that the sum of all values in the kernel remained one in these situations. The 2D smoothing operator can be applied in a cascaded fashion to allow for various levels of data smoothing, although I feel that a single application of 2D smoothing is acceptable to make results presentable and informative. Smoothing and averaging of Fourier coefficients and the fracture density attribute is straightforward and was performed using an arithmetic mean and the smoothing kernel shown in Equation 5.37; however, separate operators were developed for averaging azimuths. Arithmetic mean averaging does not work on fracture azimuth data due to the problem of phase wrapping. The problem of phase wrapping can be easily understood by attempting to average compass directions. If one were to attempt to average a compass bearing of 1 degrees and 359 degrees, the obvious answer would be the average compass direction is due North. However, the arithmetic mean of 1 and 359 would indicate an average bearing of 180

degrees, corresponding to due South. To resolve this issue, a methodology developed by Yamartino (1984) is used.

The Yamartino method was initially developed for meteorological applications. It attempts to find the average direction and standard deviation of wind direction data. The average wind direction is determined by decomposing wind direction bearings from individual data points into their sine and cosine components, averaging the sine and cosine components for all wind directions, and taking the four-quadrant arctangent of the averaged sine and cosine components. This can be seen in Equation 5.38.

$$\theta_{avg} = arctan2\left(\frac{1}{n}\sum \sin\theta_i \, , \frac{1}{n}\sum \cos\theta_i\right) \ , \tag{5.38}$$

where $arctan2$ represents the four-quadrant arctangent operator and θ_i represents the compass bearing of the ith data point. Note that Equation 5.38 displays the proper input into the MATLAB © *atan2* and *atan2d* functions, but depending on how the arctangent function is defined the sine and cosine arguments may need to be reversed. The Yamartino method was developed to average angles that are 360 degrees periodic, but azimuthal fracture orientation results are 180 degrees periodic. To resolve this, all angles were multiplied by 2 prior to averaging using Equation 5.38, and the resulting average angle was then divided by 2. This results in averaged angles ranging between -90 and 90 degrees.

Figures depicting fracture density and fracture azimuth are presented in map view, and were stretched in the inline direction by a factor of 2 to correctly display the geometry of the survey area. These figures were rotated to match the orientation of the results displayed in Chapter 4 of this thesis (i.e., north is to the left). Three different types of figures were generated. The first type of figure shows vertically averaged properties of interest, namely fracture azimuth and fracture density proxy R_2^*. The second type of figure depicts these same parameters of interest in constant time slices. The last type of

figure depicts these same parameters in “constant depth” slices. Here, constant depth does not refer to constant depth from the surface but, instead, constant depth from the top of the Haynesville. Constant depth slices were generated by grouping data in such a way that parameters that were a constant number of vertical time samples from the Haynesville top (identifiable by the first non-zero data point) were plotted together. Assuming a constant p-wave velocity of ~3 km/s, each time sample (2 ms) corresponds to approximately 3 meters of depth. Note that time represents two-way travel time (TWT). I favor constant depth slices over constant time slices, as they allow for a direct comparison between upper, middle and lower Haynesville properties. Constant depth slices also ensure that vertically changing properties do not falsely appear to be lateral changes in properties, as may be the case in the constant time slices. The Haynesville dips slightly, so a particular time slice can show upper, middle and lower Haynesville properties in different areas of the same slice, which could lead to incorrect interpretations and conclusions. Graphing functions were designed such that a user can easily choose graph type, amount of desired smoothing and parameter of interest, and graphs are automatically generated and appropriately labeled.

5.4 Generating Synthetic Data

Because the method described in this chapter is a never before used technique, analyzing synthetic data using this method is essential in proving its ability to correctly determine fracture density and to identify the appropriate fracture azimuth. When using a synthetic dataset, one knows the parameters used in its creation – in this case fracture orientation and fracture density are the parameters of interest – and thus one can compare the predicted values generated by the analysis to the real values used in generating the data. In this study, I used a program called ANIVEC to generate synthetic data.

ANIVEC is “A Reflectivity Program for Computing Synthetic Seismograms for Stratified Anisotropic Media” which uses propagator matrix theory to simulate ground motion at user-defined receiver locations. The model used in generating this synthetic data was a simple two-layer model, consisting of an isotropic upper layer and an anisotropic lower layer, as seen in Figure 5.3. Figure 5.3 indicates the properties of the upper (isotropic) layer used for all scenarios. Inputs to the program were the source type, receiver layout, and elastic stiffness tensor, density, thickness and attenuation coefficient for each layer. Quality factor (Q), which describes attenuation, was set to 500 for all cases. A 101x101 grid of receivers was used, spanning one kilometer in the positive and negative inline and crossline directions relative to the shot location. The source is located in the exact center of the receiver grid. An explosive source was used. The elastic stiffness tensor(s) of the lower anisotropic (fractured) layer were generated using Linear Slip Deformation theory as described in Section 3.4 and as shown in Equation 3.67. Fracture weaknesses were calculated in terms of fracture density (e) using Equations 5.29 – 5.31.

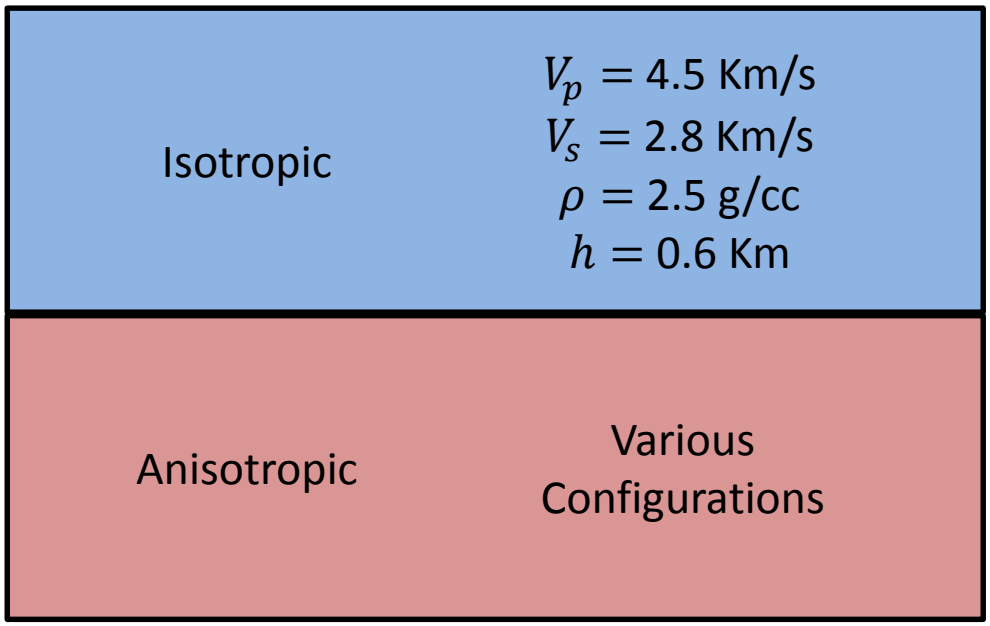

Figure 5.3: A diagram depicting the two layer model used in generating the synthetic data. P-wave velocity (V_p), S-wave velocity (V_s), density (ρ) and thickness (h) for the upper isotropic layer are shown.

A variety of anisotropic lower layers were used to simulate situations that were roughly characteristic of the Haynesville Shale. In particular, four different parameters were considered: background elastic properties (3 cases), fluid type (2 cases), degree of fracturing (2 cases), fracture azimuth (2 cases). Refer to Table 5.1 for more information regarding these properties. Recall that an isotropic background rock that has been fractured becomes effective HTI anisotropic, and a VTI background rock that has been fractured becomes effective orthorhombic anisotropic. In all cases where fracture azimuth is not 0 degrees, the method of rotating tensors described in Section 3.3 was applied. Combined, these amount to 24 different synthetic cases. These cases help to ensure that fracture density and fracture azimuth can be correctly determined under a wide range of possible scenarios. The elastic background properties used in synthetic data generation were loosely based on the work of Sone and Zoback (2013), who measured some of the

elastic properties of the Haynesville Shale. Additional synthetic data were generated for the orthorhombic case with high fracture density. In these additional cases, synthetic data were generated for all azimuths between 0 and 180 degrees in 10 degree increments, for both gas and fluid filled fractures, resulting in 38 additional synthetic cases and a total of 62 synthetic cases. These additional cases serve to ensure that fracture azimuth can be determined correctly for any possible azimuth. These added cases additionally help to prove that fracture azimuth can be correctly determined in orthorhombic media using equations which are technically only valid in HTI media.

Property	**Cases**
Background Elastic Tensor	Isotropic (a) Isotropic (b) VTI
Fluid Type	Fluid Filled Gas Filled
Degree of Fracturing	Strong ($e = 0.1$) Weak ($e = 0.02$)
Fracture Azimuth	0 Degrees 135 Degrees
Fracture Azimuth*	0 to 180 Degrees in 10 Degree Increments (Orthorhombic / Strong Fracturing Cases Only)

Table 5.1: A table showing the different properties associated with the 62 synthetic cases generated and used in this study. e represents fracture density.

After data were generated, it was lightly processed prior to being analyzed for fracture characteristics. Initially, data were imported to MATLAB © and a quality control check was performed. After data were imported to MATLAB © and passed a quality control check, NMO and trim statics corrections were performed. The NMO correction was performed using the standard hyperbolic moveout equation, and the trim statics correction examined traces for a limited number of time shifts and looked for maximum cross correlation. Combined, these shift the data such that it results in almost perfectly flat horizons. Due to the simplicity of this example, circular shifting of traces were used in both the NMO correction and the trim statics correction. After the data had been flattened, they were grouped into an azimuthal gather based on incident angle and azimuth. Azimuths ranged from 0 to 180 degrees in 15 degree increments, and incident angles ranged from 5 to 40 degrees in 5 degree increments. After azimuthal sorting had been completed, the data were ready to be input into the fracture characterization algorithm described in Section 5.3 of this chapter. Note that the binning scheme had to be adjusted slightly from what was described in Section 5.3. I developed all MATLAB © codes relating to data input, NMO correction, trim statics correction and azimuthal binning. Example data slices from before and after applying these pre-processing steps can be seen in Figure 5.4.

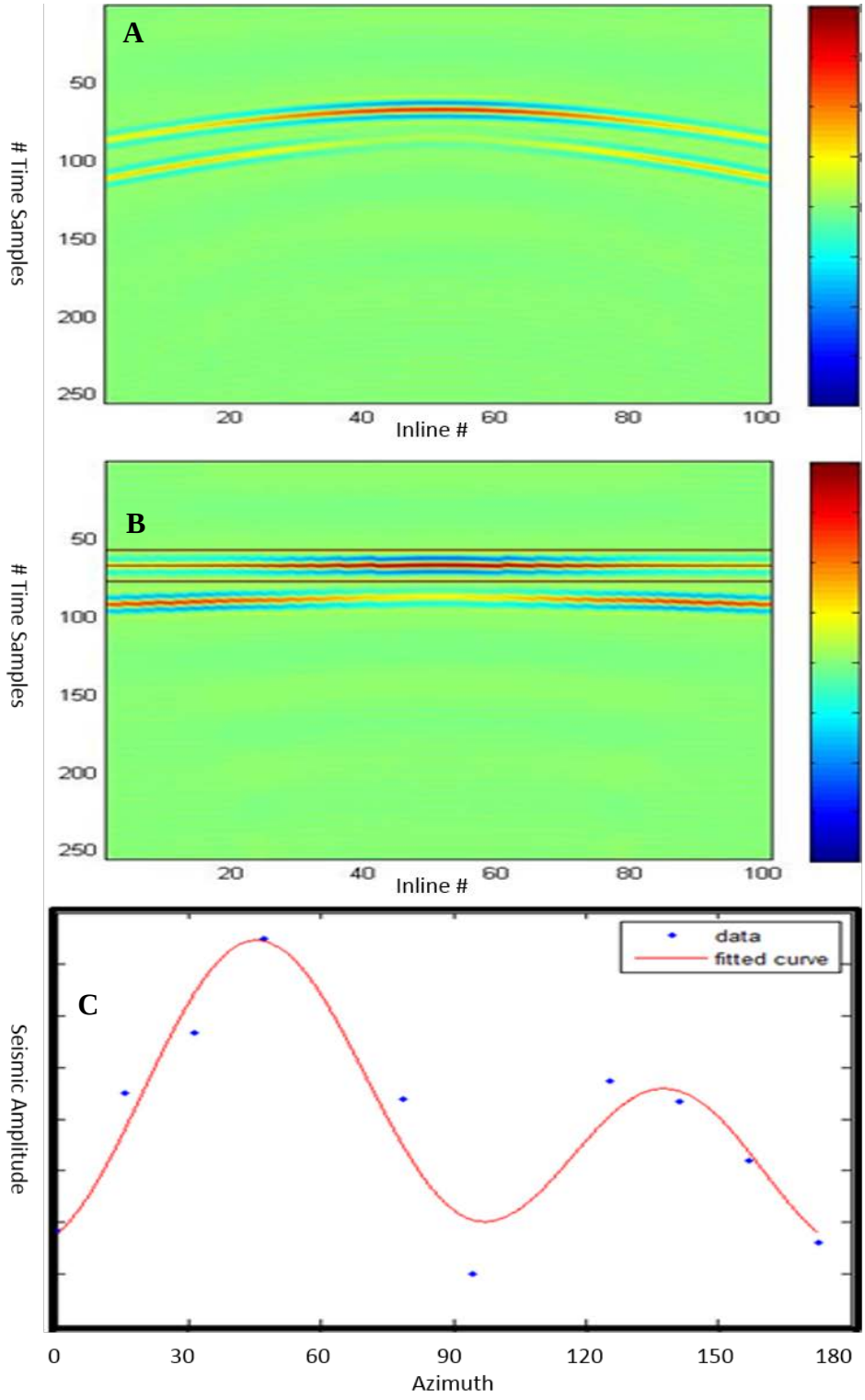

Figure 5.4: A) An example data slice of a synthetic dataset without any processing

performed. The horizontal axis represents position, the vertical axis represents time, and color represents seismic amplitude. The upper event represents the P-P reflection data which was used in this study. The lower event represents the P-S reflection which was not used.

B) An example data slice of a synthetic dataset with NMO correction and trim statics corrections performed. The horizontal axis represents position, the vertical axis represents time, and color represents seismic amplitude. The black horizontal lines are plot guides to indicate how flat the data is, however are not data themselves. The upper event represents the P-P reflection data which was used in this study. The lower event represents the P-S reflection which was not used.

C) An example section of an azimuthal gather at some time, incident angle and position. The horizontal axis represents azimuth and ranges from 0 to 180 degrees. The vertical axis represents seismic amplitude. The blue dots are individual data points and the red line is the Fourier series that the fracture characterization algorithm generates.

5.5 RESULTS

In this section I present the inversion results for fracture azimuth and fracture density. Inversion results from both the synthetic dataset and from real Haynesville data are presented. Results from fracture azimuth inversion will be presented first, followed by results from the fracture density inversion. For each set of results the synthetic example will be presented first, in order to demonstrate proof of concept.

5.5.1 Synthetic Example – Fracture Azimuth

Histograms of inverted fracture azimuth from the 24 initial synthetic cases can be seen in Figures 5.5 – 5.8. Figures 5.5 and 5.6 depict the combined results from all cases where true fracture azimuth is 0 degrees (which is identical to 180 degrees). Figures 5.7 and 5.8 depict the combined results from all cases where true fracture azimuth is 135 degrees. In these histograms the horizontal axis represents azimuth and ranges from 0 to 180 degrees, and the vertical axis represents bin count. In these figures each bin represents 5 degrees of azimuth. Figures 5.5 and 5.7 show data from all incident angles, while Figures 5.6 and 5.8 show only large offset data (incident angle > 30 degrees) results.

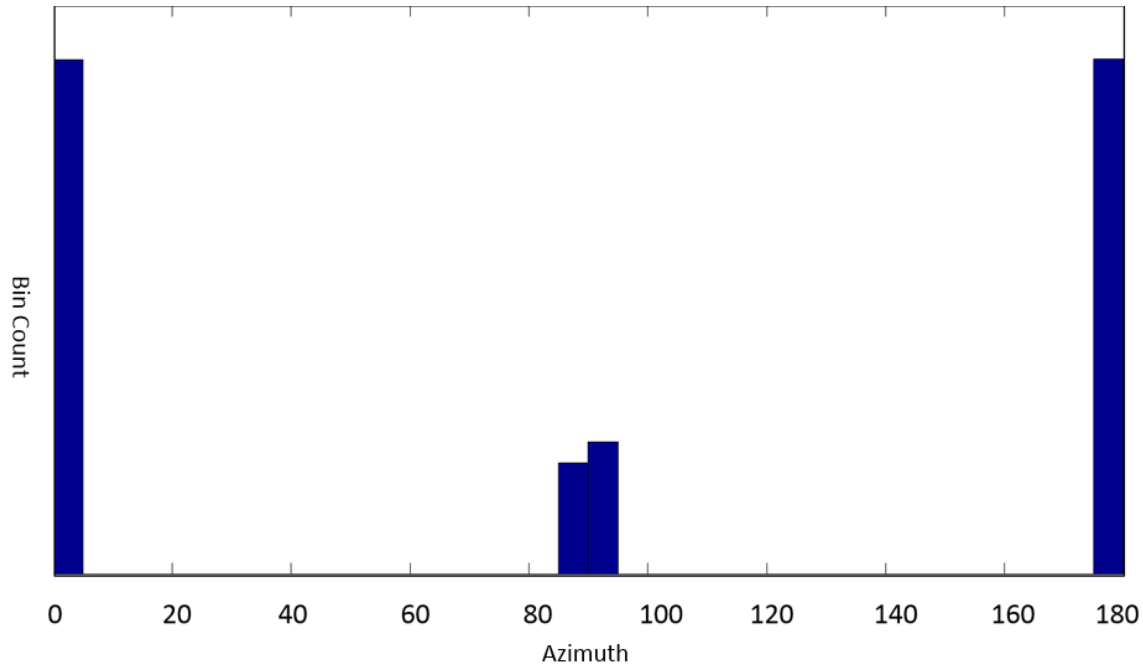

Figure 5.5: A histogram showing the combined results of fracture azimuth inversion for the 12 synthetic cases where the true fracture azimuth is 0 degrees. Note that 0 and 180 degrees represent the same azimuth. The horizontal axis represents azimuth and ranges from 0 to 180 degrees, and the vertical axis represents bin count. Each bin represents 5 degrees of azimuth. Data from all incident angles are shown.

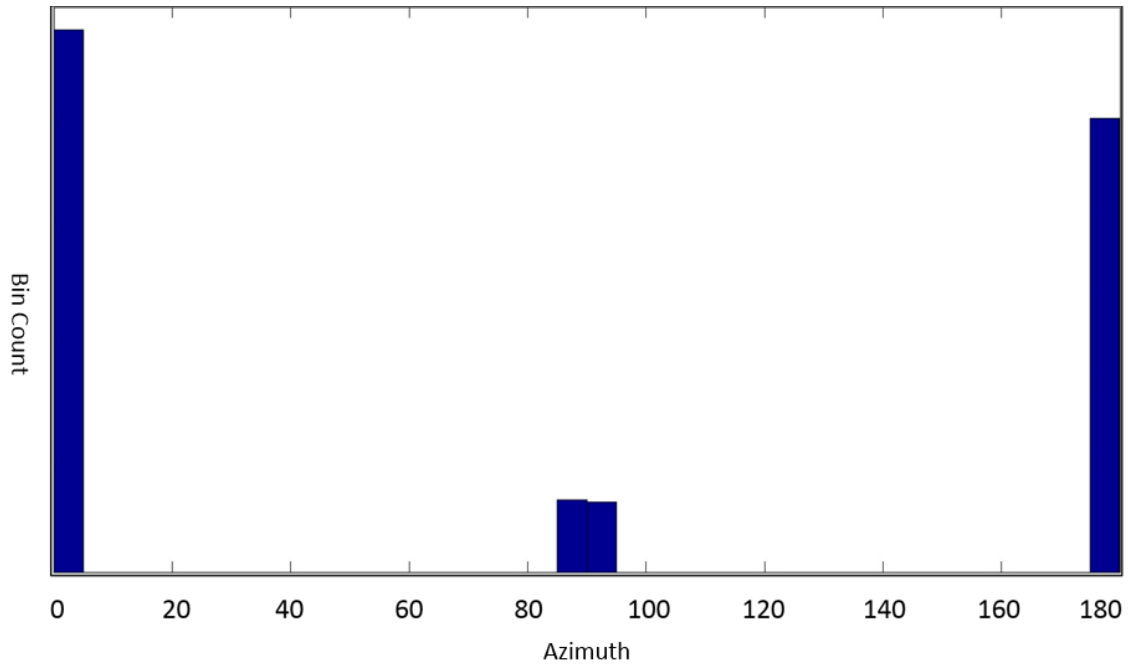

Figure 5.6: A histogram showing the combined results of fracture azimuth inversion for the 12 synthetic cases where the true fracture azimuth is 0 degrees. Note that 0 and 180 degrees represent the same azimuth. The horizontal axis represents azimuth and ranges from 0 to 180 degrees, and the vertical axis represents bin count. Each bin represents 5 degrees of azimuth. Only data corresponding to large offsets (incident angle > 30 degrees) is shown.

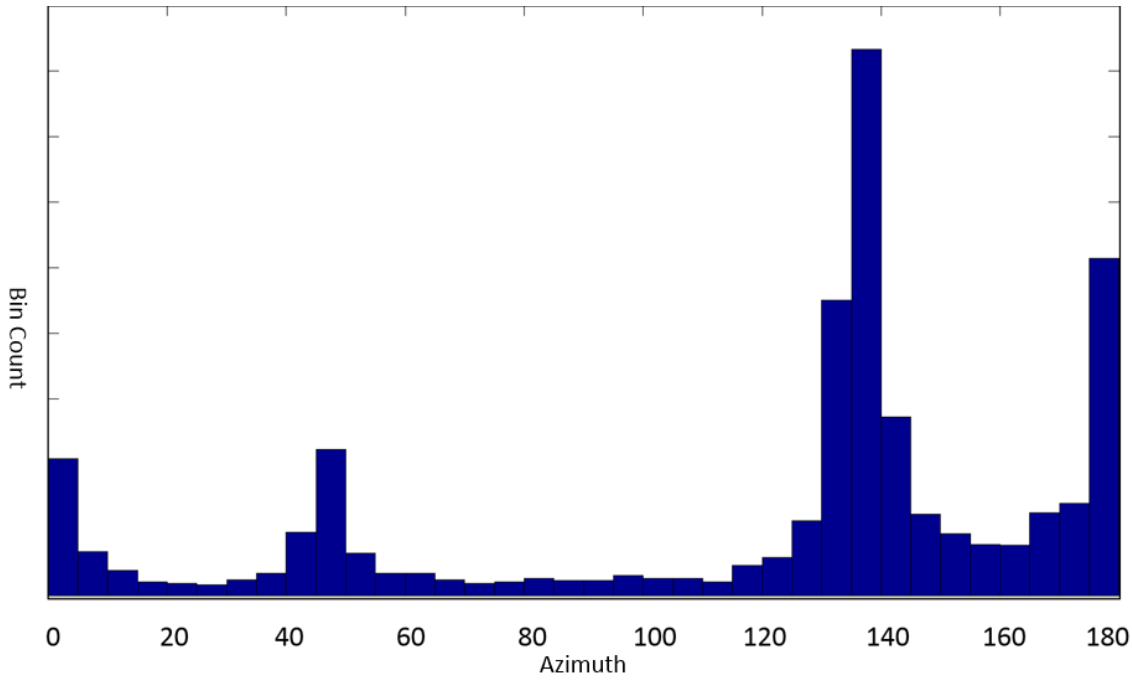

Figure 5.7: A histogram showing the combined results of fracture azimuth inversion for the 12 synthetic cases where the true fracture azimuth is 135 degrees. The horizontal axis represents azimuth and ranges from 0 to 180 degrees, and the vertical axis represents bin count. Each bin represents 5 degrees of azimuth. Data from all incident angles are shown.

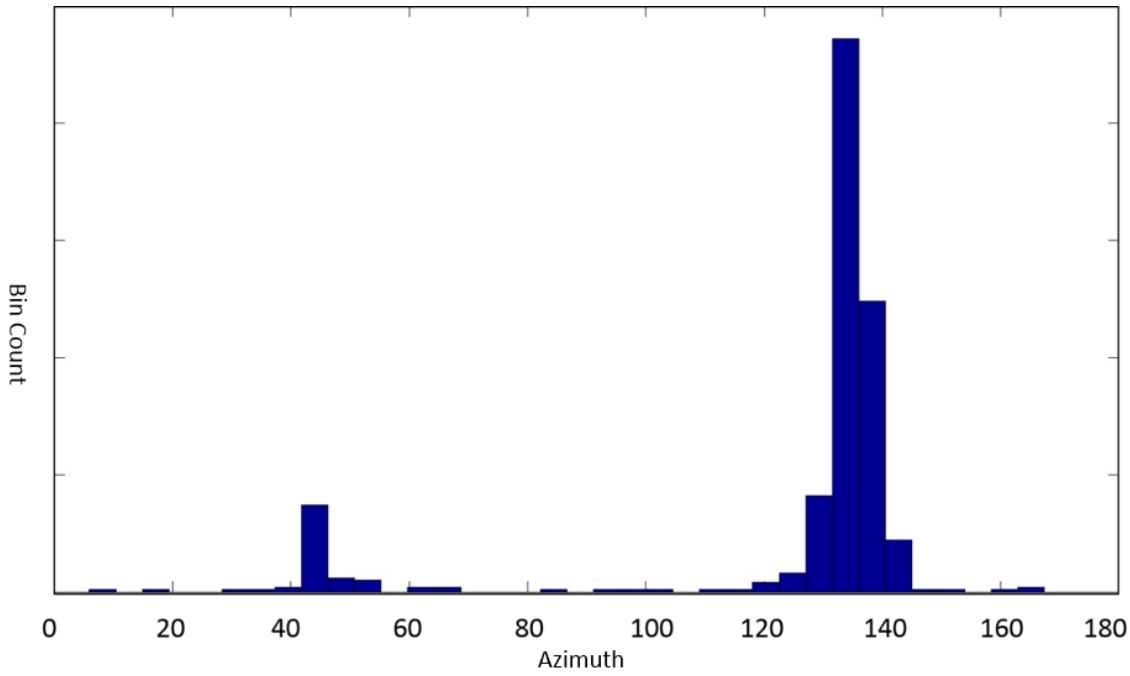

Figure 5.8: A histogram showing the combined results of fracture azimuth inversion for the 12 synthetic cases where the true fracture azimuth is 135 degrees. The horizontal axis represents azimuth and ranges from 0 to 180 degrees, and the vertical axis represents bin count. Each bin represents 5 degrees of azimuth. Only data corresponding to large offsets (incident angle > 30 degrees) is shown.

Inversion results from the 36 synthetic cases with azimuths ranging between 0 and 180 degrees in 10 degree increments are displayed in Table 5.2. All 36 synthetic examples represent the orthorhombic case with high fracture density. Results for both gas and fluid filled fractures are presented. In these cases it was presumed that the calculated azimuth was correct if the inverted azimuth was within 5 degrees of the true azimuth. For example, if the true azimuth is 70 degrees any inverted azimuth results between 65 degrees and 75 degrees would be considered correct, while all other result would be considered incorrect. Results are shown for all incident angles as well as for incident

angles greater than or equal to 30 degrees. Average results have been calculated, and the worst case scenario has been identified.

Table 5.2

True Azimuth	Fluid Type	Percent correct	Percent Correct (far offset)
0	Dry / Gas	70.8%	88.1%
	Wet	97.0%	95.2%
10	Dry / Gas	35.1%	81.0%
	Wet	67.9%	92.9%
20	Dry / Gas	32.7%	83.3%
	Wet	57.7%	92.9%
30	Dry / Gas	29.8%	88.1%
	Wet	54.8%	92.9%
40	Dry / Gas	29.8%	85.7%
	Wet	51.8%	92.9%
50	Dry / Gas	31.0%	85.7%
	Wet	51.2%	92.9%
60	Dry / Gas	31.0%	85.7%
	Wet	48.2%	90.5%
70	Dry / Gas	33.9%	83.3%
	Wet	50.6%	92.9%
80	Dry / Gas	35.1%	83.3%
	Wet	56.0%	92.9%
90	Dry / Gas	48.8%	88.1%
	Wet	69.6%	95.2%
100	Dry / Gas	35.1%	83.3%
	Wet	56.0%	92.9%
110	Dry / Gas	33.9%	83.3%
	Wet	50.6%	92.9%
120	Dry / Gas	31.0%	85.7%
	Wet	48.2%	90.5%
130	Dry / Gas	31.0%	85.7%
	Wet	51.2%	92.9%
140	Dry / Gas	29.8%	85.7%
	Wet	51.8%	92.9%
150	Dry / Gas	29.8%	88.1%
	Wet	54.8%	92.9%

True Azimuth	Fluid Type	Percent correct	Percent Correct (far offset)
160	Dry / Gas	32.7%	83.3%
	Wet	57.7%	92.9%
170	Dry / Gas	35.1%	81.0%
	Wet	67.9%	92.9%
180	Dry / Gas	70.8%	88.1%
	Wet	97.0%	95.2%
Average	Dry / Gas	37.22%	85.09%
	Wet	59.99%	92.98%
	Overall	48.61%	89.04%
Worst Case Scenario	Dry / Gas	29.76%	80.95%
	Wet	48.21%	90.48%
	Overall	29.76%	80.95%

Table 5.2: A table summarizing the results of the 38 synthetic cases with fracture azimuth ranging from 0 to 180 degrees in 10 degree increments. All cases represent the case of orthorhombic anisotropy and high fracture density. The inverted azimuth is considered correct if it lies within 5 degrees of the true azimuth. The column titled “Percent Correct” represents all data, and the column titled “Percent Correct (far offset)” represents data with an incident angle of greater than or equal to 30 degrees.

The results presented in this section are discussed in Section 5.6 of this Chapter. To summarize, it appears clear that this method is able to distinguish the correct fracture azimuth in a variety of cases with sufficient confidence. This is especially true when considering the results associated only with large angles of incidence. There is some variability in results, but when plotting a histogram of the inverted azimuth results, the correct azimuth is easily identifiable due to having the highest bin count. Thus, I feel confident in moving forward and applying this method to data from the Haynesville Shale.

5.5.2 Haynesville Data – Fracture Azimuth

Figures 5.9 – 5.11 display histograms of the inverted fracture azimuths calculated throughout the entire Haynesville dataset. Figure 5.9 shows a histogram of all available data. Figure 5.10 shows a histogram of data which corresponds to an incident angle of 25 degrees or higher. Figure 5.11 shows a histogram of data which corresponds to an incident angle of 33 degrees or higher. In all histograms the horizontal axis represents azimuth and ranges from 0 to 180 degrees.

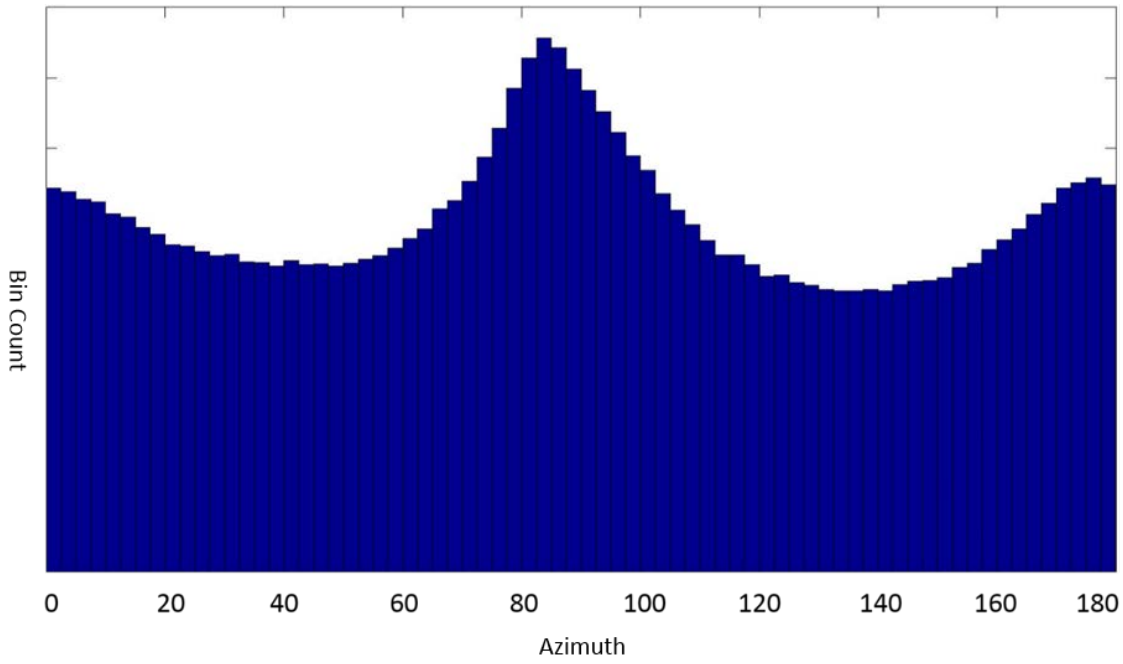

Figure 5.9: A histogram showing the combined results of fracture azimuth inversion for the Haynesville dataset. The horizontal axis represents azimuth and ranges from 0 to 180 degrees, and the vertical axis represents bin count. Each bin represents 2.5 degrees of azimuth. Data corresponding to all incident angles are shown.

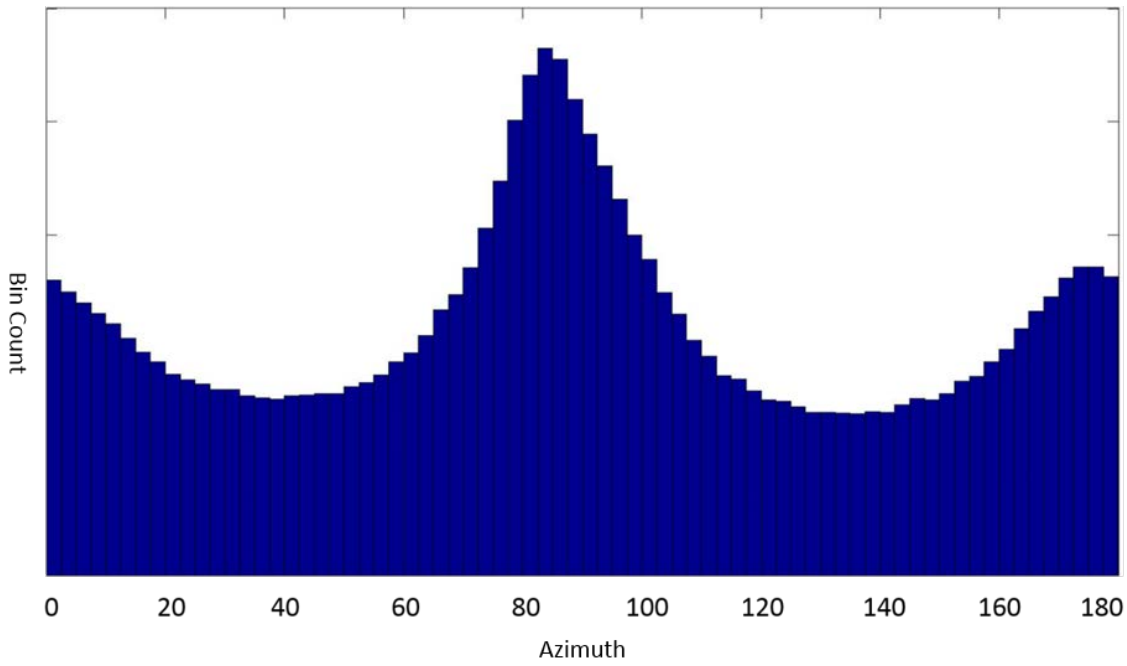

Figure 5.10: A histogram showing the combined results of fracture azimuth inversion for the Haynesville dataset. The horizontal axis represents azimuth and ranges from 0 to 180 degrees, and the vertical axis represents bin count. Each bin represents 2.5 degrees of azimuth. Data corresponding to incident angles greater than or equal to 25 degrees are shown.

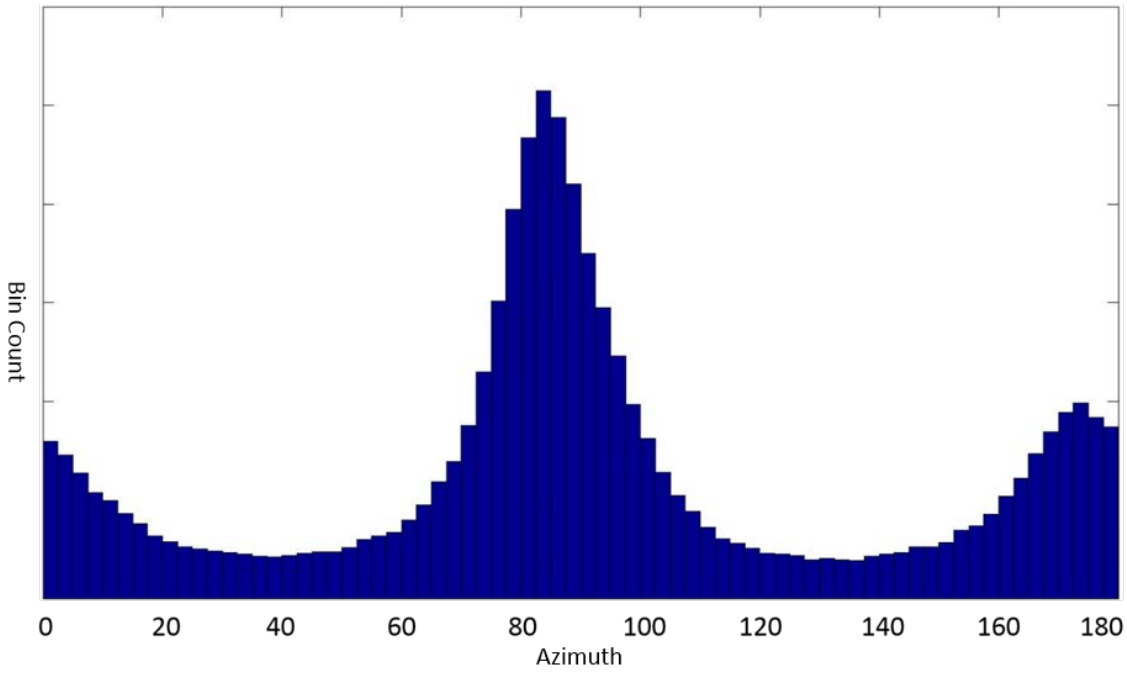

Figure 5.11: A histogram showing the combined results of fracture azimuth inversion for the Haynesville dataset. The horizontal axis represents azimuth and ranges from 0 to 180 degrees, and the vertical axis represents bin count. Each bin represents 2.5 degrees of azimuth. Data corresponding to incident angles greater than or equal to 33 degrees are shown.

All subsequent images of fracture azimuth calculated using the proposed method described in this chapter show averaged results from far incident angles (greater than or equal to 25 degrees). Averaging was performed using the Yamartino Method. Due to the fact that near incident angle information in not as reliable in determining fracture azimuth, inversion results from near incident angles will not be presented. Vertically averaged values for fracture orientation can be seen in Figure 5.12. For comparison, vertically averaged results from the novel method described in this chapter and results from the Fourier coefficient based HTI method described in Chapter 4 using an identical binning scheme can be seen in Figure 5.13. Fracture Azimuth results range from -90 to 90 degrees. Note that both -90 degrees (represented by dark blue) and 90 degrees

(represented by dark red) indicate an identical azimuth, corresponding to approximately east-west. The black arrows indicate the direction of north. All images share the same orientation.

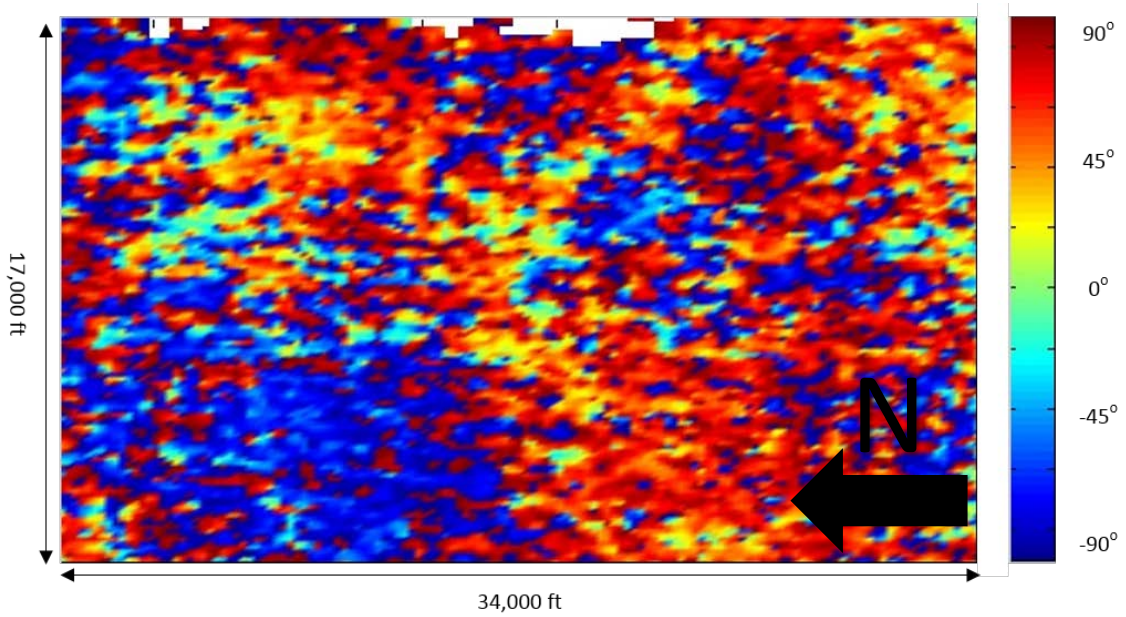

Figure 5.12: Fracture azimuth, as calculated by the proposed new Fourier coefficient decomposition method. 2-D lateral smoothing has been applied. Values have been vertically averaged throughout the Haynesville using the Yamartino method. The colorbar ranges from -90 degrees to 90 degrees. The black arrow indicates the direction of north.

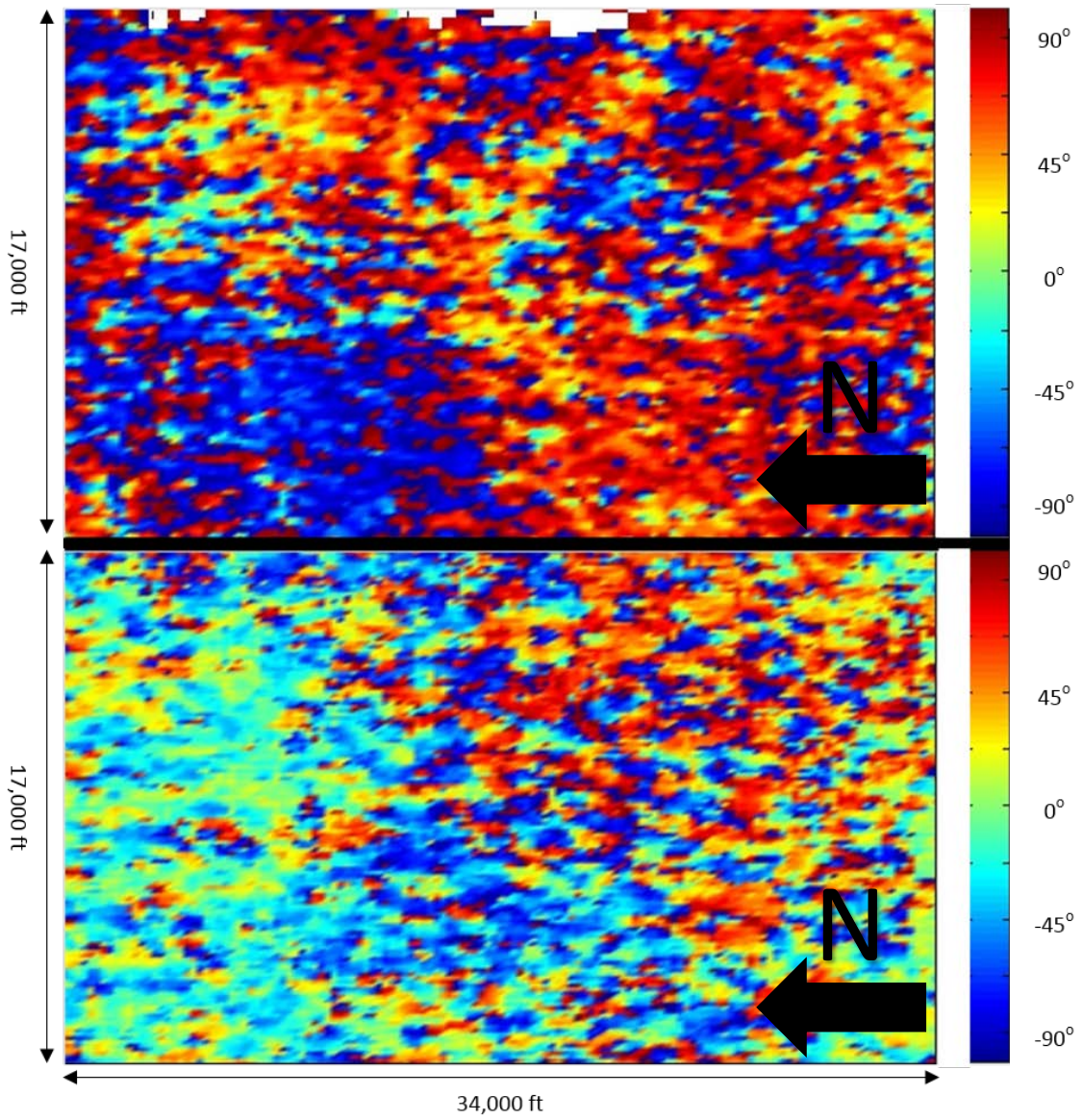

Figure 5.13: Comparison of fracture orientation as calculated by the proposed new method and the HTI Fourier coefficient decomposition based method. The top image depicts fracture orientation as calculated by the proposed new Fourier coefficient decomposition method. Data from large incident angles have been averaged, and 2-D lateral smoothing has been applied. The bottom image depicts fracture orientation as calculated by the HTI Fourier coefficient decomposition method using the phase of the r_2 Fourier coefficient. Values have been vertically averaged throughout the Haynesville using the Yamartino method. Colorbars range from -90 degrees to 90 degrees. The black arrows indicate the direction of north.

Fracture orientation results from a constant time slice that encompasses the entire Haynesville can be seen in Figure 5.14. For comparison, fracture orientation results over the same time slice from the method described in this chapter and the Fourier coefficient based HTI method described in Chapter 4 using an identical binning scheme can be seen in Figure 5.15. Fracture azimuth results range from -90 to 90 degrees. Note that both -90 degrees (represented by dark blue) and 90 degrees (represented by dark red) indicate an identical azimuth, corresponding to approximately east-west. The black arrows indicate the direction of north. All images share the same orientation.

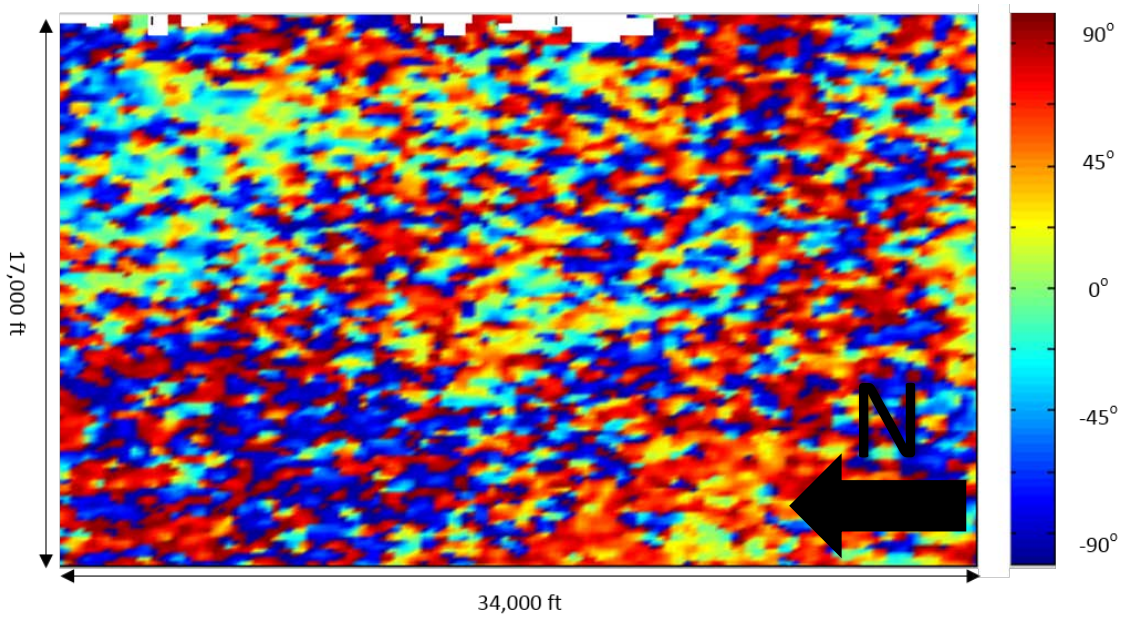

Figure 5.14: Fracture azimuth, as calculated by the proposed new Fourier coefficient decomposition method. Data from large incident angles have been averaged, and 2-D lateral smoothing has been applied. Values corresponding to a constant time of 2060 ms are shown. The colorbar ranges from -90 degrees to 90 degrees. The black arrow indicates the direction of north.

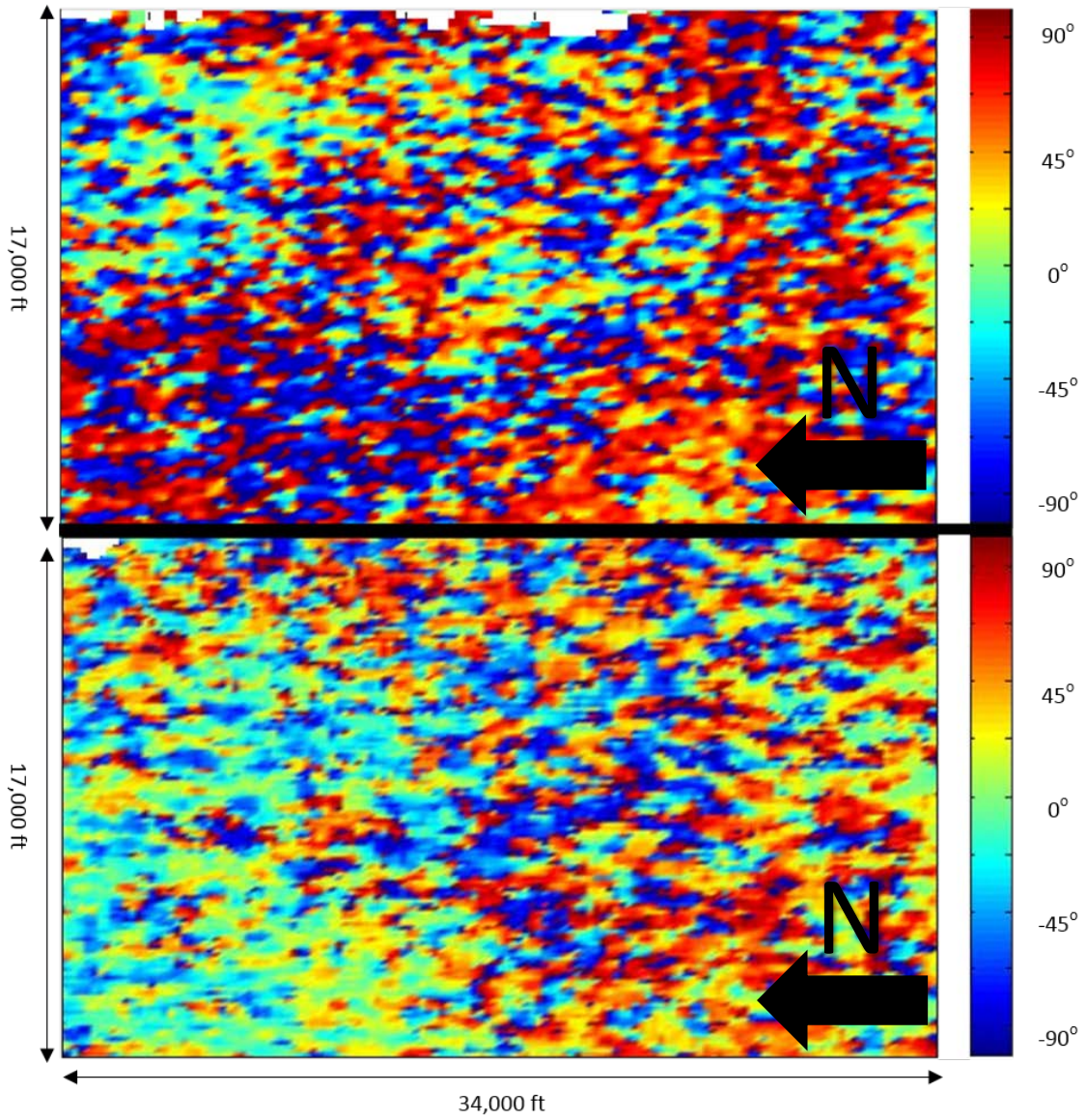

Figure 5.15: Comparison of fracture orientation as calculated by the proposed new method and the HTI Fourier coefficient decomposition based method. The top image depicts fracture orientation as calculated by the proposed new Fourier coefficient decomposition method. Data from large incident angles have been averaged, and 2-D lateral smoothing has been applied. The bottom image depicts fracture orientation as calculated by the HTI Fourier coefficient decomposition method using the phase of the r_2 Fourier coefficient. Values corresponding to a constant time of 2060 ms are shown. Colorbars range from -90 degrees to 90 degrees. The black arrows indicate the direction of north.

Fracture orientation results from constant depth slices representing 0m, 15m, 30m and 45m from the Haynesville top can be seen in Figures 5.16 – 5.19. "Constant depth" was determined by measuring a constant number of time samples from the top of the Haynesville. A comparison of results over the same depth slices from the novel method described in this chapter and the Fourier coefficient method described in Chapter 4 using an identical binning scheme can be seen in Figures 5.20 – 5.23. Fracture azimuth results range from -90 to 90 degrees. Note that both -90 degrees (represented by dark blue) and 90 degrees (represented by dark red) indicate an identical azimuth, corresponding to approximately east-west. The black arrows indicate the direction of north. All images share the same orientation.

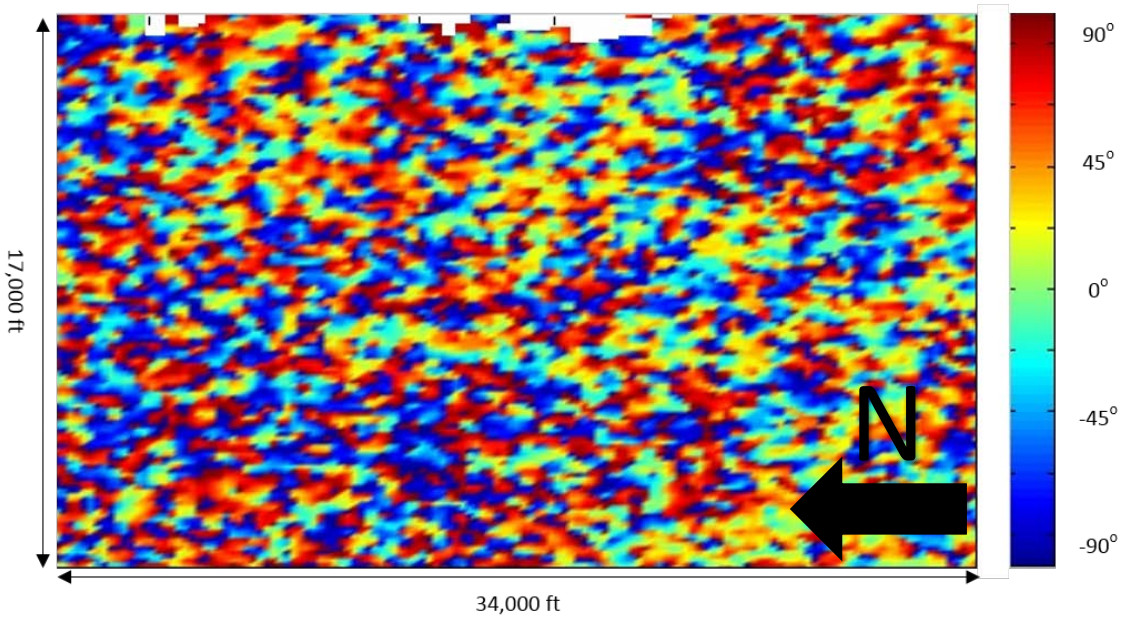

Figure 5.16: Fracture azimuth, as calculated by the proposed new Fourier coefficient decomposition method. 2-D lateral smoothing has been applied. Values corresponding to the top of the Haynesville are shown. The colorbar ranges from -90 degrees to 90 degrees. The black arrow indicates the direction of north.

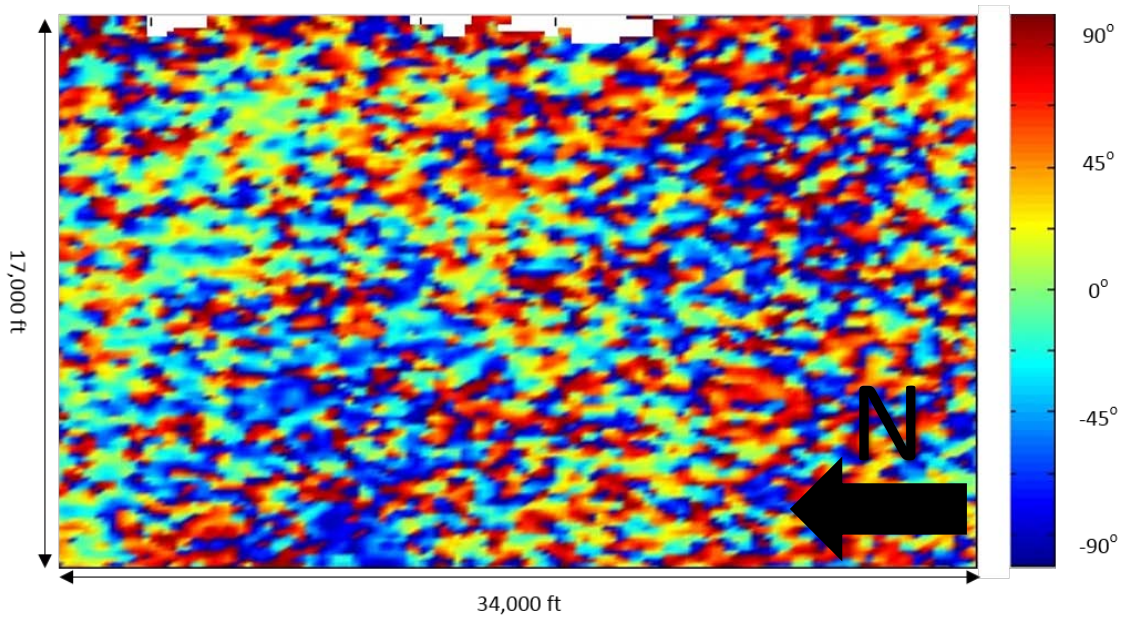

Figure 5.17: Fracture azimuth, as calculated by the proposed new Fourier coefficient decomposition method. 2-D lateral smoothing has been applied. Values corresponding to approximately 15 m from the top of the Haynesville are shown. The colorbar ranges from -90 degrees to 90 degrees. The black arrow indicates the direction of north.

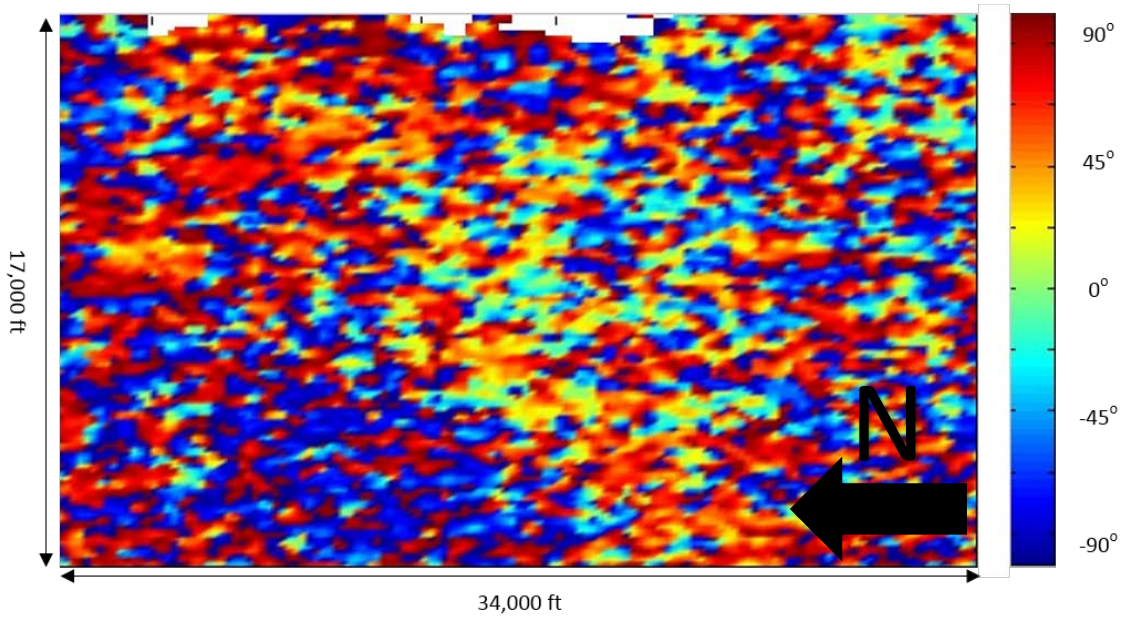

Figure 5.18: Fracture azimuth, as calculated by the proposed new Fourier coefficient decomposition method. 2-D lateral smoothing has been applied. Values corresponding to approximately 30 m from the top of the Haynesville are shown. The colorbar ranges from -90 degrees to 90 degrees. The black arrow indicates the direction of north.

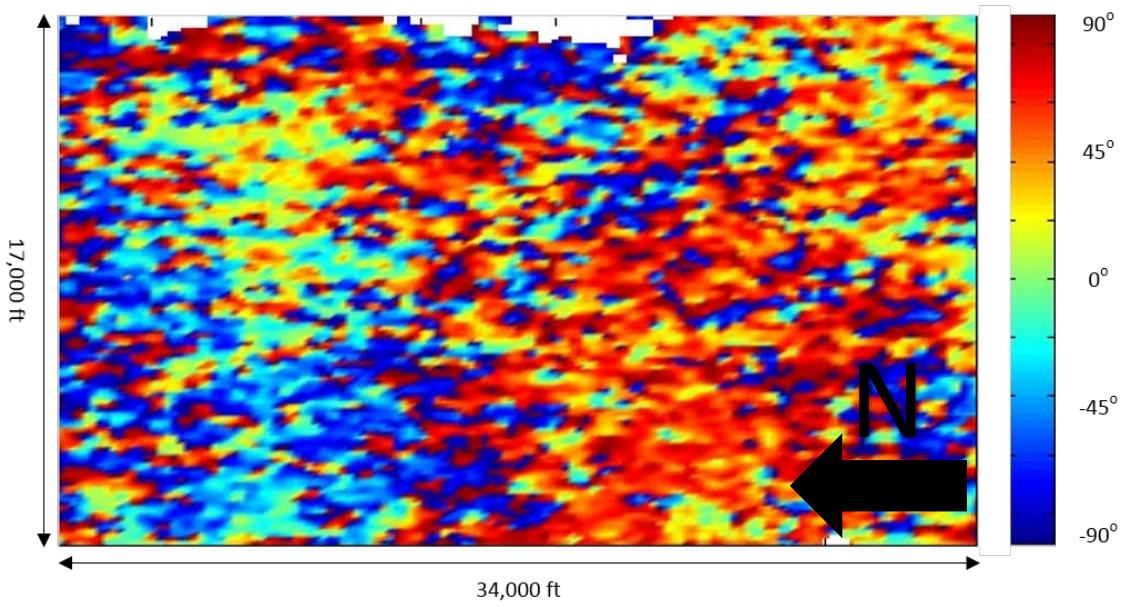

Figure 5.19: Fracture azimuth, as calculated by the proposed new Fourier coefficient decomposition method. 2-D lateral smoothing has been applied. Values corresponding to approximately 45 m from the top of the Haynesville are shown. The colorbar ranges from -90 degrees to 90 degrees. The black arrow indicates the direction of north.

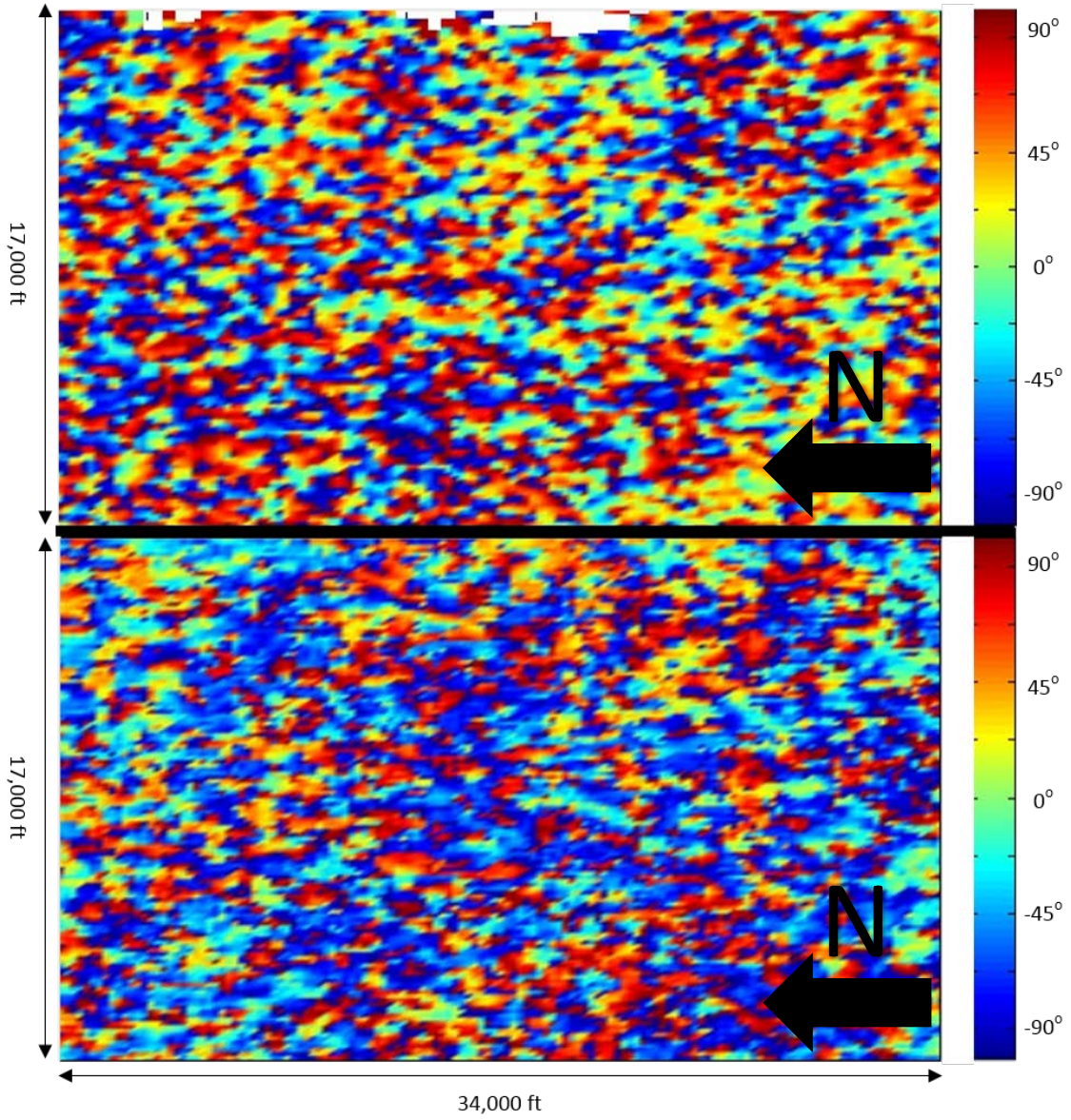

Figure 5.20: Comparison of fracture orientation as calculated by the proposed new method and the HTI Fourier coefficient decomposition based method. The top image depicts fracture orientation as calculated by the proposed new Fourier coefficient decomposition method. 2-D lateral smoothing has been applied. The bottom image depicts fracture orientation as calculated by the HTI Fourier coefficient decomposition method using the phase of the r_2 Fourier coefficient. Values corresponding to the top of the Haynesville are shown. Colorbars range from -90 degrees to 90 degrees. The black arrows indicate the direction of north.

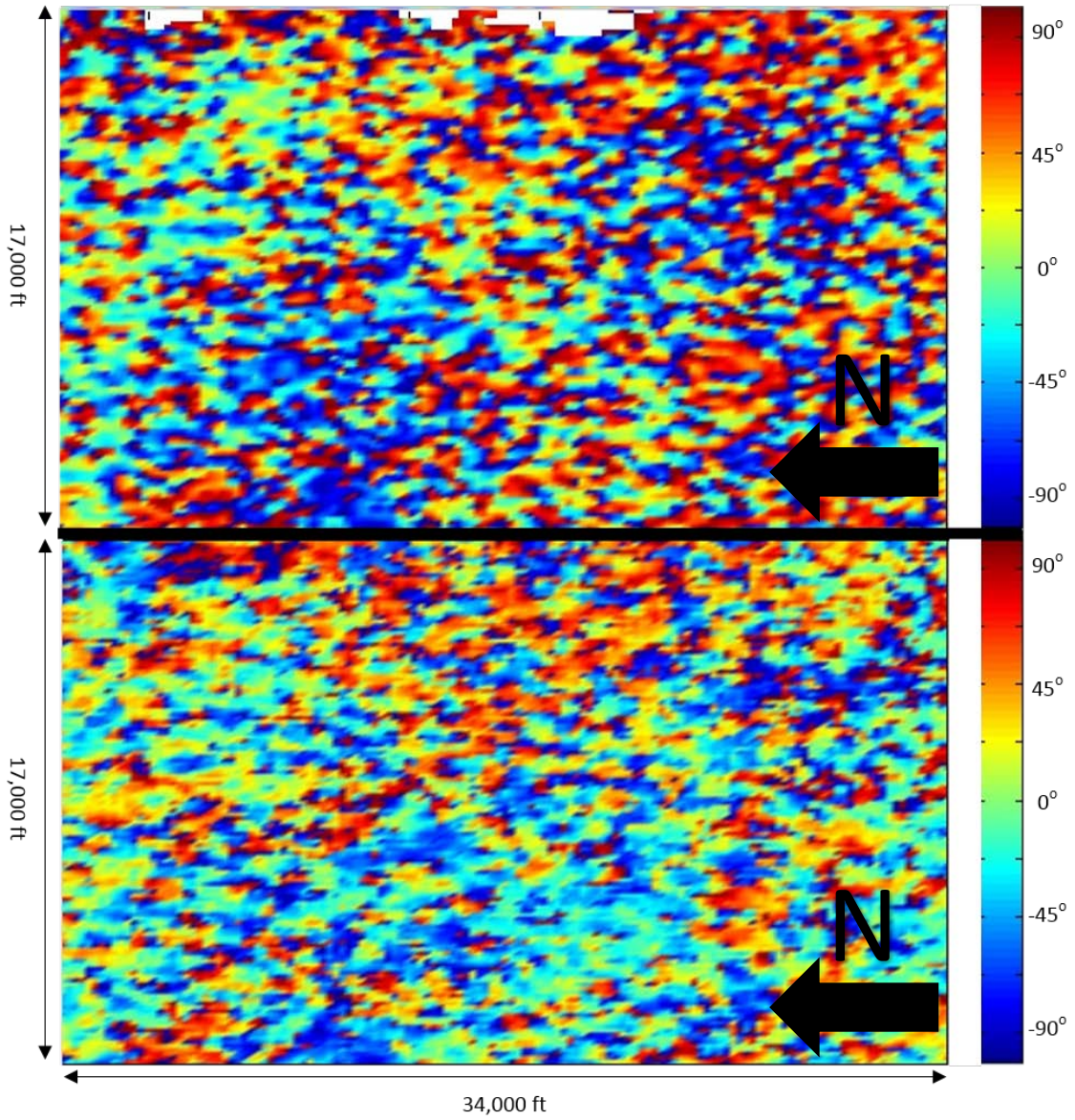

Figure 5.21: Comparison of fracture orientation as calculated by the proposed new method and the HTI Fourier coefficient decomposition based method. The top image depicts fracture orientation as calculated by the proposed new Fourier coefficient decomposition method. 2-D lateral smoothing has been applied. The bottom image depicts fracture orientation as calculated by the HTI Fourier coefficient decomposition method using the phase of the r_2 Fourier coefficient. Values corresponding to approximately 15 m from the top of the Haynesville are shown. Colorbars range from -90 degrees to 90 degrees. The black arrows indicate the direction of north.

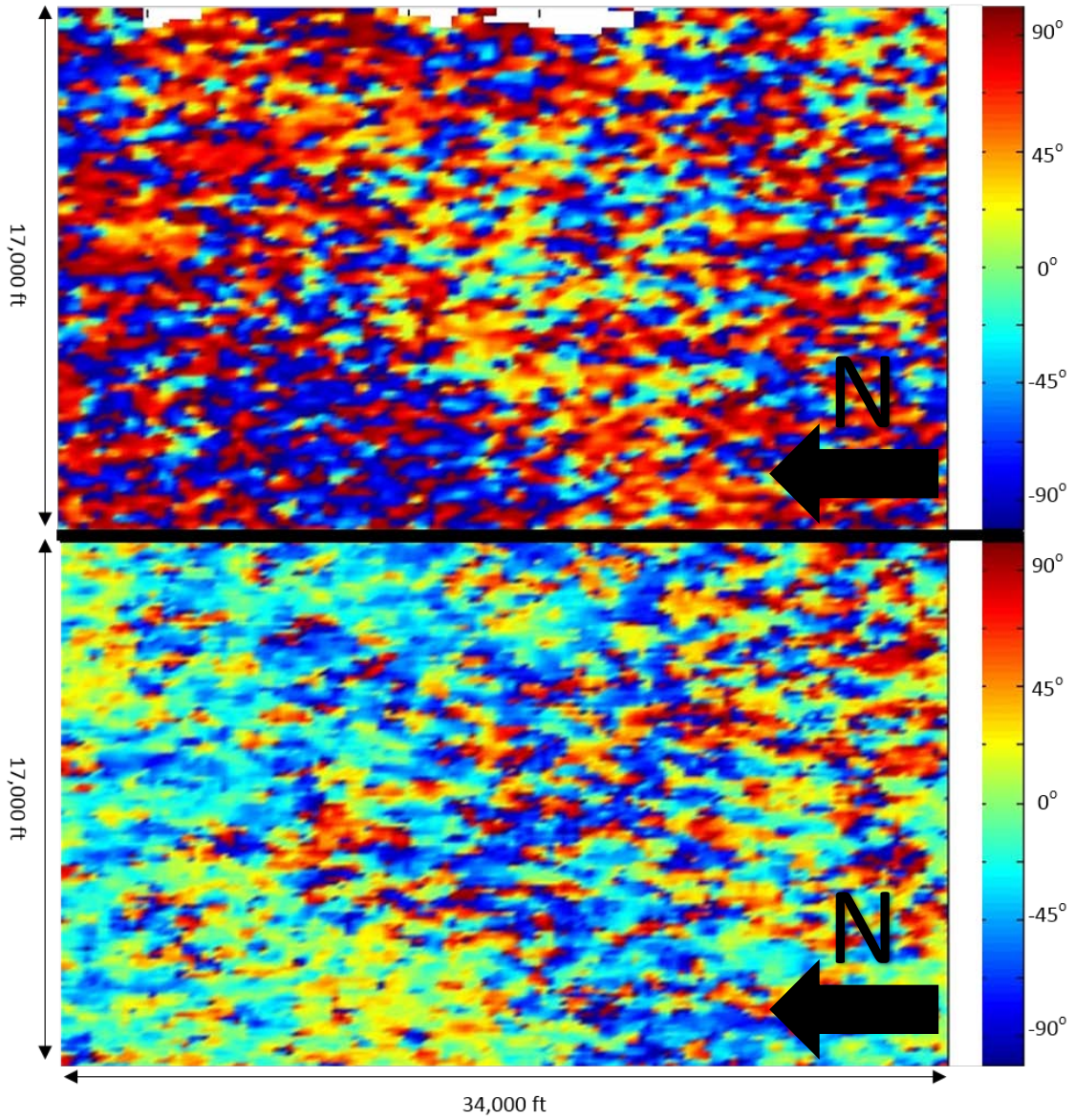

Figure 5.22: Comparison of fracture orientation as calculated by the proposed new method and the HTI Fourier coefficient decomposition based method. The top image depicts fracture orientation as calculated by the proposed new Fourier coefficient decomposition method. 2-D lateral smoothing has been applied. The bottom image depicts fracture orientation as calculated by the HTI Fourier coefficient decomposition method using the phase of the r_2 Fourier coefficient. Values corresponding to approximately 30 m from the top of the Haynesville are shown. Colorbars range from -90 degrees to 90 degrees. The black arrows indicate the direction of north.

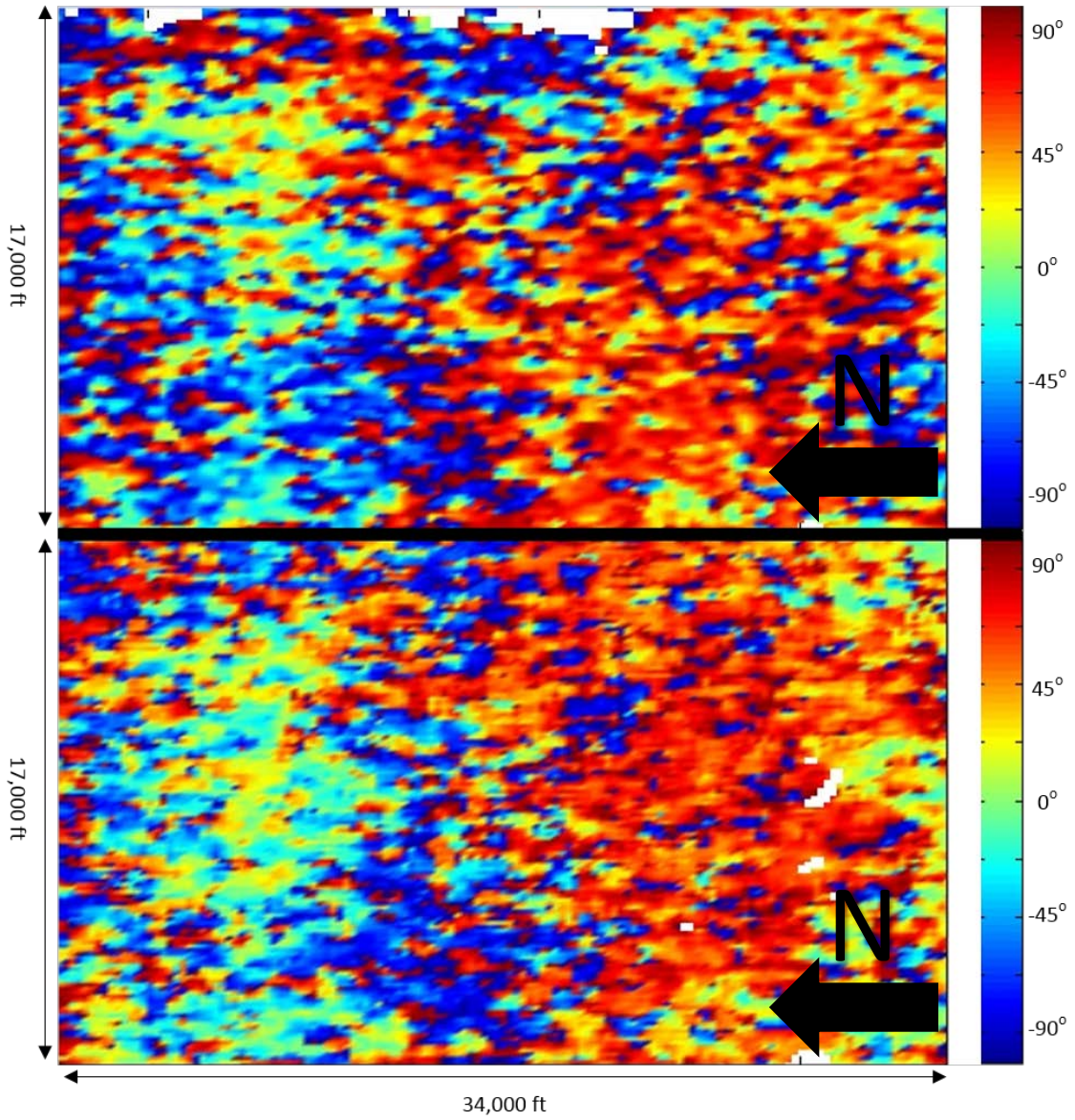

Figure 5.23: Comparison of fracture orientation as calculated by the proposed new method and the HTI Fourier coefficient decomposition based method. The top image depicts fracture orientation as calculated by the proposed new Fourier coefficient decomposition method. 2-D lateral smoothing has been applied. The bottom image depicts fracture orientation as calculated by the HTI Fourier coefficient decomposition method using the phase of the r_2 Fourier coefficient. Values corresponding to approximately 45 m from the top of the Haynesville are shown. Colorbars range from -90 degrees to 90 degrees. The black arrows indicate the direction of north.

The results presented in this section are discussed in Section 5.6 of this Chapter. To summarize, it appears that the primary fracture azimuth in the Haynesville is approximately orientated at 85 degrees, as is evident in Figures 5.10 and 5.11. This is very close to the special case of fracture azimuth equaling 90 degrees. Thus, as discussed earlier in this chapter, the algorithm used to calculate fracture density was adjusted to assume a fracture azimuth of 90 degrees.

5.5.3 Synthetic Example – Fracture Density

The results of applying the fracture density inversion to 24 synthetic data cases can be seen in Table 5.3. In Table 5.3 primary sorting is by fracture azimuth, secondary sorting is by fracture fluid and tertiary sorting is by anisotropy type. Inverted absolute values for the fracture density attribute R_2^* for both high and low fracture density cases are shown. Note that values of R_2^* should be treated as relative – this attribute is designed to be a proxy for fracture density which can distinguish areas of relatively high fracture density, but it is not capable of determining the true fracture density (i.e. the number of fractures per unit length). In order to distinguish if the algorithm can correctly determine higher fracture density, a multiplier attribute is calculated. The multiplier attribute shows the relative increase in response from the high fracture density case versus the low fracture density case when all other parameters are constant. The multiplier is also included in Table 5.3.

Fracture Azimuth	Fluid Type	Anisotropy Type	Strong Fracturing	Weak Fracturing	Multiplier
0 Degrees	Dry / Gas	HTI (a)	0.0009	0.0005	1.7713
		HTI (b)	0.0063	0.0019	3.2676
		Orthorhombic	0.0050	0.0020	2.4430
	Wet	HTI (a)	0.0115	0.0022	5.2543
		HTI (b)	0.0123	0.0026	4.7767
		Orthorhombic	0.0126	0.0028	4.5320
45 Degrees	Dry / Gas	HTI (a)	0.0011	0.0006	1.9430
		HTI (b)	0.0067	0.0024	2.8181
		Orthorhombic	0.0051	0.0024	2.1336
	Wet	HTI (a)	0.0114	0.0021	5.5407
		HTI (b)	0.0118	0.0022	5.3790
		Orthorhombic	0.0124	0.0024	5.1013

Table 5.3: A table summarizing the results of fracture density inversion for 24 synthetic cases with various properties. Inverted fracture density values for strong and weak fracturing are shown, as well as a multiplier which measures the relative difference in response between the strong and weak fracturing cases.

The results presented in this section will be discussed in Section 5.6 of this Chapter. To summarize, it appears clear that this method is able to distinguish relatively high fracture density from relatively low fracture density. The inverted multiplier between dense and sparse fracturing is somewhat lower than the true multiplier (true multiplier = 5), but areas of higher fracturing are still easily identifiable. Thus, I feel

confident in moving forward and applying this method to data from the Haynesville Shale.

5.5.4 Haynesville Data – Fracture Density

Vertically averaged values for fracture density (from R_2^*) can be seen in Figures 5.24 and 5.25. For comparison, Figures 5.26 and 5.27 show vertically averaged fracture density results from the Orthorhombic method described in this chapter and from the Fourier coefficient based HTI method described in Chapter 4 using an identical binning scheme. Values for fracture density should be treated as relative, and thus do not include bounds on the colorbar. Warmer background colors indicate higher fracture density. The black arrows indicate the direction of north. All images share the same orientation.

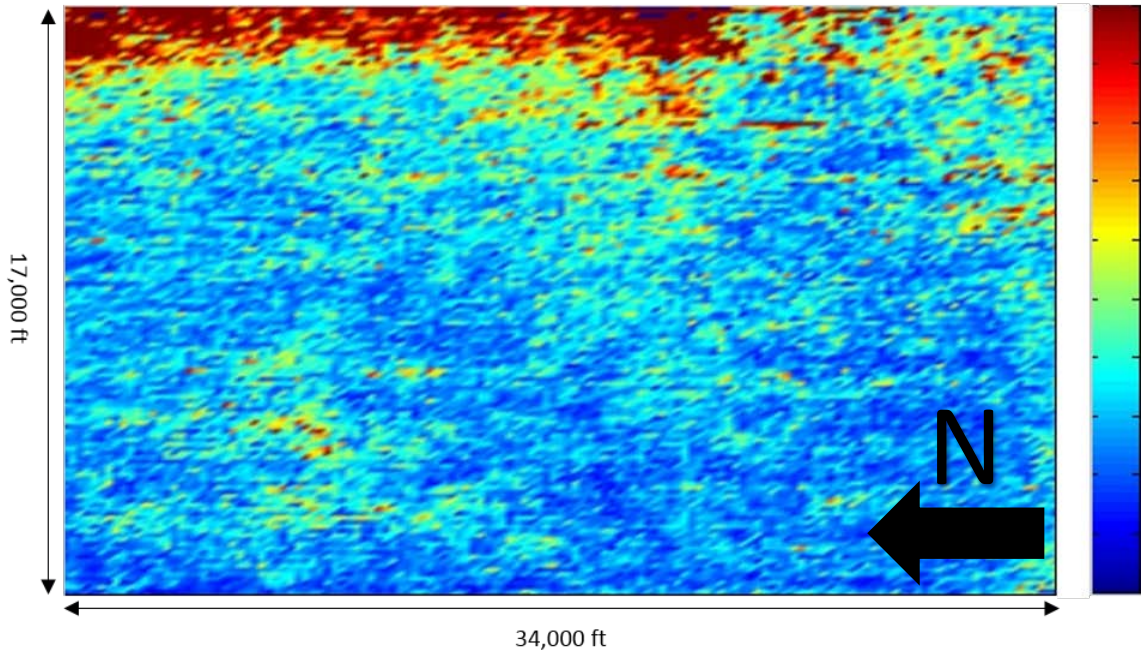

Figure 5.24: R_2^*, a proxy for fracture density, as calculated by the Orthorhombic Fourier coefficient decomposition method. R_2^* is a measure of combined evergy in w_{12} and w_{22}, corresponding to 2nd order sine and cosine terms in the Fourier series. 2-D lateral smoothing has not been applied. Values have been vertically averaged throughout the Haynesville using a simple arithmetic mean. Warmer colors indicate denser fracturing. The black arrow indicates the direction of north.

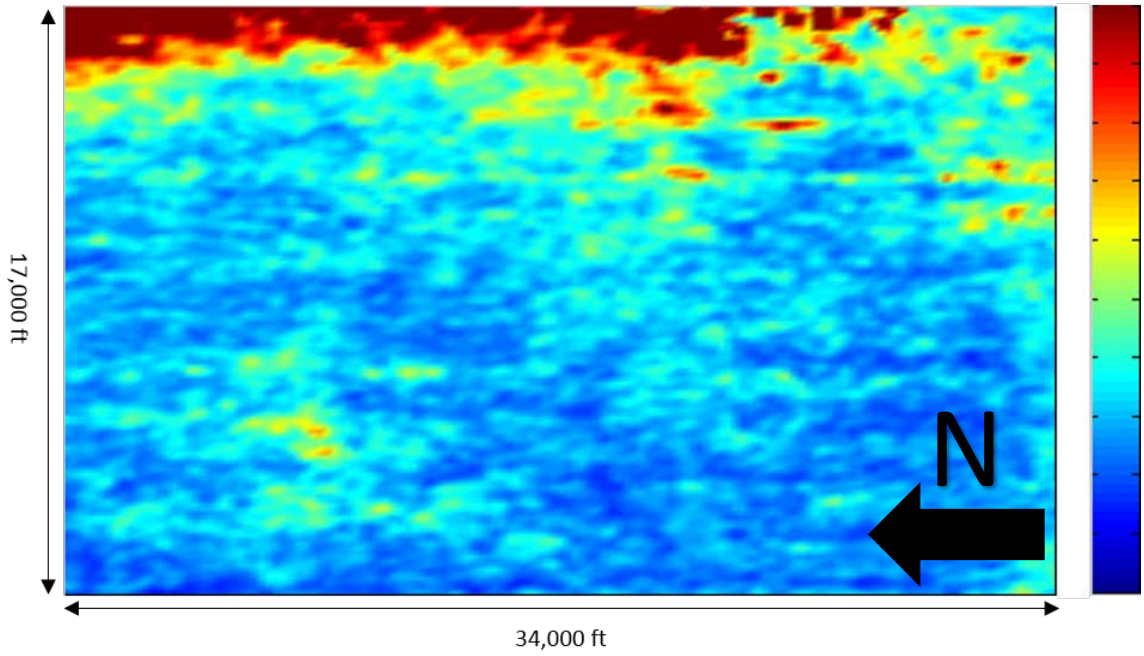

Figure 5.25: R_2^*, a proxy for fracture density, as calculated by the Orthorhombic Fourier coefficient decomposition method. R_2^* is a measure of combined evergy in w_{12} and w_{22}, corresponding to 2nd order sine and cosine terms in the Fourier series. 2-D lateral smoothing has been applied. Values have been vertically averaged throughout the Haynesville using a simple arithmetic mean. Warmer colors indicate denser fracturing. The black arrow indicates the direction of north.

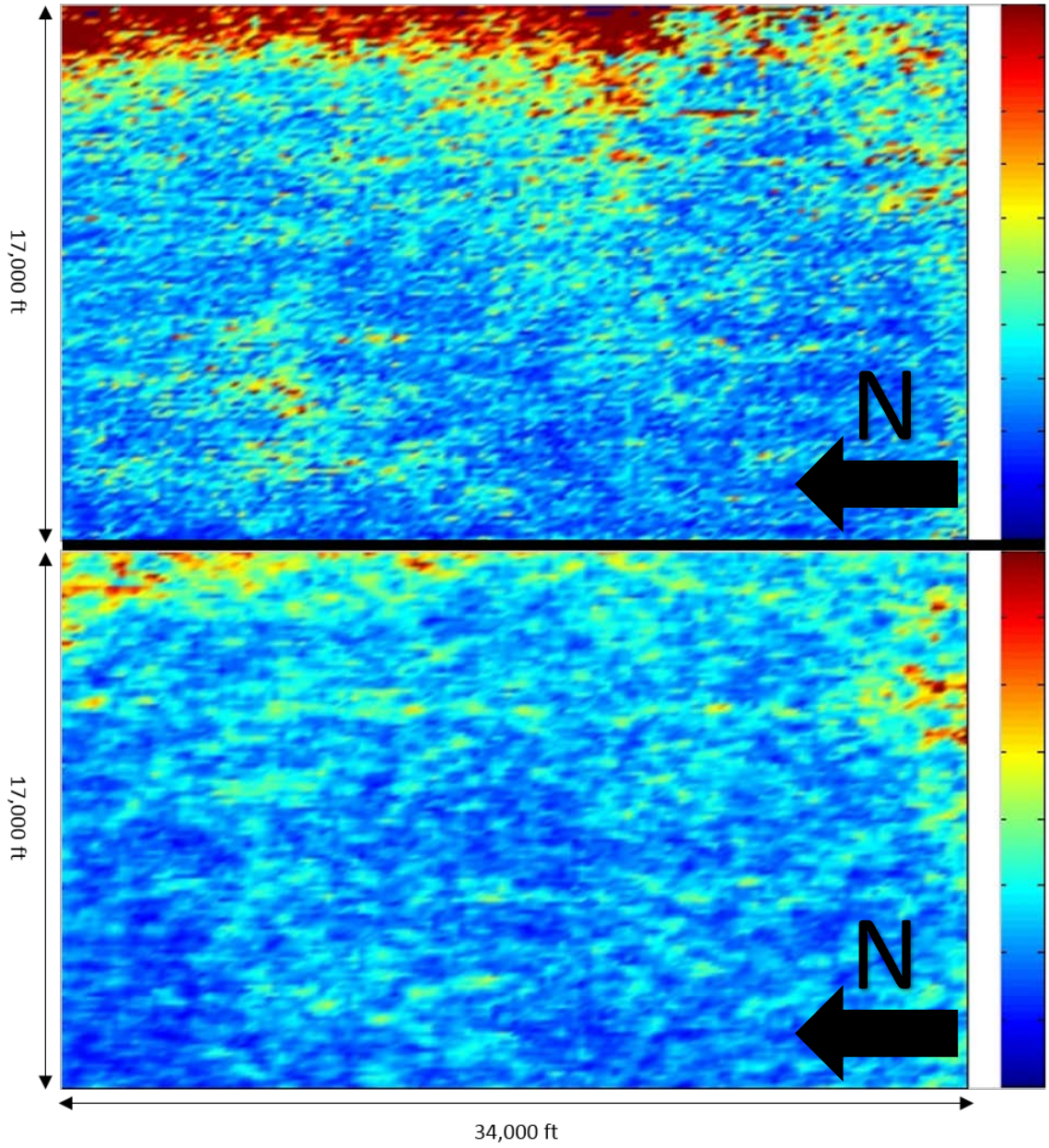

Figure 5.26: Comparison of proxies for fracture density from the Orthorhombic and HTI Fourier coefficient decomposition based methods. The top image depicts R_2^*, a proxy for fracture density, as calculated by the Orthorhombic Fourier coefficient decomposition method. 2-D lateral smoothing has not been applied. The bottom image depicts r_2 as calculated by the HTI Fourier coefficient decomposition method. The black arrows indicate the direction of north.

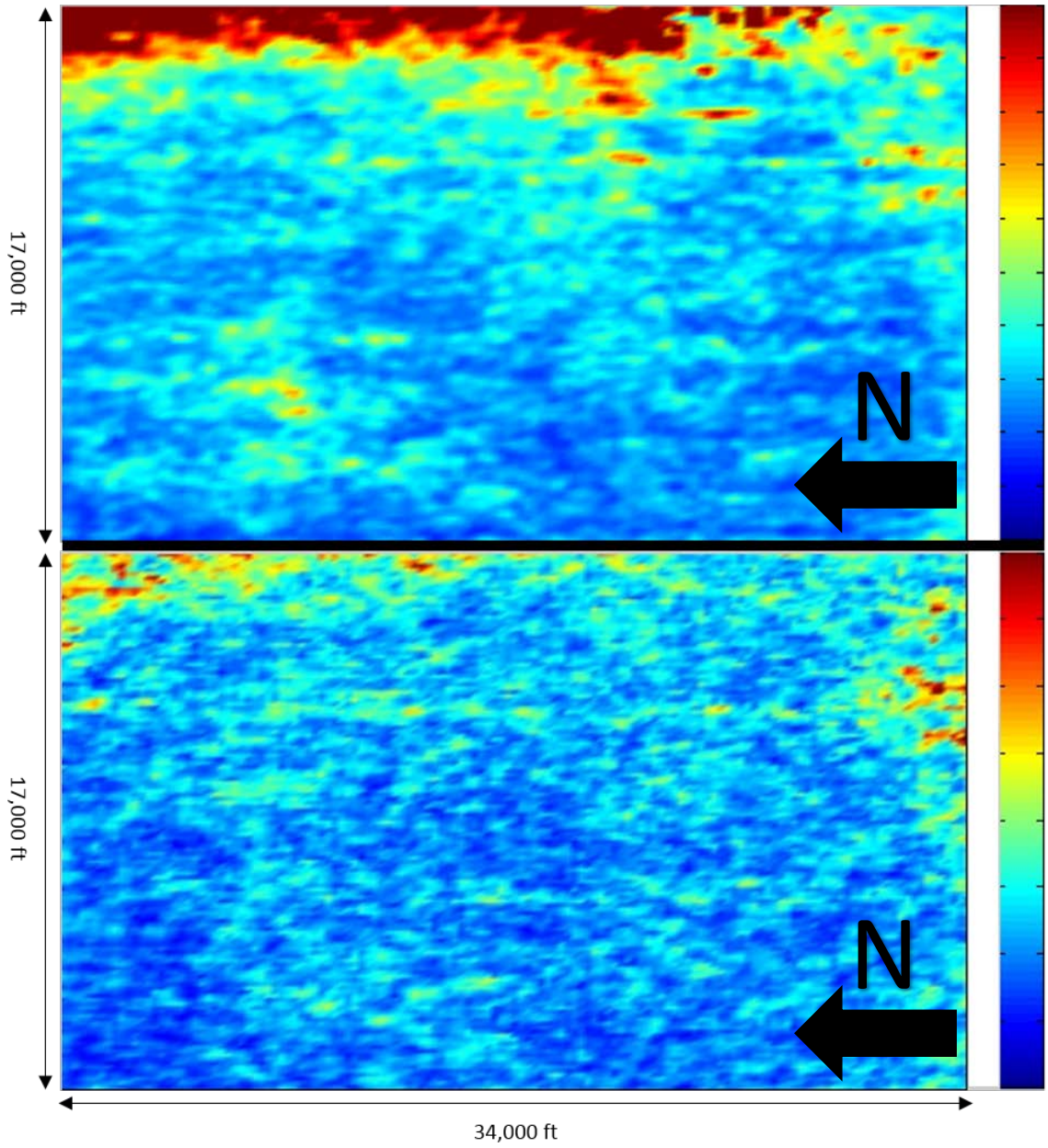

Figure 5.27: Comparison of proxies for fracture density from the Orthorhombic and HTI Fourier coefficient decomposition based methods. The top image depicts R_2^*, a proxy for fracture density, as calculated by the Orthorhombic Fourier coefficient decomposition method. 2-D lateral smoothing has been applied. The bottom image depicts r_2 as calculated by the HTI Fourier coefficient decomposition method. Values have been vertically averaged throughout the Haynesville using a simple arithmetic mean. Warmer colors indicate denser fracturing. The black arrows indicate the direction of north.

Fracture density (from R_2^*) results from a constant time slice that encompasses the entire Haynesville can be seen in Figures 5.28 and 5.29. For comparison, Figures 5.30 and 5.31 depict fracture density results over the same time slice from the orthorhombic method described in this chapter and from the Fourier coefficient based HTI method described in Chapter 4 using an identical binning scheme. Values for fracture density should be treated as relative, and thus do not include bounds on the colorbar. Warmer background colors indicate higher fracture density. The black arrows indicate the direction of north. All images share the same orientation.

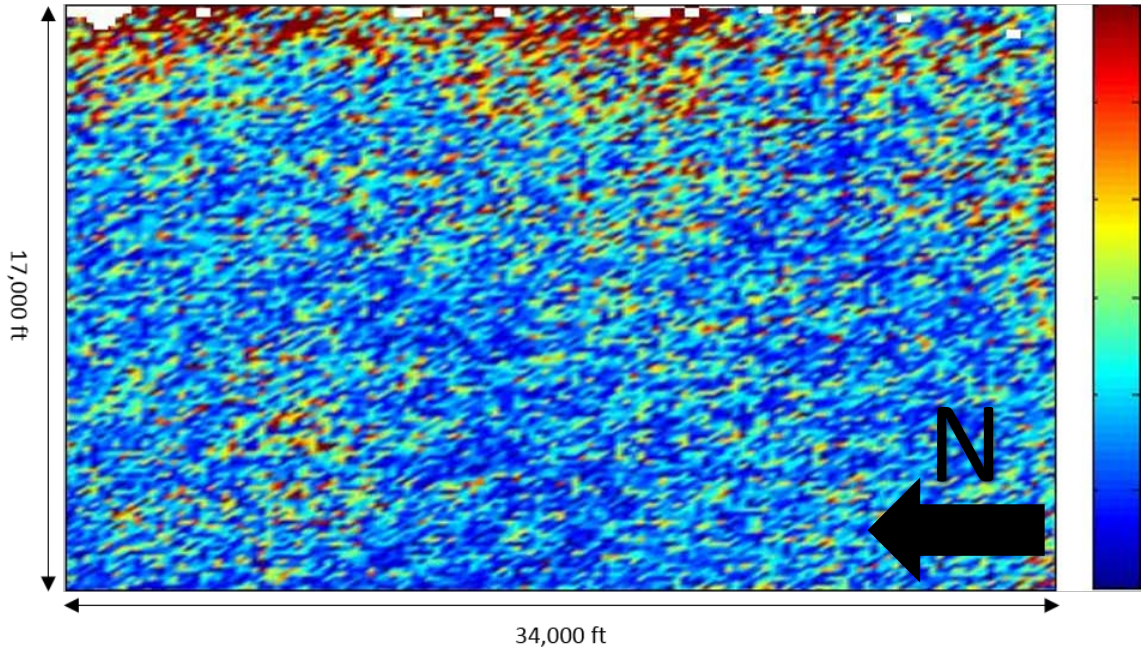

Figure 5.28: R_2^*, a proxy for fracture density, as calculated by the Orthorhombic Fourier coefficient decomposition method. R_2^* is a measure of combined evergy in w_{12} and w_{22}, corresponding to 2nd order sine and cosine terms in the Fourier series. 2-D lateral smoothing has not been applied. Values corresponding to a constant time of 2060 ms are shown. Warmer colors indicate denser fracturing. The black arrow indicates the direction of north.

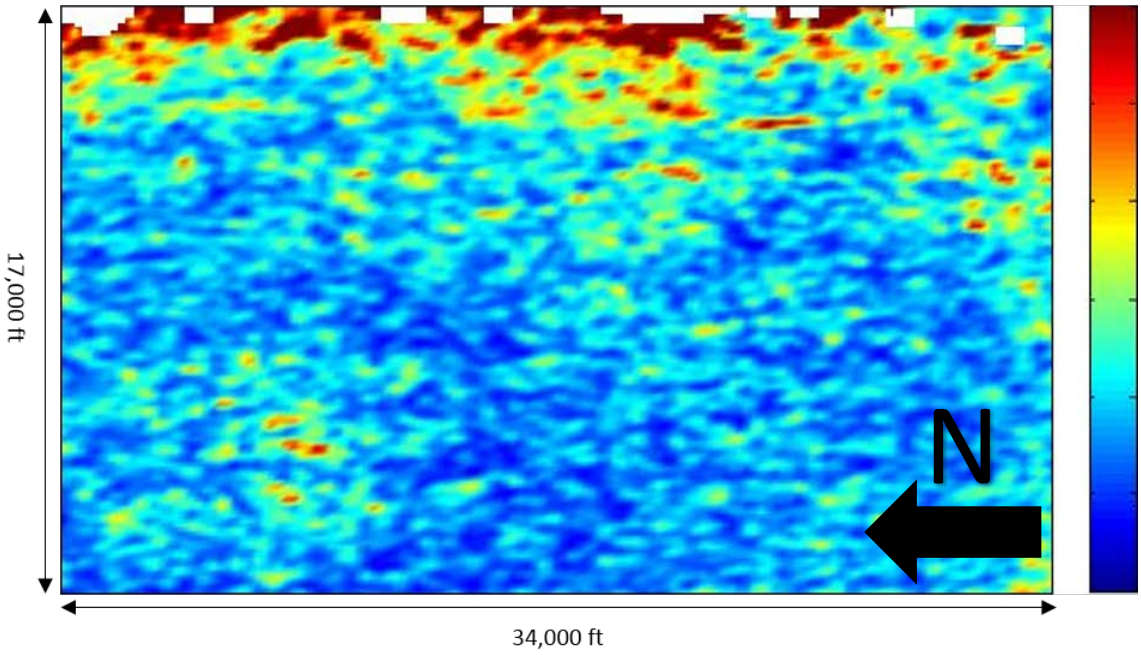

Figure 5.29: R_2^*, a proxy for fracture density, as calculated by the Orthorhombic Fourier coefficient decomposition method. R_2^* is a measure of combined evergy in w_{12} and w_{22}, corresponding to 2nd order sine and cosine terms in the Fourier series. 2-D lateral smoothing has been applied. Values corresponding to a constant time of 2060 ms are shown. Warmer colors indicate denser fracturing. The black arrow indicates the direction of north.

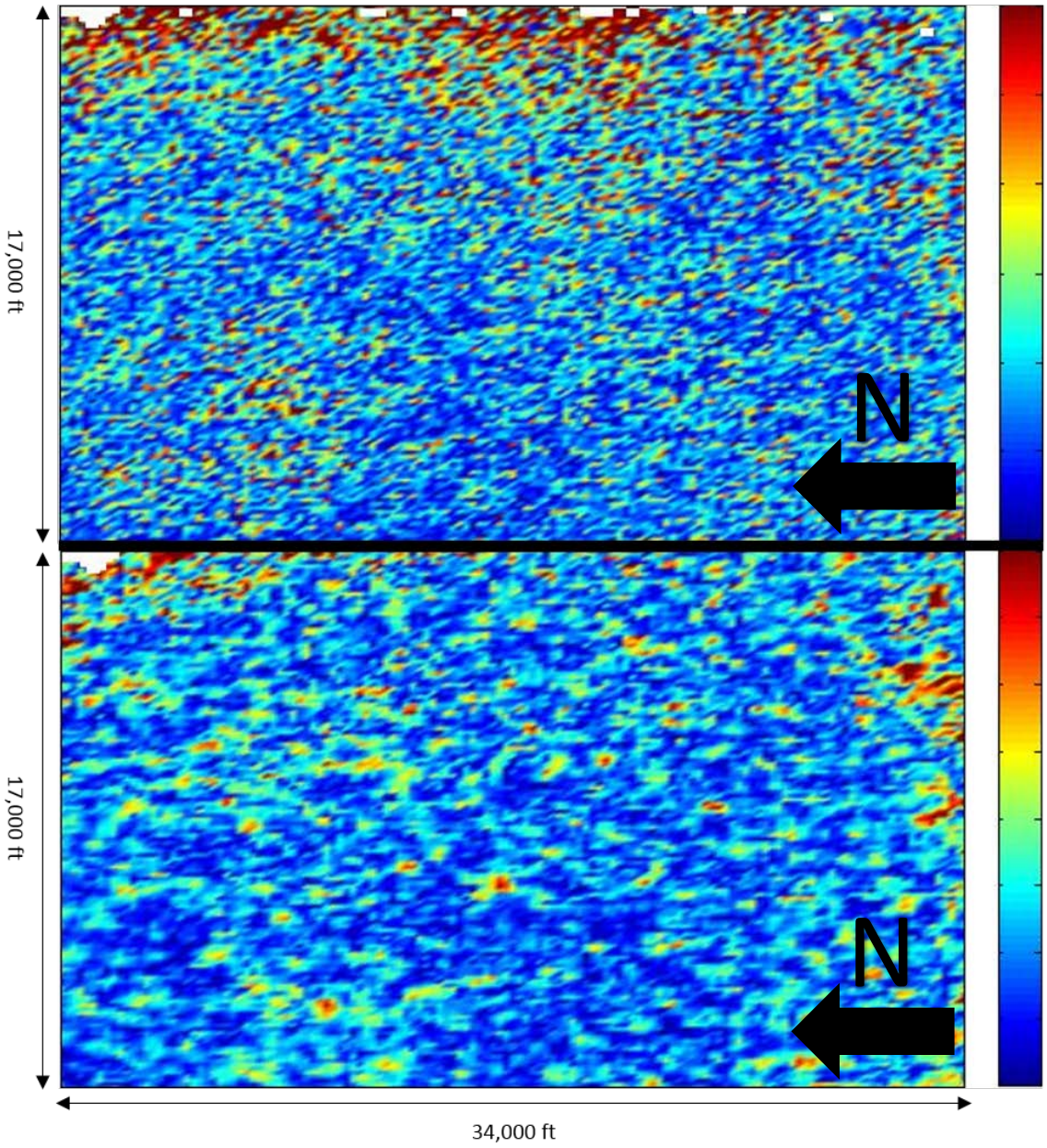

Figure 5.30: Comparison of proxies for fracture density from the Orthorhombic and HTI Fourier coefficient decomposition based methods. The top image depicts R_2^*, a proxy for fracture density, as calculated by the Orthorhombic Fourier coefficient decomposition method. 2-D lateral smoothing has not been applied. The bottom image depicts r_2 as calculated by the HTI Fourier coefficient decomposition method. Values corresponding to a constant time of 2060 ms are shown. Warmer colors indicate denser fracturing. The black arrows indicate the direction of north.

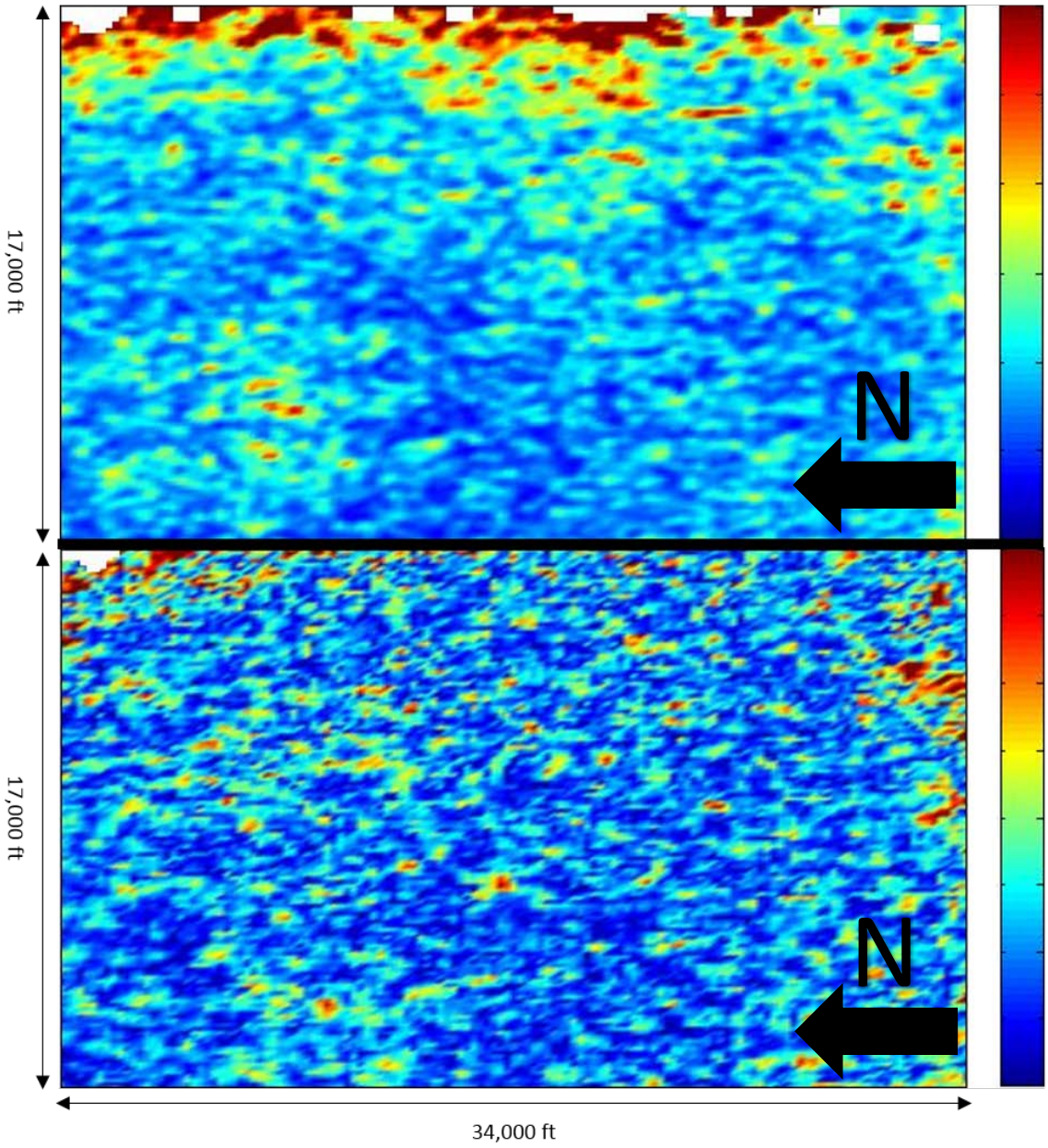

Figure 5.31: Comparison of proxies for fracture density from the Orthorhombic and HTI Fourier coefficient decomposition based methods. The top image depicts R_2^*, a proxy for fracture density, as calculated by the Orthorhombic Fourier coefficient decomposition method. 2-D lateral smoothing has been applied. The bottom image depicts r_2 as calculated by the HTI Fourier coefficient decomposition method. Values corresponding to a constant time of 2060 ms are shown. Warmer colors indicate denser fracturing. The black arrows indicate the direction of north.

Fracture density (from R_2^*) results from constant depth slices representing 0m, 15m, 30m and 45m from the Haynesville top can be seen in Figures 5.32 – 5.35. "Constant depth" was determined by measuring a constant number of time samples from the top of the Haynesville. Only laterally smoothed results will be included. A comparison of results over the same depth slices from the Orthorhombic method described in this chapter and the Fourier coefficient based HTI method described in Chapter 4 using an identical binning scheme can be seen in Figures 5.36 – 5.39. Values for fracture density should be treated as relative, and thus do not include bounds on the colorbar. Warmer background colors indicate higher fracture density. The black arrows indicate the direction of north. All images share the same orientation.

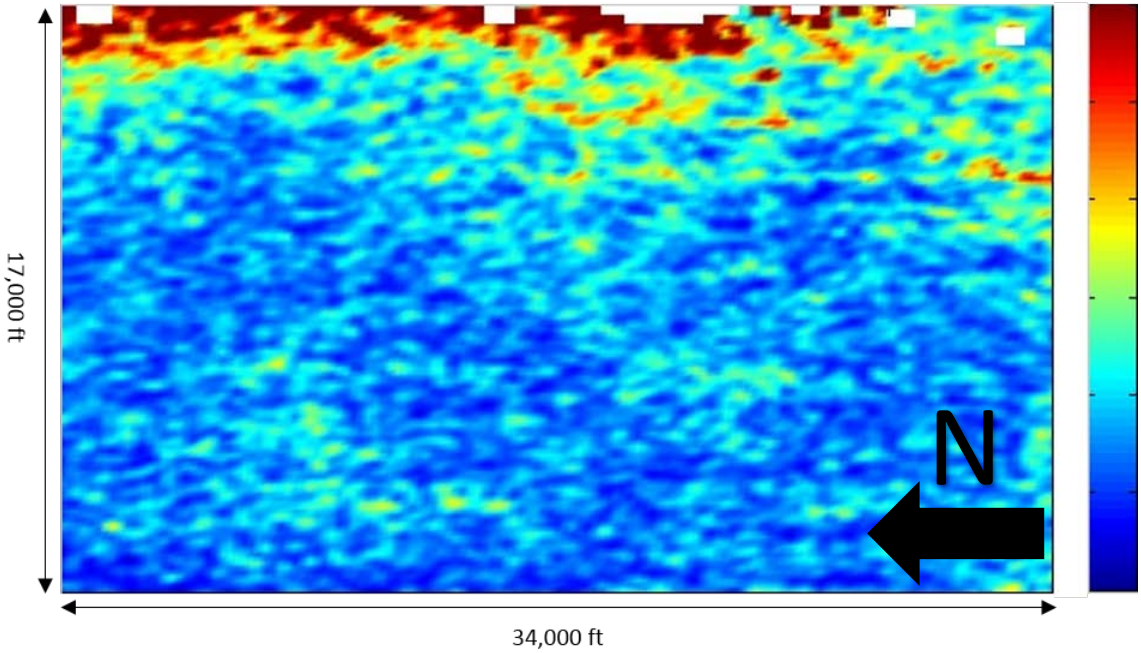

Figure 5.32: R_2^*, a proxy for fracture density, as calculated by the Orthorhombic Fourier coefficient decomposition method. R_2^* is a measure of combined evergy in w_{12} and w_{22}, corresponding to 2nd order sine and cosine terms in the Fourier series. 2-D lateral smoothing has been applied. Values corresponding to the top of the Haynesville are shown. Warmer colors indicate denser fracturing. The black arrow indicates the direction of north.

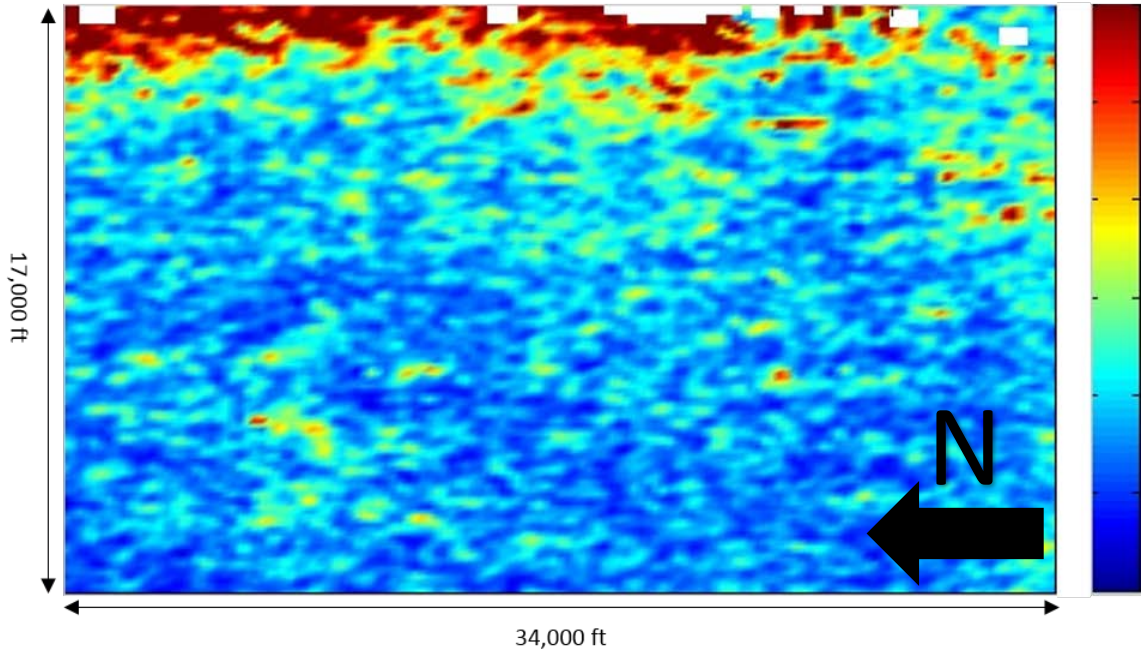

Figure 5.33: R_2^*, a proxy for fracture density, as calculated by the Orthorhombic Fourier coefficient decomposition method. R_2^* is a measure of combined evergy in w_{12} and w_{22}, corresponding to 2nd order sine and cosine terms in the Fourier series. 2-D lateral smoothing has been applied. Values corresponding to approximately 15 m from the top of the Haynesville are shown. Warmer colors indicate denser fracturing. The black arrow indicates the direction of north.

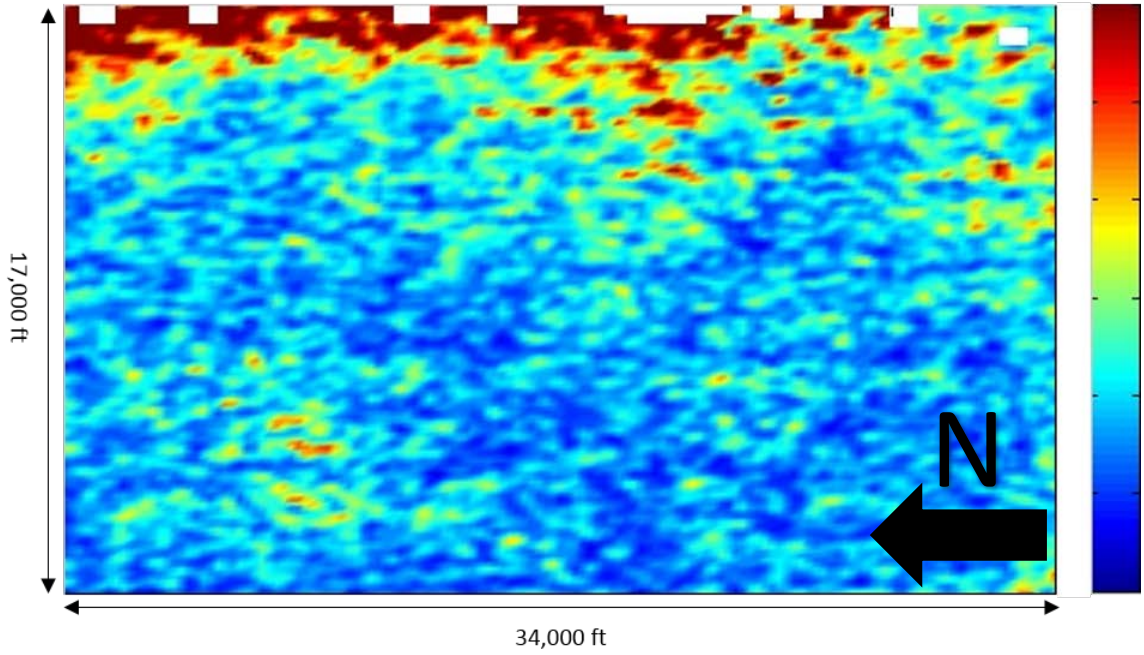

Figure 5.34: R_2^*, a proxy for fracture density, as calculated by the Orthorhombic Fourier coefficient decomposition method. R_2^* is a measure of combined evergy in w_{12} and w_{22}, corresponding to 2nd order sine and cosine terms in the Fourier series. 2-D lateral smoothing has been applied. Values corresponding to approximately 30 m from the top of the Haynesville are shown. Warmer colors indicate denser fracturing. The black arrow indicates the direction of north.

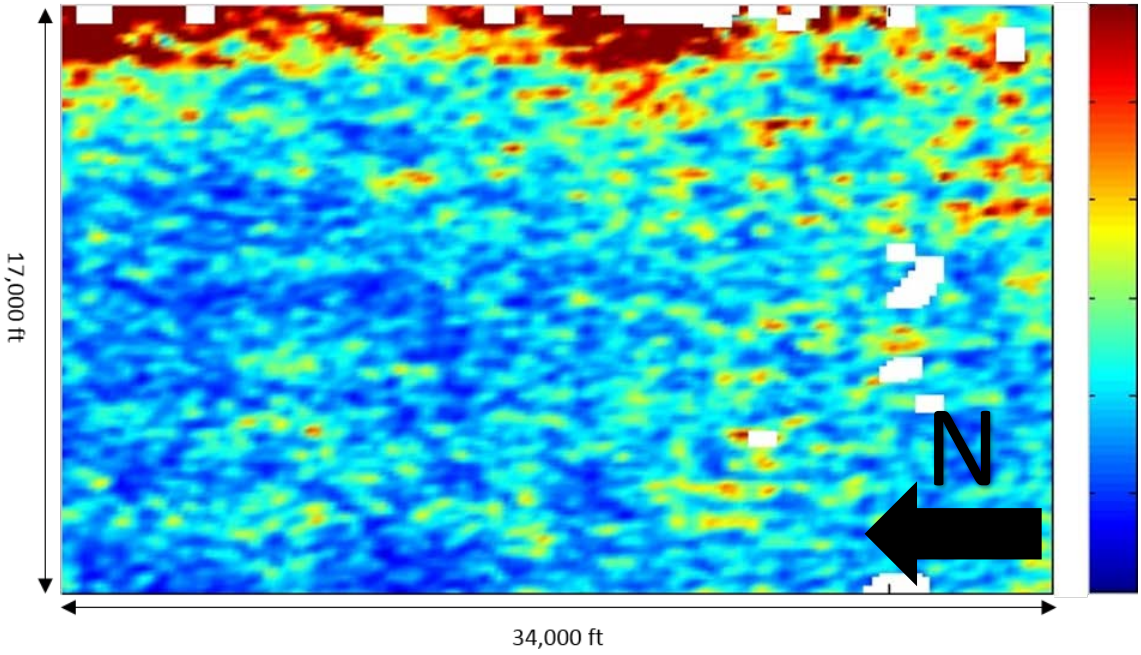

Figure 5.35: R_2^*, a proxy for fracture density, as calculated by the Orthorhombic Fourier coefficient decomposition method. R_2^* is a measure of combined evergy in w_{12} and w_{22}, corresponding to 2nd order sine and cosine terms in the Fourier series. 2-D lateral smoothing has been applied. Values corresponding to approximately 45 m from the top of the Haynesville are shown. Warmer colors indicate denser fracturing. The black arrow indicates the direction of north.

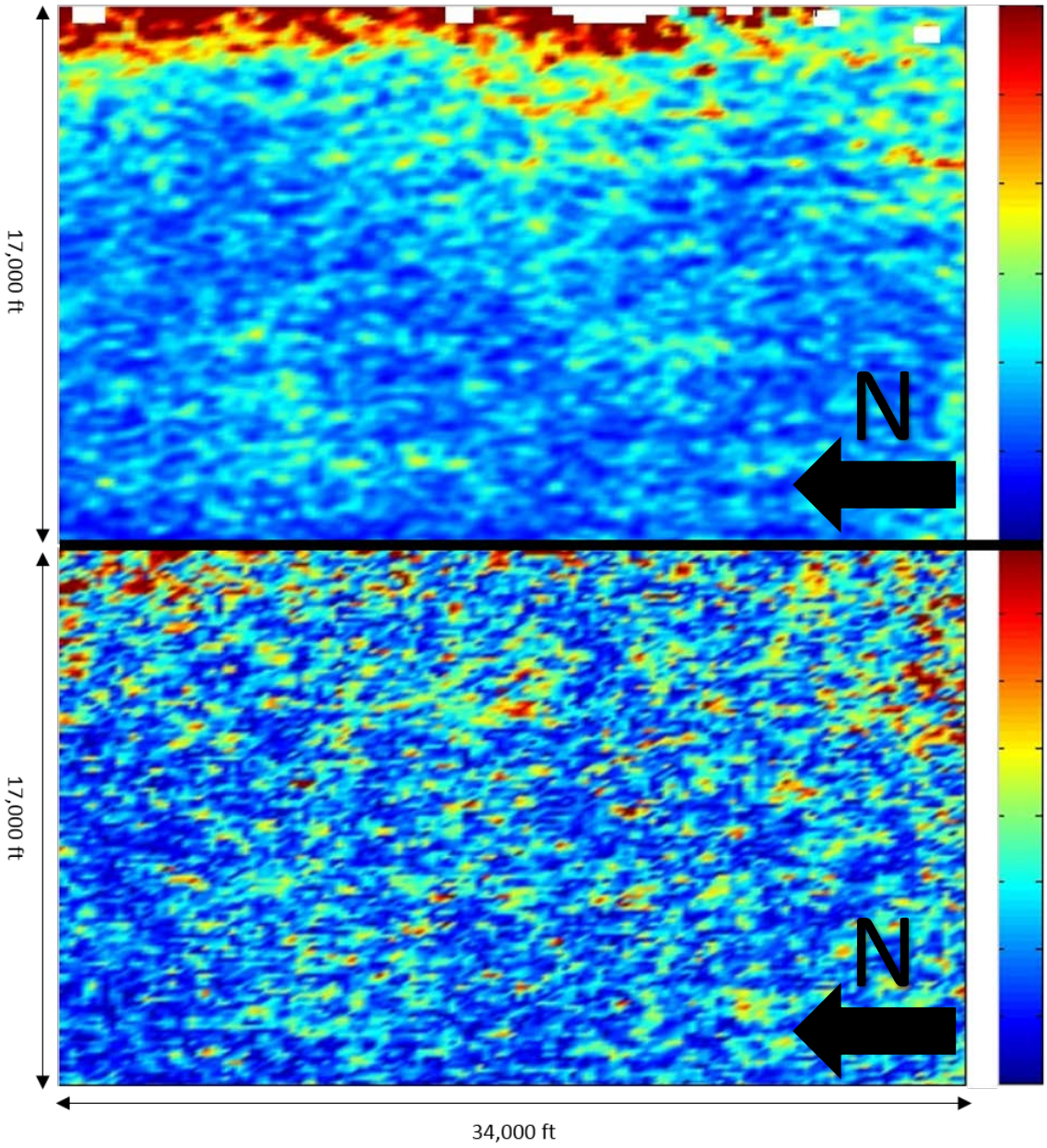

Figure 5.36: Comparison of proxies for fracture density from the Orthorhombic and HTI Fourier coefficient decomposition based methods. The top image depicts R_2^*, a proxy for fracture density, as calculated by the Orthorhombic Fourier coefficient decomposition method. 2-D lateral smoothing has been applied. The bottom image depicts r_2 as calculated by the HTI Fourier coefficient decomposition method. Values corresponding to the top of the Haynesville are shown. Warmer colors indicate denser fracturing. The black arrows indicate the direction of north.

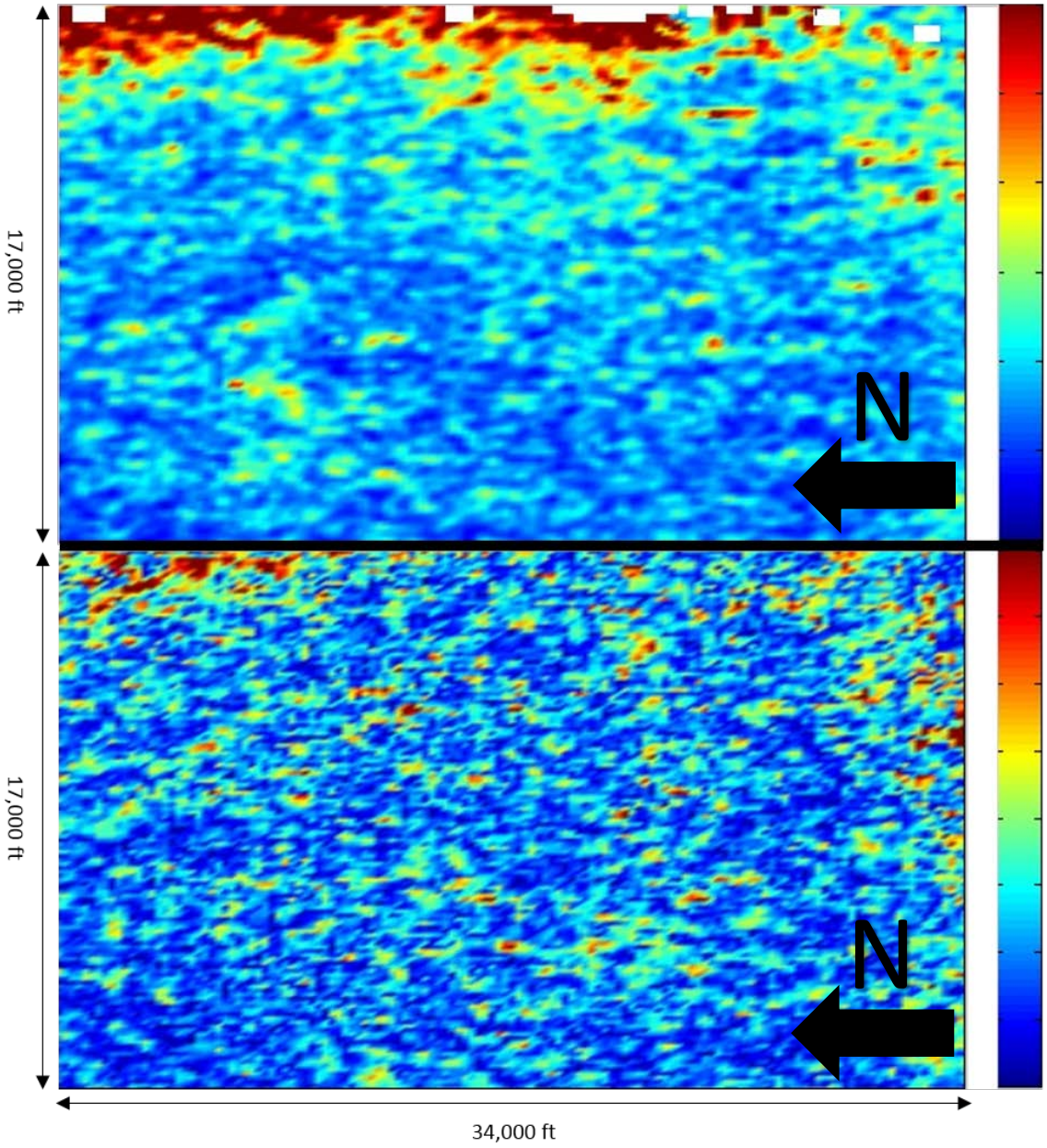

Figure 5.37: Comparison of proxies for fracture density from the Orthorhombic and HTI Fourier coefficient decomposition based methods. The top image depicts R_2^*, a proxy for fracture density, as calculated by the Orthorhombic Fourier coefficient decomposition method. 2-D lateral smoothing has been applied. The bottom image depicts r_2 as calculated by the HTI Fourier coefficient decomposition method. Values corresponding to approximately 15 m from the top of the Haynesville are shown. Warmer colors indicate denser fracturing. The black arrows indicate the direction of north.

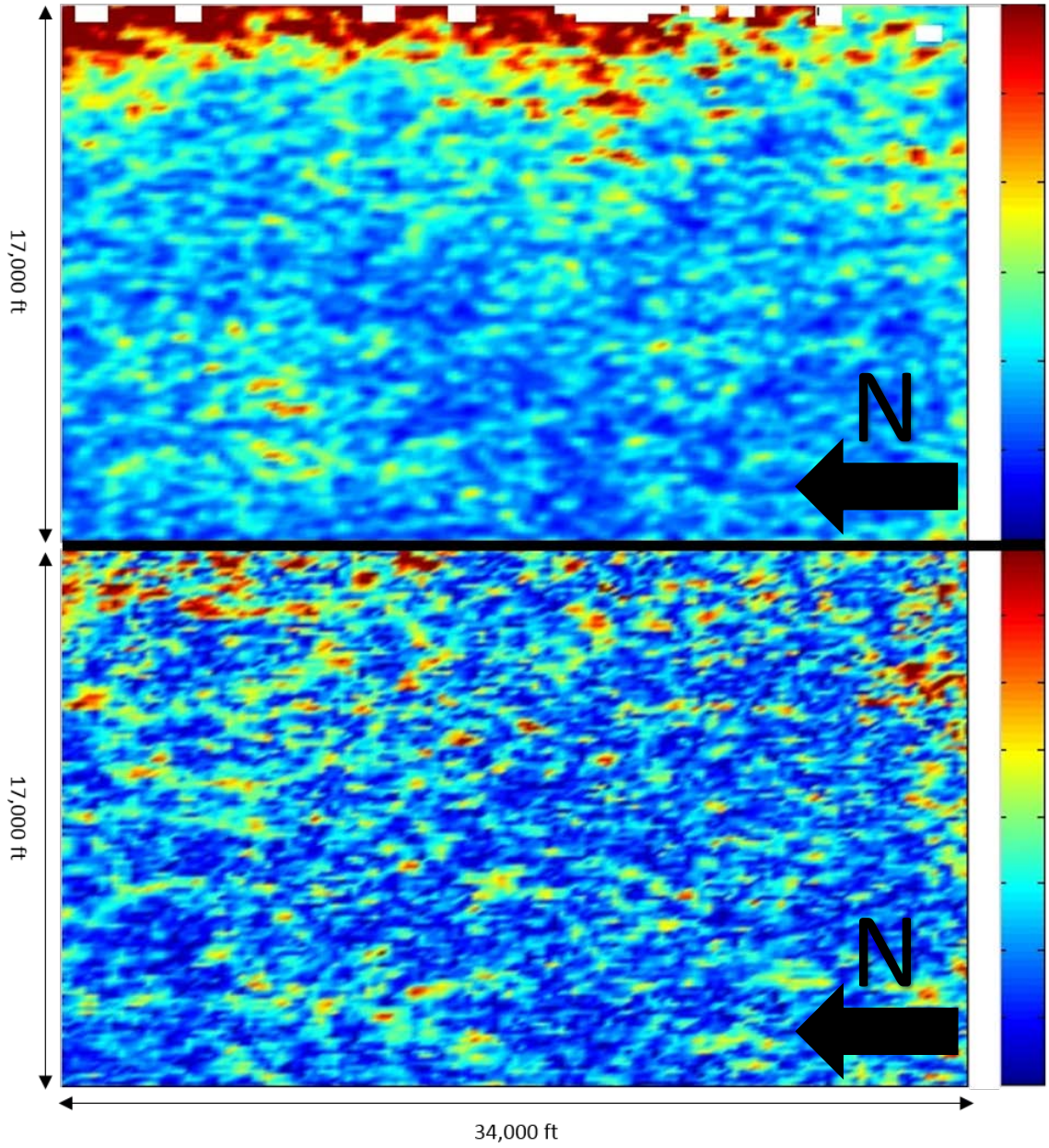

Figure 5.38: Comparison of proxies for fracture density from the Orthorhombic and HTI Fourier coefficient decomposition based methods. The top image depicts R_2^*, a proxy for fracture density, as calculated by the Orthorhombic Fourier coefficient decomposition method. 2-D lateral smoothing has been applied. The bottom image depicts r_2 as calculated by the HTI Fourier coefficient decomposition method. Values corresponding to approximately 30 m from the top of the Haynesville are shown. Warmer colors indicate denser fracturing. The black arrows indicate the direction of north.

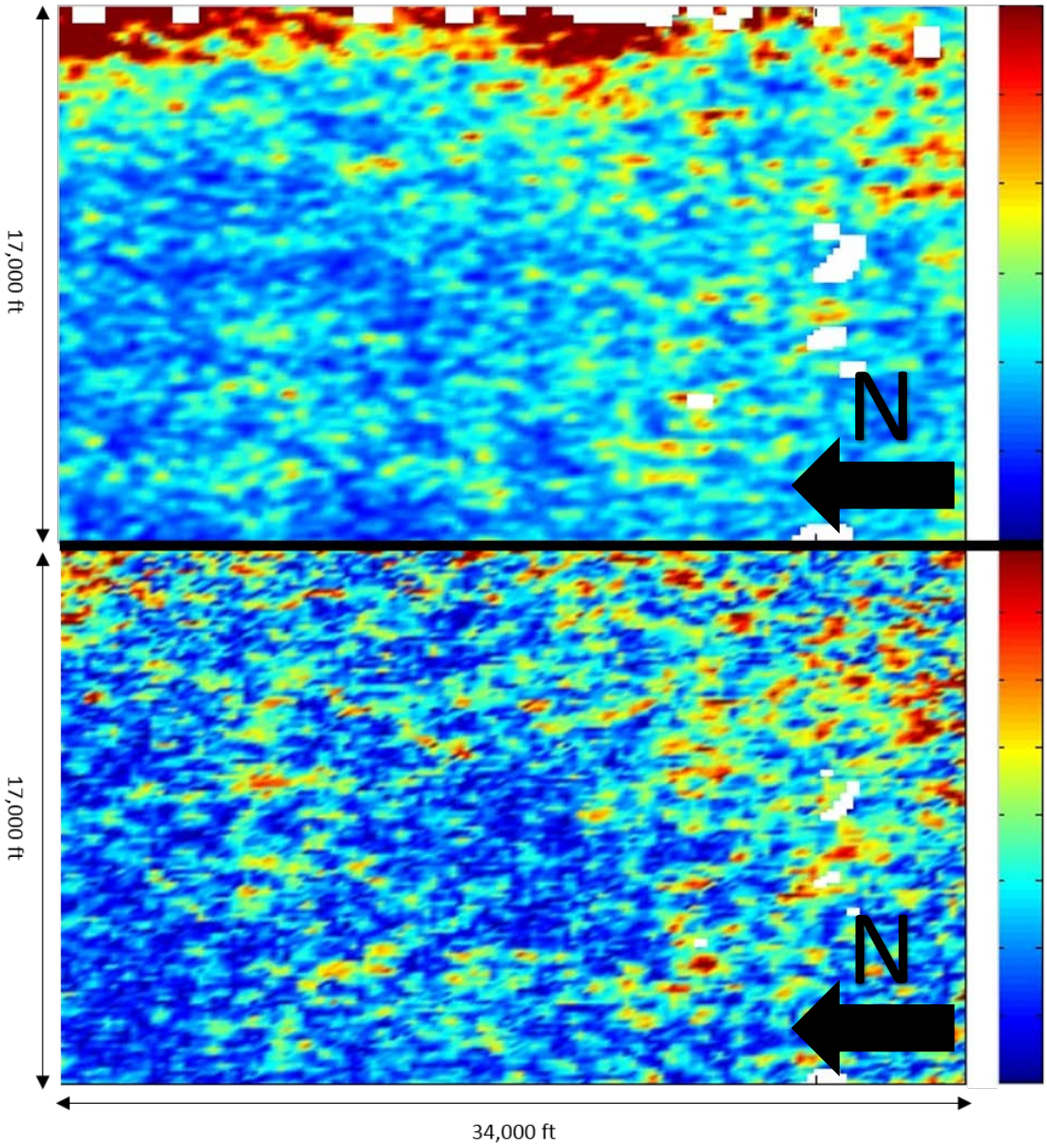

Figure 5.39: Comparison of proxies for fracture density from the Orthorhombic and HTI Fourier coefficient decomposition based methods. The top image depicts R_2^*, a proxy for fracture density, as calculated by the Orthorhombic Fourier coefficient decomposition method. 2-D lateral smoothing has been applied. The bottom image depicts r_2 as calculated by the HTI Fourier coefficient decomposition method. Values corresponding to approximately 45 m from the top of the Haynesville are shown. Warmer colors indicate denser fracturing. The black arrows indicate the direction of north.

5.6 DISCUSSION

Examining the fracture azimuth inversion results in the synthetic cases demonstrates that the proposed method works sufficiently well when only considering intermediate or relatively far offset data. Figures 5.5 – 5.8 demonstrate that it is possible to identify the correct azimuth on a histogram plot of data from all incident angles. However, it is extremely evident on a histogram plot of high incident angle data only. Unfortunately, this method does occasionally mis-assign azimuths in the perpendicular direction (i.e., 90 degrees shifted), but this only occurs in a minority of cases. In many of the misaligned cases, the reflection amplitude is very weak. Very weak reflection amplitudes can occur if a particular time sample corresponded to a zero crossing or if a particular synthetic dataset overall had very small amplitudes, as was the case in the HTI (a) data with gas filled fractures. Random noise was not explicitly added to the synthetic data, though some computational artifacts, which resemble noise, are present in the synthetic data. Thus, the signal-to-noise ratio is lower for data with weak reflection amplitudes, explaining in part why some of the azimuthal cases were misaligned.

Table 5.2 indicates that, on average, the correct azimuth is assigned roughly 85% of the time in synthetic cases where fractures are gas filled. Here I define the inverted azimuth to be correct if it is with 5 degrees of the true azimuth. If cases with very weak data are ignored, the correct azimuth is assigned more frequently. The gas filled fracture case most resembles the Haynesville, and thus my discussion will focus primarily on the synthetic cases with gas filled fractures. Table 5.2 additionally shows that even in a worst case scenario, the correct azimuth is assigned roughly 81% of the time. It is interesting to note that this method works even better in the case of fluid filled fractures, indicating it has significant potential to be applied to unconventional wet and tight oil plays.

Fracture azimuth inversion results from the Haynesville vary when comparing the Orthorhombic and HTI methods presented. It is interesting that in some instances these methods seem to be almost identical (for example in Figures 5.20, 5.21 and 5.23). In other instances, the results appear to be almost exactly 90 degree phase shifted from each other (for example in Figure 5.22). This supports the theory that the original Fourier coefficient method does not always determine the correct symmetry plane whereas the new proposed method does – resulting in a nearly exact overlap in some areas and other places to be phase shifted 90 degrees when comparing the two methods. However, the most compelling evidence that the proposed method determines the correct fracture azimuth comes from Figures 5.10 – 5.12. In Figure 5.12, which shows vertically averaged fracture azimuth, we see that an azimuth of roughly east-west (corresponding to ± 90 degrees in the figures) is extremely prevalent throughout the entire section. The histograms for far offset data, shown in Figures 5.10 and 5.11, again overwhelmingly suggest a primary fracture orientation of about 85 degrees, slightly counterclockwise rotated from an east-west orientation. Note that the inline and crossline directions of the seismic survey are rotated slightly counterclockwise of a true north-south / east-west orientation. Thus, an inverted fracture azimuth of roughly 85 degrees corresponds to a compass bearing of approximately 82 degrees. This fracture azimuth agrees very well with what is suggested by analyzing regional stress and studying fracture orientation in nearby formations, as discussed in Section 4.5.

Being that fracture azimuth is very close to 90 degrees, the special case of a 90 degree fracture azimuth was used when inverting for fracture density. I feel that the error associated with assuming a fracture azimuth which is 5 degrees incorrect is less than the increased error associated with having to invert for additional parameters. Specifically, the 5 Fourier coefficients per incident angle and 9 weights (w_{ij}'s) per time / CDP in the

general case is reduced to 4 Fourier coefficients per incident angle and 6 weights (w_{ij}'s) per time / CDP in the special case where fracture azimuth is equal to 90 degrees. This specialized case was assumed in both the synthetic example and when analyzing the Haynesville dataset.

Inversion results for fracture density from the synthetic data indicate that for any given scenario, the algorithm assigned a higher fracture density to the high fracture density case than the low fracture density case. In the case of gas filled fractures, the algorithm tended to under-estimate the magnitude of fracturing in the high fracture density case relative to the low fracture density case, with multipliers generally falling in the 2x to 3x range rather than near the true value of 5x. It is again interesting to note that this method seems to perform better in the case of fluid filled fractures, which calculated a multiplier of very close to 5x, indicating again that this proposed method has significant potential to be applied to unconventional wet and tight oil plays. Results from the HTI (b) and the orthorhombic datasets seem to be very consistent, however, results from the HTI (a) dataset with gas filled fractures seems to underestimate both absolute values of fracture density and the multiplier between strong and weak fracturing. In the case of the HTI (a) synthetic data with gas filled fractures, this likely can be attributed to the unusually small seismic amplitudes present throughout the data. Figure 5.40 compares an example data slice from the HTI (a) dataset with gas filled fractures to a data slice from the orthorhombic dataset with gas filled fractures using the same amplitude color scale. As seen in Figure 5.40, the HTI (a) dataset with gas filled fractures has significantly smaller amplitudes than the orthorhombic dataset with gas filled fractures. This indicates that this method does not work as well when seismic amplitudes are extremely weak. Thus, if trying to analyze extremely weak seismic data, one should expect the inverted results for fracture density to be unusually low.

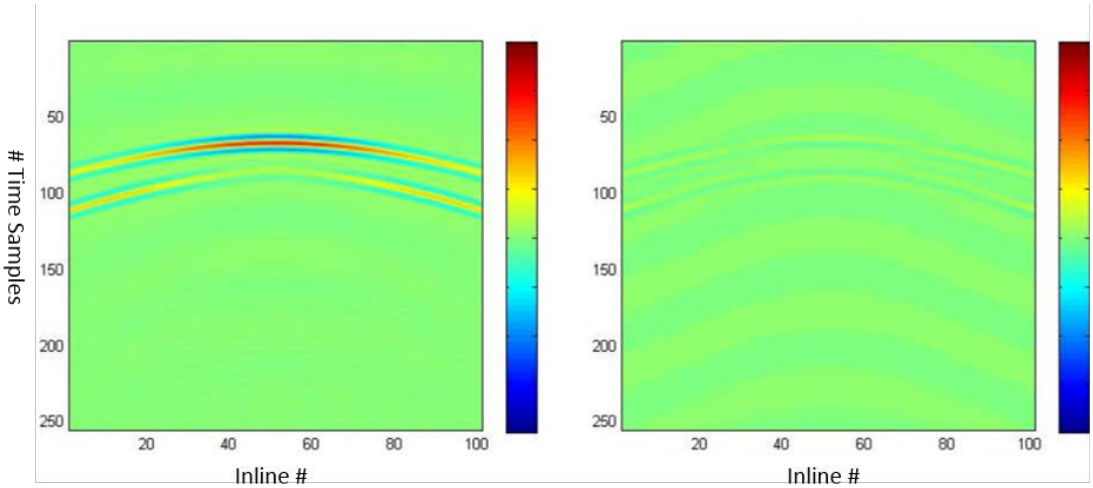

Figure 5.40: Comparison of data slices from the synthetic datasets. The left image shows a slice from the orthorhombic synthetic dataset with gas filled fractures, and the right image shows a slice from the HTI (a) dataset with gas filled fractures. The colorbar represents seismic amplitude. The same color scale is used in both images. The horizontal axis indicates position, and the vertical axis indicates time. No processing has been performed on the data.

The underestimation of fracturing in cases with high fracture density and gas filled fractures may also be a result of the fracture density chosen when generating the data. In the high fracture density cases fracture density (e) was set to 0.1, which is outside the usual realm of applicability for Linear Slip Deformation (LSD) theory to be valid. This was done intentionally to observe how this method responds to extreme fracturing. Note that in the low fracture density case, where LSD is valid, fracture density results are similar for all cases (with the exception of the HTI (a) case with gas filled fractures). However, in the high fracture density cases, results tend to diverge, especially when comparing cases with fluid filled fractures to those with gas filled fracture. This indicates that extreme fracturing may hamper this method, resulting in the observed underestimation of fracture density in cases with gas filled fractures and high fracture density. Despite this, the method is still largely able to distinguish areas with high

fracture density from those with low fracture density, even if conditions change to some extent. Note that, again excluding the HTI (a) case with gas filled fractures, the weakest response to strong fracturing is still almost a factor of two greater than the strongest response to weak fracturing. This indicates that even if there are significant lateral changes in properties, the proposed method is still able to distinguish an area of high fracture density from one of low fracture density. However, the relative difference between high and low fracture density results may not adequately represent the actual relative change in fracture density. Lastly, it is interesting to note that fracture density results from the synthetic cases where fracture azimuth is 45 degrees were very consistent to results from cases with a fracture azimuth of 0 degree. This indicates that inversion results calculated using this method may be acceptable for fracture azimuths other than 0, 90 and 180 degrees, even though the underlying equations are not technically valid for other fracture azimuths. This being said, I felt confident in moving forward to apply this proposed new method to real data from the Haynesville Shale.

Fracture density inversion results of the Haynesville Shale from both methods produced somewhat similar results, however the orthorhombic method successfully delineated a localized area of anomalously high fracture density in the Northwest corner of the survey area. This area was not distinctly identifiable in any of the HTI methods performed. This area is indicated by the black circle in Figure 5.41, which shows vertically averaged 2nd order coefficient energy R_2^* from the Orthorhombic method compared to the r_2 proxy from the HTI Fourier coefficient method. In Figure 5.41 we see that this area was somewhat identified in the HTI method, however, in the HTI method this area does not significantly stand out against the background noise. Referring back to the HTI analyses described in Chapter 4, this same area is hinted at having high fracture density, but it does not significantly stand out against the background signal in any

method (for example, see Figure 4.10). The orthorhombic method's ability to successfully distinguish this area of higher fracture density could be attributed to two possible factors:

1. The orthorhombic method explicitly accounts for the VTI component of shale by assuming orthorhombic anisotropy rather than HTI anisotropy.
2. The orthorhombic method calculates Fourier coefficients at each incident angle independently. These coefficients are then used in a second weighted least squares inversion to find weights w_{ij} that describe Fourier information at all incident angles, and which are used as a proxy for fracture density. Using weights w_{ij}, which contain information from all incident angles, results in the maximum use of data and treats the AVO component of the data as informative rather than as noise.

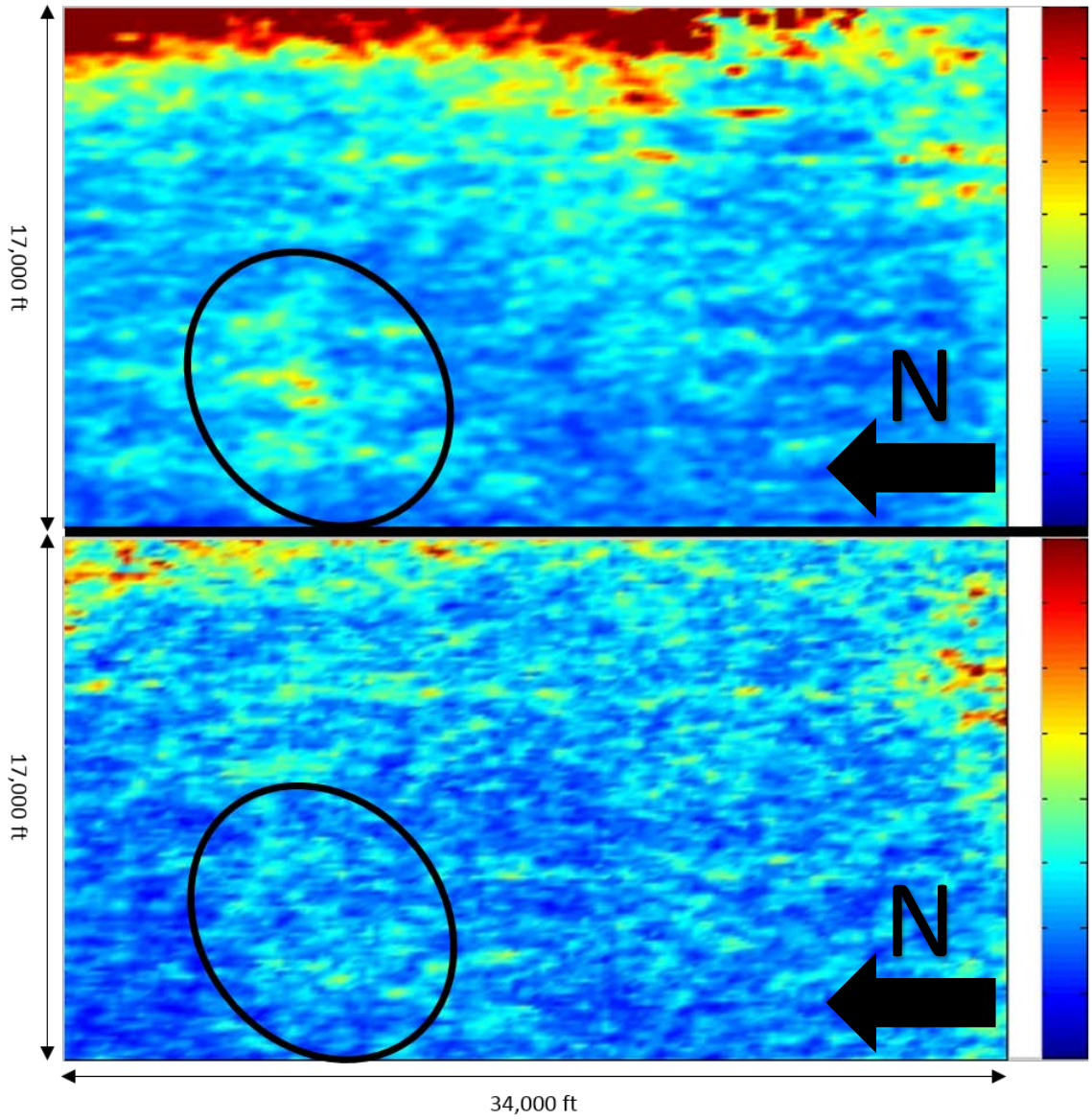

Figure 5.41: Comparison of proxies for fracture density from the Orthorhombic and HTI Fourier coefficient decomposition based methods. The top image depicts R_2^*, a proxy for fracture density, as calculated by the Orthorhombic Fourier coefficient decomposition method. 2-D lateral smoothing has been applied. The bottom image depicts r_2 as calculated by the HTI Fourier coefficient decomposition method. Values have been vertically averaged throughout the Haynesville using a simple arithmetic mean. Warmer colors indicate denser fracturing. The black circle indicates an area of anomalously high fracture density identified in the orthorhombic method. The black arrows indicate the direction of north.

While showing an increased ability to identify areas of anomalously high fracture density is an obvious triumph, the orthorhombic method employed does have some downfalls. The first shortcoming is how it deals with edge effects. While some edge effects corresponding to (falsely) anomalously high fracture density on the eastern and southern edges of the study area can be seen in the HTI results, these edge effects are very pronounced in the orthorhombic method results. This can be seen in several of the Figures presented in this chapter. In the areas exhibiting edge effects data is generally sparser, and azimuthal coverage is more limited. The increased sensitivity to edge effects may be due to the orthorhombic method considering each incident angle separately, whereas the HTI method considers all incident angles simultaneously. While considering each incident angle separately results in using AVO effects as information rather than as noise, it reduces the number of data points available for fitting at any given incident angle. When significant azimuthal data in one direction is missing, the curve fitting algorithm is inclined to fit a Fourier series with significant azimuthal variation, resulting in high fracture density inversion results, in order to better fit available data. This occurs despite the fact that the available data does not directly support this extreme azimuthal variation. An example of this phenomenon is shown in Figure 5.42. After trial and error, I decided that a minimum of eight data points would be necessary to attempt to fit a curve, believing this to be a decent tradeoff between including more data in the inversion and having sufficient confidence in fitted curves. Unfortunately, this may not have been sufficient in the areas depicting strong edge effects. Note that in Figure 5.42, the curve depicting improper fitting only contains seven data points, and thus would not be used in this analysis.

The second downfall associated with the proposed method is a significant increase in required computation time when compared to existing HTI methods. This is to

some extent unavoidable, as the methodology inherently requires more computations to be made. Nevertheless, this method can still be executed in a reasonable amount of time. When run on a windows desktop with an Intel i7-4770 processor, each analysis took approximately 3 days to run. If this were run on the entire dataset rather than a reduced 137 inline by 137 crossline portion, the relative increase in area would suggest an approximate 10 fold increase in run time, indicating that each analysis would take approximately 30 days. However, if implemented using CPU and/or GPU clusters, the run time of the analysis could be significantly reduced to acceptable levels, even when applied to very large datasets. Additional algorithm refinement could additionally reduce the required computational time. Despite taking longer to perform the analysis, the ability to successfully identify areas of higher fracture density and to correctly determine the azimuth of fracture orientation seems to justify the additional computational expense associated with the proposed method.

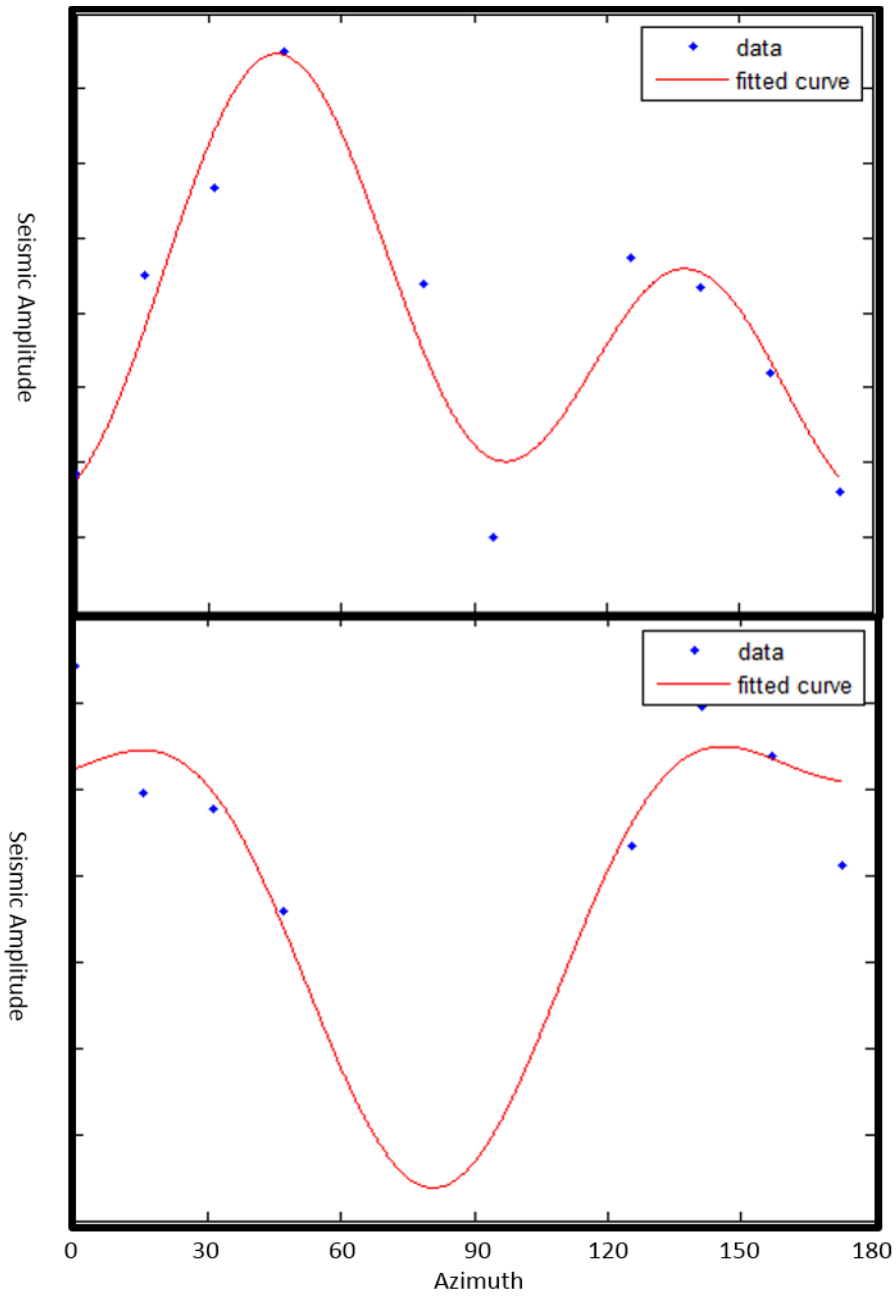

Figure 5.42: Examples of fitting a Fourier series at a specific time / location and constant incident angle with sufficient azimuthal coverage (upper) and insufficient azimuthal coverage (lower). When large chunks of azimuthal coverage are missing (lower) the curve fitting algorithm creates extreme and unrealistic features to better match available data. The X axis represents azimuth (ranging from 0 to 180 degrees), and the Y axis represents seismic amplitude.

5.7 SUMMARY

A new fracture characterization method based on Fourier decomposition of the seismic data, which is partially valid in orthorhombic anisotropic media, has been presented. In this method, a modified 4th order Fourier series was fit to azimuthal variations in the seismic data. The proposed method was applied to a variety of synthetic datasets as well as to seismic data from the Haynesville Shale. Fracture azimuth was determined by analyzing the phase of the 2nd order coefficient and then determining if a 90 degree phase shift was required. Azimuth inversion results from high incident angle data proved to be very accurate in the synthetic examples. Inversion results from the Haynesville Shale indicate that the azimuth of the predominant fracture set has a compass bearing of approximately 82 degrees, rotated slightly counterclockwise from an east-west orientation. Fracture density was determined using a proxy based on the total energy present in the 2nd order Fourier coefficients (R_2^*), found via a weighted least squares inversion of Fourier coefficient data from all incident angles. Results have been compared to an analogous HTI fracture characterization method also based on Fourier decomposition of the data. Comparing these results suggest that this novel method unambiguously determines fracture azimuth, whereas the existing HTI methods contains occasional 90 degree ambiguities. Fracture density results from the proposed orthorhombic method show an increased ability to find pockets of relatively high fracture density, although unfortunately this new method suffers from extended computation time and prominent edge effects. Future algorithm refinement and the use of CPU and/or GPU clusters to perform this analysis can resolve both these issues, making the new orthorhombic method a potentially valuable new fracture characterization tool.

Chapter 6: Conclusions and Future Work

6.1 Conclusions

The work presented in this thesis examines and implements three distinct fracture characterization methods based on analyzing azimuthal variations in seismic amplitude (AVAZ). All methods were applied to 3D seismic data of the Haynesville Shale from Panola County, Texas.

Chapter 4 described two commonly used fracture characterization techniques based on the assumption of a single closely spaced rotationally invariant fracture set imbedded in an otherwise isotropic rock, resulting in HTI anisotropy. The first technique is based on the Rüger AVO equation, and the second technique is based on decomposing the seismic data into a modified 4^{th} order Fourier series. Both methods indicate laterally variable fracture density, with generally higher fracturing in the northern part of the area. Anomalously high fracture density on the Eastern and Southern edges of the survey area are not believed to be real features. Fracture orientation results from both the Rüger method and the Fourier decomposition method had extreme variability, and ultimately proved to be unreliable due to unresolved 90 degree phase shifts present in the inverted results. The HTI Fourier decomposition method additionally inverted for normal and tangential fracture weaknesses, and used these values to calculate a fluid indicator attribute. Fracture weaknesses were incorrect by a scaling factor, however, this scaling factor is removed in the calculated fluid indicator attribute which utilizes the ratio of normal and tangential fracture weaknesses. The fluid indicator attribute indicates that fractures are likely dry or gas filled, which is consistent with a priori information of the area.

Chapter 5 describes a novel fracture characterization method based on a more generalized Fourier decomposition of the data. In this method, a modified 4^{th} order

Fourier series was fit to data at individual incident angles, and a new method to determine fracture azimuth from the 2nd order Fourier coefficient phase was implemented. This method, in synthetic examples, produced the correct azimuth about 85% of the time when considering only high incident angle information. When applied to the Haynesville dataset, inversion results indicate that the strike of the azimuth of the dominant fracture set has a compass bearing of approximately 82 degrees. Using this fracture azimuth information, a specialized version of the analysis, which is valid in orthorhombic anisotropy, was repeated to determine fracture density. After new Fourier coefficients were found at each incident angle, time, and CDP location, a weighted least squares inversion was used to invert for weights w_{ij} which describe both AVO and AVAZ aspects of the data. The weights w_{12} and w_{22}, which correspond to the 2nd order Fourier coefficients, were combined and used as a proxy for fracture density. Results were compared to an analogous HTI fracture characterization techniques. Fracture azimuth results agreed decently well, though differed in some areas by 90 degrees due to an ambiguity in determining fracture orientation in the existing HTI methods. Fracture density results from the orthorhombic method also agreed well with results from an analogous HTI method, however proved much more capable of identifying localized areas of high fracture density than the analogous HTI method.

6.2 FUTURE WORK

Future work may include revising the novel method presented in Chapter 5 such that the equations used in resolving fracture azimuth are explicitly valid in orthorhombic media. Future work may additionally include developing and implementing other fracture characterization techniques that utilize azimuthal traveltime differences (VVAZ), and which integrate the use of P-S data and well log data into the analysis. The integration of

additional data can increase confidence in inversion results for fracture orientation and fracture density.

References

Aki, Keiiti, and Paul G. Richards. *Quantitative Seismology: Theory and Methods*. San Francisco: W.H. Freeman, 1980. Print.

Alhussain, Mohammed A. *Fracture Characterization of a Carbonate Reservoir in the Arabian Peninsula*. Diss. The University of Texas at Austin, 2013. N.p.: n.p., n.d. *University of Texas Libraries*. Web.

Bakulin, Andrey, Vladimir Grechka, and Ilya Tsvankin. "Estimation of Fracture Parameters from Reflection Seismic Data—Part I: HTI Model Due to a Single Fracture Set." *Geophysics* 65.6 (2000): 1788. Web.

Bakulin, Andrey, Vladimir Grechka, and Ilya Tsvankin. "Estimation of Fracture Parameters from Reflection Seismic Data—Part II: Fractured Models with Orthorhombic Symmetry." *Geophysics* 65.6 (2000): 1803. Web.

Becker, Lauren E. *The Seismic Response to Fracture Clustering: A Finite Element Wave Propagation Study*. Thesis. The University of Texas at Austin, 2014. N.p.: n.p., n.d. *University of Texas Libraries*. Web.

Chopra, Satinder, and Kurt J. Marfurt. "Integration of Coherence and Volumetric Curvature Images." *The Leading Edge* 29.9 (2010): 1092. Web.

Downton, Jon. "Azimuthal Fourier coefficients: A Simple Method to Estimate Fracture Parameters." *SEG Expanded Abstracts* (2011): 269-73. Web.

Downton, Jon, Benjamin Roure, and Lee Hunt. "Azimuthal Fourier coefficients." *CSEG Recorder* December (2011): 22-36. Web.

Gersztenkorn, Adam, and Kurt J. Marfurt. "Eigenstructure-based Coherence Computations as an Aid to 3-D Structural and Stratigraphic Mapping." *Geophysics* 64.5 (1999): 1468. Web.

Graebner, Mark. "Plane-wave Reflection and Transmission Coefficients for a Transversely Isotropic Solid." *Geophysics* 57.11 (1992): 1512. Web.

Grechka, Vladimir, and Ilya Tsvankin. "3-D Description of Normal Moveout in Anisotropic Inhomogeneous Media." *Geophysics* 63.3 (1998): 1079. Web.

Hammes, Ursula, H. Scott Hamlin, and Thomas E. Ewing. "Geologic Analysis of the Upper Jurassic Haynesville Shale in East Texas and West Louisiana." *AAPG Bulletin* 95.10 (2011): 1643-666. Web.

Hudson, John A. "Wave Speeds and Attenuation of Elastic Waves in Material Containing Cracks." *Geophysical Journal International* 64.1 (1981): 133-50. Web.

Hunt, Lee, Satinder Chopra, Scott Reynolds, and Scott Hadley. "On Calibrating Curvature Data to Fracture Density: Causes." *CSEG Recorder* 34.10 (2009): n. pag. Web.

Orangi, Abdollah, Narayana R. Nagarajan, Mehdi M. Honarpour, and Jacob J. Rosenzweig. "Unconventional Shale Oil and Gas-Condensate Reservoir Production, Impact of Rock, Fluid, and Hydraulic Fractures." *Society of Petroleum Engineers* January (2011): n. pag. Web.

Pšenčík, Ivan, and Dirk Gajewski. "Polarization, Phase Velocity, and NMO Velocity of QP-waves in Arbitrary Weakly Anisotropic Media."*Geophysics* 63.5 (1998): 1754. Web.

Plackett, Robin L. "Some Theorems in Least Squares." *Biometrika* 37.1/2 (1950): 149. Web.

Rüger, Andreas. "P-wave Reflection Coefficients for Transversely Isotropic Models with Vertical and Horizontal Axis of Symmetry." *Geophysics* 62.3 (1997): 713. Web.

Rüger, Andreas, and Ilya Tsvankin. "Using AVO for Fracture Detection: Analytic Basis and Practical Solutions." *The Leading Edge* 16.10 (1997): 1429. Web.

Schoenberg, Michael. "Elastic Wave Behavior across Linear Slip Interfaces."*The Journal of the Acoustical Society of America* 68.5 (1980): 1516. Web.

Schoenberg, Michael, and Colin Sayers. "Seismic Anisotropy of Fractured Rock." *Geophysics* 60.1 (1995): 204. Web.

Sen, Mrinal. *GEO 390D - Seismology III*. University of Texas at Austin, n.d. Web.

Sen, Mrinal. *GEO 384M - Inverse Theory*. University of Texas at Austin, n.d. Web.

Shaw, Ranjit K., and Mrinal K. Sen. "Use of AVOA Data to Estimate Fluid Indicator in a Vertically Fractured Medium." *Geophysics* 71.3 (2006): C15. Web.

Sone, Hiroki, and Mark D. Zoback. "Mechanical Properties of Shale-gas Reservoir Rocks — Part 1: Static and Dynamic Elastic Properties and Anisotropy." *Geophysics* 78.5 (2013): n. pag. Web.

Strijker, Geertje, Giovanni Bertotti, and Stefan M. Luthi. "Multi-scale Fracture Network Analysis from an Outcrop Analogue: A Case Study from the Cambro-Ordovician Clastic Succession in Petra, Jordan." *Marine and Petroleum Geology* 38.1 (2012): 104-16. Web.

Sun, Sam Z., Di Wang, and Xinyuan Zhou. "3D Amplitude-Preserved Full-Azimuth Anisotropic Imaging and CRP Gathering: An Appealing Method for Integrated Fracture Detection." *SEG Expanded Abstracts* (2013): n. pag. Print.

Xiao, Lizhi, and Kui Li. "Characteristics of the Nuclear Magnetic Resonance Logging Response in Fracture Oil and Gas Reservoirs." *New Journal of Physics* 13 (2011): n. pag. Web.

Xu, Yong, and Yongyi Li. "Uncertainties in Azimuthal AVO Analysis." *CSEG Expanded Abstracts* (2001): 24-27. Web.

Yamartino, Robert J. "A Comparison of Several “Single-Pass” Estimators of the Standard Deviation of Wind Direction." *Journal of Climate and Applied Meteorology* 23.9 (1984): 1362-366. Web.

Yenugu, Malleswar, and Kurt J. Marfurt. "Relation between Seismic Curvatures and Fractures Identified from Image Logs - Application to the Mississippian Reservoirs of Oklahoma, USA." SEG Technical Program Expanded Abstracts 2011, n.d. Web.

Zoeppritz, Karl. "Erdbebenwellen VII B: über Reflexion Und Durchgang Seismischer Wellen Durch Unstetigkeitsflächen." *Mathematisch-Physikalische Klasse* (1919): 66-84. Web.

Vita

Anthony Barone was born in San Diego, California in 1990. Upon graduating from Westview High School in 2008, Anthony attended the University of California at Berkeley, where he earned a Bachelor's of Arts in Geophysics in 2012. Anthony continued his education as a graduate student at The University of Texas at Austin, Jackson School of Geosciences, where he graduated and earned a Master's of Science in Geological Science with an emphasis in Geophysics in the summer of 2015. Following graduation, Anthony began pursuing a Doctor of Philosophy in Geological Sciences with an emphasis in Geophysics at The University of Texas at Austin.

Email: abarone@utexas.edu

This thesis was typed by Anthony William Barone.